TECHNISCHE UNIVERSITÄT WIEN
Vienna University of Technology

DISSERTATION

Relevance of the irreversible degradation of superconducting Nb_3Sn wires and cables caused by transverse stress at room temperature within the FCC study at CERN

Ausgeführt zum Zwecke der Erlangung des akademischen Grades eines Doktors der technischen Wissenschaften unter der Leitung von

Priv.Doz. Dipl.-Ing. Dr.tech. Michael Eisterer
E141
Atominstitut

eingereicht an der Technischen Universität Wien
Fakultät für Physik

von

Dipl.-Ing. Patrick Ebermann
Matrikelnummer 0825085
Hofuren 49
4574 Nennigkofen, Schweiz

Genf, 23. September 2019

Unterschrift

Acknowledgment

I am very thankful to my university supervisor, Michael Eisterer at the Vienna University of Technology, Atominstitut, as well as my supervisor at CERN, Friedrich Lackner. I am also grateful to the head of the Austrian CERN PhD programme, Michael Benedikt.

In addition, a thank you to my colleagues at the CryoLab (CERN), especially to Torsten Köttig, who continuously supported me during the design, build-up and improvement of the cryostat insert for the wire measurements. I also thank Jérôme Fleiter and his colleagues from the FRESCA cable test station (CERN) for the collaboration regarding the cable measurements.

Finally, I would like to thank my student and post-doctoral colleagues at CERN and the Atominstitut for the countless technical and scientific discussions as well as the collaboration in various projects.

My special gratitude goes to my life partner Doris for her loving support and patience.

Kurzfassung

Die **Future Circular Collider (FCC)** Studie ist eine Forschungsstudie, die die Realisierbarkeit und das Konzept eines zukünftigen Teilchenbeschleunigers als Nachfolger des Large Hadron Colliders (LHC) erarbeitet. Die Studie untersucht den Bau eines ringförmigen Beschleunigers mit einem Umfang von 80 km bis 100 km und soll für Anwendungen über den Kapazitäten des High Luminositiy LHC (HL-LHC), voraussichtlich nach 2035, dienen. Als endgültige Betriebsart ist ein Protonenbeschleuniger (FCC-hh) mit einer Kollisionsenergie von bis zu 100 TeV und einer Luminosität von $5 \cdot 10^{38}\,\mathrm{m}^{-2}\,\mathrm{s}^{-1}$ bis $30 \cdot 10^{38}\,\mathrm{m}^{-2}\,\mathrm{s}^{-1}$ vorgesehen.

Ein Teil der Sudie ist die Forschung und Entwicklung von **supraleitenden Ablenkmagneten** mit einem nominalen Feld von 16 T bis 20 T bei einer Betriebstemperatur zwischen 4.3 K und 1.9 K. **Nb_3Sn-Multifilamentdrähte** wurden als Grundlage für den Leiter ausgewählt. Um den Bau und Betrieb solcher Beschleunigermagnete zu erforschen und zu entwickeln, wurde ein 16 T Dipol-Programm gestartet. Neben vielen anderen Aspekten wird die Fertigung dieser Beschleunigermagneten untersucht. Das geplante supraleitende Material Nb_3Sn ist sehr spröde und seine Eigenschaften sind druckabhängig. Aus diesem Grund ist eine Charakterisierung des mechanischen Verhaltens sowie der Degradation der supraleitenden Eigenschaften auf Grund der mechanischen Belastungen für die Fertigung der Spulen sowie den Bau der Magnete entscheidend.

Die supraleitenden Spulen werden aus unreagierten Nb_3Sn Rutherford-Kabeln gewickelt und anschließend einer Wärmebehandlung mit Temperaturen von bis zu 650 °C unterzogen, wodurch sich die supraleitende A-15 Phase Nb_3Sn bildet („wind and react"-Technik). Anschließend werden die Spulen inklusive Instrumentierung und Quench-Heizern mittels Vakuum-Druck-Verfahren mit Epoxidharz imprägniert, wobei die Rutherford-Kabel zuvor mit einer Fieberglas-Isolation umwickelt worden sind. Jegliche Bewegungen des Leiters können zu einer Störung des Betriebes oder im ungünstigsten Fall zur Zerstörung des Magneten führen. Aus diesem Grund werden die imprägnierten Spulen dauerhaft vorgespannt. So können die stromführenden Leiter der enormen Lorentzkraft während des Betriebes standhalten. Die Vorspannvorrichtung supraleitender Magnete, realisiert durch beispielsweise Collars oder Bladder-and-Key Systeme, spannen die Spulen beim Zusammensetzen des Magneten mit 70 MPa bis 150 MPa vor, woraus eine beabsichtigte bleibende Vorspannung von 50 MPa bis 120 MPa resultiert. Abhängig von den Fertigungsgenauigkeiten kann es entlang der Spule während des Vorspannungsprozesses zu lokalen Stressspitzen kommen, die den Supraleiter beschädigen und somit eine unbeabsichtigte irreversible Degradation hervorrufen können.

Ziel dieser Arbeit ist die Analyse der irreversiblen Degradation des Supraleiters, verursacht durch transversalen Stress bei Raumtemperatur, der repräsentativ für die mechanischen Belastungen während der Fertigung, im Speziellen des Vorspannungsprozesses, steht. Ein Experiment an Kabeln wurde ausgearbeitet, um so den Degradationsvorgang nahe der realen Situation während des Vorspannungsprozesses nachzubilden. Zusätzlich wurde ein Experiment mit Drähten durchgeführt, um den Mechanismus und die Ursache des Degradationsprozesses im Detail zu analysieren. Dazu wurde die Arbeit in folgende **Teilbereiche** aufgeteilt:

- Eine existierende **hydraulische Presse** wurde modernisiert, um einen homogenen Druck auf Kabel- und Drahtproben auszuüben. Hydraulische Steuerkomponenten sowie Instrumentierungen wurden erneuert, um einen genauen und zuverlässigen Betrieb zu gewährleisten. Um die Homogenität der Druckverteilung auf die Proben zu optimieren, wurden druckempfindliche Folien in Kombination mit einer selbstentwickelten Evaluierungssoftware genutzt. Die hydraulische Presse wurde für die beiden in der Folge beschriebenen Experimente verwendet.

- **Imprägnierte Rutherford-Kabel** wurden mit transversalem Druck bei Raumtemperatur belastet und anschließend wurde ihr kritischer Strom in der FRESCA Kabelteststation des CERN bei Tieftemperatur gemessen. Dieser Vorgang wurde iterativ mit steigendem Drucklevel wiederholt. Die FRESCA Kabelteststation verfügt über eine Stromquelle mit bis zu 32 kA und einen Dipolmagneten mit einem nominalen Feld von 9.6 T. Die Probe kann mittels Kühlung mit flüssigem oder supraflüssigem Helium bei einer Temperatur von 4.3 K oder 1.9 K gemessen werden.

- Um den Degradationseffekt genauer zu untersuchen sowie auch das Spektrum an Messmethoden zu erweitern, wurden ebenso die Auswirkungen des transversalen Stresses auf **einzelne Drähte** bei Raumtemperatur untersucht. Dazu wurden Drähte mittels der oben erwähnten hydraulischen Presse mit Druck belastet. Nach jedem Drucklevel wurde eine Transportstrommessung von bis zu 150 A im Selbstfeld mittels eines **selbstentwickelten Kryostatenaufbaus** durchgeführt. Der supraleitende Draht wurde konduktiv, mittels flüssigen Heliums eines Phasenseparators und Wärmetauschern, gekühlt. Anstatt eines außen angelegten Magnetfeldes wurde die Probentemperatur

bis nahe der kritischen Temperatur erhöht, um so den kritischen Strom in einen realisierbaren Bereich zu schieben. Dieses unübliche Konzept wurde zum einem gewählt um mechanisches Beanspruchen, d.h. Lorentz Kräfte, während den Tieftemperaturmessungen zu vermeiden. Zum anderen wurde eine **alternative kosteneffiziente Messmethode zur Charakterisierung supraleitender Drähte** mit hohem Durchsatz demonstriert. Der Kryostatenaufbau diente als Machbarkeitsstudie einer Messstation für Drähte ohne zusätzlichen Magneten und ohne kontinuierliche Versorgung von flüssigem Helium, d.h. eine Realisierung mit einem kryogenen Kühlsystem (zweistufigem Cryocooler). Ergänzend wurden kurze Probenstücke mit äquivalentem Druck belastet und einer Magnetisierungsmessung mit einem SQUID Magnetometer unterzogen, um die Transportstrommessungen zu überprüfen. Weiters wurde eine Röntgentomographie belasteter und unbelasteter Proben veranlasst, um mittels Finite-Elemente-Analyse die Druckverteilung im Draht, im Speziellen auf die supraleitenden Sub-Elemente, zu simulieren.

- Zusätzlich wurden belastete und unbelastete Kabel- sowie Drahtproben einer metallographischen Studie unterzogen, um so in einer **Elektronenrastermikroskopie** die Degradation der (Mikro-) Struktur zu untersuchen.

Die Messung des kritischen Stroms der **imprägnierten Rutherford-Kabel** zeigte eine erste Degradation nach einer Belastung von 175 MPa. Dies geht einher mit den Ergebnissen der Mikroskopie, die erste Brüche in den supraleitenden Sub-Elementen nach einer Belastung von 175 MPa nachgewissen hat. Die Brüche verlaufen vorwiegend in longitudinaler Richtung, im Gegensatz zu Brüchen, die von Biege- oder Axialbelastung verursacht werden.

Im Rahmen des **Drahtprojekts** konnte der Degradationsprozess des kritischen Stroms und weiterer intrinsischer supraleitender Eigenschaften grundlegender untersucht werden. Die Mikroskopie zeigte eine erste plastische Deformation nach einer Belastung von 50 MPa und eine Entstehung von Brüchen in den fragilen Sub-Elementen nach einer Belastung von 100 MPa. Die plastische Deformation der Kupfermatrix erzeugt eine verbleibende Vorspannung auf die supraleitenden Sub-Elemente, wodurch eine Veränderung der druckabhängigen Eigenschaften festgestellt werden konnte. Ab einer Belastung von 100 MPa beginnt die Degradation, verursacht durch Brüche im supraleitenden Material.

Sowohl die realisierte Transportstrommessung nahe der kritischen Temperatur als auch die Magnetisierungsmessungen zeigten sich als geeignet um irreversible Auswirkungen von transversalem Stress bei Raumtemperatur auf die supraleitenden Eigenschaften zu beobachten.

Abstract

The **Future Circular Collider (FCC)** study is aiming to develop a conceptual design for a future particle accelerator for objectives beyond the capabilities of the Large Hadron Collider (LHC) including its high luminosity upgrade, which is planned to expire after 2035. The study investigates the feasibility of a circular collider with a circumference between 80 km and 100 km. The final option is a hadron collider (FCC-hh) to achieve a collision energy of up to 100 TeV and a luminosity of $5 \cdot 10^{38}\,\mathrm{m^{-2}\,s^{-1}}$ to $30 \cdot 10^{38}\,\mathrm{m^{-2}\,s^{-1}}$.

One part of the study is the research and development of **superconducting bending magnets** with a nominal field of 16 T to 20 T at an operational temperature between 4.3 K and 1.9 K. **Multi-filamentary Nb_3Sn wires** are considered as the baseline for the conductor. Therefore, a 16 T dipole development programme was launched to investigate the feasibility of fabricating and operating high field accelerator magnets with the required performance. Among other research topics, the magnet manufacturing process is studied. The high brittleness and strain sensitivity of Nb_3Sn make research on the mechanical limits of the coil at magnet manufacturing and its effects on the electrical performance essential. One of the objectives of this technology programme is the investigation of the degradation of the conductor during the magnet assembly.

The Nb_3Sn coils are wound of non-reacted Rutherford cables and subjected to a reaction heat treatment of up to 650 °C, in which the superconducting A-15 phase Nb_3Sn is formed ("wind and react" technique). Afterwards, the coil including the instrumentation and quench heaters are impregnated with epoxy resin to ensure electrical insulation between the cable turns, which are initially separated by braided fibre glass. Regardless of the geometry of the coil, enormous Lorentz forces during operation require mechanical force-restraining structures to prevent movements of the superconductor. These movements can cause training or disturbance quenches followed by a failure of the magnet. Force-restraining structures are applying high nominal stress in the order of 70 MPa to 150 MPa on the coil during magnet assembly. This is implemented with e.g. collars or bladder-and-key concepts resulting in a desired residual pre-stress between 50 MPa to 120 MPa. Depending on the homogeneity of the stress and the production accuracy, the application of the load may cause even higher local stresses leading to undesired irreversible damage of the superconductor.

The objective of this thesis is to analyse the irreversible performance loss of the superconductor caused by transverse compressive stress exerted at room temperature during the magnet assembly, especially the force-restraining procedure. First, a cable study was launched to gain quantitative results of the degradation under conditions mimicking the real situation during the magnet assembly. Additional, the degradation mechanism was investigated in detail on single wires. Following this approach, the presented thesis consists of the following **subtasks**:

- An existing **hydraulic press** was refurbished to guarantee a well-defined homogeneous stress application on the specimens. State-of-the-art hydraulic components and calibrated instrumentation were used to ensure accurate and reliable operation. To facilitate the optimisation of the stress homogeneity on the specimen's surface, an evaluation software for pressure-sensitive films was developed. The refurbished press served as a necessary and essential tool in the major experiments explained below.

- **Impregnated Rutherford cable** double stacks were exposed to transverse compressive stress and their electrical performance was tested in the FRESCA cable test station. FRESCA compatible samples were iteratively exposed to homogeneous stress at room temperature by using the above mentioned hydraulic press. Subsequently, their critical current was measured at low temperature. The FRESCA cable test station supplies a test current of up to 32 kA and a nominal background magnetic field of 9.6 T. The sample can be cooled to a temperature of 4.3 K or 1.9 K by using liquid or superfluid helium, respectively.

- To investigate the effect of degradation in a more general case and to widen the spectrum of measurement methods, the degradation of **single wires** due to transversal stress at room temperature was also measured. For this purpose, single wires were exposed to stress by the above mentioned hydraulic press. Subsequently, transport current measurements were performed in a **self-designed cryostat setup** with a test current of up to 150 A. The sample was conductively cooled by the use of liquid helium, a phase separator and heat exchangers. Instead of using an applied magnetic field to shift the critical current into the accessible range, the temperature was adjusted close to the critical temperature. This unusual measurement principle was chosen, on the one hand, to avoid additional forces, i.e. Lorentz force, during the low-temperature measurements. On the other hand, **an alternative method was demonstrated to characterise superconducting wires** in

a cost-efficient way with high throughput. The setup served as a feasibility study for a measurement station for wires without a background magnet and without continually supplying liquid helium, i.e. an implementation with a cryogenic refrigerator system (two-stage cryocooler). For confirmation of these transport current measurements, a magnetisation measurement campaign of short samples was performed with a SQUID magnetometer. Moreover, an X-ray tomography following a finite element analysis was performed to get the stress distribution within the wire, especially on the sub-elements.

- Finally, a supplementary metallographic preparation of specimens, wires and cables after stress exertion, was carried out. This was performed to investigate the changes in the (micro-) structure with a **scanning electron microscope**.

The measurement of a **double cable stack** with a particular configuration and impregnation showed a start of degradation of the critical current at 175 MPa. These results are correlated with the crack initiation in the Nb_3Sn sub-elements revealed by the metallographic observation, leading to current sharing within the cable. The induced cracks are mainly in longitudinal direction, contrasting fracture shapes caused by bending or axial loads.

The **wire investigation** provided a detailed picture of the degradation process of the critical current as well as the intrinsic properties of the superconductor, independent of the cable or coil properties. The microscopy analysis revealed that the plastic deformation of the wire started at 50 MPa, and the crack initiation at 100 MPa. The plastic deformation of the copper matrix below the crack initiation threshold generated a residual strain on the superconducting sub-elements. This resulted consequently in the change of strain-depending properties of the superconductor. After applying 100 MPa, the performance of the wire decreased due to the fracture of the sub-elements.

Both, implemented transport current measurements close to the critical temperature and the magnetisation measurements were shown to be suitable to monitor irreversible effects after the application of transverse stress at room temperature.

Contents

List of abbreviations & symbols

Frequently used abbreviations and symbols in the presented thesis are summarised here.

Abbreviations

BSE	Backscattered electron
EDX	Energy dispersive X-ray spectroscopy
FCC	Future circular collider
FEM	Finite element method
FRESCA	Facility for reception test of superconducting cables
HL-LHC	High luminosity LHC
HTS	High-temperature superconductors
LHC	Large hardon collider
LTS	Low-temperature superconductors
MQE	Minimum quench energy
MQXF	Low-β^* quadrupole in the intersection region of the planned HL-LHC
NPZ	Normal propagation zone
ODE	Ordinary differential equation
OM	Optical microscope
PID	Proportional-integral-derivative
PIT	Power-in-tube
RHT	Reaction heat treatment
RRP	Restacked-rod process
RSO	Reciprocating sample option
RT	Room temperature
SE	Secondary electron
SEM	Scanning electron microscope
SQUID	Superconducting quantum interference device
USL	Unified scaling law

Symbols

The magnetic flux density B in Tesla is commonly designated as the magnetic field in the literature of applied superconductivity, which is performed in this work as well. All quantities are in SI units, except stated otherwise.

Constants

$\hbar$	Reduced Planck's constant
Φ_0	Magnetic flux quantum
μ_0	magnetic field constant

Notation

$\mathbf{F}$	Vector F
F	Amount of vector $\mathbf{F}$
$\mathbf{e}_\mathrm{i}$	Unit vector in direction of i

Variables

A	Area
$A_{\text{A-15}}$	Average A-15 area of Nb_3Sn composite wire
A_{proj}	Central longitudinal cross-section of a cylindrical wire
A_{nom}	Nominal area of cable
b	Reduced magnetic field
B	Magnetic field inside the material
B_{c}	(Thermodynamic) critical field
B_{c1}	Lower critical field
B_{c2}	Upper critical field
$B_{\text{c2}}{}^{*}$	Effective upper critical field
c	Specific heat capacity
E	Electrical field
E_{c}	Electrical field criterion
F	Force
$f(b)$	General pinning force function
f	Frequency
$g(\varepsilon)$	Strain scaling law
$h(t)$	Temperature scaling law
I	Electrical current
I_{c}	Critical current
J	Electrical current density
J_{c}	Critical current density
l	Electronic mean free path
L	Length of sample, Machine luminosity, Voltage tape distance
n	Resistive transition index
N	Number of sub-element
m	Magnetic moment
m'	In-phase magnetic moment of AC measurement
m''	Out-of-phase magnetic moment of AC measurement
m_{irr}	Irreversible magnetic moment
Q	Heat energy
RRR	Residual resistance ratio
t	Time, Reduced temperature
T	Temperature
T_{c}	Critical temperature
$T_{\text{c}}{}^{*}$	Effective critical temperature
T_{cs}	Current sharing temperature
ε	Strain
ε_0	Intrinsic strain
ε_{m}	Thermal-induced pre-strain
V	Electrical voltage
ΔT_{c}	Width of resistive transition
$\varkappa$	Ginzburg-Landau parameter
λ	Thermal conductivity
λ_{L}	London penetration depth
ρ	Electrical resistivity
ρ_{m}	Volume mass density
ρ_{i}	Inner radius of superconducting sub-element
ρ_{o}	Outer radius of superconducting sub-element
σ	Mechanical stress
σ_{nom}	Nominal (target) stress
$\sigma_{\text{LC},\Sigma}$	Actual stress evaluated by installed load cells
ξ	Ginzburg-Landau coherence length
ξ_{BCS}	BCS coherence length
χ'	In-phase magnetic AC susceptibility
χ''	Out-of-phase magnetic AC susceptibility

Chapter 1

Introduction

The first chapter of this thesis gives an introduction through the physical background, the motivation for the topic as well as an overview of the performed experiments. Section 1.1 introduces the aims and tasks of CERN and the currently ongoing FCC design study for a new circular particle collider, at which this work is targeting. Section 1.2 gives an overview of superconductivity as well as the technical implementation of superconducting Nb_3Sn wires, especially the Restacked-Rod Process (RRP), and the specified assessment criteria. An overview of superconducting magnets and their manufacturing process is given in section 1.3. It will highlight the challenges and potential difficulties while building Nb_3Sn accelerator magnets. Specifically, the ongoing fabrication of the 11 T dipole magnets for the HL-LHC project will lead to the task definition explained in section 1.5. This allows developing the described strategy on how to investigate the degradation as close as possible to the real conditions during magnet assembly in correlation with a fundamental analysis of the degradation process and its reasons.

1.1 CERN & FCC design study

The European Organisation of Nuclear Research (CERN) was established in 1954 on the French frontier in the west of the Swiss canton Geneva. It has more than 20 member states and employs about 2600 scientists, engineers and technician together with around 14000 visiting users. The core competence of CERN is accelerator science and particle physics. It operates various accelerators, a decelerator and further necessary infrastructure needed for high-energy physics research.

1.1.1 LHC

An overview of CERN's current high-energy physics infrastructure can be seen in figure 1.1, which serves for various experiments with different objectives.

The current largest accelerator is the Large Hadron Collider (LHC), having a collision energy of 7 TeV and a maximal luminosity of $10^{38}\,\mathrm{m^{-2}\,s^{-1}}$ at his full commissioning 2010 [28]. It is housed in the civil engineering infrastructure of the former Large Electron Positron Collider (LEP) [182], which was in operating between 1989 and 2000. In the period from 2010 to 2023, the LHC is planned to reach within two long-term shutdowns a collision energy up to 14 TeV and a luminosity up to $2 \cdot 10^{38}\,\mathrm{m^{-2}\,s^{-1}}$.

The most known purpose is the experimental confirmation of the standard model of particle physics, especially the Higgs mechanism, as well as aspects regarding super-symmetric partners of particles. A remarkable achievement of the LHC, beside the demonstration of large scale accelerator technology, was the confirmation of the Higgs boson in July 2012, leading ultimately to the Nobel prize in physics in October 2013.

The two most comprehensive identification parameters of particle colliders are the collision energy and the machine luminosity. The collision energy, the available energy to produce new particle as a collision product, is given by the sum of the beam energies in the case of the LHC, a circular collider. The luminosity L is the ratio of the number of detected events N_D per second to the interaction cross-section σ given by

$$\frac{\mathrm{d}N_\mathrm{D}}{\mathrm{d}t} = L\,\sigma \tag{1.1}$$

in $\mathrm{m^{-2}\,s^{-1}}$, which depends only on the beam parameters. Hence it is a measure for the beam focusing conditions at the interaction point (IP) surrounded by the experimental detector [28].

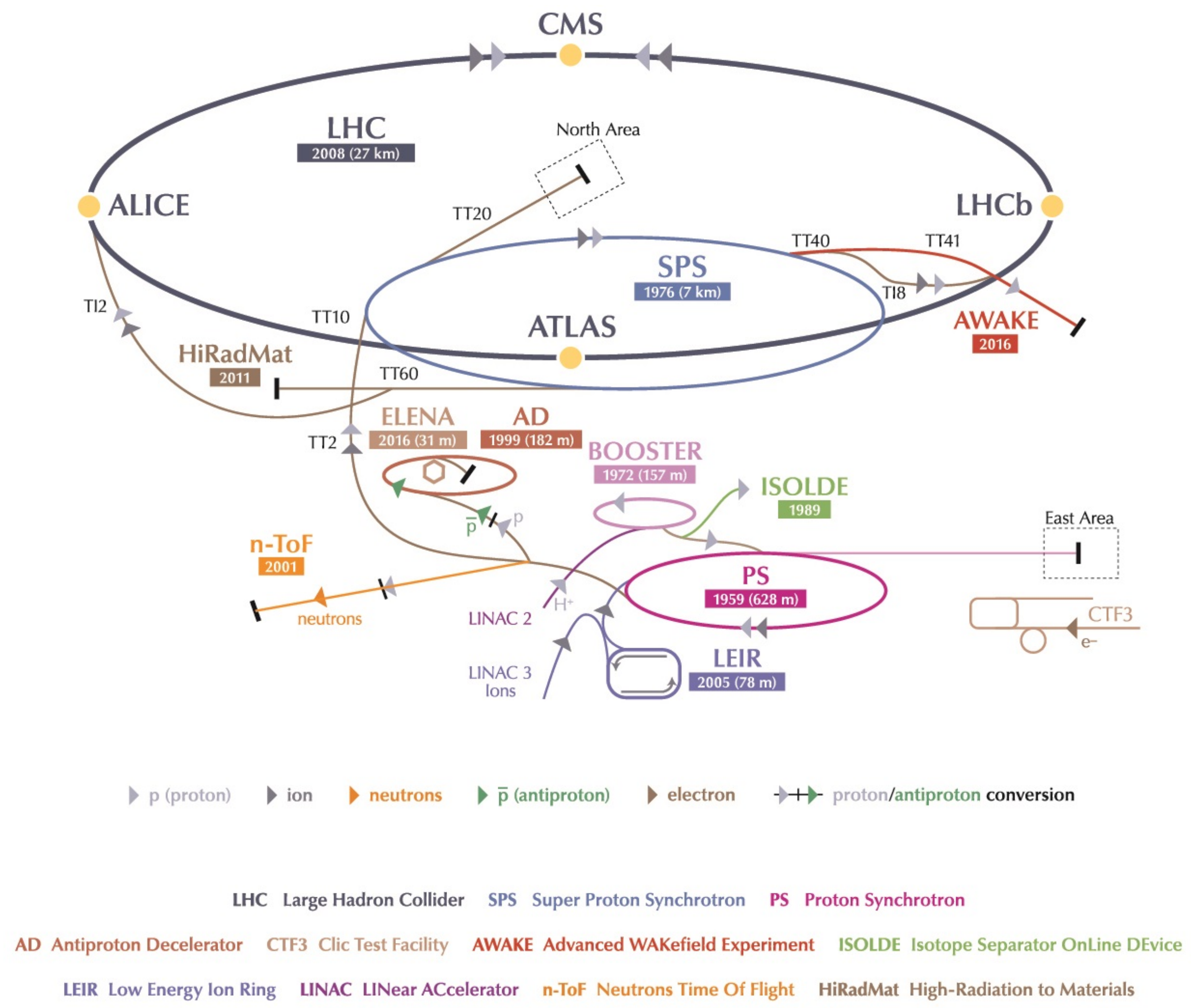

Figure 1.1: Overview of the current accelerator infrastructure of CERN. The largest accelerator, the LHC, a circular collider for protons and heavy ions, had a nominal collision energy of 7 TeV and a luminosity of $10^{38}\,\mathrm{m^{-2}\,s^{-1}}$ at the full commissioning in 2010. Information taken from reference [28].

In general, the LHC is a circular twin-aperture proton collider, an alternative-gradient synchrotron with two counter-rotating proton beams and four major collision experiments. The particle beams are steered on the circular trajectory by using superconducting twin-aperture Nb-Ti dipole magnets with a nominal field of 8.3 T operating at 1.9 K in superfluid helium.

The alternative-gradient concept [23, 37, 38, 39], also-called strong focusing scheme, aims at focusing the particle beam by using quadrupole magnets. A quadrupole magnet in combination with an additional quadrupole magnet rotated by a quarter-turn are called FODO cell in the sense of beam optics. It is performing alternatively a focusing of the beam in horizontal and vertical direction, which ensures the required bundling of the beam and hence affecting the luminosity. This is performed by Nb-Ti quadrupole magnets with a field gradient up to $215\,\mathrm{T\,m^{-1}}$ operating at 1.9 K, beside sextuple, decapole and octupole magnets for additional beam corrections.

The protons are cascaded accelerated by the use of the other accelerators within the CERN infrastructure, as shown in figure 1.1:

- The linear accelerator LINAC 2 initially accelerates the protons, which are extracted from hydrogen gas by a duoplasmatron proton ion source, to a kinetic energy of 50 MeV.
- Then they are transferred to Proton Synchrotron Booster (PSB), where they gain further energy and get extracted at 1.4 GeV.
- Injected in the Proton Synchrotron (PS), the particles are getting more accelerated to a kinetic energy of 25 GeV.
- Subsequently, the Super Proton Synchrotron (SPS) increases the proton energy to 450 GeV and forward them finally to the LHC.

The LHC is thus iteratively filled with proton bunches within a duration of approximately 15 min by using fast-pulsed kicker magnets and additional deflecting systems to change the trajectory for injection. After the LHC is fully filled with 2808 bunches and a nominal spacing of 25 ns, high-frequency cavities accelerate the beams from the injected 450 GeV to 7 TeV in approximately 30 min. This requires also a continuous ramp-up of the bending (dipole) magnets to their nominal field.

Afterwards, the two beams are controlled pointing against each other at the interaction points in physics operation of the LHC, which are located in the experimental detectors. The outcome of a particles collision is a shower of different types of particles, which are intended to be identified by the detectors. The recording of the collisions experiments allows the reconstruction of the trajectory, momentum and energy of the resulting particles. The largest detector systems installed at the LHC are ATLAS [94] and CMS [95] with the highest luminosity followed by the ALICE [93] and LHCb detectors [96]. In order to process the tremendous amount of measurement data generated by the LHC experiments, CERN created the LHC computer grid [49], which uses various computing centres of more than 40 countries.

After around 10 h to 20 h the quality of the beams is decayed due to the many collisions and consequently the beams are disposed via the beam dumping system near the CMS infrastructure so that the refill for the next run of the LHC can start.

Finally, it has to be mentioned, that the LHC is also constructed for heavy ions collision experiments. Highly-charged lead ions are produced by an ECR ion source and initially accelerated by the linear accelerator LINAC 3 before reaching the final kinetic energy in the LHC via the above-mentioned accelerators chain. The collision of the particles is detected, for example, by the ALICE experiment [93] (cf. figure 1.1) and the emerged temperatures and energy densities are intending to prove and study the quark-gluon plasma.

The currently large-scale development obligation of CERN is the enhancement of the LHC within the High Luminosity LHC project (HL-LHC) [6]. The primary objectives are the increase of the luminosity to $5 \cdot 10^{38}\,\mathrm{m^{-2}\,s^{-1}}$ beside many other upgrades until around 2025, as indicated in figure 1.2(b).

This includes multiple upgrades of accelerator technology, such as new technologies for beam collimation and upgrades of the cryogenic infrastructure. Furthermore, some improvements to prevent accelerator ageing are planned, for instance, improvement of quench protection and exchange of radiation exposed electronics. The most relevant work within the HL-LHC regarding the presented thesis are the development of state-of-the-art Nb_3Sn accelerator magnets, which was originally performed in a collaboration with the U.S. LHC accelerator research programme (US-LARP) [73]. More particularly, the 11 T dipole magnet [136] and the MXQF quadrupole magnets [90] are developed, which are produced for the following described purposes:

- Dispersion suppressor (DS) regions:
  The developed 11 m long 11 T dipole magnets are planned to substitute the longer LHC main dipole magnets (14.2 m, 8.3 T) in the dispersion suppressor regions by generating the same bending angle within a shorter distance. The retained longitudinal space will be used to install additional beam collimation systems to increase the beam quality. Collimators are passive accelerator components to protect the beam tube and magnets from particles, which are deviating from the desired beam trajectory.

- Inner triplets:
  The inner triplets are the closest group of focusing magnets to the interaction point. Due to the high luminosity upgrade, these magnets are exposed to higher radiation. An early failure due to radiation damage is planned to be prevented by exchanging the existing quadrupole in the critical region to low-β^* quadrupole magnets, the so-called MQXF magnets with lengths of 4.2 m and 7.15 m. The parameter β^* is referred to the distance from the interaction point at which the beam width is twice as wide as the interaction point.

The specimens, which were used to produce data for the present thesis, originate from the projects mentioned above. The development and research of Nb_3Sn accelerator magnets is a valuable gain of knowledge for the next large-scale project of CERN, described in the next section.

1.1.2 FCC design study

The next long-term goal of CERN to discover high-energy physics beyond the LHC capabilities is the extension of their infrastructure by a new particle accelerator, so-called Future Circular Collider (FCC) [1, 2, 3]. Its objectives and feasibility are investigated within the FCC study since 2013, whereby it focuses on the potential of a hadron and a lepton circular collider, as well as a hadron-lepton scenario is

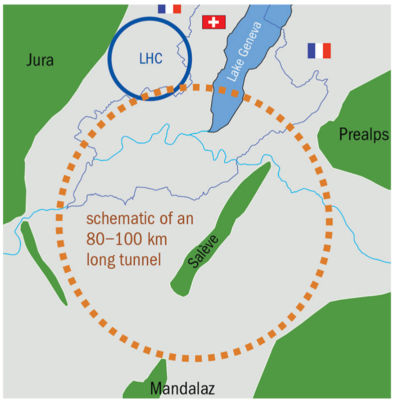

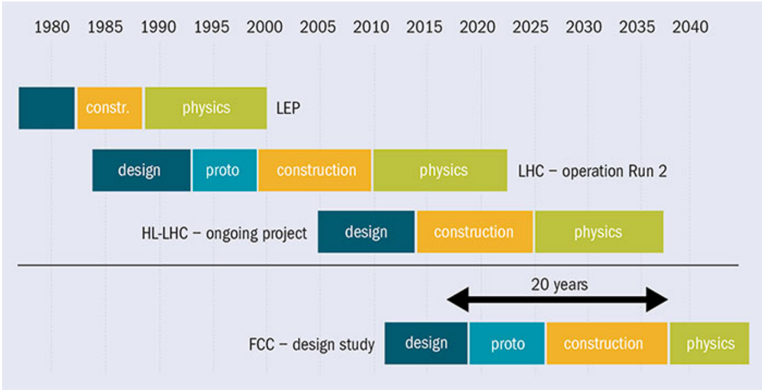

Figure 1.2: Future circular collider study. **(a)** Schematic of planned tunnel **(b)** Planned time schedule in contrast with past and ongoing projects. Information taken from reference [104, p.34].

being considered. Therefore, an underground tunnel with a circumference of 80 km to 100 km including caverns for experimental detectors in the Geneva region is studied, as indicated in figure 1.2(a). The final goal is the FCC-hh, a hadron collider, followed after the operation end of the FCC-ee, a lepton collider. The conceptual design for the FCC-hh is targeting a collision energy of 100 TeV and a luminosity in the range of $5 \cdot 10^{38}\,\mathrm{m^{-2}\,s^{-1}}$ to $30 \cdot 10^{38}\,\mathrm{m^{-2}\,s^{-1}}$ with a possible physics operation starting at around 2040. To reach these parameters with an 100 km circumstance collider, bending magnets with a nominal field of 16 T to 20 T and focusing magnets with a field gradient of around $360\,\mathrm{T\,m^{-1}}$ are targeted.

An achievement of a particle collider of this scale requires a wide-range technology programme and the magnet research is covered by the 16 T dipole development programme [143, 166, 167]. A comprehensive investigation regarding the magnet types and the conductor is imposed. Therefore a re-evaluation of possible magnet designs, such as $\cos(\vartheta)$ [105], canted-$\cos(\vartheta)$ [33] and block coil [100] is performed. The superconducting material, Nb_3Sn, is considered as the baseline material. Therefore, a nonCu critical current density[1] of $1.5 \cdot 10^{9}\,\mathrm{A\,m^{-2}}$ at 16 T and 4.2 K is been striven for Nb_3Sn wires, which requires research and development of the superconducting material on a fundamental level. Recently, a possible feasibility was achieved by S. Balachandran *et al.* [9] and further scientific approaches are discussed by e.g. M. Eisterer [50].

One of the studies in the frame of the 16 T dipole development programme is the manufacturing of Nb_3Sn accelerator magnets [88]. The brittleness and strain-sensitivity of Nb_3Sn make research on the mechanical limits for the coil winding process and magnet assembly substantial. The mechanical properties of Nb_3Sn wires require a sophisticated manufacturing concept with higher demands on fabrication processes and tolerances compared to the LHC magnets using Nb-Ti superconductors. One of the objectives of this sub-task is the degradation analysis of the conductor during the magnet assembly, which was the initiation of the present work.

1.2 Applied superconductivity & Nb_3Sn wires

This section gives a compact overview of applied superconductivity focusing on the knowledge applied in this work. In order to keep a suitable length of the section, the literature of M. Tinkham [165] for the theory of superconductivity, R. Flückiger *et al.* [63] for the scientific research on Nb_3Sn wires as well as J. W. Ekin [54] for the critical current measurements and data analysis is recommended.

1.2.1 Superconductivity

Technical superconductors for high field magnets, i.e. superconductors with an adequate critical current in the form of wires, were researched and developed in many steps:

- The first liquefaction of helium performed by H. Kamerlingh Onnes in 1908 made an unexplored low-temperature range accessible for material characterisation. The superconducting phase was first discovered by G. Holst and H. Kamerlingh Onnes [75, 171] while performing resistivity measurement of high-purity mercury at these temperatures. Certain materials lose their resistivity if

[1] The nonCu critical current density $J_{c,nonCu}$ of a Nb_3Sn wire is equal to the critical current over the nonCu area of the wire's cross-section (cf. section 3.2.3).

they are cooled below a specific temperature, so-called critical temperature T_c. Furthermore, they must not be exposed to an external magnetic field higher than a certain level, the critical field B_c, to remain superconducting. For instance, mercury is in the superconducting state below 4.2 K and 0.04 T. Unfortunately, the low critical fields inhibited technical use at that stage. Another insightful discovery was made in 1933 by W. Meißner and R. Ochsenfeld [109]. They discovered that the materials in superconducting state expel applied magnetic fields, i.e. exhibit perfect diamagnetism (Meißner effect), which differentiates superconductivity from ideal conductivity. The behaviour of these so-called type-I superconductors or the Meißner phase is described phenomenologically by e.g. F. and H. London [99]. Afterwards A. B. Pippard [121] introduced a non-local generalisation of the London equations and introduced a coherence length.

One of the most revealing theories about superconductivity is the Bardeen-Cooper-Schrieffer (BCS) theory published in 1957 [11]. It describes the so-called conventional superconductors, i.e. phonon-mediated superconductivity. Put crudely, the microscopic theory describes the superconductivity as an interaction between electrons via the vibration of the crystal lattice, i.e. phonon-mediated electron-electron interaction, confirmed by various subsequent experiments. At $T = 0$, the electron density of state $N(E)$ around the Fermi level $E_F \pm \Delta$ is equal to zero. Whereby the energy gap $\Delta < 2\hbar\omega_D$ with ω_D as the Debye frequency is typically two or three orders of magnitude smaller than the Fermi level. Two electrons with opposite spin and momentum occupied in this energy gap combine to a so-called Cooper-pair, coupled by phonons. These pairs with a whole-numbered spin, condensate to a coherent matter wave, which prevents them from scattering with the crystal lattice. Thus, it enables current flow without resistivity. The superconducting state is energetically favourable and an excitation of the electrons must exceed the binding energy the Cooper-pairs to break them. It was possible to derive a relation between the critical temperature T_c and the observable energy gap Δ. The energy gap depends primary on the Debye energy ω_D, the electron density of states at the Fermi level $N(E_F)$ and the electron-phonon coupling potential V. It should be mentioned that the BCS theory is limited to the weak-coupling approximation. G. M. Eliashberg [59] introduced and W. L. McMillan [108] further developed an extension beyond the weak-coupling superconductivity, which describes superconductivity in Nb_3Sn more accurately. The theory defines the attractive electon-phonon coupling constant λ_{EP} as well as the repulsive Coulomb interaction between the electrons μ^* to describe an expression for T_c. The material parameter λ_{EP} depends on the so-called Eliashberg function $\alpha^2(\omega)F(\omega)$, whereby $F(\omega)$ is the density states of phonons and $\alpha(\omega)$ is the electron-phonon coupling.

- In 1935, so-called type-II superconductors were discovered by J. N. Rjabinin and L. W. Schubnikov [127, 151]. These materials adopt in an mixed phase, so-called Schubnikov phase, between the Meißner and normal-conducting phase. Consequently, the materials expel the applied magnetic field until the lower critical field B_{c1}, equivalent to type-I superconductors before transforming to the Schubnikov phase. In this phase, it is energetically more favourable that the magnetic field penetrates the material in form of flux vortices. Accordingly, the total energy is lowered by the amount of the surface energy $\Delta E \propto (\xi - \lambda_L){B_c}^2$ with the thermodynamic critical field B_c, according to the GLAG theory. Consequently, the materials stay superconducting until the so-called upper critical field B_{c2}, before they transform into the normal-conducting phase. The upper critical field can be far above ten Teslas depending on the respective material or alloy. The flux of a single vortex, also-called Abrikosov vortex, amounts to the magnetic flux quantum Φ_0. In general, they are arranged in a triangular lattice in parallel to the applied magnetic field. The fluxoid quantisation in superconductors was first experimentally demonstrated by B. S. Deaver and W. M. Fairbank [42] as well as R. Doll and M. Näbauer [44] in 1961 and confirmed the prediction of the GLAG theory.

  The GLAG theory named after V. L. Ginzburg, L. Landau, A. A. Abrikosov and L. P. Gor'kov, often also called Ginzburg-Landau theory [4, 71, 91], is the second valuable theory regarding superconductivity, which was published in the 1950s. The macroscopic theory, based on thermodynamics and valid for temperatures close to T_c, clarifies many phenomena of type-I and type-II superconductors by modelling superconductivity as a thermodynamic phase. Without going into detail, type-I and type-II superconductors are distinguishable, if the corresponding Ginzburg-Landau parameter $\varkappa = \lambda_L/\xi$ amounts more or less than $1/\sqrt{2}$, respectively. It is used to derive B_{c1} and B_{c2} from B_c, which is linked to the difference of the thermodynamic Gibbs free energy of the normal and superconducting phase.

  Unfortunately, ideal type-II superconductors cannot transport current without resistance. The transport current provokes naturally Lorentz forces on the flux vortices. This leads consequently to movements of the vortices, so-called flux flow, described by e.g. the Bardeen-Stephen model [10].

Table 1.1: Characteristic parameters of the A-15 compound Nb_3Sn [74, 115, 120]. *At zero temperature.

Debye temperature Θ_D	234 K
Critical temperature T_c	18 K
Ginzburg-Landau coefficient $\varkappa^*$	34
Ginzburg-Landau coherence length ξ^*	3.6 nm
Lattice parameter at RT a	0.5293 nm
London penetration depth λ^*	124 nm
Lower critical field B_{c1}	38 mT
Superconducting energy gap Δ^*	3.4 meV
Sommerfeld constant γ	13.7 mJ K^{-2} mol^{-1}
Thermodynamic critical field B_c	520 mT
Upper critical field $B_{c2}{}^*$	25 T

According to Faraday's law, these movements induce an electrical field and hence dissipation. The phenomenon can be modelled with the so-called flux flow resistance, which is proportional to the applied magnetic field.

- Finally, type-II superconductors with pinning centres, so-called hard superconductors, make a stationary (DC) transport current without any resistance possible and consequently technical use feasible. These pinning centres, energetically-favoured defects in the crystalline structure, anchor the vortices and suppress the dissipative flux flow. The threshold when the Lorentz force exceeds the pinning force determines the critical current. Pinning centres are implemented purposefully in type-II superconductors to achieve high critical currents, which is the primary objective of optimisations for superconducting wires. In the case of Nb_3Sn wires, grain boundaries form the pinning mechanism primary. Consequently, a decreasing of the grain size during the phase formation is desired and investigated. The achieved critical current determined by the pinning ability is an extrinsic property, compared to the intrinsic critical temperature and critical fields of the superconductor. It is bound by the substantially higher intrinsic depairing current density J_d predicted by the GLAG theory.

  However, the pinning mechanism is also responsible for irreversible magnetisation and hence causing hysteresis losses, described by e.g. the Bean's critical state model [18] (cf. section 3.4.1). Moreover, the above-mentioned disorder and impurities in hard superconductors, which are intended for the flux pinning, are inherently affecting the electronic mean free path l of the material. Consequently, the superconducting behaviour and its intrinsic parameters are significantly changed. For instance, the electronic specific heat coefficient (i.e. Sommerfeld constant) γ and the resistive state resistivity ρ_n are dominated by l. They are influencing Ginzburg-Landau parameter $\varkappa$ according to the Gor'kov-Goodman relation, which is coupled again to the critical fields B_{c1} and B_{c2}. The influence of the electronic mean free path l is further elaborated in the works of P. G. de-Gennes [43], L. P. Gor'kov [72] and K. Maki [102, 103]. Without going in detail, one can distinguish between superconductors in the clean and dirty limit, i.e. $l \gg \xi_{BCS}$ and $l \ll \xi_{BCS}$ with the BCS coherence length ξ_{BCS}, respectively. Technical superconductors can be assumed at the dirty limit, where the electronic mean free path is much smaller than the BCS coherence length due to their impurities and disorder. This justified also the use of the Werthamer-Helfand-Hohenberg (WHH) method in this work [76, 77, 177] (cf. section 3.4.2).

- The discovery of superconductivity in cuprate compounds, often called high-temperature superconductors (HTS) with critical temperatures above the boiling point of nitrogen 77.4 K, in 1987 [19] should be mentioned for magnet applications [172]. Also magnesium diboride and iron-based compounds, discovered 2001 [117] and 2006 [82], respectively, are considered as promising materials for technical applications in the future.

Today, the most important technical superconductors in commercial composite wires are the alloy Nb-Ti and the intermetallic compound Nb_3Sn, which belong to the so-called low-temperature superconductors (LTS). Their superconductivity behaviour was discovered 1961 [79] and 1954 [107], respectively. Nb-Ti has an A-2 crystal structure, a critical temperature of 9.2 K and an upper critical field of 14.5 T. The properties of Nb_3Sn are summarised in table 1.1. Although Nb_3Sn was discovered first and has more attractive properties for magnet application, the brittle A-15 material is technologically challenging, so that many applications are implemented preferably with the more ductile Nb-Ti.

1.2.2 Superconducting composite wires

In order to build a superconducting coil for a high field magnet, the hard superconductor is fabricated in "stabilised" composite wire [83]. A SEM micrograph of a typical Nb_3Sn wire is shown in figure 2.2. The primary reasons for the concept are briefly analysed:

- First, the superconductor within the wire is arranged in filaments or sub-elements with a preferable size smaller than 70 µm and embedded in a matrix of highly-conductive metal, e.g. copper (Cu). This high surface-to-volume ratio surrounded by cooper is targeting a good thermal stabilisation of the superconductor primarily. It allows the transport current to flow temporarily in the copper and prevents that a local quench[2] propagates over the entire wire or coil. A local resistive transition can be caused by short-term current overload, mechanical damage or flux jumps and is mitigated by the stabilised design. The ratio of copper to superconductor is a typical design decision resulting in a compromise of thermal stability and current density of the coil. It is experimentally quantified by e.g. the Normal Propagation Zone (NPZ) or the Minimum Quench Energy (MQE).

- The second reason for a multi-filamentary design is the reduction of loss regarding changing magnetic fields, e.g. the ramping of the magnet to its nominal field or generating alternating magnetic fields. The pinning mechanism, which is instrumentalised to achieve a high critical current, causes the mentioned magnetic hysteric behaviour. The magnetisation and their associated loss are reduced by smaller filament size. Also, the field error in magnets caused by the hysteric behaviour as well as flux jumps are decreased, and the design decision regarding the filament size is based on such aspects.

- According to Faraday's Law, applied changing magnetic fields generate circular screening currents in the filaments, which are coupled via the copper matrix. This phenomenon poses an additional load in the filaments without contribution to the transport current. Hence, it decreases the stability regarding current overload. To counteract the so-called interfilament coupling, the bundle of filaments is twisted. This transposition is apparent in the SEM micrograph of the chemically-extracted Nb_3Sn sub-elements in figure 2.7.

- Eddy currents in the copper matrix of wires within a magnet coil lead to undesired Joule heating and hence decrease also the stability of the particular wire. Consequently, wires are bundled to twisted cable, e.g. Rutherford cables in the case of LHC accelerator magnets. In general, a compromise has to be made between a sufficient interstrand contact resistance to suppress eddy currents and a low interstrand contact resistance to allow current sharing in the case of a local quench within the cable.

Commercial wires are typically fabricated by extrusion processes. In the case of Nb-Ti, the superconducting rods are embedded in the copper cylinder ingots having a significantly larger diameter and lower length compared the final wire. Subsequently, the composite is extruded to the desired diameter and length.

The fragile nature of Nb_3Sn inhibits a winding without damage or performance degradation. Hence, the necessary components for forming the Nb_3Sn are summarised in sub-elements and extruded within a wire. Consequently, many Nb_3Sn wire designs are implemented with higher sub-element diameters compared to Nb-Ti filaments. The non-reacted wire can be deformed and wound to a coil. Afterwards, a reaction heat treatment (RHT) of the wound coil up to roughly 650 °C transfers the components into Nb_3Sn ("wind and react" technique), as explained in section 1.3. Beside the A-15 formation of the sub-elements, the copper stabiliser of the wire gets highly annealed at these temperatures, which increases its conductivity and hence leads to a better thermal stability. Today, the three most renowned state-of-the-art Nb_3Sn wire architectures for accelerator magnets are listed in table 1.2.

Wires used in this work are exclusively distributed-barrier internal tin wires, fabricated according to the Restacked-Rod Process (RRP) explained in section 2.1. The primary advantage of this wire architecture is the high critical current. However, the relative large sub-elements of typically 50 µm are responsible for high irreversible magnetisation, resulting in high loss during the ramping of a magnet build with RRP wires. Within the HL-LHC upgrade, the 11 T dipole magnet and the MQXF quadrupoles are produced with RRP wires and a mixture of RRP and PIT wires, respectively.

In order to assess and compare the essential performance of superconducting wires phenomenologically, the standard IEC61788-2 [157] defines the "DC critical current measurement for Nb_3Sn composite

[2] A quench is called an uncontrolled transition between the superconducting and the resistive state generating heat dissipation.

Table 1.2: Overview of the renowned state-of-the-art Nb_3Sn wire architectures [133].

Type	Sub-element size µm	$J_{c,nonCu}(12\,T, 4.2\,K)$ $A\,m^{-2}$
Bronze-process	2 to 4	$\sim 0.9 \cdot 10^9$
Internal tin (single-barrier)	3 to 6	$\sim 1.0 \cdot 10^9$
Internal tin (distributed-barrier)	30 to 50	$\sim 2.9 \cdot 10^9$
Powder-in-tube (PIT)	40 to 70	$\sim 2.7 \cdot 10^9$

superconductors". The superconducting wire is transferred from the superconducting to the resistive state in a controlled way by ramping the transport at a constant temperature. The resistive transition follows a power law and defines the critical current I_c as well as the resistive transition index n, as described in section 3.2.3 and 3.3.3. In order to assess the copper stabiliser, which embeds the sub-element, the residual-resistance-ratio (RRR) is often referred [156].

1.2.3 Unified scaling law for flux pinning in technical superconductors

The essential behaviour of Nb_3Sn wires is described by the Unified Scaling Law (USL) of J. W. Ekin [54], based on experimental data, and further elaborated in references [55, 58, 57]. It is commonly used to derive the function $I_c(B, T)$, which is also known as the critical surface in magnet design. It is illustrated in figure 1.5 and frequently used to define the nominal operation point of a superconductor within a magnet as well as to assess load or temperature margin. By using the USL the most essential properties of a superconductor for magnet design are taken into account:

- The *critical current density* J_c, an extrinsic property depending on the volume pinning force F_p, determined by the micro-structure of the material and additional alloy components.
- The *critical temperature* T_c and the *upper critical field* B_{c2} are intrinsic properties of the material. They depend primary on the crystal structure and atomic scale characteristics. They vary only a few percent by depending on the fabrication process and the ratio of additional alloy components.
- Besides the three primary parameters, the *mechanical strain* ε, influences significantly the superconducting behaviour. Wires in coils are pre-tensioning due to the coil winding process and additionally exposed to high Lorentz forces during the magnet operation. Moreover, the wires are loaded inherently with thermal-induced pre-compression ε_m, considering the formation of the A-15 phase at roughly 650 °C and an operating temperature below 18 K. Consequently, the intrinsic strain $\varepsilon_0 = \varepsilon - \varepsilon_m$ is defined. The thermal-induced pre-compressive pre-strain $\varepsilon_m \approx 0.3\,\%$ depends strongly on the architecture and material of the composite wire. With the introduction of the strain ε, the four-dimensional critical surface $I_c(B, T, \varepsilon)$ can be defined as performed in the reference [53].

Within this work, interpolations and scaling are performed on the base of the USL, described as follows. The pinning mechanism is quantified by the volume pinning force F_p, as mentioned above. It counteracts the Lorentz force F_L to prevent depinning and movements of flux vortices. The threshold, where the Lorentz force $F_L = J \times B$ exceeds the maximal pinning force F_p, defines the end of the lossless transport current and hence the critical current density J_c. This can be expressed as

$$F_p = F_L = J_c B. \tag{1.2}$$

Equation 1.2 implies that **J** is perpendicular to **B**, which describes the dominant situation within a magnet. The USL formulates the pinning force

$$F_p = J_c B = C\, K(t, \varepsilon_0)\, f(b) \tag{1.3}$$

with a constant C, the pre-factor $K(t, \varepsilon_0)$ and the general pinning force function $f(b)$. The reduced temperature t is defined as

$$t = \frac{T}{T_c{}^*(\varepsilon_0)}, \tag{1.4}$$

where $T_c{}^*(\varepsilon_0)$ is the effective critical temperature depending on the intrinsic strain ε_0. The reduced field b is defined as

$$b = \frac{B}{B_{c2}{}^*(t, \varepsilon_0)}, \tag{1.5}$$

where $B_{c2}{}^*(t, \varepsilon_0)$ is the effective upper critical field depending on the reduced temperature t and the intrinsic strain ε_0. The effective values $T_c{}^*$ and $B_{c2}{}^*$ are determined by the particular extrapolated scaling functions intercepting with the respective abscissa. In general, they are not identical to the critical temperature T_c and the upper critical field B_{c2}, respectively. The effective values do not consider inhomogeneity effects of the respective wire architecture occurring by temperatures close to T_c or vanishing magnetic field.

The general pinning force function for constant temperature t and strain ε is described by

$$f(b) = b^p (1-b)^q, \tag{1.6}$$

where the parameter p and q dominate the low-field part and high-field part, respectively. The two parts are split by the maximum of the function at $b_{max} = p/p+q$. In particular, the pinning theory of Kramer [86] predicts $p = 0.5$ and $q = 2$, which shows a good correlation with the measurement data of Nb_3Sn wires. Thus, the equation $F_p = J_c B = C\, b^{0.5}(1-b)^2$ is frequently used for interpolation of the critical current at particular applied fields. Therefore, the fit approximation $I_c = C'\, b^{-0.5}(1-b)^2$ with C', b as fitting parameters is applied to the measurement data. Moreover, the Kramer model is used to extrapolate the effective upper critical field $B_{c2}{}^*$, which is located in a difficult accessible measurement region in the case of Nb_3Sn. The above-mentioned relation

$$J_c B = C\, b^{0.5}(1-b)^2 \qquad \text{can be transferred to} \qquad J_c{}^{0.5} B^{0.25} \propto 1 - \frac{B}{B_{c2}{}^*}. \tag{1.7}$$

The expression $J_c{}^{0.5} B^{0.25}$, which can be obtained by the measurement data, forms a straight line over B. It is intersecting the abscissa at $B_{c2}{}^*$ and can be calculated accordingly. Under the assumption $B_{c2} \approx B_{c2}{}^*$, this method can be used to assess the upper critical field B_{c2} and is also known as the Kramer plot or Kramer extrapolation.

The effective upper critical field $B_{c2}{}^*(t, \varepsilon)$ is depending on the temperature t and the strain ε. Therefore the behaviour is separated into two functions

$$B_{c2}{}^*(t, \varepsilon_0) = B_{c2}{}^*(0,0)\, b_{c2}(t)\, b_{c2}(\varepsilon_0) \quad \text{with} \quad B_{c2}{}^*(0,0) = B_{c2}{}^*(0) \tag{1.8}$$

and

$$\begin{aligned} B_{c2}{}^*(t) &= B_{c2}{}^*(0)\, b_{c2}(t), \\ B_{c2}{}^*(\varepsilon_0) &= B_{c2}{}^*(0)\, b_{c2}(\varepsilon_0). \end{aligned} \tag{1.9}$$

The temperature-dependency is known as

$$b_{c2}(t) = (1 - t^{\nu}), \tag{1.10}$$

where $\nu \approx 1.5$ shows a good agreement with the experimental data for Nb_3Sn wires. Within the so-called moderate strain region $-0.5\,\% < \varepsilon_0 < \varepsilon_{0,irr} \approx 0.4\,\%$, the strain dependency is modelled by the power law approximation

$$b_{c2}(\varepsilon_0) = (1 - a|\varepsilon_0|^u). \tag{1.11}$$

An extraction of J. W. Ekin [54] in figure 1.3 shows the correlation of the fit function with the measurement data of binary multi-filamentary Nb_3Sn wires. The exponent parameter can be assumed with $u \approx 1.7$ and the strain-sensitivity parameter a is in the range of 900 to 1250 for Nb_3Sn [53]. The experimental data for tension ($\varepsilon_0 > 0$) are slightly steeper than for compression ($\varepsilon_0 < 0$). Consequently, the parameters a^+ and a^- for tension and compression strain, respectively, are defined for detailed scaling.

The strain dependence of the effective critical temperature within the moderate strain region can be expressed with the strain behaviour of the upper critical field

$$T_c{}^*(\varepsilon_0) = T_c{}^*(0) \left[\frac{B_{c2}{}^*(\varepsilon)}{B_{c2}{}^*(0)} \right]^{1/w} = T_c{}^*(0)(1 - a|\varepsilon_0|^u)^{1/w} \tag{1.12}$$

with $w \approx 3$ for Nb_3Sn, shown in figure 1.4(a).

Under the assumption that the pre-factor $K(t, \varepsilon_0)$ can also be separated in a strain and temperature depending part $K(t, \varepsilon_0) = g(\varepsilon_0)\, h(t)$, the USL can be expressed in its separable form

$$F_p = J_c B = C\, g(\varepsilon_0)\, h(t)\, f(b). \tag{1.13}$$

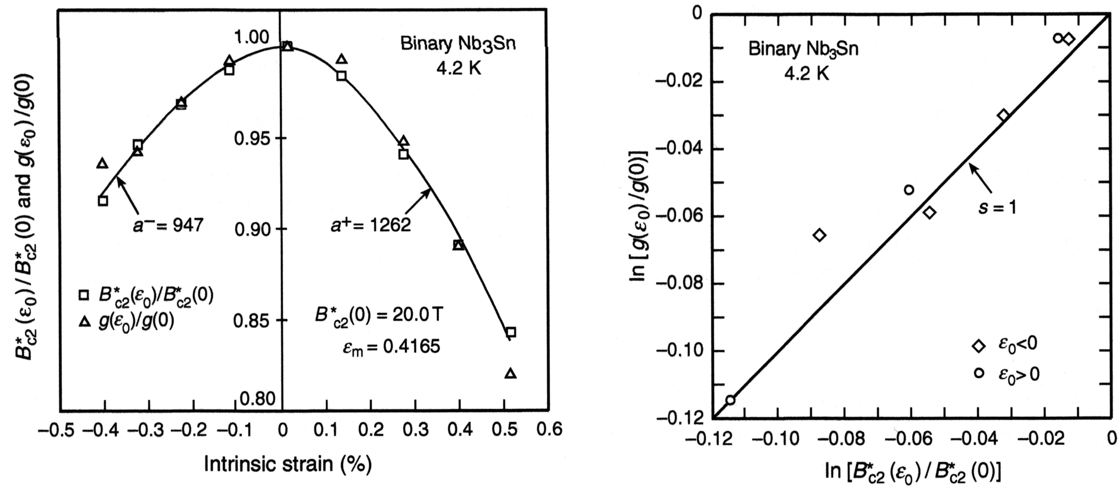

(a) (b)

Figure 1.3: **(a)** The strain dependency of the normalised intrinsic parameter $B_{c2}^*(\varepsilon_0)/B_{c2}^*(0)$ and the normalised strain scaling function $g(\varepsilon_0)/g(0)$ within moderate strain. **(b)** Logarithmic plot of $g(\varepsilon_0)/g(0)$ versus $B_{c2}^*(\varepsilon_0)/B_{c2}^*(0)$ for evaluation of parameter s. Information taken from reference [54, p.451].

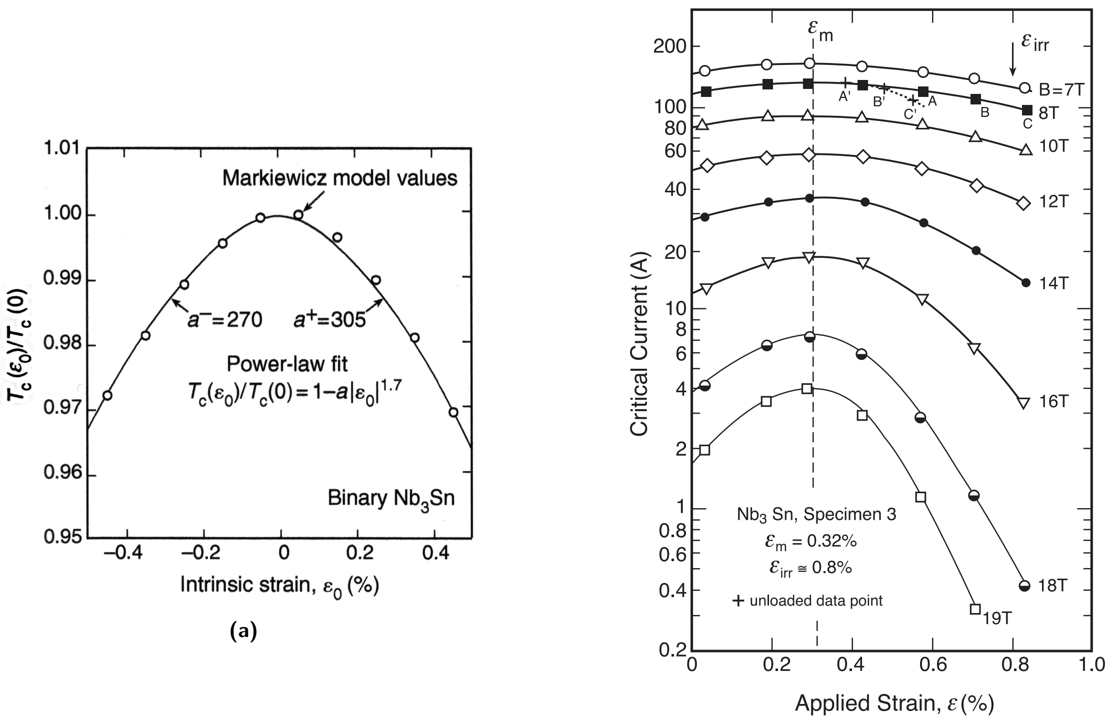

(a) (b)

Figure 1.4: The strain dependency of **(a)** the normalised intrinsic parameter $T_c(\varepsilon_0)/T_c(0)$ and **(b)** the critical current $I_c(\varepsilon)$. Information taken from reference [54, p.445] and [54, p.435], respectively.

The temperature scaling law $h(t)$ is defined as

$$h(t) = h(0)\left[\frac{B_{c2}{}^*(t)}{B_{c2}{}^*(0)}\right]^{\eta} = h(0)\,(1-t^{\nu})^{\eta} \tag{1.14}$$

with $\eta \approx 2.5$ for Nb_3Sn and shows a good agreement with the transport current measurements $I_c(T)$ within the wire investigation in section 4.2.2.

Finally, the strain scaling function $g(\varepsilon_0)$ can be expressed within the moderate strain region by the obtained strain dependency of the upper critical field

$$g(\varepsilon_0) = g(0)\left[\frac{B_{c2}{}^*(\varepsilon)}{B_{c2}{}^*(0)}\right]^{s} = g(0)(1-a|\varepsilon_0|^{u})^{s}, \tag{1.15}$$

where $s \approx 1$ could be identified for Nb_3Sn, shown in figure 1.3. The almost consisting power-law behaviour of $T_c{}^*(\varepsilon_0)$, $B_{c2}{}^*(\varepsilon_0)$ and $g(\varepsilon_0)$ within the moderate strain region is assumed to arise from the phonon anharmonicity of the crystal lattice. This reversible effect is further discussed in section 1.4.

After a certain stress level, the conductor does not recover from the load any more, which can be observed by the degradation of a subsequent non-loaded measurement. Hence, an additional irreversible effect is influencing the I_c performance, which is explained by using figure 1.4(b) as follows. After exposing the wire with a strain $\varepsilon = 0.6$ (measurement point A), the subsequent non-loaded measurement shows still a residual strain (measurement point A'). This can be explained by the fact that materials of the wire, e.g. the copper stabiliser, are plastically deformed and exert a residual strain on the superconductor. As long as the performance of the wire recovers on a particular point on the $I_c(\varepsilon)$ curve, the superconductor is unharmed conclusively. This also implies measurement point B followed by non-loaded measurement point B'. After a threshold, i.e. measurement point C, the wire does not fully recover, which can be seen by a subsequent non-loaded measurement (point C'). Hence, the wire is degraded irreversibly, which is assumed to be caused by fractures of the superconducting material. This so-called irreversible strain limit ε_{irr}, i.e. in the present case at point C ($\varepsilon \approx 0.8$), is an essential threshold for magnet design and should not be reached in any case after the RHT. Despite the fact that high-compressive strain in coils should not be an intended state in a magnet, the regime $\varepsilon < -0.5\,\%$ is also investigated and modelled with a power law approximation [55].

1.2.4 NearT_c concept

Within the wire investigation, transport critical current measurements were performed exclusively in self-field. This was decided due to the following restrictions:

- In order to protect the specimen from undesired damage during the measurements, the use of an applied field was excluded.
- An alternative cost-efficient measurement method should be demonstrated and verified, which enables low-temperature measurements without a background magnet and continuous supply of liquid helium (^{4}He).

In order to reason and explain the chosen measurement principle, some established background knowledge is introduced. Based on the USL for constant strain, the mentioned critical surface $I_c(B,T)$ can be expressed as

$$I_c = \frac{F_p}{B} = C\,B^{-1}\,h(t)\,f(b), \tag{1.16}$$

and shown in figure 1.5. Underneath that surface, the conductor is superconducting and above it reverts to the resistive state. By using critical current tests at specific applied fields and temperatures, the surface can be scaled and is frequently used for assessments in magnet design.

The most common type of critical current tests is the measurement of $I_c(B)$ at a constant temperature T, i.e. I_c-B curves labelled in figure 1.5. This is mostly implemented by winding the Nb_3Sn wire on a barrel, e.g. VAMAS barrel [24], and subsequently reacted within the RHT process. Afterwards, the sample is cooled down below its critical temperature within a cryostat equipped with the necessary instrumentation, e.g. current leads and a background solenoid magnet. Under the considerations of the thermodynamic properties of liquid (^{4}He I) and superfluid helium (^{4}He II), helium at the temperature of 4.2 K or 1.9 K is preferred as a coolant.

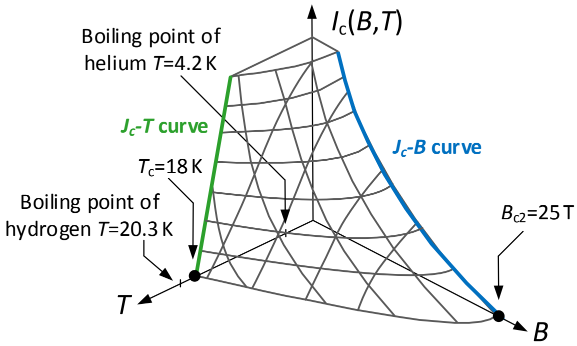

Figure 1.5: Critical surface $I_c(B,T)$ derived from the USL for assessment of the conductor's operation point and margin within magnet design. Additional the boiling point of hydrogen and helium is annotated. Helium is the mostly used cryogenic liquid to test and use LTS composite wires, such as Nb_3Sn wires.

One of the advantages of cooling the sample with boiling ^{4}He I is the quasi-isothermally absorption of heat energy by the latent heat of vaporisation, which stabilises naturally the sample temperature. Moreover, the specific heat capacity of liquid helium is several orders of magnitude higher than the one of commonly-used metals at these temperatures. The outstanding properties of ^{4}He II as a coolant are the very high specific heat capacity and thermal conductivity besides the absence of boiling and viscosity.

To shift the critical current $I_c(B)$ in an experimentally accessible range, i.e. below the maximal current of the used power supply, the applied field is increased. The resulting measurement range by the use of a 300 A current source and a 15 T background magnet is labelled in figure 1.6(a). This is performed by setting the applied field and subsequently ramping the current during voltage recording until the resistive transition occurs. The quench protection cut off the current supply to prevent damage of the wire due to Joule heating. The critical current is determined preferably according to the standard IEC61788-2 [157]. The measurement point $I_c(12\,\mathrm{T}, 4.2\,\mathrm{K})$ is often used to compare the performance of different wires (cf. table 1.2).

In the present work, a background magnet was not available. Consequently, the above-mentioned shift of I_c with high applied fields was not utilisable. Instead, the temperature was raised alternatively and stabilised. Hence, variable-temperature measurements of the critical current $I_c(T)$ were chosen, as illustrated with I_c-T curve in figure 1.5. Test currents up to 150 A require a shift of the temperature close to the critical temperature T_c, which reasons the name NearT_c concept. It stands in contrast to the frequently-used measurement temperatures 4.2 K and 1.9 K mentioned earlier. The typical measurement range is labelled within the critical surface in figure 1.6(b). The chosen measurement range enables some technological advantages:

- The absence of the background magnet has primary economical reasons. Moreover, a sophisticated mounting of the sample is not mandatory.
- Due to the high operation temperature far above the boiling point of helium, an implementation of a cryogenic refrigerator system (cryocooler) can be taken into account. In this case, the cooling power of the system is the limiting factor regarding the maximal test current. A closed-loop refrigerator system would supersede the continuous supply of liquid helium and enables a high measurement throughput considering the cool-down duration of established systems.

However, the NearT_c concept has also inherent drawbacks. A shift of the temperature instead of the magnetic field leads to higher requirements regarding the temperature stability. The stability of temperature has to satisfy the slope $\mathrm{d}I_c/\mathrm{d}T$ in the respective measurement range.

I_c-T curves are frequently used to assess the temperature margin of a superconducting wire and, in principle, there is more than one way to implement a variable-temperature measurement. One of the offering solutions is to put the sample in a cryogenic liquid bath and regulate the pressure of the cryostat. The temperature of the sample can be reduced by evacuating the gas space of the cryostat. Accordingly, an increase of the cryostat's pressure results in an increase of the boiling temperature. Hence, the boiling point of the liquid and consequently the sample temperature is reduced as a function of the pressure along the saturation vapour pressure curve. Helium is thus called saturated (two-phase) helium while operating in this two-phase region of the phase diagram. In general, the upper boundary of this evacuating-pressurising technique is given by the critical point of the respective cryogenic liquid.

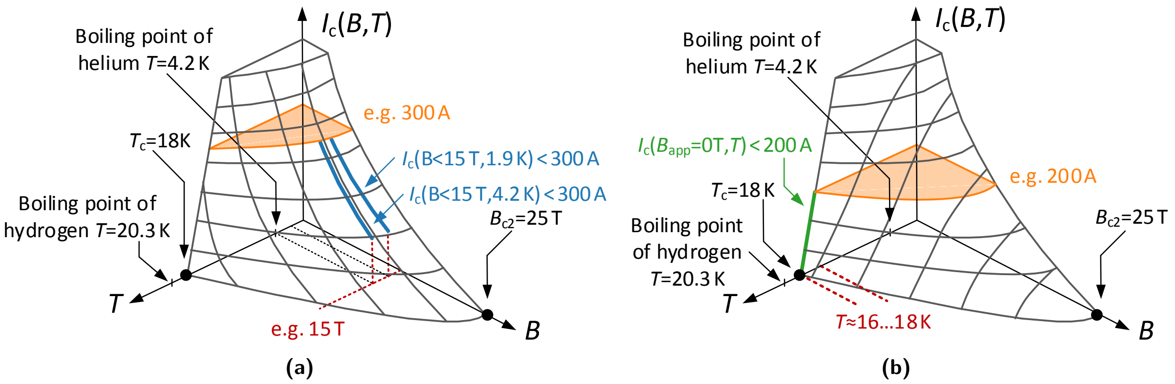

Figure 1.6: Illustration of the measurement region by the aid of the critical surface $I_c(B,T)$. **(a)** Measurement range by the use of a background magnet up to 17 T at 4.2 K or 1.9 K with liquid or superfluid helium, respectively. **(b)** Measurement range in self-field by adjusting the sample temperature close to the critical temperature, so-called NearT_c concept.

However, the pressure of the cryostat or dewar vessel is practically limited by the recommended safety limits, e.g. in the range of the double atmospheric pressure. The bottom temperature limit is reached at the triple point of the particular coolant.

The temperature of this targeting concept amounts roughly to the range of 15 K to 20 K determined by the properties of Nb_3Sn. Consequently, the number of selectable liquid coolants is restricted. Nitrogen (N_2) has a triple point of 63.2 K and hence can not be used for these temperatures. In the case of ^4He, the critical point is reached already at 5.2 K and 2.2 bar. Hence, without an applied field, the critical current of Nb_3Sn wires in this temperature range is technologically difficult to reach. Nevertheless, saturated helium is often used to reach temperatures below its lambda point at 2.17 K and 0.05 bar by evacuation. Hydrogen (H_2) has a triple point at 13.8 K and 0.07 bar, and the required temperature range can be achieved with the experimentally accessible pressure. Unfortunately, hydrogen is barely used as a coolant, due to the risk of explosion of the boiled-off gas while mixed with air. A mixture of hydrogen with air in the ratio of 4 % to 75 % is flammable and needs to be appropriately treated.

Within this work, a cryostat setup based on a pressure-regulated helium phase separator was designed and implemented to emulate and test the feasibility of a refrigerator-based cooling system. The conductively-cooled sample, a Nb_3Sn wire with test currents up to 150 A, was mounted on a portable sample holder in a vacuum atmosphere. The specific construction is explained in section 3.3 and its operation is discussed in section 4.2. Former and similar experiments of Nb_3Sn close to the critical temperature T_c are mentioned in the literature review in section 1.4.

1.3 Accelerator magnets & their manufacturing

This section introduces briefly superconducting accelerator magnets and the production of Nb_3Sn accelerator magnets. It is focusing on the necessary technological background for the presented thesis. Considering that the field of accelerator magnets is well elaborated with a long history, the literature of L. Rossi *et al.* [128] or S. Russenschuck [132] is advised to consult.

1.3.1 Accelerator magnets

The dipole magnets of a circular collider steer the charged particles, i.e. the beam, on the desired bent trajectory according to the Lorentz force. The maximal achievable bending field in the beam aperture implemented by the dipole magnets determines the bending radius of the beam and hence the radius of the collider. It is one of the significant factors regarding the estimation of costs. Based on the calculation of the motion of a charged particle in a constant magnetic field, the beam energy of a circular collider can be assessed by

$$E_{\text{beam}} \approx 0.3\, R\, B_0 \tag{1.17}$$

in TeV. The variable R identifies the radius of the beam trajectory inside the bending field in km and B_0 defines the magnetic bending field in Tesla [132]. Thus, in order to increase the achievable beam energy of a particle collider either the radius or the bending magnetic field has to be increased. In practice, the radius R of the beam implemented by the dipole magnets has to be smaller than the actual radius of a collider. This is necessary because not the entire circumference of a collider is available for dipole magnets, e.g. the intersection regions, which is usually described by the dipole filling factor of a particle collider.

Moreover, the focusing magnets, in particularly the low-β^* quadrupole magnets, are influencing the luminosity L at the interaction point, which broadly spoken affects the efficiency of a collider. Thus, the development of magnets is essential for the advancement of particle colliders.

Most normal-conducting magnets for colliders are commonly implemented by coils made of copper surrounding a flux-leading yoke, which is also often called iron yoke. The yoke consists of laminations made of magnetically-soft ferromagnetic material, e.g. iron or soft ferrites, as shown in figure 1.8. The particle beam is exposed to the magnetic field by locating it in the air gap of the yoke. The current density of the copper coils is limited by the generated Joule heating to several $10^6\,\mathrm{A\,m^{-2}}$, whereby the engineering current density is used in magnet design generally[3]. The generated magnetic field is concentrated and guided by the iron yoke and is technologically limited by the saturation flux density of the used ferromagnetic material, which is typically between 1 T to 1.8 T. The decisive field quality is determined by the shape of the yoke poles or pole shoes, which is also the reason why they are often called iron-dominated magnets.

Although superconducting magnets replaced normal-conducting in the large colliders with high-rigidity particle beams, they are still broadly used and optimised within high-energy physic experiments. Pulsed kicker and septa magnets, which are used to extract and inject particle bursts within the CERN accelerator infrastructure (cf. figure 1.1), are normal-conducting. Moreover, the FCC-ee is considered to be implemented with twin-aperture normal-conducting magnets [111].

Due to the demand of high-energy physics experiments to reach still higher nominal fields and gradients in bending and focusing magnets, respectively, the seek of higher current densities was necessary. This barrier of accelerator technology could be overcome by the research and development of superconducting magnets. By operating coils made of superconducting composite wires underneath its critical current, located in a cryostat, engineering current densities above $5 \cdot 10^8\,\mathrm{A\,m^{-2}}$ got feasibly with vanishingly small Joule heating. The first superconducting accelerator magnets had been constructed in the late 1970s at CERN [22]. The Nb-Ti quadrupole magnets were used in the intersection region of in the Intersecting Storage Rings (ISR) to increase the luminosity and had a peak field of 5.3 T. The first entirely superconducting collider was the Tevatron at the FNAL operating from 1983 to 2011 by using Nb-Ti composite wires.

The conventional superconducting accelerator magnets are so-called coil-dominated magnets. Hence, the field shape is mostly formed by the layout of the coil, shown in figure 1.9. This means the distribution of the current density in the two-dimensional space perpendicular to the beam direction is responsible for the field shape, due to the absence of flux-leading yoke. An adequate coil modelling is mandatory to achieve a proper field quality. Correspondingly, I. Rabi [126] demonstrated that a pure transverse dipole field $\mathbf{B} = B\,\mathbf{e}_\mathrm{y}$, as well as higher order multipoles, can be achieved by a combination of intersection ellipse with opposite current polarity. The corresponding configuration shown in figure 1.7(a) generates in the aperture a perfect uniform dipole field

$$\mathbf{B} = \mu_0\, J_0\, c\, \frac{b}{a+b}\, \mathbf{e}_\mathrm{y}. \tag{1.18}$$

Moreover, it can be demonstrated that a ring with the thickness of t with a current density distribution of $J = -J_0 \cos(\vartheta)$ also generates an pure dipole field in the aperture with a magnitude of

$$\mathbf{B} = \frac{\mu_0 J_0}{2}\, t\, \mathbf{e}_\mathrm{y}, \tag{1.19}$$

as illustrated in figure 1.7(b). Accordingly, the current distribution $J = -J_0 \cos(n\varphi)$ generates a field of an $2n$-multipole with n as a positive whole number. The $\cos(\varphi)$-depending current density in a ring is barely technically feasible, but a block-wise approximation can be implemented to approach the ideal current density distribution, as can be seen in figure 1.7(c). The field inside the coil shell of this arrangement is not a perfect dipole and in general written as

$$\mathbf{B}(\rho,\varphi) = B_\rho(\rho,\varphi)\, \mathbf{e}_\rho + B_\varphi(\rho,\varphi)\, \mathbf{e}_\varphi. \tag{1.20}$$

It can be shown that fields in accelerator magnets, i.e. two-dimensional magnetic field generated by a transverse current distribution surrounding the aperture, are describable by coefficients of a Fourier

[3]The engineering current density $J_\mathrm{c,ENG,coil}$ of magnets is defined as the current of the coil divided by the entire cross-section of the coil (cf. section 3.2.3).

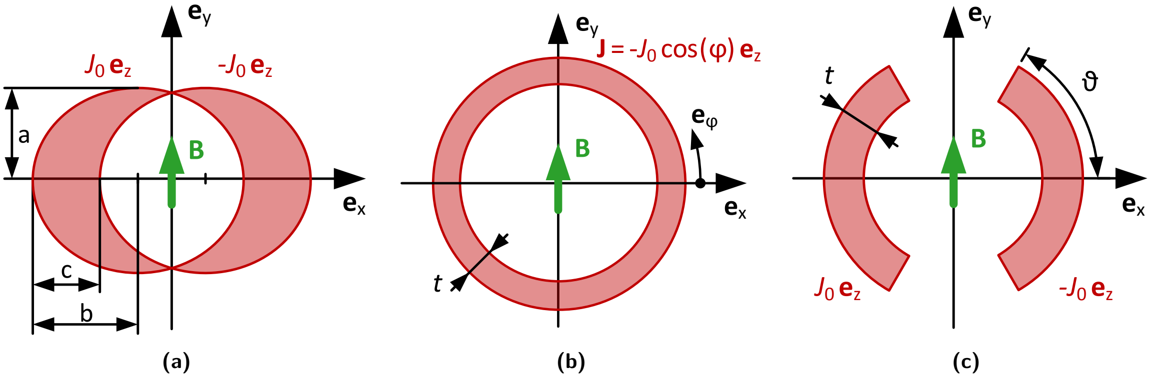

Figure 1.7: Two-dimensional layout of current density distributions to achieve a transverse dipole field with coil-dominated magnets. **(a)** Perfect uniform dipole field generated by intersecting ellipse of current densities. **(b)** Dipole field by generated by a ring with $\cos(\vartheta)$-depending current density. **(c)** Arc-shaped shell segments with constant current distribution to technically implement the dipole field of (b).

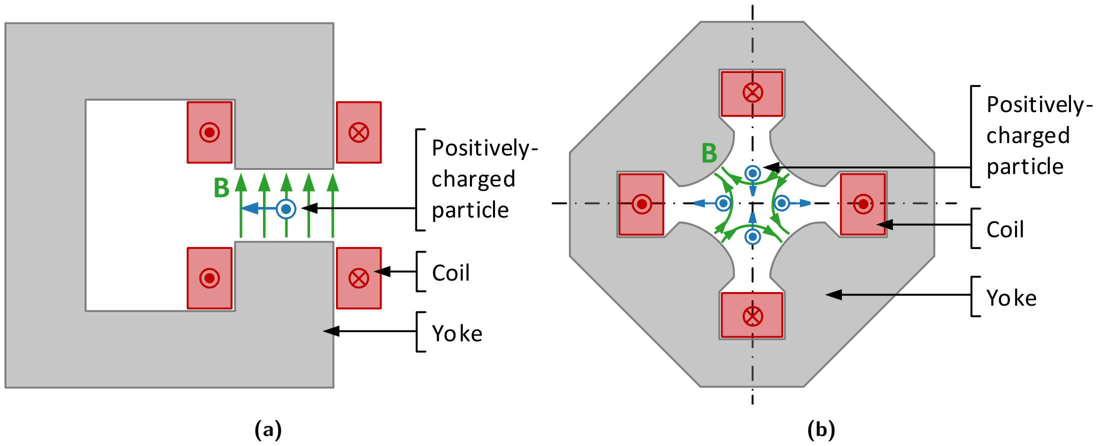

Figure 1.8: Iron-dominated accelerator magnets with a moving positively-charged particle in the aperture affected by the Lorentz force. The magnetic field is guided in the ferromagnetic yoke and the field quality in the air gap is mainly dominated by the iron pole shape. **(a)** C-shaped dipole magnet to bend the particle beam. **(b)** Quadrupole magnet to focus the particle beam vertically.

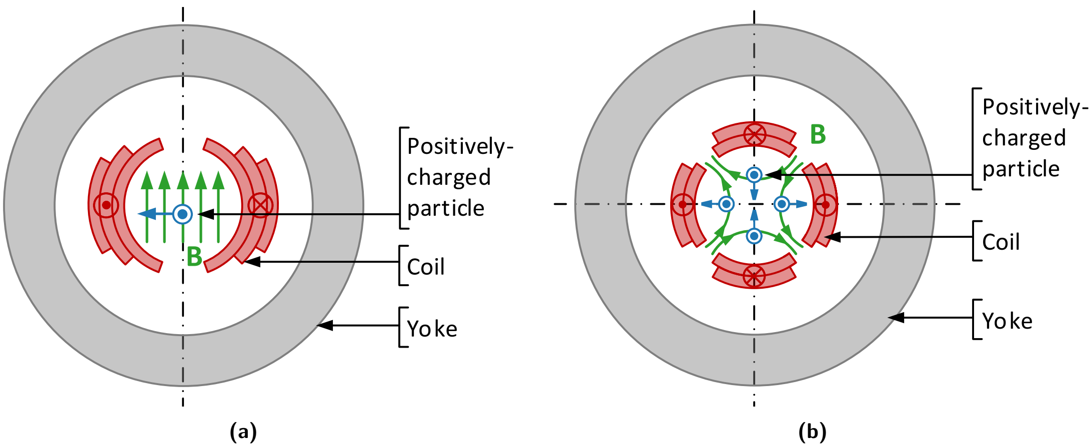

Figure 1.9: Coil-dominated accelerator magnets with a moving positively-charged particle in the aperture affected by the Lorentz force. The magnetic field distribution is mainly dominated by layout of the coil and the yoke is only employed for shielding. **(a)** Dipole magnet to bend the particle beam. **(b)** Quadrupole magnet to focus the particle beam vertically.

series expansion along the circle. This method is commonly used and often called multipole coefficients or field harmonics. For example, errors of the particular design from the ideal field distribution are often assessed by field harmonics at a particular reference radius, e.g. in the case of the 11 T dipole development [84]. The desired dipole component B_1, i.e. Fourier coefficient $n = 1$, of figure 1.7(c) leads to a field inside the aperture of

$$\mathbf{B} = B_1 \mathbf{e}_\mathrm{y} = \frac{2\mu_0}{\pi} J_0 \, t \, \sin(\vartheta) \, \mathbf{e}_\mathrm{y}, \tag{1.21}$$

whereby the dipole coefficient is clearly higher than the undesired multipole coefficients of higher orders. To achieve an optimal conductor arrangement concerning a specific optimisation criterion, e.g. field quality or energy efficiency, nested layers (cf. figure 1.9) or block coil arrangements (cf. figure 1.13) are widely used implementations.

To design the desired two-dimensional coil layout based on the laws of electromagnetism, numerical methods such as finite-element and boundary-element methods are used in state-of-the-art tools for magnet design. At CERN, the electromagnetic simulation and optimisation programme ROXIE for accelerator magnets was developed [129, 7]. However, also analytical approaches were developed and used in the past. For instance, R. A. Beth [21] introduced the concept of complex multipoles by employing the complex analysis. At this point, it has to be mentioned that the usual conceptual design of magnets are based on blocks or cables with homogeneous-distributed engineering current density, such as the field calculation of the cable specimen in section 3.2.2. Hence, current variations within these blocks are often not included in the optimisation of the magnetic field distribution.

A significant drawback of the coil-dominated magnets is given by the fact that the coils are located within high-field regions of the generated magnetic field unavoidably, which is also an important fact for the presented work. This implies consequently that the coils, i.e. the current-carrying conductor, are exposed to high magnetic fields and thus high electromagnetic forces. A dedicated mechanical design including force-restraining structures is necessary to counteract the Lorentz force and to prevent a destruction of the magnet. The mechanical design, which is especially crucial by using the brittle Nb_3Sn superconductor, is further discussed in the next section.

One of the broadly used implementation of coil-dominating superconducting accelerator magnets are the $\cos(\vartheta)$-design, i.e. the LHC dipoles and quadruples as well as the above-mentioned 11 T dipole magnet for the HL-LHC. It aims to approximate this above-explained current distribution with shell-shaped coils. In simplified terms, two-curved saddle coils are located around the beam aperture, as shown in figure 1.10. To approach the desired $\cos(\vartheta)$-layout, nested layers and insulated wedges are placed, according to the field optimisation results. For instance, four layers are discussed for the FCC 16 T dipole conceptual design [105]. The final coil design of the 11 T dipole magnet consists of two layers with four inner blocks and two outer blocks, as illustrated in figure 1.13(b) and 1.14(b). These nested coil packs are surrounded and pre-stressed by a non-magnetic austenitic steel collar to ensure mechanical support. Furthermore, the collared coil assemblies are enclosed by a ferromagnetic yoke to protect the surrounding area from the generated magnetic field. This is further encased by stainless steel shells and constitutes the helium vessel, so-called cold mass. The cold mass is placed in a cryostat vacuum vessel after assembling it with cryogenic insulation material, so-called superinsulation. The 11 T dipole cold mass is shown in figure 1.13(a), which is planned to exchange the LHC main dipole in the LHC cryostat within the DS regions shown in figure 1.15.

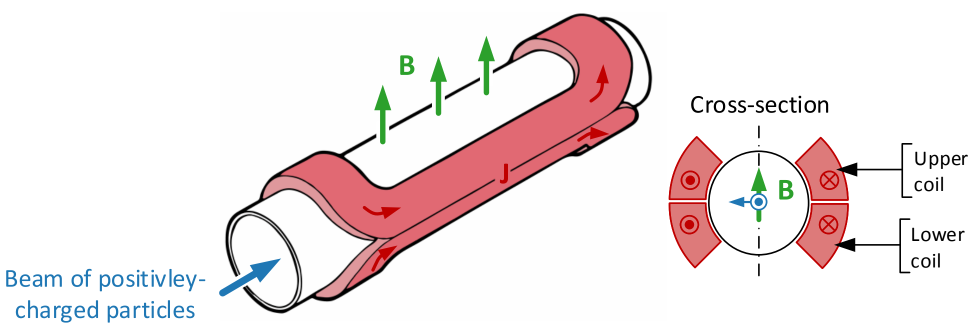

Figure 1.10: Schematic of the $\cos(\vartheta)$ dipole magnet design. Two-curved saddle coils are surrounding the particle beam aperture and generating a magnetic dipole field. Information taken from reference [179] and edited by the presenting author.

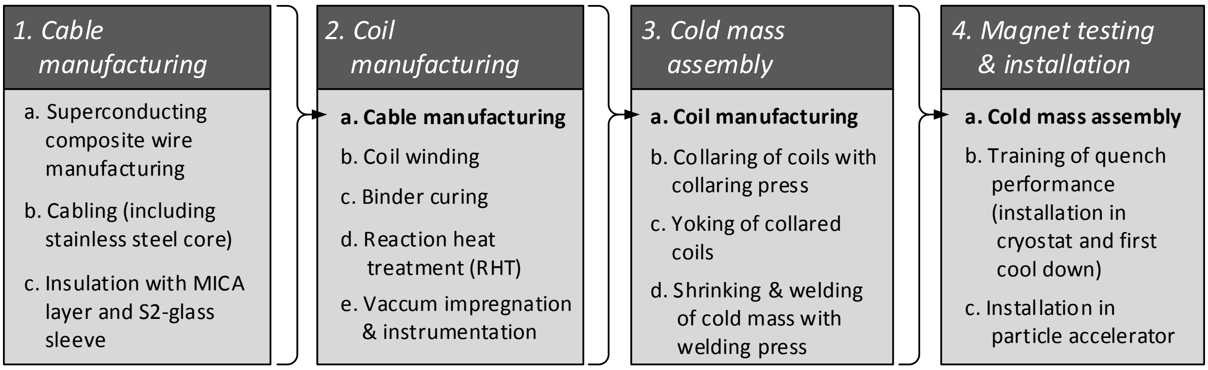

Figure 1.11: Fabrication processes of the Nb_3Sn 11 T dipole magnets at CERN according to the "wind and react" manufacturing technique.

1.3.2 Manufacturing of the Nb_3Sn 11 T dipole magnet

After the introductory reasoning of the design and structure of superconducting coil-dominated magnets, their fabrication is discussed. The HL-LHC 11 T dipole production is already well specified and the most samples of the thesis originate from the corresponding development. Consequently the fabrication of Nb_3Sn accelerator magnet production will be explained by the example of the 11 T dipole production [87, 135, 136], which also provides valuable knowledge for the planned FCC magnet development. The primary steps are illustrated in figure 1.11 and described as follows:

1. Cable manufacturing

First, the delivered Nb_3Sn composite wires are "cabled" to so-called Rutherford cables at CERN (TE-MSC-SCD) shown in figure 1.12 [30, 130]. This highly-compacted cable type was proposed by the Rutherford laboratories for magnet design in the early 1970s. Thus, 40 non-reacted Nb_3Sn wires are rolled to a hollow, twisted tube and subsequently pressed to two fully-transposed layers, as shown in the micrograph in figure 1.12(b).

The periodical transposition pitch aims for reducing induced eddy currents during the ramping of the magnet. Additionally, a non-magnetic austenitic steel core is placed in the centre to increase the adjacent resistance between the two layers and hence enable fast cycling of the magnet [155]. For comparison, the Nb-Ti wires used for the LHC magnets were also fabricated to Rutherford cables and coated additionally with an aluminium alloy for increasing the interstrand contact resistance [139].

As a final conductor for the 11 T dipole magnet, the wire RRP108/127 with 108 superconducting Nb_3Sn sub-elements and an average size of 46 µm was chosen (cf. table 2.3). The Restacked-Rod Process is further described in section 2.1, and the final cable properties are listed in table 2.2 (column "Specimen 2"). In order to wind a coil in an arc segment shape, the Rutherford cable is flatted with an angle, so-called keystone angle α. According to the mentioned "wind and react" technique the wires are cabled in the non-reacted condition. Otherwise, the brittle Nb_3Sn sub-elements would be demolished during the cabling or winding process resulting in a poorly superconducting performance. However, the necessary substantial deformation of the wire on the cable edges during the cabling can lead to a rupture of the niobium barrier (cf. figure 1.12(b)) [62]. Consequently, the tin core of the sub-elements could leak out during the reaction heat treatment above 230 °C. This would contaminate the high-purity copper matrix resulting in a degradation of the *RRR* and hence loss of stabilisation performance.

After the cabling, the Rutherford cable gets insulated with a S-2 glass sleeve braided over a C-shaped Mica layer shown in figure 1.12(a), to ensure electrical insulation up to a breakdown voltage of 10 kV after the reaction heat treatment of up to 650 °C [150].

2. Coil manufacturing

In the next step, the cables are wound to cos(ϑ)-coils, i.e. curved saddle coils, with a four degree of freedom winding machine at CERN (TE-MSC-LMF) [122, 123]. The first and second layer of the 11 T dipole coils are wound around a mandrel with saddle-shape ends including the filling wedges according to the magnet design. Respectively, two coils are put together to fully surround the beam aperture and generate the designed field distribution.

Subsequently, after the winding and equipping the coil layers with the necessary instrumentation, e.g. voltage-taps, they are cured under moderate thermal treatment in the range of 150 °C to 190 °C. The ceramic binder for the curing aims for the necessary stabilisation support of the double layer coils for

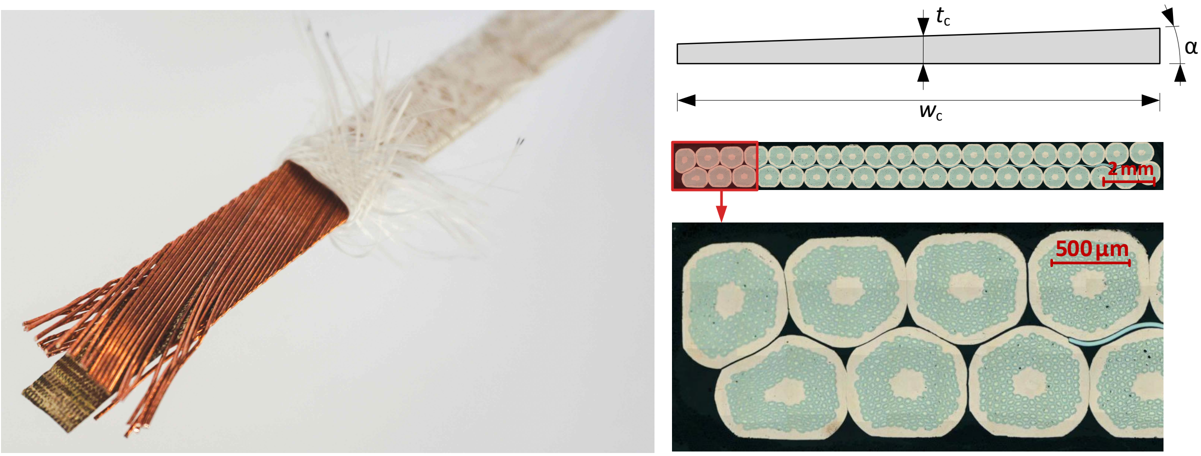

(a) **(b)**

Figure 1.12: Rutherford cable for the 11 T dipole development made of 40 Nb_3Sn strands with a nominal cross-section dimension $w_c \times t_c = (14.7 \times 1.25)\,\text{mm}^2$, a keystone angle $\alpha = 0.79°$ and a transposition pitch of 100 mm. **(a)** Picture of the slightly untwisted non-reacted cable with the austenitic steel core and S-2 glass sleeve. The C-shaped Mika foil for additional insulation is not pictured. **(b)** Schematic and optical microscopy of the transverse cross-section after the reaction heat treatment and impregnation. The resulting deformation of the wires and sub-elements as well as the core at the thin edge can be seen enlarged in the bottom micrograph.

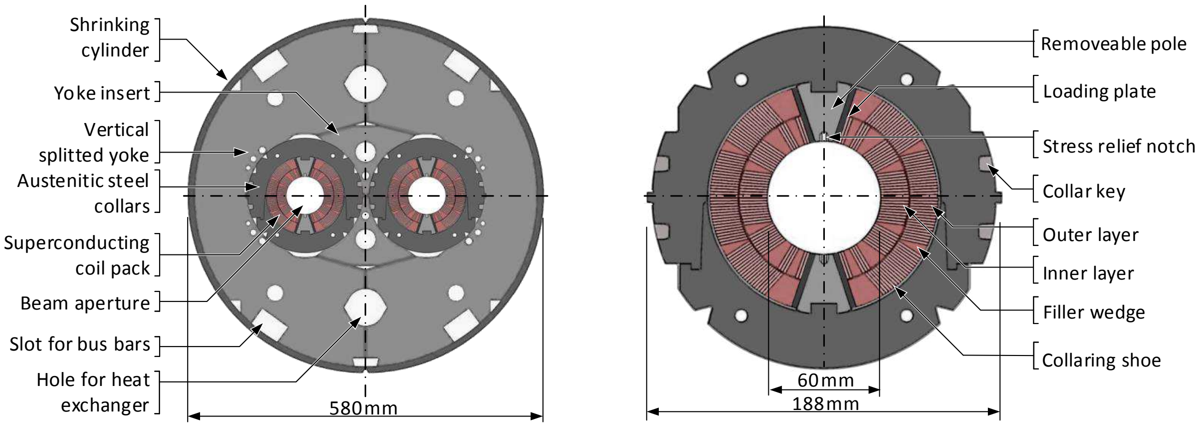

(a) **(b)**

Figure 1.13: Schematic of the cross-section of the 11 T dipole magnet. **(a)** Final cold mass assembly. **(b)** Collared coils from a single aperture enlarged from (a). Information taken from reference [34] and edited by the presenting author.

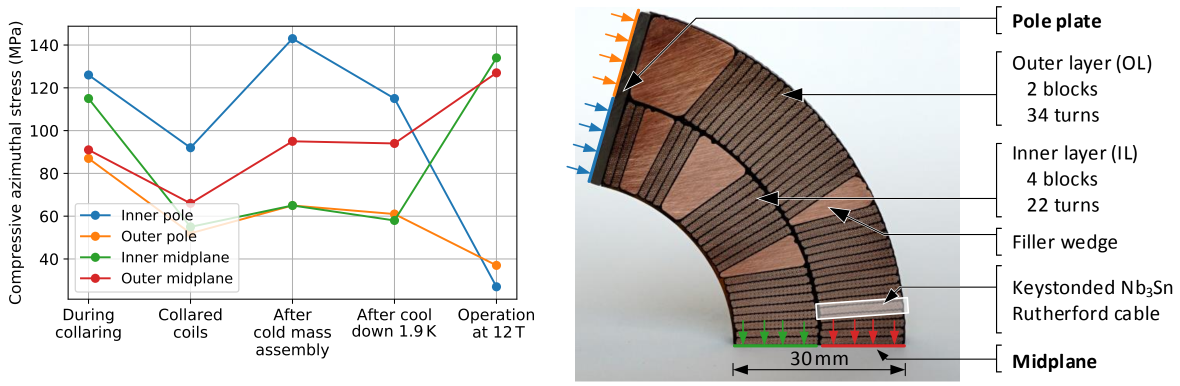

(a) **(b)**

Figure 1.14: Stress distribution within a coil quadrant of the 11 T dipole magnet. **(a)** Assessment of the coil pre-stress in pole and mid-plane region over the manufacturing steps by the aid of FEM. Information taken from reference [84]. **(b)** Extracted coil quadrant of the reacted and impregnated coils.

the following manipulations.

After the winding, the coils are subjected to the necessary RHT, accordingly to the "wind and react" technique. The approximately 5.4 m long coils are placed into a reaction mould and transported into a heat treatment furnace [90]. The RHT is performed according to the wire manufacturer in three temperature dwells up to 650 °C with a specified homogeneity down to ±3 °C [136]. Including the temperature ramps of 50 °C h^{-1} the RHT has a duration of approximately 200 h, which is further described in section 2.1.

After the Nb_3Sn A-15 phase is formed, the coil should not be deformed to prevent breakage of the sub-elements, which would affect the superconducting performance negatively.

Subsequently, the coils get impregnated with epoxy resin CTD101K. They are placed in an impregnation mould for vacuum pressure impregnation (VPI) in order to guarantee the necessary mechanical stability for the brittle Nb_3Sn superconductor for the magnet assembly. The 11 T dipole design intends a mounting of the necessary quench heaters after the impregnation. An extracted part of a reacted and impregnated coil is pictured in figure 1.14(b).

3. Cold mass assembly

After the successful manufacturing of the four double-layer coils for the twin aperture, they are grouped to the helium vessel, so-called cold mass assembly.

In order to withstand the high electromagnetic forces during operation, the two coils per aperture are pre-strained by force-restraining structures, known as collar. It is made of packs of austenitic steel laminations with vanishing magnetic susceptibility. The coils, including the beam pipes, are placed between the intermeshing collar. A finished collared coil group is shown in figure 1.13(b). In order to pre-stress the coils a pressure is exposed to the collared coils by using a hydraulic press, so-called collaring press. The collaring keys are inserted under pressure so that a residual pre-stress is maintained after releasing the collaring press.

The magnet assembly process, in particular the collaring process, is considered as one of the most crucial steps of magnet manufacturing regarding the mechanical design. The local stress distribution within the coil must locally not exceed the irreversible strain limit of the Nb_3Sn superconductor. Considering that this has to be guaranteed over the entire length of the 5.4 m long coils, a complex composite material, it is a technological challenge and required components with low manufacturing tolerances. The mechanical concept of the 11 T dipole magnet considered to transfer the stress azimuthally by the removable poles with stress relief notches [84, 5]. It guarantees a local azimuthal compressive stress smaller than 150 MPa during all manufacturing steps and operation, which is commonly used as the pre-stress limit without irreversible damage.

Afterwards, the collared coils are equipped with the yoke insert and subsequently surrounded by the vertically split yoke. The yoke insert aims to apply a symmetrically load on the collared coils during the following shrinking process. The yoke, made of ferrite laminations, shields the magnetic field. Afterwards, the entire assembly is placed in between two 10 mm thick stainless steel shells, the shrinking cylinder. The two shells get closed and are welded under a hydraulic press, so-called welding press, to guarantee an additional compaction of the assembly. The finished assembly can be seen in figure 1.13(a).

After the cold mass assembly is closed, it gets covered by a super-insulation and located in a vacuum vessel with the necessary feed-through for electrical connection and subjected to the first tests at low temperature.

4. Magnet testing and installation

Before the magnet is ready for the installation and operation, it is tested at CERN (TE-MSC-TF). The magnet is cooled down with superfluid helium to its operation point of 1.9 K. Every superconducting magnet has to be trained to reach its nominal respectively ultimate performance level. This consists of iteratively ramping the current of the superconducting coils until a quench. In order to prevent damage, every superconducting magnet is equipped with voltage-taps and so-called quench heaters. This safety facility is used to perform a safe and spatial-homogeneous transition of the entire coil to the normal-conducting state in the case of a local quench. The stored energy of magnet is then absorbed by resistors. The iterative quenching of a virgin magnet is followed by progressive improvement. Until several times, the improvement saturates, and the nominal performance of the magnet is reached [136].

The origin of the training phenomenon is assumed to be caused by slight movements of the conductor within the virgin coil compound under the influence of the tremendous electromagnetic forces. These quenches caused by such movements get reduced after the conductor reaches its final position by the training process, i.e. it is extensively embedded. The behaviour varies widely and depends on the conductor type, the coil geometry and the manufacturing of the magnet. The training procedure was also applied to the impregnated cable specimens, as described in section 4.1.2.

After the training, the superconducting magnet is ready to be installed in the LHC in the DS region during the future long-term shut down of the LHC, as mentioned in section 1.1.

Finally mentioned, the substantial mechanical concept of the cold mass considers the coils pre-stress in two parts, the collaring and shrinking. First FEM analysis of M. Karppinen *et al.* [84] regarding the stress distribution within the coil cross-section pointed out that the stress peak values during the manufacturing are similar to those at full operation at 1.9 K and 12 T. The FEM is based on a model considering cables with homogeneous material properties, hence local stress concentration effects of wires or even sub-elements with voids are not studied. The maximal values at the inner and outer mid-plane as well as pole plate of a quarter section after the crucial manufacturing steps are extracted and summarised in figure 1.14.

Considering that the mechanical properties are temperature-sensitive and the manufacturing uncertainties have to be accepted to a certain extent, a damage of the brittle conductor due to be manufacturing can occur. Moreover, the need for higher pre-stress for the 16 T magnets is discussed for the current designs to counteract the higher electromagnetic forces on the conductor. In combination with the high strain-sensitivity of the used Nb_3Sn wires, this has been the original motivation of studying the irreversible degradation of the superconductor caused by necessary applied stress during manufacturing. The investigation is covered by the 16 T dipole development programme, wound conductor task [88], which includes the presented work. The concretisation of the arising problem, as well as the reason for the chosen experiments to investigate this topic, is explained in section 1.5.

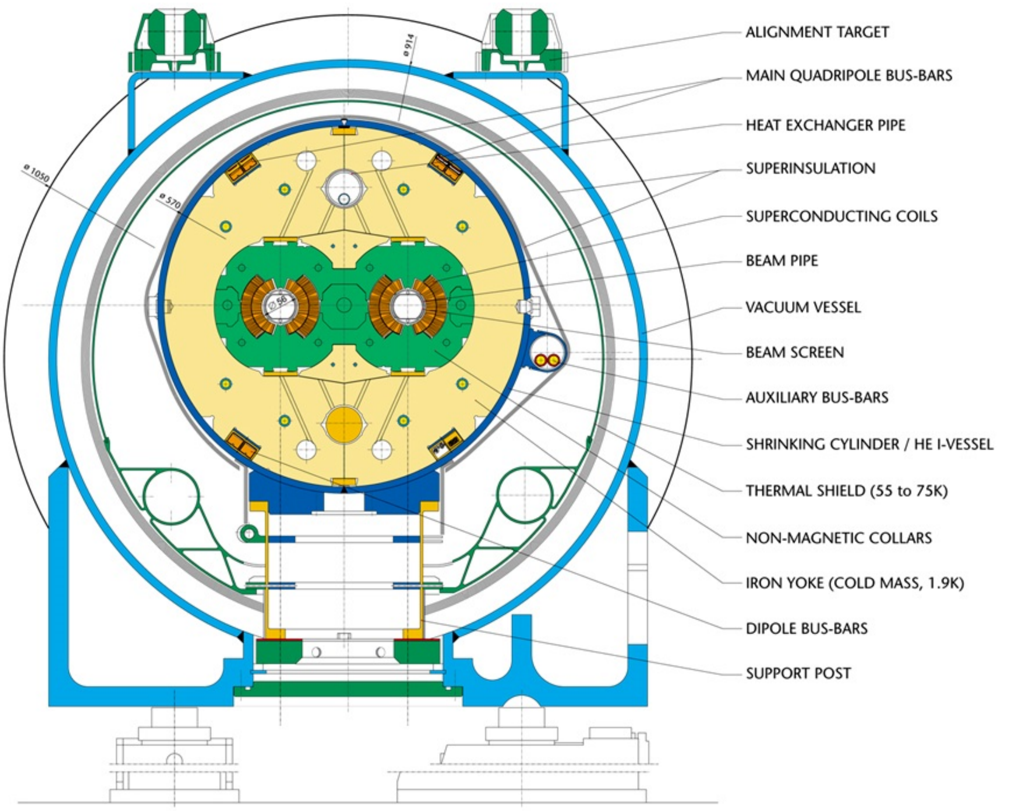

Figure 1.15: Cross-section of the LHC dipole magnet. A twin-aperture coil-dominated made of Nb-Ti superconductors. Information taken from reference [34].

1.4 Former investigations & literature research

Due to the technological importance of the strain dependency within the magnet design, broad-based studies on wires and cables with different purposes and arrangements were performed in the past. Many load cases and identification measurements performed on **superconducting composite wires** could be found within the author's literature research.

- J. W. Ekin [52] performed I_c-ε measurements with a stress-free cooling cryostat. The superconducting wire is not soldered or constrained in any other way during the cool-down, which allows measurements at the intrinsic pre-strain condition.
- In order to test the superconducting properties as a function of axial load, two common types are established serving to investigate stress, e.g. caused by the winding process of a magnet coil.

  The so-called Walter's spring [174] is a coil sample holder, which can apply axial tension or compression on a long superconducting wire by twisting or untwisting the spring, respectively. The University of Geneva published several experiments based on the Walter's spring, which includes also a modification to exert transverse stress on impregnated and non-impregnated Nb_3Sn wires [31, 35, 114, 145, 168].

  Another established possibility to apply axial stress was designed by B. ten Haken *et al.* [159] using an U-bending beam. The sample is soldered on the back of a U-spring, which can emulate axial tension or compression on the soldered wire by applying force on the arms on the other side. Although the sample length is limited, it performs the stress in axial direction without almost no undesired bending effects and is further used in recent experiments by M. G. T. Mentink [110]. Due to the short sample length of the U-spring configuration, which inherently reduces the accuracy of the I_c measurements, A. Godeke *et al.* [66, 67] designed an additional bending device in a cylindrical shape, so-called Packman.
- An experimental cryostat setup to analyse the hoop stress on wires within a ring-coil was designed by J. W. Ekin [52], which emulates the dominant load case within solenoid magnets.
- W. Goldacker *et al.* [68] designed a bending strain rig for continuous bending of high-temperature superconductor at 77 K, which can be used to determine essential properties for magnet design, e.g. maximal bending radius.

The properties of **superconducting cables** were often tested as a function of the transverse stress. The dominating load case on a superconducting coil compound in a $\cos(\vartheta)$-magnet (cf. section 1.3) is in azimuthal direction. In order to simplify the experimental arrangement, cables are exposed to transverse stress.

- The University of Twente houses a cryogenic press, which can load superconducting cables with more than 250 MPa perpendicular to an applied field of up to 15 T [41, 27, 161, 170, 186].
- At CERN, B. Bordini *et al.* [26, 25] performed measurements with a FRESCA-compatible sample holder for transverse stress up to 155 MPa parallel to an applied field of 10 T, based on an aluminium shell and a bladder-and-key system.
- A short sample test facility was used in the Fermi National Accelerator Laboratory (FNAL) to apply transverse stress on Nb_3Sn Rutherford cables [13].
- The Kalsruher Institute of Technology (KIT) implemented a setup for high-temperature superconductors to measure samples exposed to transverse stress [17].

All mentioned experiments are optimised to a specific purpose, and the respective stress application has to be considered while comparing results. Also, the constraints due to the different thermal contraction of the sample and the material of the respective sample holder have to be taken into account [163]. Some of the experiments are focusing on the fundamental reasoning of the physical behaviour. Other of them are designed to be as close as possible to the final operation condition within a magnet, to deliver reliable parameters for magnet design.

Despite the continuous experiments regarding strain at cryogenic temperatures, the impact of stress on the superconducting properties caused by the manufacturing of magnets is hardly investigated. Within the author's literature research only view tests could be found, although FEM analysis showed high stresses on Nb_3Sn coils during the mechanical force-restraining procedure [84]. For instance, B. Jakob *et al.* [80] performed tests on impregnated Nb_3Sn Rutherford cables made of a bronze-process wire for the design of a 1 m Nb_3Sn demonstrator magnet in the frame of the LHC investigations in 1990.

Regarding the developed **experimental NearT_c concept** some alternative implementations to reach variable-temperature measurements were published in the past. They aimed primarily at evaluating the temperature margin of a wire's performance or confirming the temperature dependency of USL using a gaseous helium environment. For instance, B. ten Haken *et al.* [160] performed variable-temperature measurements above the atmospheric boiling point of helium with currents up to around 120 A. L. F.

Goodrich *et al.* [70] implemented a variable sample temperature in the range of 4 K to 20 K with test currents up to 200 A by using a helium gas flow cryostat. Subsequently, L. F. Goodrich *et al.* [69] implemented additionally an apparatus with current leads for up to 400 A and a sample temperature range of 4 K to 200 K.

Based on the given introduction in this chapter, **the influence of stress and strain on the performance of Nb_3Sn composite wires** can be divided into three categories:

1. The **intrinsic properties of superconductivity material** are influenced by stress and strain. In conventional superconductors, superconductivity depends on the coupling of phonons, and the electronic system. Phonons are a property of the crystal lattice, which is directly affected by stress and strain. It is presumed that the cause of the strain-dependency of the intrinsic properties is strain-induced phonon anharmonicity. For instance, D. F. Valentine *et al.* [169] provided a model of the strain-dependency by the means of the Eliashberg theory [59], especially the formulation of W. L. McMillan [108]. The publication emphasizes a broadening of the phonon spectrum, due to the anharmonic phonon generation. Consequently, the electron-phonon coupling is reduced, which leads to the decrease of the intrinsic properties. Recently, W. D. Markiewicz [106] devised a model of $T_c(\varepsilon)$ by the help of the phonon spectrum and the Eliashberg function (cf. figure 1.4(a)). Additionally, M. G. T. Mentink [110] performed a microscopic computation complementing experimental data.

2. In the case of state-of-the-art Nb_3Sn wires the **flux pinning**, which is decisive for the **critical current**, is mostly created by the grain boundaries. Strain on the superconducting material influences its micro-structure, i.e. disorder or dislocation, and hence the pinning behaviour. For comparison, pinnings centres in commercial Nb-Ti wires, which are primary α-Ti precipitates, are generated by a thermo-mechanical treatment. Additionally, $J_c(B, T)$ is indirectly influenced by the strain-dependency of upper critical field B_{c2} and critical temperature T_c.

3. High stress deforms the **copper matrix and residual pre-stress** can be induced. Further exposure of stress leads to **fractures and hence to interruptions of the superconducting sub-elements** in transport current flow direction, which harm the **thermal stability of the composite wire**. These extrinsic irreversible processes are depending strongly on the mechanical properties of the particular material, e.g. Young's modulus or yield strength. It should be noted that the sub-elements already suffer pre-strain by design of the composite wire, namely the thermal-induced pre-compression ε_m.

The impact regarding this phenomena is depending on the geometric structure of the composite wire, i.e. how the stress is distributed and effectively applied on the superconducting marital, i.e. sub-elements. High-energy X-ray diffraction experiments and analysis of the lattice parameter revealed a mixture of hydrostatic and deviatoric deformation during stress application [116]. Generally, the irreversible impact of stress is given by the plastic deformation of the copper matrix and the fracture of the superconducting material, which is also the focus of the presented work.

1.5 Scope & overview of thesis

The topic of the thesis belongs to one of three subtasks of the wound conductor task of the FCC 16 T dipole development programme, which is further described in section 1.1.

The original objective of this thesis is to determine the performance loss of the superconductor due to the manufacturing of accelerator magnets. It can be assumed that the degradation of the conductor is provoked after the RHT of the Nb_3Sn coil, which forms the brittle A-15 phase and makes the compound conductor vulnerable to mechanically damages, i.e. it has then a very low acceptance of induced mechanical stress. As already emphasised in section 1.3, the most critical part of the magnet assembly is the force-restraining procedure including welding of the shrinking cylinder, which applies the required pre-stress to the superconducting coil with high pressure of up to 150 MPa. For the manufacturing of magnets with higher nominal fields, higher pre-stresses are contemplated to counteract the higher Lorentz forces during operation.

The most dominating load case on a coil of an accelerator magnet is in azimuthal compressive or transverse compressive direction, depending on the magnet type. In general, the dominating force on an individual cable in the coil can be assumed to be in transverse direction. This **concretises the topic to the quantification and causes analysis of the degradation of Nb_3Sn cables and wires due to transverse stress at room temperature**. Consequently, the investigation stands in contrast to the currently well-investigated stress at low temperature, which is annotated in the literature research. The manufacturing and test of the entire coils were excluded for economical and experimental reasons and hence the investigation was split into the following parts to fulfil the objectives as sketched in figure 1.16:

- **Development of homogeneous stress application**
  The stress application on the cables and wires was performed based on applying pressure with a hydraulic press. Therefore, the hydraulic system was refurbished, including calibrated load cells, to measure the force applied to the specimens. In order to measure and further optimise the stress distribution, pressure-sensitive films were used. In order to allow the analysis and overlapping of the multilayer films, an evaluation script was developed.

- **Cable investigation**
  Impregnated Rutherford cable double stacks were loaded with transverse stress at RT and subsequently tested in the FRESCA cable test station at CERN. This experiment provides results similar to the actual application in a magnet coil, which is considered as a valuable contribution to the magnet design and to the refinement of the manufacturing process. Moreover, the results include mechanical effects of the coil and cable compound, e.g. mechanical behaviour of the epoxy resin and cable geometry. In parallel, the working group performed an X-ray tomography for a FEM model to estimate the partial stress within the compound conductor.

  Therefore, three state-of-the-art Nb_3Sn cable specimens from the HL-LHC were prepared and tested, which also includes the fabrication inaccuracies of the cables. A loaded and non-loaded part of the first specimen was metallographically prepared and investigated with a SEM, as described below.

- **Wire investigation and research of alternative measurement methods**
  Although the cable experiment is close to the actual application, it only delivers information on a specific cable configuration and has to be repeated if the cable properties are changed. The results include electrodynamic effects of the cable, which makes the analysis of the actual cause difficult. Moreover, cables or coil tests are highly demanding and only the critical current I_c could be evaluated in the experiment mentioned above. For that reason, a simplified experiment based on a single wire was launched to perform a root cause analysis about the degradation of the superconducting material independent of the actual cable or coil configuration.

  This investigation was split into the following parts. First, a cryostat insert was developed to perform transport current measurements up to 150 A on a straight wire in self-field. This should prevent damage of the specimen due to the Lorentz force, and furthermore, it should demonstrate alternative measurement methods. A characterisation of superconducting wires without the need of a background magnet and a continuous supply of liquid helium (LHe) should be verified. The latter is achievable since the system has not necessarily to be cooled down to the boiling point of helium and hence can be operated preferably with a cryogenic refrigerator system. The measurements were complemented by low-resistance measurements, and consequently by the evaluation of critical temperature T_c and residual resistance ratio RRR. The second part was a confirmation of the transport results by magnetisation measurements with a SQUID magnetometer, which was used to determine the critical current density J_c, the critical temperature T_c and the upper critical field B_{c2}. This should also clarify the suitability of magnetometric methods for crack detection since magnetometry is also a less demanding characterisation method for superconductors. An additional part was a microscopy campaign to detect and analyse cracks in the sub-elements caused by transverse stress. This offers a reflection of the behaviour of the measured (macroscopic) superconducting properties.

  Moreover, the working group subjected loaded wires to an X-ray tomography in order to develop a FEM model. Subsequently, a FEM simulation was performed to assess the stress condition within the wire, especially the residual strain due to plastic deformations. This links the local stress to the measured I_c degradation and observed crack initiation. This universal information could be further used to estimate the I_c degradation based on a FEM stress analysis of any specific cable or coil cross-section, which tracks the local stress values on the sub-elements [40]. It could be used to receive a preliminary assessment of crack formations and I_c degradation caused by transverse stress at RT of various configurations, e.g. different impregnation materials and strand diameters without costly cable or coil tests.

- **Microscopic investigations and development of metallographic procedure**
  In order to deliver more information on the pretended leading cause of degradation, the fracture of the Nb_3Sn, a further microscopic investigation was mandatory. Initial non-destructive X-ray

tomography turned out to be insufficient, which was the trigger of metallographic investigations to observe cracks formation in the sub-elements. Metallographic techniques were developed to detect and characterise cracks in transversal and longitudinal layers. Furthermore, chemical extraction with nitric acid was performed to confirm the reliability of the mechanical preparation.

The document is divided into the following scientific structure:

- **Chapter 1** informs about the technical and physical background knowledge used in the thesis. Furthermore, it gives an overview of the current ongoing investigations within the research community of Nb_3Sn material and accelerator magnets. Finally, it introduces the topic and describes the experiments within this thesis.
- **Chapter 2** lists all analysed specimens including their properties as well as the metallographic preparation for the SEM, developed within this thesis.
- **Chapter 3** provides a detailed description of the used methods to achieve the results. All systems, especially the self-designed cryostat insert for the wire investigation, are described. Furthermore, all procedures for measurements and data evaluation are explained.
- **Chapter 4** presents all relevant data and provides a detailed discussion of the measurements. It presents the achieved results, put then into context with previous publications and refers to the corresponding published theories. The conclusion and outlook are summarised in the last sections.

The work of the presented thesis was published to a great extent by the presenting author in two journal articles [47, 48] as main author and a conference publication [180] as a co-author. Moreover, internal technical notes were composed at CERN [46, 65].

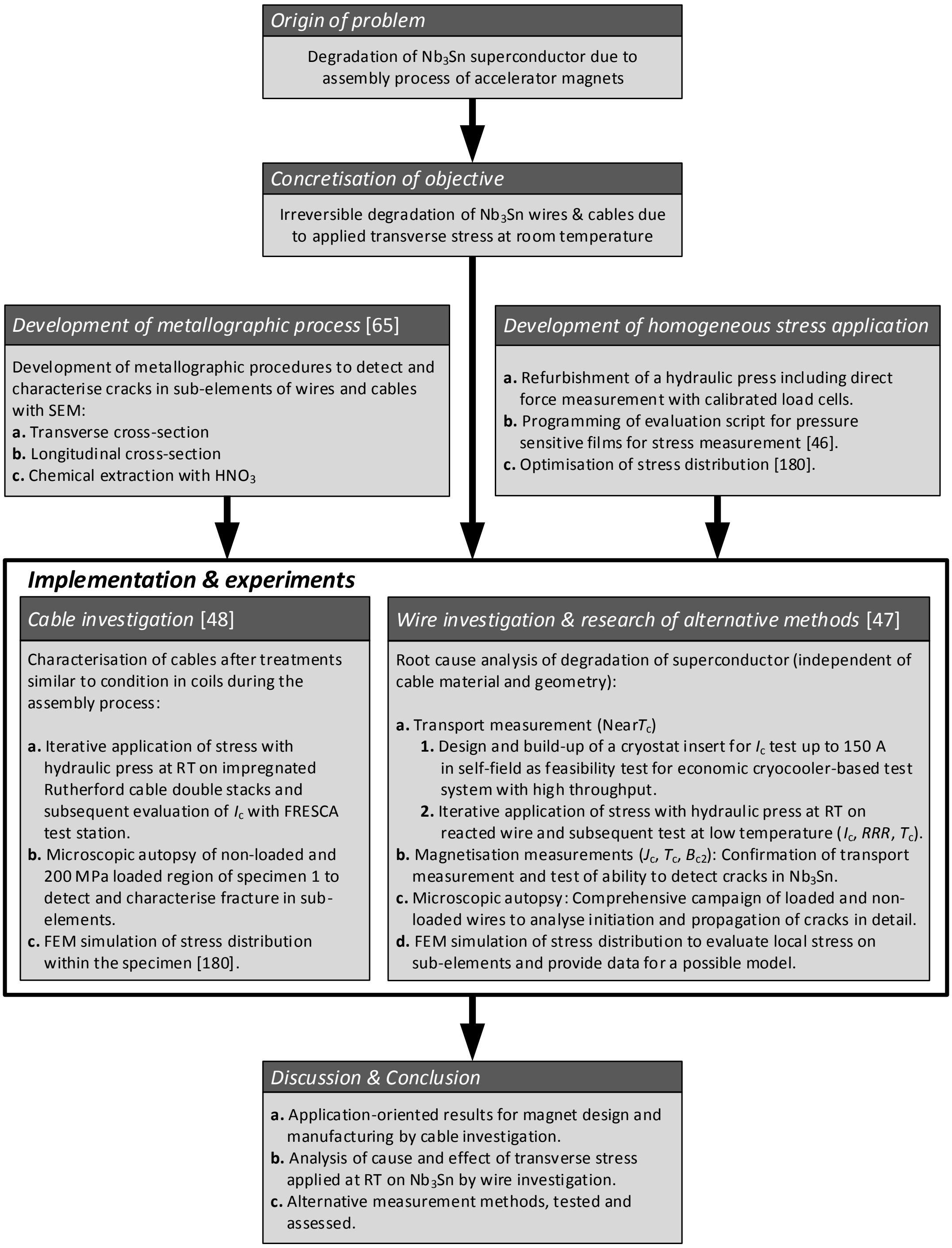

Figure 1.16: Overview and guideline of presented work.

Chapter 2

Specimen specification & preparation

This chapter describes the measured specimens and necessary preparations to investigate the degradation process of the superconductor caused by transverse stress applied at room temperature. Section 2.1 presents the wire specimen for the NearT_c transport current measurements and the magnetisation measurements with the SQUID magnetometer. The cable specimens, impregnated Rutherford cable double stacks produced to be tested in the FRESCA cable test station, are explained in section 2.2. Finally, section 2.3 summarises the metallographic techniques, which were employed for the autopsy of the specimen. Especially for the characterisation of crack formation in the sub-elements, a scanning electron microscope was used.

2.1 Wire for transport current & magnetisation measurements

For the wire investigation the Nb_3Sn compound wire RRP144/169, with the specification summarised in table 2.1, was chosen. Due to the brittleness of Nb_3Sn, it cannot be directly processed from bulk to a usable superconducting compound wire, as emphasised in section 1.2. Thus, the wires were subjected to the RHT according to the manufacturer in Argon atmosphere. This was performed by putting 16 mm long pieces of the wire in straight ceramic cavities and inserting them into the horizontal tube furnace *Carbolite GHC 12/750* at CERN.

Table 2.1: Specification of the wire RRP144/169, which was used for the wire investigation and the first cable specimen HT15OC0190. OST is a part of Bruker Energy and Supercon Technologies (BEST) since the end of 2016.

Manufacturer	Oxford Superconducting Technology (OST)
Type	RRP144/169
Cu/nonCu ratio	1.08
No. of sub-elements	144
Wire diameter	0.7 mm
Sub-element diameter	41 µm
Sub-element shape	hexagonal
Pitch length	14 mm (right-handed)
RHT	48 h at 210 °C 48 h at 400 °C 50 h at 650 °C

2.1.1 Wire type & reaction heat treatment

A microscopy of the chosen wire before and after the reaction heat treatment (RHT) can be seen in figure 2.1 and figure 2.2, respectively. Figure 2.1(b) shows the non-reacted sub-elements in detail. Every distributed-barrier internal tin wire, in the present case a RRP wire, is housing a tin (Sn) core. The core is surrounded by niobium (Nb) filaments, embedded in copper (Cu) and finally surrounded by a niobium barrier. The primary purpose of the barrier is to avoid the diffusion of tin to the high-purity copper matrix during RHT. This would lead to a reduction of the *RRR* and the thermal stability of the wire.

In the first steps of the RHT, i.e. in the range of 200 °C to 500 °C, the tin of the core is diffusing in radial direction and mixing with the inter-filamentary copper. This is performed to seek a homogeneous tin concentration of 18 to 25 at.% within the sub-element, which is mandatory to form a stable Nb_3Sn phase later on [32, 113]. The desired A-15 phase Nb_3Sn is formed with the niobium filaments in the following final high-temperature step at approximately 650 °C. Additional doping agents, in the presented case titanium rods, are implemented among niobium filaments to optimise, for instance, intrinsic properties like the critical temperature T_c and upper critical magnetic field B_{c2}.

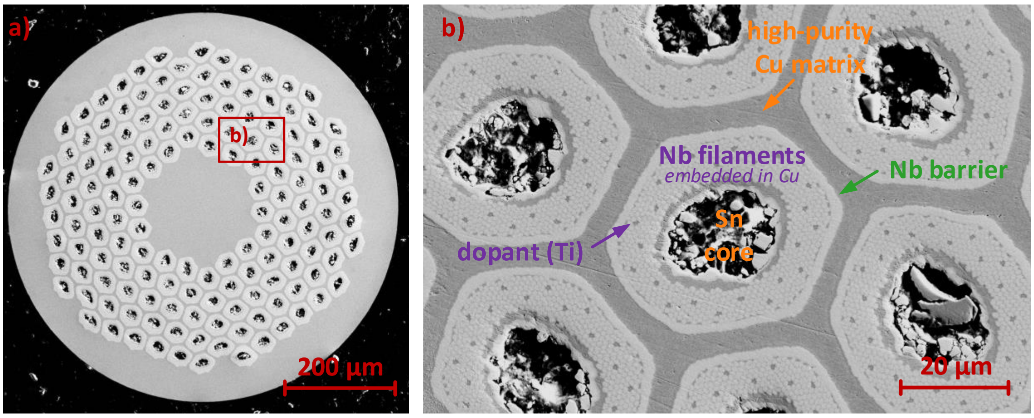

Figure 2.1: SEM micrographs of the non-reacted wire specimen RRP144/169. **(a)** Overview of the wire with a diameter of 0.7 mm and 144 sub-elements. **(b)** Detailed view of the non-reacted sub-elements with their labelled components, received by an energy dispersive X-ray analysis (EDX).

Figure 2.2 shows the fully reacted wire after the RHT, especially the superconducting Nb_3Sn sub-elements in the right part. The outer brighter layer of the sub-elements is superconducting Nb_3Sn and the core consists of residual bronze. As explained in section 1.2, the critical current is determined by pinning of the flux vortices. Without going into detail, it has to be mentioned that the volume pinning force is primarily depending on the micro-structure of the material, especially on the grain boundaries in the case of Nb_3Sn wires [140, 164]. Due to the reaction process during RHT the average grain boundary size is roughly 100 nm to 200 nm. Consequently, the refinement of the grain size is currently subject of further research [183, 184] and a possible strategy to reach the FCC Nb_3Sn target performance of $1.5 \cdot 10^9\,\mathrm{A\,m^{-2}}$ at 16 T and 4.2 K [167]. However, large grains with an average size of 2 µm are formed on the inner border of the sub-elements additionally. Their contribution to transport current is minimal, which could especially be observed in Power-In-Tube (PIT) Nb_3Sn wires [158].

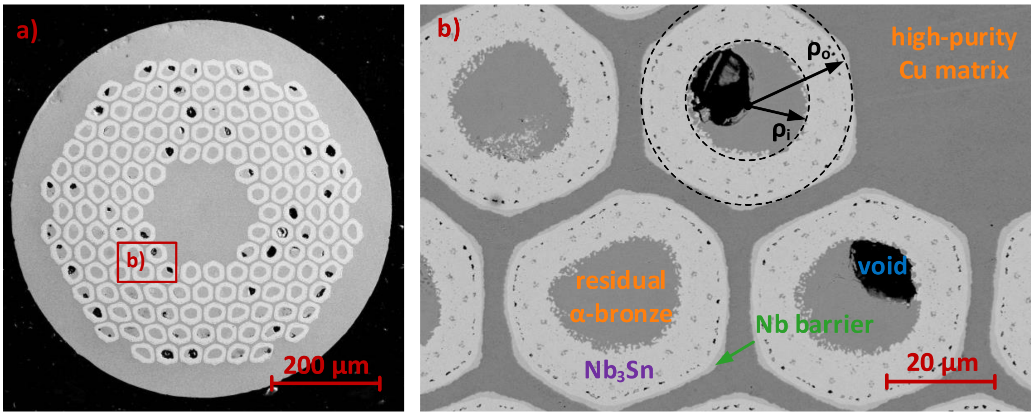

Figure 2.2: SEM micrographs of the reacted wire specimen RRP144/169. **(a)** Overview. **(b)** Detailed view of the reacted superconducting sub-elements including the inner and outer radius ρ_i and ρ_o used for the calculation in accordance with the magnetisation measurements.

Another undesired effect caused by the reaction process is the formation of so-called Kirkendall voids [137, 138], labelled in figure 2.2. The inherent phenomenon is also objective of recent research regarding the optimisation of the RHT [12, 35, 185]. They are mainly formed during the mixture of tin and copper in the lower temperature dwells and can be traced back to a volume density change during the phase transformations. These cavities in the centre of the reacted sub-elements have an essential impact on mechanical properties and the irreversible I_c degradation, as further discussed in chapter 4.

2.1.2 Specimens

The reacted 160 mm long specimen for the NearT_c transport current measurements was soldered with Sn-Pb solder alloy on the sample holder without any additional preparation steps, as further described in section 3.3. The wire and the current plates, connected with the transport bars, were heated homogeneously and only slightly above the solder's liquidus temperature (roughly 200 °C) to avoid any thermal gradients during soldering. Subsequently, the wire was placed carefully in the intended grove filled with solder. Afterwards, the voltage leads made of enamelled copper wire were soldered, as can be seen in figure 3.14.

It should be noted that the current connector length of 40 mm and the voltage-tap distance of 64 mm is a multiple of the sub-element pitch length (cf. table 2.1) in order to guarantee a homogeneous current distribution within the voltage-tap placements [51, 56].

Specimens for the magnetisation measurement and microscopic autopsy were cut in small pieces with the diamond wire saw *Diamond WireTech DWS 250*. Therefore, reacted 60 mm long wires were exposed to transverse stress, as described in section 3.1. Later, small pieces of the middle of the stressed region were extracted by cutting. This ensured the same amount of stress as performed on the NearT_c specimen, and avoided short samples extracted from the end of the stress region. Figure 2.6 shows a longitudinal autopsy of the cut, which revealed a crack penetration depth caused to the cut of less than 50 µm.

Wires for the magnetisation measurement were cut in approximately 4 mm long specimens, as can be seen in figure 3.22(b). The length was chosen in order to fulfil the requirements for the used models, which are discussed in section 3.4. Wires for the microscopic observation as well as the sawing procedure are further explained in section 2.3.

2.2 Impregnated cables for transport current measurements

The cable investigation implies the measurements of three specimens, which were specially prepared for cable performance characterisation. The Rutherford cable types, used in the first two specimens, were designed for the 11 T dipole project and the later originates from the MQXF quadrupole development. The cables are manufactured at CERN [30, 130], and their specifications are listed in table 2.2.

The cables used for specimen 1 and specimen 2 are both from the 11 T dipole development, and consequently had the same cross-section dimensions and transposition pitch. Specimen 1 was made of the same strand as used in the wire investigations (cf. table 2.1). The specifications of the strands used in the other two cables are summarised in table 2.3 and 2.4, respectively. The strand of the specimen 3 had a higher diameter, which resulted in a larger cable cross-section dimension. All cables were keystoned, equipped with a stainless steel core and insulated with a braided S-2 glass sleeve [150], as applied for the coil production.

Table 2.2: Specification of the cables used for the specimens within the cable investigation.

	Specimen 1	Specimen 2	Specimen 3
Cable ID	HT15OC0190	HT15OC0210	HT16OC0217
Manufacturer		CERN	
Project	11 T dipole	11 T dipole	MQXF quadrupole
Strand type	RRP144/169	RRP108/127	RRP108/127
Strand diameter	0.7 mm	0.7 mm	0.85 mm
Number of strands		40	
Transposition pitch	100 mm	100 mm	109 mm
Transposition direction		left-handed	
Width	14.7 mm	14.7 mm	18.15 mm
Middle thickness	1.25 mm	1.25 mm	1.525 mm
Keystone angle	0.79°	0.79°	0.4°
Thin edge compaction	17.95 %	17.95 %	15.42 %
Thick edge compaction	3.48 %	3.48 %	5.17 %
Core material		316LN (austenitic steel)	
Core dimension		12 mm × 24.3 µm	
Insulation material		S-2 glass braiding sleeve	
Insulation thickness		0.2 mm	
Additional insulation	none	C-shape Mika	none

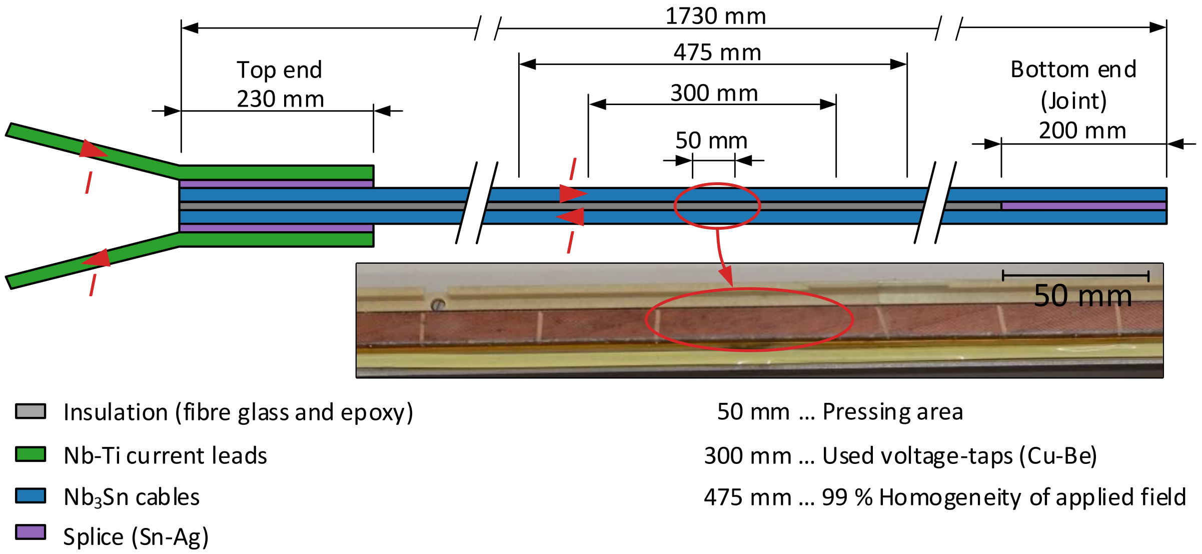

Figure 2.3: Schematics including dimensions of the FRESCA-compatible cable specimens, keystoned-compensated Rutherford cable double stacks with Nb-Ti current leads. An image of specimen 1 including voltage-taps (cable type HT15OC0190), in the opened FRESCA sample holder, can be seen in the bottom right part.

2.2.1 FRESCA-compatible specimens

The specimens were made as shown in figure 2.3 to meet two requirements, applying transverse stress on the reacted and impregnated specimen and characterising it in the FRESCA test station. An approximately 1.7 m long keystoned-compensated Rutherford cable double stack was made of a single cable type. The typical cross-section can be seen in figure 2.4. This arrangement allowed a planar surface to apply transverse stress and ensured a closed measurement circuit for the I_c measurements. The manufacturing of the samples was carried out at CERN as described:

1. The already insulated non-reacted cables got wrapped together with a 0.2 mm thick S-2 glass braided band. Subsequently, voltage-taps made of copper-beryllium (Cu-Be) were laterally placed over the entire cable width, underneath the sleeve at certain locations. The location and purpose of the specific voltage-tap is further described in section 3.2. In order to prevent short-circuits between the cables, the voltage-taps of the upper and lower cable were mounted with a shift of 20 mm. The insulation on the bottom end was removed, and a 200 mm long copper foil was placed between the cables to create an electrical connection.

2. The prepared specimen was subjected to the mandatory RHT to form the superconducting A-15 phase in the sub-elements. This was performed by housing the samples in a dedicated reaction mould and using the furnace *Carbolite GLO 750KE/09-1G*. Additionally, the voltage-taps and the copper foil were bonded inherently by diffusion at these high temperatures.

3. In the next step, the bottom ends were soldered together with Sn-Ag solder alloy forming the so-called bottom joint. Afterwards, the specimen was impregnated within a dedicated impregnation mould by vacuum pressure impregnation (VPI) with epoxy resin CTD101K, whereby the top end was covered for further processing. The average gap between the two cables within the stack was approximately 0.3 mm.

4. In the last step, the necessary ductile Nb-Ti current leads were soldered to the top end of the double stack over a length of 230 mm. They were subsequently used to electrically connect the specimen with the sample holder insert of the FRESCA test station. Finally, the lateral part of the voltage-taps was revealed for soldering with the signal wiring.

As indicated in figure 2.3, the test current I was fed by the current leads and the bottom part of the cables were soldered together. Hence, by connecting the specimen to the current source, an anti-parallel current flow is generated. Both cables were equipped with voltage-taps, in order to allow a simultaneous measurement and analysis. An area with a length of 50 mm was defined for pressing in the centre of the specimen. This ensures a pressing area over a half pitch length without voltage-taps. Moreover, the placement guarantees I_c measurements in the desired high-homogeneity region of the applied field of the FRESCA test station. According to the test run at the beginning of each measurement session, the splices on the top and bottom end had a resistance in the range of 0.3 nΩ at low temperature [20].

Specimen 1 and 2 were impregnated without additional layers and had a nominal cross-section area of (15.6 × 1.8) mm^2, which can be seen in figure 2.4(a). Thus, the stress exertion was performed on the epoxy resin.

At the end of the investigations, another test configuration was chosen for the specimen 3 by impregnating additional titanium bars parallel to the cable stack in a sandwich arrangement, as can be seen in figure 2.4(b). The titanium bars with a cross-section of (18.7 × 2.1) mm^2 as well as the larger MQXF cable type enlarged the specimen cross-section to (19.3 × 9.0) mm^2.

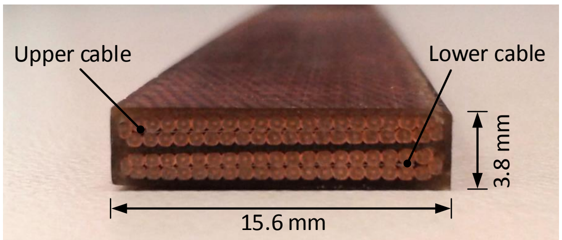

(a)

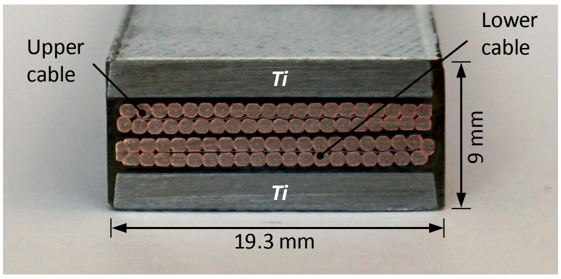

(b)

Figure 2.4: Pictures of the specimens' cross-sections, impregnated Rutherford cable double stacks. **(a)** Specimen 1 and 2 with the cable types HT15OC0190 and HT15OC0210, respectively (for the 11 T dipole development). **(b)** The additional specimen 3 with the cable type HT16OC0217 (for the MXQF quadrupole development) and titanium shims in sandwich arrangement.

Table 2.3: Specification of the wire RRP108/127 (Ø=0.7 mm), which was used for the second cable specimen HT15OC0210.

Manufacturer	see table 2.1
Type	RRP108/127
Cu/nonCu ratio	1.15
No. of sub-elements	108
Wire diameter	0.7 mm
Sub-element diameter	46 µm
Sub-element shape	hexagonal
Pitch length	14 mm (right-handed)
RHT	see table 2.1

Table 2.4: Specification of the wire RRP108/127 (Ø=0.85 mm), which was used for the second cable specimen HT16OC0217.

Manufacturer	see table 2.1
Type	RRP108/127
Cu/nonCu ratio	1.2
No. of sub-elements	108
Wire diameter	0.85 mm
Sub-element diameter	55 µm
Sub-element shape	hexagonal
Pitch length	19 mm (right-handed)
RHT	see table 2.1

2.3 Metallographic preparation techniques

Previous publications indicated that in the high-stress range the crack formation in the brittle Nb_3Sn sub-elements is the leading cause of performance loss [31], [54, p.436]. Hence, the investigation of the cracks in sub-elements and the search for proper tools

- to detect cracks and analyse their propagation,
- to determinate the stress threshold of crack initiation and
- to investigate their relevance to the critical current degradation,

was essential. Initial non-destructive X-ray computed tomography of loaded specimens delivered only insufficient resolution for crack detection and analysis [48], which was the reason to further deepen the metallographic research and development.

Considering that the already very brittle Nb_3Sn sub-elements with potential cracks are hosting cavities, i.e. voids, and are embedded in a soft-annealed copper matrix, it is a metallographic challenge to reveal cracks unequivocally without any polishing damage. Sophisticated polishing is necessary to

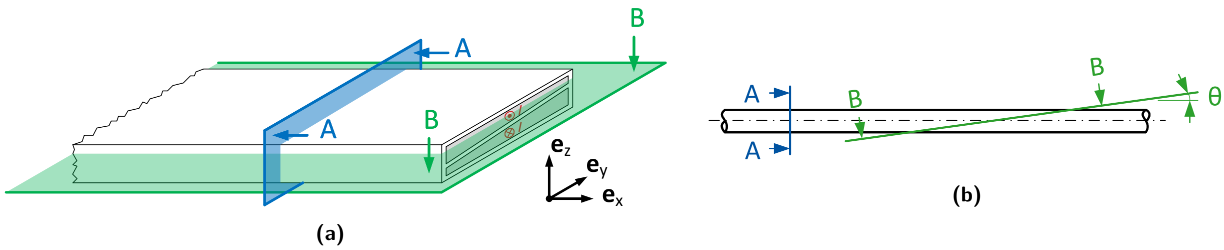

Figure 2.5: Schematics of the prepared layers to detect and characterise cracks in the Nb_3Sn sub-elements (A-A: transverse cross-section, B-B: longitudinal cross-section). **(a)** Layers in the case of the cable specimen. **(b)** Layers in the case of the wire specimens. To explore the entire cross-section longitudinally, the preparation of the longitudinal cross-section was performed with a tilt angle of approximately $\theta = 2°$.

reliably reveal the sub-elements and in particular the cracks, which are in the range of a few micrometres, from this given surface with fluctuating hardness. Furthermore, the behaviour of cracks formation, especially caused by transverse stress, was barely investigated in the past.

Within the author's literature research, only a few investigations about metallographic extraction of cracks in Nb_3Sn compound wires could be found, e.g. regarding cracks caused by axial and bending stress by M. C. Jewell *et al.* [81] and electromagnetic forces by C. Sanabria *et al.* [134]. On the base this information status, the following three supplementary techniques were chosen, further developed and evaluated for crack examination:

1. Preparation of the **transverse cross-section**, i.e. perpendicular to the current flow, which is denoted with A-A or YZ-plane in figure 2.5. This common method delivers already after rudimentary polishing general information of the wire, e.g. the number of sub-elements, average sub-element size and condition of the superconducting area. In the presented work, more extensive polishing was necessary for crack detection. The transverse cross-section was primarily used to detect cracks as well as to reveal the crack distribution and density within the cable and the wire.

2. Preparation of the **longitudinal cross-section**, which is denoted with B-B or XY-plane in figure 2.5. This method was used to characterise the shape and propagation of the cracks. For the latter wire investigation, the longitudinal cross-section was made with a tilt angle of approximately $\theta = 2°$, to explore several layers simultaneously.

3. **Chemical extraction of the sub-elements with nitric acid (HNO_3)**. Nitric acid reacts with and especially dissolves copper, which reveals the sub-elements without any mechanical treatment. This method was only used within the wire investigation to confirm the results received from the methods explained above.

After completing the final load step of 200 MPa of cable specimen 1, a metallographic preparation for crack examination was launched. In order to exclude ambiguities and misinterpretation, a non-loaded part of the approximately 1.7 m specimen was metallographically prepared as well.

On the base of this success, a metallographic campaign within the wire investigation was developed. Wires of the same type, as used for the transport current and magnetisation measurement, were loaded with particular stress from 0 MPa to 200 MPa and metallographically prepared for the microscopic investigation to detect the crack initiation and analyse the crack formation and behaviour in detail. Therefore, the chemical extraction of the Nb_3Sn was exercised to confirm the results of transversal and longitudinal cross-sections. Similar to the cable specimen examination, the non-loaded case was also examined to guarantee an unobjectionable preparation, which does not cause cracks.

Following metallographic steps were performed to prepare the transverse and longitudinal cross-section of cables and wires for electron microscopy:

1. The specimens were carefully cut by using the above-mentioned diamond wire saw with a speed less of than $2.5\,\mathrm{m\,s^{-1}}$. The specimens were cut into approximately 25 mm long pieces. A later observation shows a penetration depth of the cracks caused by the cut of less than 50 µm, which can be seen in figure 2.6. Considering that the following grinding and polishing steps removed more than 0.7 mm of the surface vertically and the longitudinal cross-sections were only observed in the centre of the sample, this circumstance did not influence the investigation.

2. The specimens were embedded in cold epoxy resin by vacuum pressure impregnation.

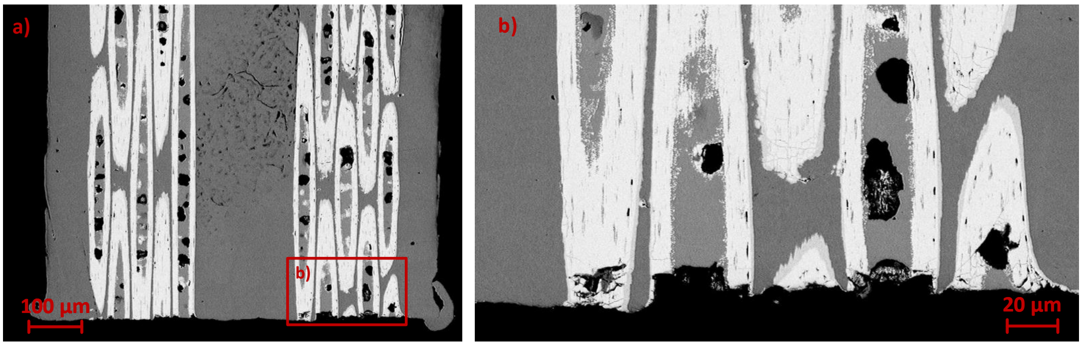

Figure 2.6: SEM micrographs of the end of the specimen. One can see that the cracks influenced by the cut propagate less than 50 µm. This result can be treated as a quality check, that the observed cracks in the centre of the specimen are not influenced by the cut with the diamond wire saw.

3. Subsequently, the surface was ground with fine-grained Silicon Carbide (SiC) grinding paper up to the target level.
4. The surface was polished with polishing paper in combination with water-based diamond paste as well as a vibratory polisher with colloidal silica.
5. As the last step, the surface was automatically cleaned with a mixture of water rinsing and ultrasound, followed by drying.
6. Before the start of the electron microscopy session, the sample was sputter-coated with several nanometres of a gold-palladium alloy (Au-Pd), to preventively improve the signal-to-noise ratio and hence receive better quality of the SEM images.

Wire specimens for chemical extraction of the sub-elements were exposed to HNO_3 50 vol.%, rinsed with distilled water, dried and subsequently also studied in a scanning electron microscope. Embedded samples were sprinkled with a few drops of HNO_3, which led to the dissolution of the copper by roughly 300 µm after an exposure time of 60 min. A typical result is pictured in figure 2.7, observed from a small tilted view. Furthermore, the outer surface of the niobium barrier and the inner boundary of the Nb_3Sn area, the diffusion zone, can be observed. Moreover, loose wires with a length of approximately 25 mm were dipped into a bath of HNO_3 for roughly 20 min. These wires were only dipped half into the acid and for a relatively short time to prevent the copper matrix from dissolving entirely by capillary attraction. The metallographic processes described in this section are additionally summarised in reference [65] and made a crack evaluation down to a size of 0.5 µm within this work feasibly.

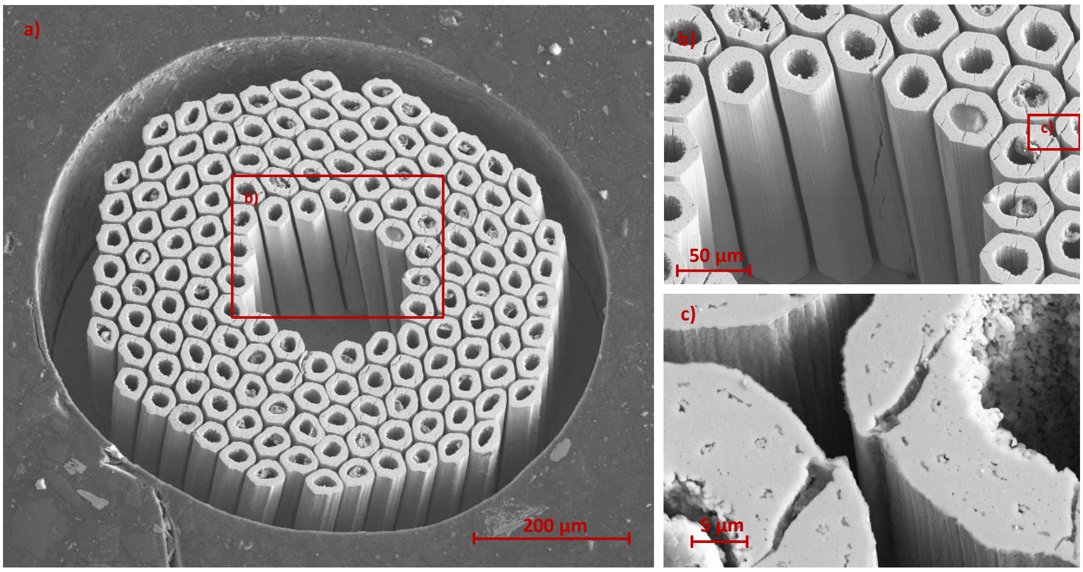

Figure 2.7: SEM micrographs of chemical extracted sub-elements of a loaded and embedded wire with nitric acid. This metallographic technique allowed the examination of the sub-elements without any mechanical treatment. Due to the dissolution of the cooper, the intended twist of the sub-elements as well as their inner and outer border are clearly visible.

Chapter 3

Measurement procedures

The measurement methods and procedures used and elaborated in this thesis are presented in this chapter. Section 3.1 describes the used hydraulic press system, the self-programmed evaluation script for pressure-sensitive films as well as the stress application on cable and wire specimens. The FRESCA cable test station used to determinate the degradation on impregnated cables after a certain stress level at RT is described in section 3.2. The implementation of the transport current measurement near the critical temperature for loaded wires, so-called NearT_c, is elaborated in section 3.3. Section 3.4 explains the measurement methods used with the SQUID magnetometer to obtain the critical current as well as the intrinsic parameter T_c and B_{c2} of wires after a particular transverse stress at RT.

3.1 Application of transverse stress at room temperature

In order to apply a well-defined homogeneous transverse compressive stress on Rutherford cables and wires at room temperature, a hydraulic press was refurbished and can be seen in figure 3.1. The hydraulic jack with a maximal force of 200 kN is powered by a hydraulic circuit with a nominal pressure of 150 bar. The resulting pressure on the piston can be controlled by an analogue proportional valve with a 4–20 mA current loop. Major renewals have been implemented to the system allowing adequate loading of the specimens:

- Purchase of a new state-of-the-art proportional valve with an integrated digital axis controller (*Bosch Rexroth 4WRPDH*) to ensure an accurate feed-back controlled adjustment of the hydraulic pressure.
- Design of a new pressing insert to apply homogeneous pressure distribution on the specimens, which is also emphasised in figure 3.1 [180]. The applied force was evaluated by implementing four calibrated load cells (*Burster Druckkraftsensor 8526*) with a measurement range from 0 MPa to 200 MPa and an accuracy of 0.05 %. They were arranged in a planar rectangle with a side length of 85 mm. The support points of the load cells were horizontally aligned with stainless steel shims to an accuracy 5 µm in order to achieve equivalent load balance. Furthermore, the pressing die was manufactured with a radius of 3 mm to prevent stress peaks at the end of the pressing area.
- In addition to the direct force measurement, pressure-sensitive films from *FujiFilm Corporation* [64] were used to analyse and optimise the stress distribution on the surface of the specimen. These so-called *Prescale films* can be placed as an intermediate layer on the pressure surface and deliver a two-dimensional red-colour density imprint of the pressurised area. This allows an evaluation of the pressure independently of the force measurement.

Prescale films are available in certain measurement ranges, whereby the types MS (10 MPa to 50 MPa), HS (50 MPa to 130 MPa), HHS (130 MPa to 300 MPa) were used in the presented work. They have a spatial resolution of 0.1 mm and the pressure accuracy is ±10 % according to the manual. The two-dimensional red-colour density imprint is proportional to the applied pressure. The available manual allows a comparison with the reference colour samples and the measured pressure can be visualised in a diagram.

To evaluate the stress distribution quantitatively the Prescale films were scanned and the digital images were analysed with a self-designed script written in *MathWorks MATLAB* using the Image Processing Toolbox [162]. Every pixel i of the image is associated with a colour density value x_i. This value is subsequently transferred to an intermediate quantity $y_i = g(x_i)$ by the use of the spline-interpolation

Figure 3.1: Picture of the setup for applying transverse compressive stress on the cable and wire specimens. 1. Pressing insert, 2. Hydraulic jack, 3. Hydraulic circuit, 4. Supports with support bar, 5. Control unit, 6. Load cells.

function $g(x)$, which is achieved from the scanned reference colour samples. The intermediate quantity is further converted to the required pressure value $\sigma_i = f(y_i)$ in MPa by the spline-interpolation function $f(y)$, which is derived from the plot in the manual. Hence, the software uses the composition function

$$h(x_i) = (f \circ g)(x_i) = \sigma_i \tag{3.1}$$

to determinate the measured pressure σ_i out of a colour density value x_i of the pixel i. Due to necessary bijectivity of $h(x)$, the inverse function $x = h^{-1}(\sigma)$ can be derived. Pixels, which are too bright or dark for the evaluation, can consequently be deleted in advance. Figure 3.2 shows a typical input and output of the programmed software, whereby pressure values outside the measurement range of the film are coloured white.

Moreover, the stress values of the entire pressing area A_{P} can be used to integrate numerically the force F_{P}. It can be compared with the entire force $F_{\mathrm{LC},\Sigma}$ measured by the calibrated load cells

$$F_{\mathrm{LC},\Sigma} = \sum_{j=0}^{3} F_{\mathrm{LC},j} \approx F_{\mathrm{P}} = \sum_{i=0}^{n} h(x_i)\, A_{\mathrm{P}}, \tag{3.2}$$

where $F_{\mathrm{LC},j}$ is the force measured by the load cell j and used for confirmation. The explained algorithm above is further described and verified in the reference [46].

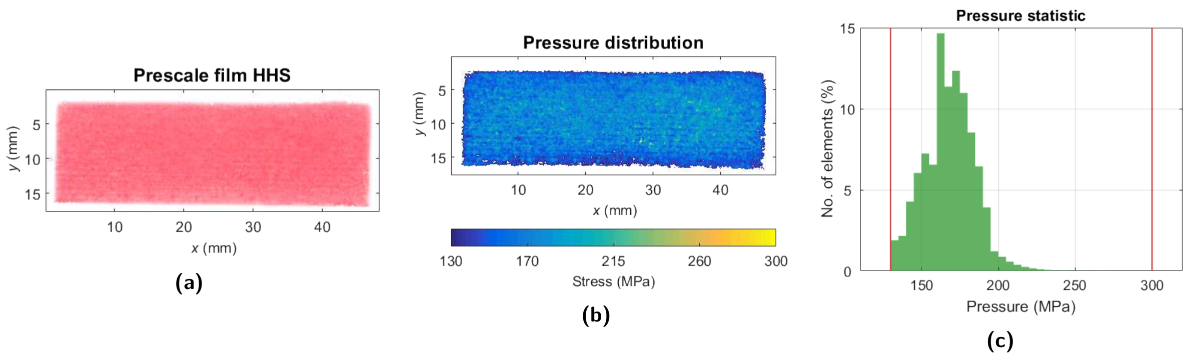

Figure 3.2: **(a)** Typical input, a loaded Prescale film, and **(b, c)** output of the self-written evaluation script for pressure-sensitive Prescale films. The analysed HHS film originates from the application of 175 MPa on specimen 1. The white areas in (b) are points outside of the range of the films function provided in the manual, i.e. either too high or too low for the film.

3.1.1 Transverse stress on cables

The FRESCA-compatible cable specimens were exposed to a certain stress level for a duration of approximately 2 min. This allows reaching a high reliability of the pressure-sensitive films, as recommended in the manual [64]. Afterwards, the sample was transported to the FRESCA cable test station to measure the critical current. This procedure was performed iteratively with increasing stress levels until a critical current degradation of around 10 % could be observed.

For the stress application on the nearly 2 m long specimens, a 2 m long and 35 mm wide portable support bar and supports were established to prevent any damage due to handling (cf. figure 3.1). The specimen, including current leads, were placed on the support plate and slid into the pressing insert. After aligning the specimen to the defined pressing area with an effective length of 44 mm (cf. figure 2.3) the pressing procedure was performed, which can be seen in figure 3.4(a). The load cell signals, as well as the pressure-sensitive films, were used to evaluate the applied load on the specimen. The measured stress, represented in section 4.1, was recorded from the calibrated force measurement and the nominal pressing area. The pressure-sensitive films served as a quality indicator to validate that the stress was distributed during the stress exertion uniformly. The pressing arrangement was chosen as schematically

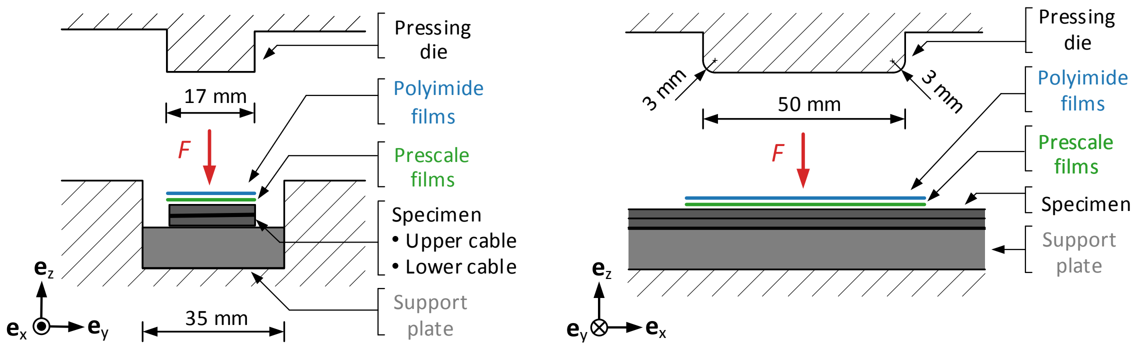

(a) (b)

Figure 3.3: Schematic view of pressing configuration for applying transverse stress on the Rutherford cable stacks. **(a)** Side view. **(b)** Front view.

shown in figure 3.3. In the beginning, several intermediate layers of different materials (In, Sn-Ag and Sn-Pb) were tested to improve further the homogeneity of the stress on the specimen. It was concluded, that a 1 mm thick intermediate layer of eight Polyimide foils reached the best result. Accordingly, the final pressing arrangement was defined with pressure-sensitive films underneath the Polyimide foils. In order to extend the stress measurement range, films of the type HHS, HS and MS were stacked. Figure 3.4(b) shows the used configuration of Polyimide and Prescale films after the stress exertion.

Furthermore, a non-destructive X-ray tomography of equivalent specimens was performed within the working group to develop a FEM model and investigate with *ANSYS* the stress distribution within the cross-section of the specimen, a complicated composite compound [85, 180].

(a) (b)

Figure 3.4: **(a)** Picture of specimen 1 (cable HT15OC0190) in the pressing tool and **(b)** 1 mm thick Polyimide foil stack intermediate layer (top) with pressure-sensitive films (bottom) after applying a nominal stress of 175 MPa.

3.1.2 Transverse stress on wires

The wire specimens were exposed to transverse stress for 2 min with the same hydraulic system and pressing die, as used for the cable specimens.

Samples for the magnetisation measurements and the microscopy campaign were exposed to stress by putting them on the ground plate of the pressing tool and afterwards cut into pieces with a wire diamond saw for further investigations.

The specimen for the transport current measurement was pressed assembled into the sample holder, which can be seen in figure 3.14. It was exposed to a certain stress at RT and afterwards, the electrical properties were measured with the NearT_c setup, as described in section 3.3. This was performed iteratively until heavy degradation could be detected. For the stress procedure, the sample holder current connectors were fixed via stainless steel bars to prevent any movement of the wire during the press procedure. Afterwards, the middle plate was exchanged by a stainless steel plate to ensure a planar and aligned pressing surface. The pressing area was defined in the middle of the sample within the voltage-taps to prevent stress peaks due to the soldering points.

The final pressing configuration, as sketched in figure 3.5, was defined without any intermediate layers, which is the result of a previously executed test study. The objective was to apply well-defined stress and a similar crack distribution along the transverse cross-section, as observed in the loaded strands within the cables (cf. figure 4.9). Based on a microscopic investigation of loaded wires from different pressing arrangements, the approach could be reached by the absence of intermediate layers. For this reason, it had refrained from the concepts of past investigations. For instance, G. Mondonico *et al.* [114] sought a hydrostatic stress configuration within an impregnation. C. Calzolaio *et al.* [31] achieved a shape-conforming stress by using a cylindrical groove. Both experiments implemented the stress application during operation at low temperature. For the analysis in section 4.2 the direct force measurement and the projected area, i.e. $(0.7 \times 44)\,\text{mm}^2$, were used to determine the stress on the wire.

In order to further investigate the stress distribution, an X-ray tomography of loaded and non-loaded wires was launched within the working group to develop a FEM model for *ANSYS*. Subsequently, a FEM analysis was performed to assess the stress distribution within the wire, especially the local stress on the sub-elements [40, 47].

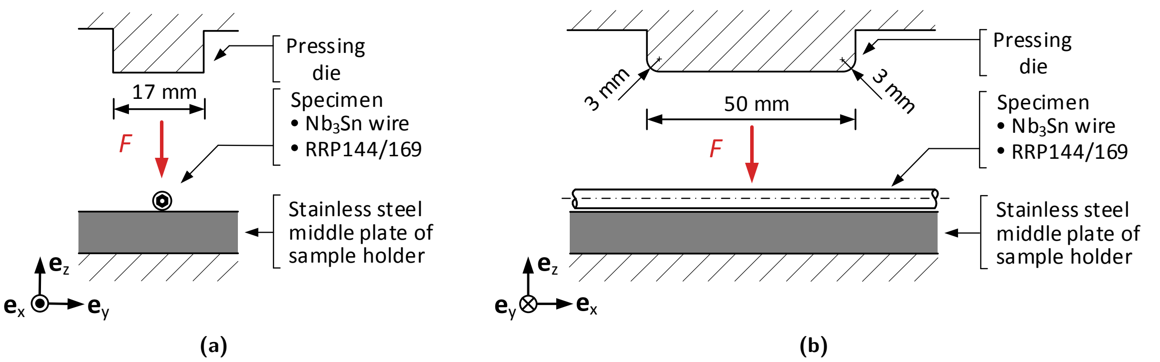

Figure 3.5: Schematic view of pressing configuration for applying transverse stress on the wires. **(a)** Side view. **(b)** Front view.

3.2 Measurements of cables with the FRESCA test station

The transport critical current measurements of the cable specimens after the application of a certain stress level were performed with the FRESCA cable test station at CERN (TE-MSC-SCD). The Facility for Reception test of Superconducting Cables, so-called FRESCA, was built for the R&D of superconducting cables for LHC magnets [173]. It can be seen in figure 3.6 and the major properties are:

- A current source of up to 32 kA for the sample measurement circuit.
- A background magnet with an operating field of up to 9.6 T and a 99 % homogeneity within approx. 50 mm perpendicular to the sample current.
- A specimen cooling at 4.3 K with liquid helium and at 1.9 K with superfluid helium, both slightly above the atmospheric pressure.

(a) **(b)**

Figure 3.6: Pictures of the FRESCA cable test station. **(a)** Overview. 1. Embedded vertical double-bath cryostat, 2. Power source for sample (32 kA) and Nb-Ti background magnet, (16 kA) 3. Water-cooled current leads 4. Helium liquefier for the CERN building 165, 5. Liquid helium buffer dewar (6000 L), 6. Cran for changing the samples, **(b)** Detailed view of the FRESCA cryostat.

A schematic of the system can be seen in figure 3.7(a). The test station is a "double cryostat concept" and both are vertical double-bath cryostats, which have an entire helium consumption of roughly 200 L h^{-1} in full operation. The upper baths are operating at 4.3 K and the lower baths can be operated down to 1.9 K cooled by heat exchangers. Lambda plates thermally separate the 4.3 K baths from the 1.9 K parts.

The Nb-Ti dipole magnet [92] is housed in the outer cryostat independently and only warmed up for maintenance reasons. The magnet generates the applied field up to 9.6 T and is equipped with 18 kA current leads. Although it was designed for 10 T at a temperature of 1.9 K, a maximal value 9.6 T is recommended for continuous operation. The about 1.7 m long magnet with an aperture of 88 mm was designed to ensure field homogeneity of a $^{B_{\mathrm{app}}}/_{\max(B_{\mathrm{app}})} = 99\,\%$ in the centre along 475 mm. The inner cryostat houses the cylindrical sample chamber with an aperture of 77 mm and is equipped with 32 kA current leads. Furthermore, the test station is assembled with a rotating system to turn the sample over 90°.

In order to perform measurements, the cable specimen, which is described in section 2.2, is placed in the sample holder. It is pre-strained in between a sandwich of fibreglass laminate spacer (G10) and stainless steel plates. Afterwards, the equipped sample holder is mounted in a cylindrical collar to avoid movements of the sample due to the electromagnetic forces, which is illustrated figure 3.7(b). The sample holder is fixed by a cardan joint including current leads, helium transfer line and signal wiring to the sample insert and subsequently inserted into the inner cryostat. The current leads of the specimens are clamped with indium foils to the sample insert, which leads to a contact resistance of typically below 3 nΩ. The cold part of the measurement circuit has an entire resistance in the range of 10 nΩ at low temperature.

The acquisition system consists of a low- and a high-frequency system. The former provides high voltage resolution and is used to record the voltage-current (V-I) and voltage-field (V-H) curves, respectively, during transport current measurements. Voltage-taps in the high-field region and the direct current-current transformers (DCCT) signal of the sample current are connected to two nanovoltmeters with a resolution of 1 nV and a sampling time down to 350 ms. The high-frequency system with a lower voltage resolution is used for monitoring and interpretation of the quench behaviour. It consists of a 15-channel acquisition system with a sampling time down to 50 µs per channel in mV-range. Additional "Potaim" cards, bipolar comparator circuits made by CERN, are used for quench detection. The temperature of the sample holder is evaluated by calibrated *LakeShore Cernox CX-1050* NTC temperature sensors. The current of the background magnet and the sample is regulated and measured by using also DCCT. Figure 3.8 illustrates the location of the most important voltage-taps mounted on the cable specimens. The pressed area was defined in the middle of the Nb_3Sn sample and thus the voltage-taps

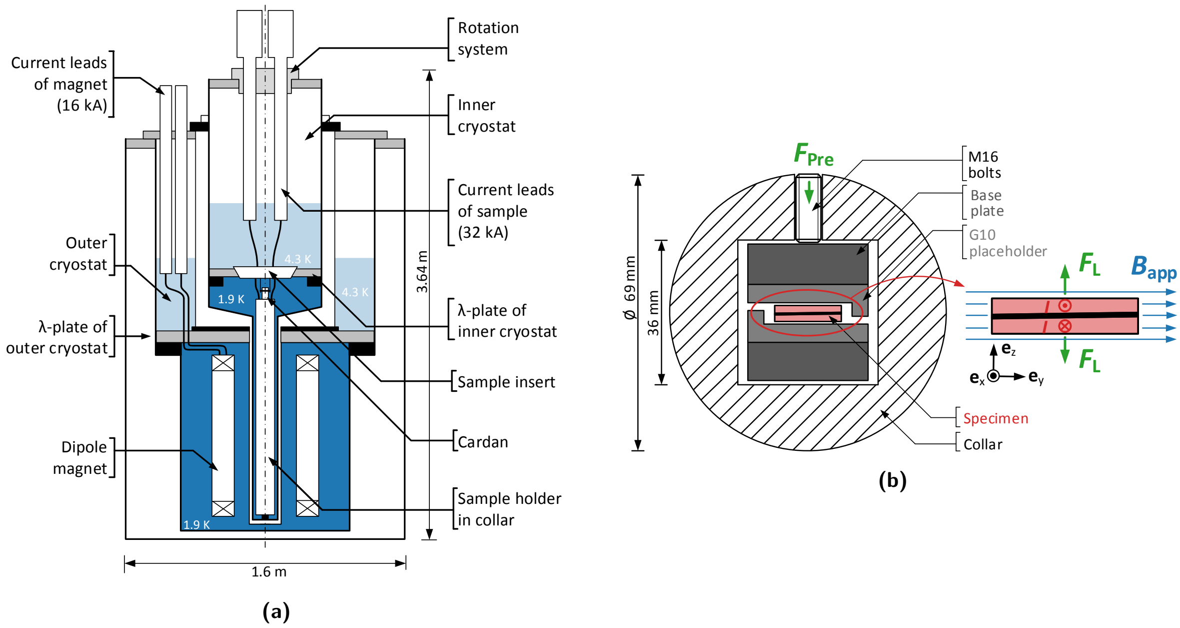

Figure 3.7: (a) Schematic view of the FRESCA test station. **(b)** Specimen in sample holder consisting of sandwich configuration in collar during the final experimental condition.

labelled with GLx, FMx, ENx with $x = 1$ for cable 1 (upper) and $x = 2$ for cable 2 (lower), respectively, are intended for the recording of the V-I curves. Primarily the voltage-tap pairs within the high-homogeneity field region were used, i.e. GLx with a distance of 300 mm. The current-transfer length is consequently approximately 500 mm after a current contact length of 230 mm and 200 mm, respectively. Besides, the specimen is equipped with additional voltage-taps to detect a premature quench outside the pressing area and consequently a corruption of the measurement. Therefore, the voltage drops of the following parts were observed during every measurement, which can also be seen in figure 3.8 and are explained in the next section:

- Bottom end (joint): $1VT05 - 2VT05$
- Top end of cable x: $xVT17 - xV014$
- Clamping of cable x: $xVT19 - xV017$
- Nb_3Sn cables: $1VT14 - 2VT14$
- Specimen: $1VT17 - 2VT17$
- System: $1VT19 - 2VT19$

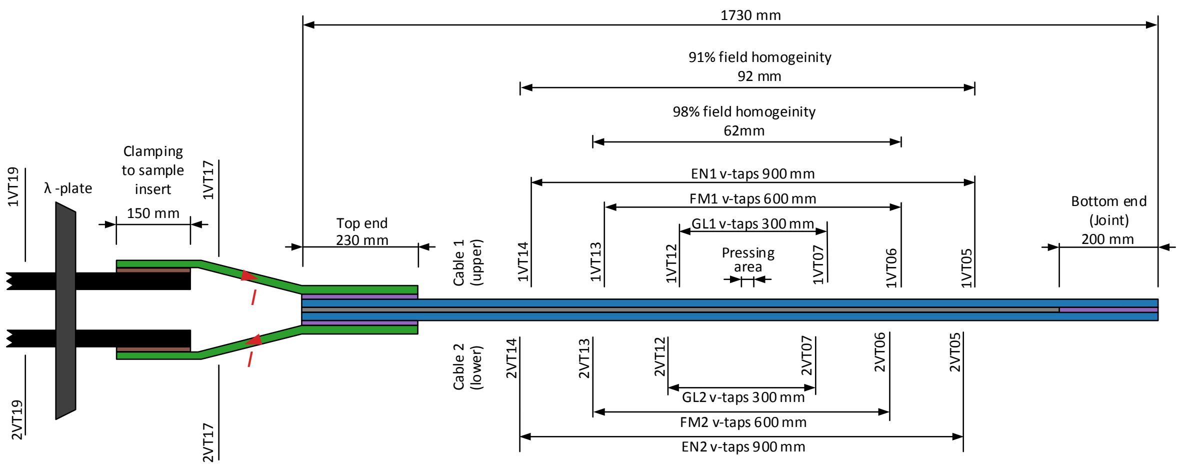

Figure 3.8: Schematic view of the specimen including voltage-tap placements in relation to the location of the high-homogeneity region of the applied magnetic field. In the present work only voltage-tap signals within the region of a field homogeneity of $B_{app}/\max(B_{app}) \geq 98\,\%$ were used for the analysis.

3.2.1 Experimental condition & measurement procedure

After loading the specimen described in section 3.1.1, it was assembled into the sample holder for the I_c measurement in the FRESCA cable test station.

The necessary pre-stress of 50 MPa was applied at RT by using M16 bolts every 40 mm of the collar, which is illustrated with F_{Pre} in figure 3.7(b). Subsequently, it was inserted into the aperture of the test station and the specimen was cooled down. The I_c measurements were performed with current ramps of 100 A s^{-1} during 4.3 K and in the virgin state also at 1.9 K. The background field from 7 T to 9.6 T was applied perpendicular to the current and parallel to the long edge of the cable (cf. figure 3.7(b) right).

Fig 3.9 gives an overview of the typical measurement and monitoring signals during a recording of a V-I relation. The corresponding embedded plots are magnifying the essential part of the original plot. Figures 3.9(a) shows the raw data of the low-frequency acquisition system with the higher accuracy used for the analysis. The following voltage measurement points, after stopping the current supply, were not used for the analysis and can be traced down to electrodynamic and thermal processes within the cables, e.g. inter-strand current sharing, due to the sharp current cut. The monitoring signals obtained with the high-frequency acquisition system give information about the quench location to prevent misinterpretation, which are drawn in figure 3.9(b). The additional small plot shows the signals during the resistive transition in detail. It can be observed clearly, that the Nb_3Sn cables, equipped with the voltage-taps ENx, FMx, GLx, got resistive before the top and bottom splices, which indicates a successful measurement process of the cables. Therefore, the delay between the resistive transition of each cable was observed to ensure an independent quench occurrence of the cables. The delay has to be shorter than 7.4 ms to guarantee that the heat transfer or the quench propagation in one cable didn't cause the quench in the other, which was the objective in earlier research activities [60].

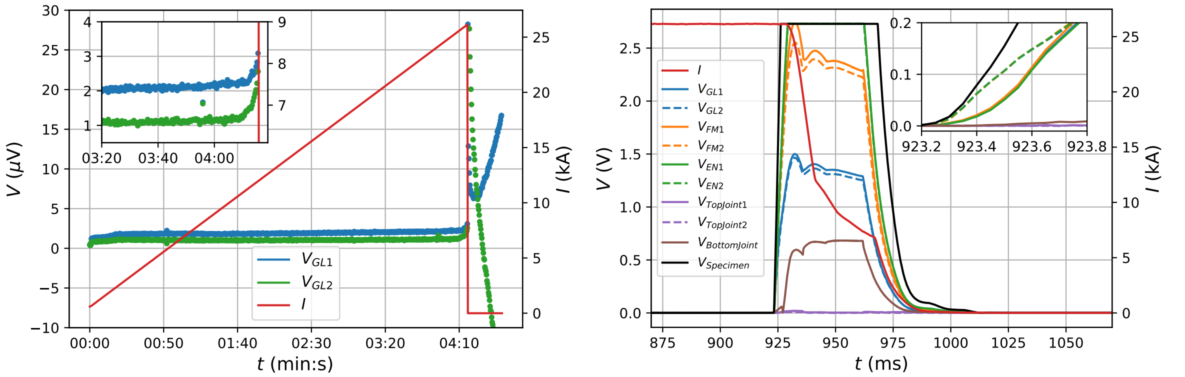

(a) (b)

Figure 3.9: **(a)** Measurement and **(b)** monitoring signals during a typical V-I recording. It can be seen clearly in magnifying plot in (b), that the current leads on the top ($V_{TopJoint x}$) and the joint on bottom ($V_{BottomJoint}$) are not quenching or quenching after the actual specimen (V_{GLx}, V_{FMx}, V_{ENx}). The measurement range of the fast monitoring system is limited to 3 V. The small plot in (a) enlarged the resistive transition used for the analysis before the quench detection was triggered.

3.2.2 Self-field correction

For the analysis of the cable results in section 4.1, the peak field B_{peak} within the specimen on the superconductor was used.

The magnetic self-field $B_{self}(\mathbf{r})$ of the specimen, which is linearly proportional to the current I, is non-uniform. Its local peak value can be more than 20 % of the applied field $B_{app}(\mathbf{r})$ during the measurements. Hence, the self-field has to be considered in the results to present the critical currents with respect to the actual magnetic condition within the specimen, especially of the superconductor. Based on the electromagnetic situation of the specimen's cross-section drawn in figure 3.7(b), the entire magnetic field at a specific location can be computed by the superposition of the homogeneous applied field and the inhomogeneous self-field

$$\mathbf{B}(\mathbf{r}) = \mathbf{B}_{app}(\mathbf{r}) + \mathbf{B}_{self}(\mathbf{r}, I) \tag{3.3}$$

with the applied field $\mathbf{B}_{app}(\mathbf{r}) = \mathbf{B}_{app} = B_{app}\mathbf{e}_y$, the self-field $\mathbf{B}_{self} = B_{self}\mathbf{e}_{B_{self}} = B_{self,y}\mathbf{e}_y + B_{self,z}\mathbf{e}_z$, the specimen current I and the position vector $\mathbf{r}$. The peak field B_{peak}, which is used for the analysis, is

Table 3.1: FEM results for the 11 T and MQXF cable specimen configuration.

I (kA)	$\max_{\mathbf{r}}(B_{\mathrm{self,11\,T}})$ (T)	$\max_{\mathbf{r}}(B_{\mathrm{self,MQXF}})$ (T)
10	0.80	0.65
20	1.60	1.29
32	2.55	2.07

further defined as the sum of the applied field and the maximum value of the self-field

$$B_{\mathrm{peak}} := B_{\mathrm{app}} + \max_{\mathbf{r}}(B_{\mathrm{self}}(\mathbf{r}, I)). \tag{3.4}$$

In order to get an estimation of the magnetic self-field, a two-dimensional magneto-static FEM of the specimen's cross-section including its environment was performed with *ANSYS Maxwell*. It solves numerically the Biot–Savart law for every location on the surface (YZ-plane). Therefore, the following idealisations of the specimen were made:

- Reduction of the cable to a trapezoidal cross-section with homogeneous current density $J = I/A$ with the nominal cross-section area A, i.e. effects of a particular strand or sub-element are neglected.
- The twist pitch of the cable is ignored, i.e. the current is parallel to x-axis, which restricts the magnetic self-field to the YZ-plane.
- The environment of the cables, e.g. epoxy resin, stainless steel and liquid helium, was idealised as vacuum atmosphere, i.e. $\mu_r = 1$.
- The field is constant in x direction, which represents the high-field region in the middle of the specimen.

Figure 3.10 and figure 3.11 show the FEM results of the two specimen types, the 11 T cable and MQXF cable configuration, respectively. They have a maximal magnetic field of 2.55 T and 2.07 T, respectively, at a current of $I_{\mathrm{max}} = 32$ kA. A magnetic field concentration is formed within the 0.3 mm wide gap between the cables, due to the anti-parallel current flow, which can be easily checked by the use of the Ampere's Law $\nabla \times \mathbf{B} = \mu_0 \mathbf{J}$.

The location of the maximum value $\max_{\mathbf{r}}[B_{\mathrm{self}}(\mathbf{r}, I)]$ is in the centre region of the specimen, more precisely on the border of the cables, due to the point-symmetric layout of the specimen. This implies that the maximal field in the specimen is also the maximal field in the cables' superconducting area, which was the final reason to use it for the analysis. This means also that the earliest quench can be expected in the middle centre strands of the specimen, which can be checked by the use of the Kramer relation of superconductors $J_{\mathrm{c}}(b) \propto b^{-1/2}(1 - b^{1/2})$ with $b = B/B_{\mathrm{c2}}{}^*$. The maximal field gradient within the cables, carrying the maximal current of 32 kA, is approximately 2.2 T mm^{-1} and 1.4 T mm^{-1} for the 11 T and the MQXF cable configuration, respectively.

In order to achieve the maximum magnetic self-field as a function of the current, the simulation was performed with 10 kA, 20 kA and 32 kA and listed in table 3.1. Thus, the linear behaviour

$$\max_{\mathbf{r}}[B_{\mathrm{self}}(\mathbf{r}, I)] = k_{\mathrm{I}} I \tag{3.5}$$

with a correction factor k_{I} of 80 mT kA^{-1} and 65 mT kA^{-1} for the 11 T and MQXF cable specimen, respectively, was confirmed. Consequently, these above derived parameters were used to present the results of the cables $I_{\mathrm{c}}(B_{\mathrm{peak}})$ with $B_{\mathrm{peak}} = B_{\mathrm{app}} + k_{\mathrm{I}} I$ in section 4.1.

As a reference for the cable measurements, also the critical currents $I_{\mathrm{c}}(B)$ of the virgin wires, i.e. strands in non-cabled condition, are presented in section 4.1. These results were obtained by transport current measurements with an ITER VAMAS barrel at CERN (TE-MSC-SCD) according to the standard [157]. The superconducting wire is wound on the barrel with a diameter of roughly 20 mm and measured with an applied field parallel to the barrel axis. The angle between the wounded wire and the applied field is approximately 88°. In order to present these results in comparison with the cable results, the actual magnetic field during the measurements has to be determined, which consists also of the applied field of the background magnet and the self-field of the measured wire. Obtained by using a FEM simulation by B. Bordini [24], the actual local peak field on the superconductor during the measurement, is given by

$$B_{\mathrm{peak,wire}} = B_{\mathrm{app}} + B_{\mathrm{self,wire}}(I) \tag{3.6}$$

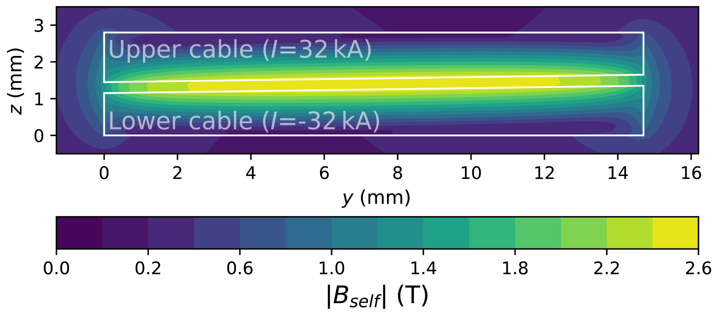

Figure 3.10: Magnetic self-field of the 11 T cable configuration with a current of $I_{\max} = 32\,\text{kA}$, obtained by a FEM simulation. The maximum is located in the centre region of the specimen, more precisely on the border of the cables, and is in the order of 2.55 T.

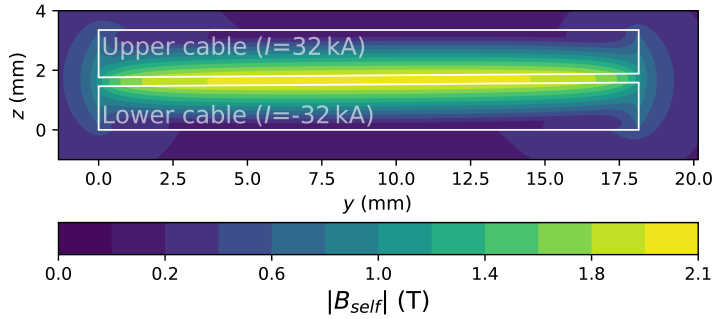

Figure 3.11: Magnetic self-field of the MQXF cable configuration with a current of $I_{\max} = 32\,\text{kA}$, obtained by a FEM simulation. The maximum is located in the centre region of the specimen, more precisely on the border of the cables, and is in the order of 2.07 T.

with $B_{\text{self,wire}}(I) = \mu_0 I/2\pi r - 9 \cdot 10^{-5}\,\text{T}\,\text{A}^{-1} \cdot I$, where r is the outer radius of the sub-element array within the cylinder wire and I is the test current. Additional to the self-field correction, the critical current $I_c(B_{\text{peak,wire}})$ of the wire was multiplied by the number of strands of the respective cable and plotted together with the cable results.

In order to put the transverse stress applied at RT in comparison with the force during the electrical measurements, the entire electromagnetic respectively Lorentz force F_L on the cables in the specimen was calculated. In general, the local electromagnetic force density on an infinitesimal element in a current-carrying conductor is defined as

$$\mathbf{f}(\mathbf{r}) = \mathbf{J}(\mathbf{r}) \times \mathbf{B}(\mathbf{r}). \tag{3.7}$$

The cumulated force on the conductor, e.g. wire or cable, can be obtained by integration over its volume $\mathcal{V}$

$$\mathbf{F} = \int_{\mathcal{V}} \mathbf{J}(\mathbf{r}) \times \mathbf{B}(\mathbf{r})\,\mathrm{d}\mathcal{V}. \tag{3.8}$$

Taking into account of the above idealisations, the problem can be described independently of the length of the conductor and the common length-related force

$$\mathbf{F}' = \frac{\mathbf{F}}{l} = \int_{\mathcal{A}} \mathbf{J}(\mathbf{r}) \times \mathbf{B}(\mathbf{r})\,\mathrm{d}\mathcal{A} \tag{3.9}$$

was further derived, where A is the cross-section of the conductor, i.e. a single cable in the present case, perpendicular to the current flow. The current density of a single cable is defined as $\mathbf{J} = I/A\,\mathbf{e}_x$ and with the magnetic field $\mathbf{B}(\mathbf{r}) = \mathbf{B}_{\text{app}} + \mathbf{B}_{\text{self}}(\mathbf{r})$ computed above, the entire length-related force $F_L{}'$ on a single cable can be written as

$$\mathbf{F}_L{}' = \int_{\mathcal{A}} \mathbf{J}(\mathbf{r}) \times \mathbf{B}(\mathbf{r})\,\mathrm{d}\mathcal{A} = \int_{\mathcal{A}} \frac{I}{A}\mathbf{e}_x \times \mathbf{B}(\mathbf{r})\,\mathrm{d}\mathcal{A} = \frac{I}{A}\int_{\mathcal{A}} \mathbf{e}_x \times \left[\mathbf{B}_{\text{app}} + \mathbf{B}_{\text{self}}(\mathbf{r})\right]\mathrm{d}\mathcal{A}. \tag{3.10}$$

The applied magnetic field, i.e. $\mathbf{B}_{\text{app}}(\mathbf{r}) = \mathbf{B}_{\text{app}} = B_{\text{app}}\mathbf{e}_y$, and the magnetic self-field can be written as

Table 3.2: Length-related forces in y and z direction of the upper cable within the specimen derived from FEM simulation for $I_{max} = 32\,kA$ and $B_{app,max} = 9.6\,T$.

	$F_{L,z}'$ $kN\,m^{-1}$	$F_{L,y}'$ $kN\,m^{-1}$
11 T	341.4	1.9
MQXF	336.0	0.6

$\mathbf{B}_{self}(\mathbf{r}) = B_{self,y}(\mathbf{r})\mathbf{e}_y + B_{self,z}(\mathbf{r})\mathbf{e}_z$ due to the current flow explicitly in x direction, which leads to

$$\begin{aligned}\mathbf{F}_L' &= I\left(\frac{1}{A}\int_{\mathcal{A}} \mathbf{e}_x \times B_{app}\mathbf{e}_y \,\mathrm{d}\mathcal{A} + \frac{1}{A}\int_{\mathcal{A}} \mathbf{e}_x \times B_{self,y}(\mathbf{r})\mathbf{e}_y + \mathbf{e}_x \times B_z(\mathbf{r})\mathbf{e}_z \,\mathrm{d}\mathcal{A}\right) \\ &= I\Bigg(\underbrace{\frac{1}{A}\int_{\mathcal{A}} B_{app}\,\mathrm{d}\mathcal{A}}_{B_{app}}\,\mathbf{e}_z + \underbrace{\frac{1}{A}\int_{\mathcal{A}} B_{self,y}(\mathbf{r})\,\mathrm{d}\mathcal{A}}_{\overline{B}_{self,y}(\mathcal{A})}\,\mathbf{e}_z + \underbrace{\frac{1}{A}\int_{\mathcal{A}} B_{self,z}(\mathbf{r})\,\mathrm{d}\mathcal{A}}_{\overline{B}_{self,z}(\mathcal{A})}\,(-\mathbf{e}_y)\Bigg).\end{aligned} \tag{3.11}$$

The defined quantities $\overline{B}_y(\mathcal{A})$ and $\overline{B}_z(\mathcal{A})$ can be assumed as the average value of the self-field over the cable cross-section in the y and z direction, respectively. Hence, the length-related force on a single cable can be summarised as

$$\mathbf{F}_L' = \underbrace{I\left[B_{app} + \overline{B}_{self,y}(\mathcal{A})\right]}_{F_{L,z}'}\,\mathbf{e}_z - \underbrace{I\overline{B}_{self,z}(\mathcal{A})}_{F_{L,y}'}\,\mathbf{e}_y. \tag{3.12}$$

Consequently, the z and y component of the magnetic field causes an electromagnetic force in y and z direction, respectively. This circumstance can be easily checked by applying the common Lorentz force law for a current-carrying wire $\mathbf{F}_L = Il\mathbf{e}_I \times \mathbf{B}$, where l is the length of the wire within magnetic field $\mathbf{B}$ the and $\mathbf{e}_I$ the direction of electrical current I.

Nevertheless, the self-field B_{self} is only a fracture of the applied field B_{app}, as derived above. Hence, the primary share of the force is in z direction ($F_{L,z}' \gg F_{L,y}'$) driven by the applied field B_{app}, which can be obtained from the FEM results listed in table 3.2. The cable-independent part due to the applied field amounts to $32\,kA \cdot 9.6\,T = 307.2\,kN\,m^{-1}$, which is much lower compared to the electromagnetic forces of $4\,MN\,m^{-1}$ of the LHC main dipole coils at nominal operation [132].

The two cables repel each other due to the anti-parallel current flow (cf. figure 3.7(b)) and the self-field contributes only marginally to the force parallel and anti-parallel to the z-axis, respectively. The length-related force component $F_{L,y}'$ represent the lateral force, which is sensitive to the keystone angle of the cables.

The most interesting force for the investigation is in z direction, because the applied stress at RT is also in z direction. The highest electromagnetic force can be assumed with the maximal current of 32 kA during the maximal applied field 9.6 T. The high-field region in the middle of the specimen has a length of $l = 475\,mm$ and hence the entire force within this area can be derived by $F_{L,z} = F_{L,z}'l$. In order to estimate the maximal stress parallel to the long edge on a cable, which can be compared to the stress application at RT, the maximal force with the cable width w are used to derive

$$\sigma_L \approx \frac{F_{L,z}}{l \cdot w} = \frac{F_{L,z}'}{w} = \begin{cases} 23.2\,MPa, & \text{for 11 T configuration} \\ 18.2\,MPa, & \text{for MQXF configuration} \end{cases} \tag{3.13}$$

with a current $I_{max} = 32\,kA$, an applied field of $B_{app,max} = 9.6\,T$ and the nominal cable width w of 14.7 mm and 18.5 mm for the 11 T and MQXF cable, respectively. Considering that the highest current is hardly reached during the I_c measurements, the estimated maximal stress σ_L on a cable (XY-plane) during the measurement is lower than the half of the lowest stress level applied at RT and hence not considered in the results.

3.2.3 Data evaluation

As described above, the critical current was determined by recording $V(I)$ curves to evaluate the degradation due to transverse stress at RT. The standard for evaluating the critical current of Nb_3Sn composite superconductor [157] recommends an electrical field or a resistivity criterion. The most common criterion, which was chosen for the present work, is the electrical field criterion and accordingly the $V(I)$

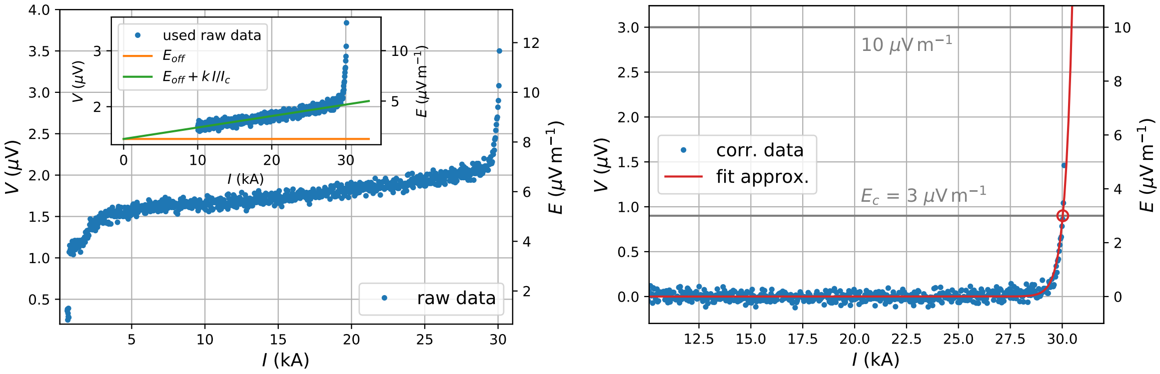

(a) (b)

Figure 3.12: Critical current evaluation of a typical cable $V(I)$ recording. **(a)** Raw data points of a V-I recording at $T = 4.3\,\mathrm{K}$ until the quench. The small plot shows the estimation of the undesired constant and linear part caused by experimental condition in contrast to the raw data above 10 kA used for the analysis. **(b)** Critical current determination according to electrical field definition $E(I = I_c) = E_c$ with $E_c = 3\,\mu\mathrm{V\,m^{-1}}$ from the corrected data, i.e. after the reassessment of the undesired thermoelectric, the induction voltage (constant) and the resistive part (linear).

relations at a particular and constant temperature can be expressed by the power law

$$E(I) = E_c \left(\frac{I}{I_c}\right)^n . \tag{3.14}$$

Therefore, the electrical field along the specimen is defined by $E = V/l$ with the voltage of the specimen V and the voltage-tap spacing l. Hence, the critical current is defined as that current when the electrical field E transcends the constant threshold E_c, i.e. $E(I = I_c) = E_c$. A threshold of $10\,\mu\mathrm{V\,m^{-1}}$ is recommended for LTS such as Nb_3Sn and Nb-Ti and is restricted practically by the noise level of the voltage signal and the precision of the measurement equipment. The resistive transition index n, so-called n value, shall be derived by the slope of the $E(I)$ relation in a double logarithmic reference frame in the region of the I_c determination point.

Experimental measurements are not perfect and undesired systematic influences have to be reassessed retrospectively. In practise, constant and linear effects caused by the experimental arrangement are relevant:

- The constant component appears unavoidable by the thermoelectric and inductive voltage. The latter is depending on the current ramp rate.
- The linear component is caused mostly by the current-transfer voltage, which represents the resistive junction from the current leads to the superconducting specimen and can be minimised a priori by a sufficient long current-transfer length.

In general, cable measurements have to be performed inherently with higher currents resulting in higher energy dissipation during the measured resistive transition, which led to an earlier stop of the recording compared to wire measurements. Thus, only data points far below the recommended criterion were recorded, which is visualised by the corrected $V(I)$ relation of a typical cable measurement in figure 3.12(b). Moreover, the undesired constant and linear components of the corresponding raw data in figure 3.12(a) are recognizable.

Due to the above explained facts, it was decided to evaluate the critical current of cables by using a curve fitting as follows. Initially, the criterion E_c was reduced from the recommended $10\,\mu\mathrm{V\,m^{-1}}$ to $3\,\mu\mathrm{V\,m^{-1}}$ in order to prevent extrapolation uncertainties, i.e. to ensure that measurement points are available at the I_c determination point. Figure 3.12(a) shows a typical V-I raw curve, from which data points above 10 kA were used to fit the function

$$E(I) = E_c \left(\frac{I}{I_c}\right)^n + E_{\mathrm{offset}} + k\,\frac{I}{I_c} \tag{3.15}$$

with I_c in A, E_{offset} in $\mu\mathrm{V\,m^{-1}}$, k in $\mu\mathrm{V\,m^{-1}}$ and n as fitting parameters. The first term represents the desired "pure" resistive transition of the superconductor. The latter two represent undesired constant and linear effects caused by the experimental conditions. The small plot in figure 3.12(a) shows the

Table 3.3: Inner and outer radii, ρ_o and ρ_i, respectively, as well as the superconducting area $A_{A\text{-}15}$ of all wires used within this work, obtained by SEM.

Wire type	d_{nom} (mm)	N (-)	ρ_o (µm)	ρ_i (µm)	$A_{A\text{-}15}$ (mm^2)	Utilisation
RRP 144/169	0.7	144	20.4	11.1	0.133	Wire investigation and cable specimen 1
RRP 108/127	0.7	108	23.0	11.5	0.135	cable specimen 2
RRP 108/127	0.85	108	27.5	13.5	0.195	cable specimen 3

estimation of these terms, which were used to achieve the corrected data in figure 3.12(b). Finally, the critical current was determined as the interpolated current value of the corrected fit function at 3 µV m^{-1}, which is annotated with the red marker.

All I_c values are additional converted into the critical current density J_c, mostly giving by a secondary axis in chapter 4. Therefore, the effective superconducting area $A_{A\text{-}15}$ is used, i.e. the Nb_3Sn area of all N sub-elements within a wire. For that purpose, the sub-elements are idealised as annuli with ρ_o and ρ_i as the outer and inner radius, respectively, which is illustrated in figure 2.2. Thus, the used critical current density within this work is defined as

$$J_c = J_{c,A\text{-}15} = \frac{I_c}{A_{A\text{-}15}} \quad \text{with} \quad A_{A\text{-}15} = N\pi({\rho_o}^2 - {\rho_i}^2), \tag{3.16}$$

which is in accordance with the derived magnetisation model (cf. equation 3.41). The radii ρ_o and ρ_i of the used wires, which were obtained by the microscopic investigation, are summaries with the calculated $A_{A\text{-}15}$ in table 3.3. In the case of the cable results, the area $A_{A\text{-}15}$ was consequently multiplied by the number of strands to consider the entire Nb_3Sn area within the cable compound. The number of strands was in all cables equals 40, i.e. $A_{A\text{-}15,cable} = 40\,A_{A\text{-}15}$.

Nevertheless, the nonCu critical current density $J_{c,nonCu}$ is frequently mentioned in the referenced publications. The Cu/nonCu ratio $\varkappa_{Cu/nonCu}$ indicates the ratio of the copper to non-copper materials, e.g. tin and niobium, within the cross-section of a non-reacted wire and is given in its specification. Hence, the corresponding critical current density is defined as

$$J_{c,nonCu} = \frac{I_c}{A_{nonCu}} \quad \text{with} \quad A_{nonCu} = \frac{A_{wire}}{1 + \varkappa_{Cu/nonCu}}, \tag{3.17}$$

where $A_{wire} = \pi r^2$ is the area of the wire cross-section with the radius r. Basically, it includes beside the Nb_3Sn also the tin core and the residual α-bronze after the RHT, which does not distribute to the current transport. Due to the fact that $A_{nonCu} > A_{A\text{-}15}$ follows $J_{c,nonCu} < J_{c,A\text{-}15}$.

Within the magnet design, the engineering critical current density of the wire $J_{c,ENG,wire}$ and the cable $J_{c,ENG,cable}$ are often used. They are defined as the critical current over the entire cross-section of the wire A_{wire} and the cable A_{cable}, respectively. The relation between these both is depending on the packing factor of the cable, which is also listed in section 2.2 for the investigated types.

3.3 Measurements of wire with the NearT_c setup

After the application of stress on the wire, explained in section 3.1, the electrical properties were measured with a self-build cryostat setup, which is described in this section. The building of the setup and the measurements were performed in the CryoLab at CERN (TE-CRG-CI). The measurement concept foresees $I_c(T)$ measurements in magnetic self-field near the critical temperature up to 150 A, so-called NearT_c, and leads consequently to higher demand on the control accuracy of the sample temperature. The concept is further explained in section 1.2.4. This concept was chosen on the one hand to demonstrate an alternative measurement method, and on the other hand, to prevent any Lorentz force during the measurement leading to additional damage of the sample. The major design requirements for this transport current measurement were:

- The stress application and I_c measurements using the same specimen, i.e. iterative experiment procedure, as performed on the cable specimens.
- No removal of the voltage-taps at all process steps to ensure always the same voltage-tap distance after every stress level.

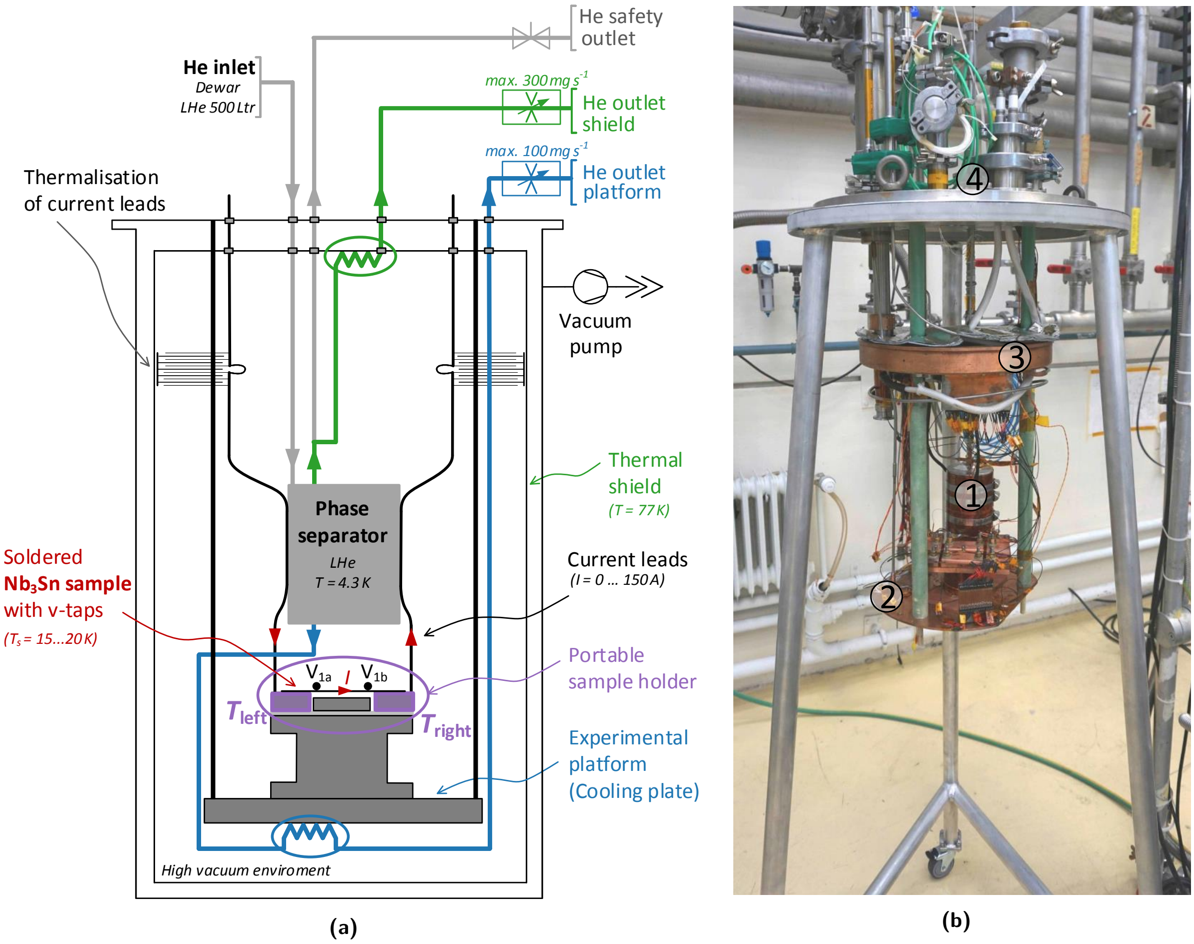

Figure 3.13: (a) Schematic of cryostat setup assembled in a vacuum chamber including sample holder and cryogenic peripheral **(b)** Picture of the cryostat setup outside the vacuum chamber. 1. Phase separator, 2. Experiment platform, 3. Fixation for thermal shield, 4. Electrical and cryogenics feed-troughs.

- The hydraulic press described in section 3.1.1 has to be used to exert uniform transverse stress at room temperature. Moreover, the specimen should not be disassembled from the sample holder during all iterations, to prevent damage due to handling operations.

Therefore, an adequate sample holder was designed, as explained below. Moreover, a low-resistance measurement was established to extend the investigation of the critical temperature T_c and the *RRR*.

3.3.1 Cryogenic sub-system & sample holder

The setup consists of a cryostat insert including a phase separator with one inlet, which was connected to a 500 L liquid helium dewar steadily, as indicated in figure 3.13(a). For the measurements, the entire setup was transferred to a vacuum chamber and sealed. Subsequently, an insulation vacuum atmosphere below 10^{-6} mbar was established to suppress thermal convection and conduction through the residual gas content.

The phase separator had two outlets. The upper vapour outlet, drawn in green in figure 3.13(a), was connected to the heat exchanger of the thermal shield, which additionally thermalised the current leads. The bottom liquid outlet, drawn in blue in figure 3.13(a), was connected to the heat exchanger of the experimental platform, which was carrying the sample holder. Hence, the specimen was cooled by conduction via the two connector plates, which are marked in purple in figure 3.13(a). By using two helium mass flow controllers (*Bronkhorst Low-Δ-Flow controller*) at the above-described outlets, the sample was cooled down slightly below T_c. The pressure of the dewar was controlled to ensure proper operation of the flow controller and to avoid pressure depending temperature variation.

At the base temperature of approximately 13 K, ensured by the mass flow controller, the fine stabilisation of the sample temperature close to the critical temperature was performed. This was achieved by controlling the temperature of each connector plate independently with a 5 W heater resistor and

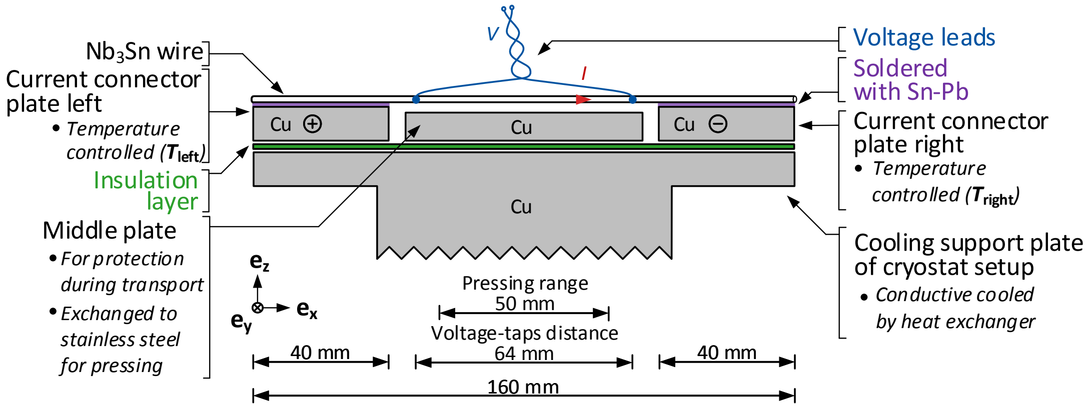

Figure 3.14: Schematic of sample holder including sample assembled in the cryostat setup.

a calibrated NTC temperature sensor (*LakeShore Cernox CX-1070*) with a calibration accuracy of ±4 mK. The plate temperatures T_{left} and T_{right} were feed-back controlled by a *Lakeshore temperature controller 336*. The sample temperature T_s was further defined as the arithmetic mean value

$$T_s = \frac{T_{\text{left}} + T_{\text{right}}}{2}, \tag{3.18}$$

and consequently, indirect regulated by the plate temperatures. As a homogeneity parameter served the temperature difference

$$\Delta T_s = |T_{\text{left}} - T_{\text{right}}| \tag{3.19}$$

of the plates.

The portable sample holder indicated in figure 3.13 had a size of $(160 \times 100 \times 10)\,\text{mm}^3$ and a detailed sketch is shown in figure 3.14. The specimen, a 160 mm long Nb_3Sn RRP144/169 wire, was soldered on the two current connector plates made of copper $(40 \times 100 \times 10)\,\text{mm}^3$. The sample was soldered on each plate with a contact length of 40 mm and the current leads were clamped on the back. The voltage-taps with a distance of $l = 64\,\text{mm}$ were placed symmetrically outside the pressing zone and never removed to ensure the same measurement length. For the transport and pressing, the three plates were connected by stainless steel bars to prevent the specimen from moving and sustaining damage. After the pressing procedure explained in section 3.1.2, the sample holder was mounted again in the cryostat setup for low-temperature measurements. The connector plates were screwed on with low torque, only to prevent unwanted strain due to thermal contraction. The assembled sample holder in the cryostat setup can be seen in figure 3.15 including mounted current leads and temperature sensors.

In order to monitor the system, additional voltage-taps and temperature sensor, e.g. Pt100 (PTC), were placed on appropriate positions of the system and measured by the four-lead-measurement method using a measurement current of 1 mA. The entire cryostat setup, with all used functionalities, is summarised in the Piping and Instrumentation Diagram (PID) in figure 3.21 at the end of the section.

3.3.2 Electrical sub-system & current leads estimation

Figure 3.13(a) shows the electrical measurement circuit. The setup was equipped with passively cooled current leads made of copper and designed for 150 A. They are clamped with indium foils to the current connector plates, which provide the connection of the high-current feed-through connectors outside the vacuum chamber. The electrical measurement circuit was powered by a 200 A current source (*Delta Elektronika SM30-200*) and the specimen current was measured by using a shunt resistor with $0.25\,\text{m}\Omega \pm 0.25\,\%$. The twisted voltage leads made of Cu, for recording the V-I and V-T curves, were directly routed through to the low-temperature vacuum chamber. The other signal wiring, made of low-temperature coefficient material, was collectively transferred to the chamber by using two 40-pin electrical vacuum connector.

Nanovoltmeters (*Keithley multimeter model 2001*) with a resolution of 10 nV were used to measure the specimen and the shunt voltage. The superconducting transport properties were characterised by performing critical current measurements $I_c|_{T=\text{const.}}$ at specific temperature steps $T_s = T_c \ldots T_c - 1\,\text{K}$ and current-sharing temperature measurements $T_{cs}|_{I=\text{const.}}$ during specific current steps $I = 1\,\text{A} \ldots 100\,\text{A}$. The latter had the advantages that the Joule energy of the remaining part of the electrical measurement circuit stays constant during the entire recording, which led to higher stability. The measurements were performed with a recording sampling time of 200 ms.

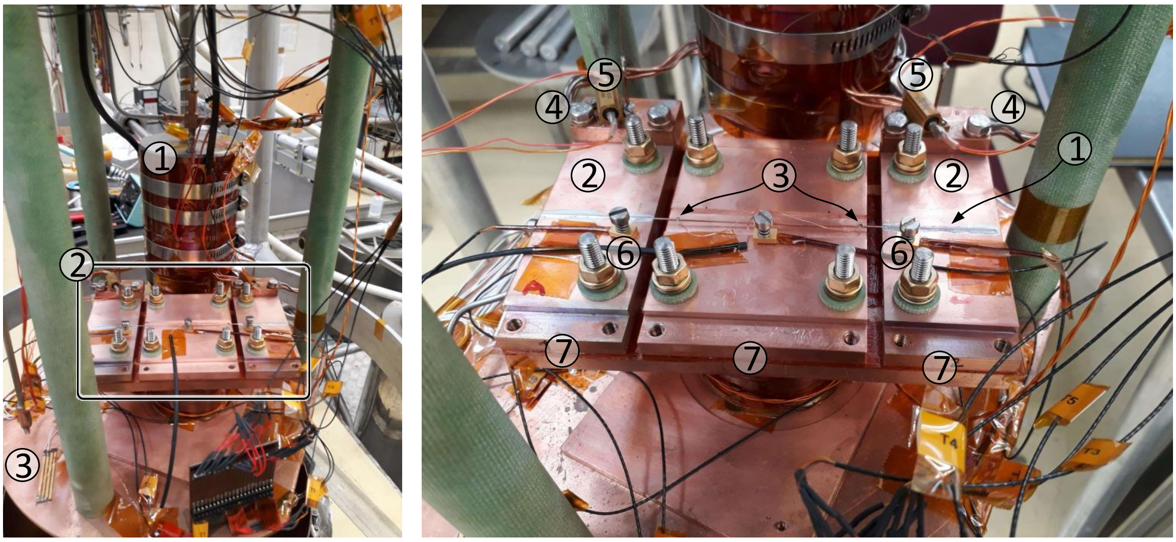

(a) (b)

Figure 3.15: Pictures of the sample holder in the cryostat setup. **(a)** Setup with phase separator in the rear and assembled sample holder in the front, 1. Phase separator, 2. Sample holder including sample 3. Cooling plate **(b)** Installed sample holder, 1. Specimen, 2. Current connection plates, 3. Voltage-taps, 4. Current leads connections, 5. Heaters, 6. Temperature sensor, 7. Groove for transport lock (stainless steel bars).

In order to evaluate also the critical temperature T_c and to get an estimation of the temperature range for the high-current measurements, a thermovoltage-compensated resistance measurement was carried out. The thermoelectric voltage V_{EMF} is constant and inherently associated to low-temperature measurements. Thus, compensation within the resistance measurements was necessary. In the present work, this was implemented by making two measurements with currents of opposite polarity within a single measurement cycle. Each final measurement point was a result of a voltage measurement of the specimen with positive current polarity $V_{M+} = V_{EMF} + RI$ and a negative polarity $V_{M-} = V_{EMF} + RI$. In the end of the 1.5 s long measurement cycle, the thermoelectric voltage was cancelled by combining these measurements and calculating the actual voltage drop at the sample

$$V_M := \frac{V_{M+} + V_{M-}}{2} = IR. \tag{3.20}$$

The resistance of the specimen was than obtained by $R = {}^{V_M}/_{I}$. The used measurement current I was 100 mA, which led to a current density of $J = 0.75\,\mathrm{A\,mm^{-2}}$ within the sub-elements. Considering that only low temperature ramps up to $0.2\,\mathrm{K\,min^{-1}}$ were used, the temperature-depending change of V_{EMF} was neglected. Figure 3.20 shows typical data recording obtained by using the established measurement routines, including the corresponding analysis.

The further instrumentation, e.g. additional voltage-taps and temperature sensors, were acquired by using a nanovoltmeter (*Keithley multimeter model 2001*) equipped with a scanner card. Consequently, the contact resistance and the resistance of the current leads could be analysed by using the further installed voltage-taps, which is presented in section 4.2.

All measurement and control devices were connected via GPIB or USB with a PC, which is schematically shown in figure 3.17. For controlling and data recording, a software written in Python using the instrumentation library PyVISA [124] and the scientific library SciPy [144] was developed. The measurement environment, including the operating cryostat, can by seen in figure 3.16.

In order to install the current leads, a first estimation was carried out. The passively-cooled two-stage current leads were thermalised at the thermal shield by using interception electric breaks and at the phase separator, which is drawn in figure 3.13. This leads to the separation of a warm and a cold part modelled with fix temperatures on their ends. The warm part was installed from outside, $T_{warm,upper} = 290\,\mathrm{K}$, to the thermal shield, assumed with $T_{warm,lower} = 77\,\mathrm{K}$. The cold part was connected from the thermal shield $T_{cold,upper} = 77\,\mathrm{K}$ to the phase separator, $T_{cold,lower} = 4\,\mathrm{K}$. The objective of the estimation was, to find the optimal cross-section A of the current lead to minimise the heat influx from outside. This leads to a compromise of heat conduction, which decreases by reducing the cross-section, and the Joule heating, which is decreasing with increasing the cross-section.

An overview of the matter was made by modelling a single current lead as an one-dimensional con-

(a) **(b)**

Figure 3.16: Pictures of the measurement environment. **(a)** Measurement station. **(b)** Cryostat setup in vacuum chamber during operation including vacuum pump system in the background.

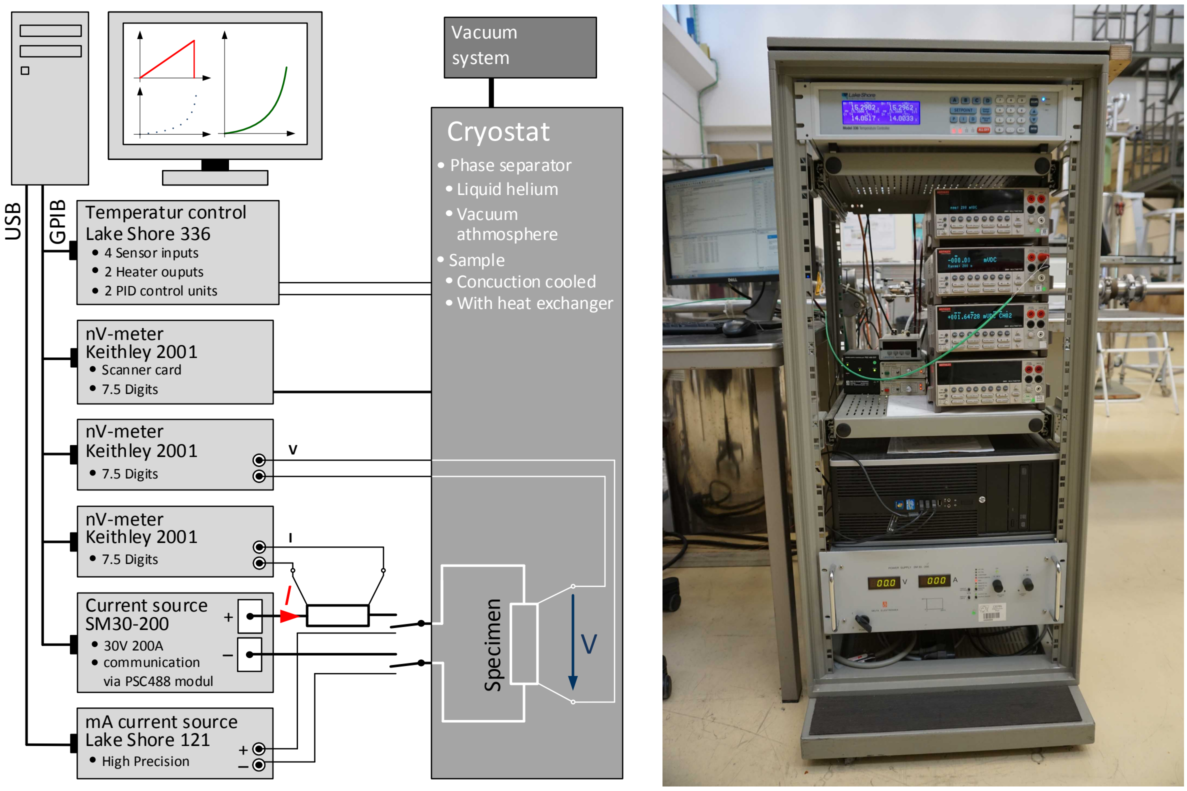

(a) **(b)**

Figure 3.17: Measurement and control system. **(a)** Schematics and wiring of equipment. **(b)** Picture of measurement tower installed next to the cryostat.

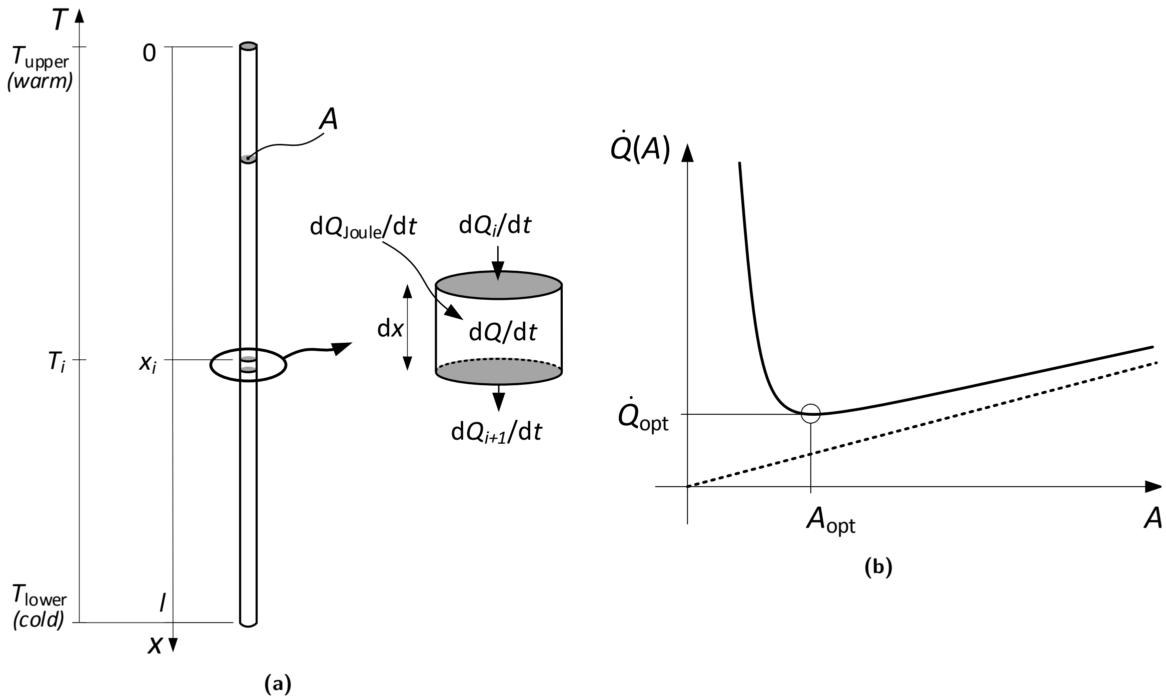

Figure 3.18: Model of a passively-cooled current lead. **(a)** Idealised infinitesimal model to derive the heat influx of a high-current lead. **(b)** Heat transfer at the cold end as a function of the cross-section with (solid line) and without (dashed line) a constant current.

ductor with the cross-section A, the length l and the current I as illustrated in figure 3.18(a). The steady state heat power equation for an infinitesimal slice $\mathrm{d}V = A\,\mathrm{d}x$ of the current lead can be postulated as

$$\frac{\mathrm{d}Q}{\mathrm{d}t} = \frac{\mathrm{d}Q_i}{\mathrm{d}t} - \frac{\mathrm{d}Q_{i+1}}{\mathrm{d}t} + \frac{\mathrm{d}Q_{\mathrm{Joule}}}{\mathrm{d}t} \tag{3.21}$$

with

- the total heat energy stored in the slice $\mathrm{d}Q$ with the specific heat capacity $c = \frac{1}{\rho_\mathrm{m}\mathrm{d}V}\frac{\mathrm{d}Q}{\mathrm{d}T}$ and the volume mass density ρ_m,
- the incoming heat energy from the warm end by heat conduction $\frac{\mathrm{d}Q_i}{\mathrm{d}t} = -\lambda A \frac{\partial T(x_i)}{\partial x}$ with the thermal conductivity λ and the temperature T,
- the outgoing heat energy to the cold end by heat conduction $\frac{\mathrm{d}Q_{i+1}}{\mathrm{d}t} = -\lambda A \frac{\partial}{\partial x}\left[T(x_i) + \frac{\partial T(x_i)}{\partial x}\mathrm{d}x\right]$ and
- the Joule heating $\frac{\mathrm{d}Q_{\mathrm{Joule}}}{\mathrm{d}t} = I^2 \rho \frac{\mathrm{d}x}{A}$ caused by electrical current I with the electrical resistivity ρ.

By using the above-listed aspects, the equation 3.21 can be written for the general case ($x = x_i$) and in the settled condition ($\dot{T} = 0$) as

$$\frac{\partial^2 T}{\partial x^2} = -\frac{I^2 \rho}{\lambda A^2}. \tag{3.22}$$

The temperature along x of the one-dimensional model can be derived from the linear ODE second order (equation 3.22) with $\Delta T = T_{\mathrm{upper}} - T_{\mathrm{lower}}$ and the boundary conditions $T(x = 0) = T_{\mathrm{upper}}$ and $T(x = l) = T_{\mathrm{lower}}$

$$T(x) = -\frac{\rho I^2}{2A^2\lambda}x^2 + \left(-\frac{\Delta T}{l} + \frac{\rho I^2 l}{2A^2\lambda}\right)x + T_{\mathrm{upper}}. \tag{3.23}$$

To get the desired heat flux through the cross-section of the cold end ($x = l$) one has to use the heat conductivity equation

$$\dot{Q}\big|_{x=l} = -A\lambda \frac{\partial T}{\partial x}\bigg|_{x=l} = A\lambda\frac{\Delta T}{l} + \frac{\rho I^2}{2}\frac{l}{A} = \dot{Q}(A), \tag{3.24}$$

Table 3.4: Optimisation of the cross-section area A of the current leads, made of copper ($RRR = 100$) to minimise heat influx.

	warm part	cold part
T_{upper}	290 K	77 K
T_{lower}	77 K	4 K
l	0.6 m	0.6 m
I	150 A	150 A
A_{opt}	25 mm^2	9 mm^2
$\dot{Q}_{opt}$	6.15 W	1.2 W
A_{used}	25 mm^2	10 mm^2

which can be interpreted as a function of the cross-section, as shown in figure 3.18(b). For a large cross-section area, the Joule heating has only minor impact and the entire influx is converging to exclusive thermal transfer. If the cross-section area is chosen to be small, the influx is dominated by the Joule heating. The local minima of this function, hence the desired optimal cross-section area A_{opt}, and the corresponding minimum heat input $\dot{Q}_{opt}$ is given by

$$A|_{\min\limits_{A>0} \dot{Q}(A)} = A_{opt} = \sqrt{\frac{\rho}{2\lambda\Delta T}} Il \quad \text{and} \tag{3.25}$$

$$\min_{A>0} \dot{Q}(A) = \dot{Q}_{opt} = I\sqrt{2\rho\lambda\Delta T}, \quad \text{respectively.} \tag{3.26}$$

The optimal cross-section area is often reported independently of the application depending quantities as the shape factor

$$SF = \left(\frac{Il}{A}\right)_{opt} = \sqrt{\frac{2\lambda\Delta T}{\rho}}, \tag{3.27}$$

and can be looked up in graphs for given material properties in the relevant specialised literature, e.g. the references [54]. For the present work and under consideration of the temperature dependence of thermal conductivity $\lambda(T)$ and the resistivity $\rho(T)$ of copper assumed with $RRR = 100$, the shape factor $SF = 3.6 \cdot 10^6\,\mathrm{A\,m^{-1}}$ for the warm part with $T_{upper} = 290\,\mathrm{K}$ and $T_{lower} = 77\,\mathrm{K}$ was chosen, based on R. McFee [125]. For the cold part, $SF = 10 \cdot 10^6\,\mathrm{A\,m^{-1}}$ was used. This led to an optimum cross-section of 25 mm^2 and 9 mm^2 for the warm and the cold part, respectively, for a current of 150 A and a length of 0.6 m. The results are summarised in table 3.4. In this context, it has to be mentioned that an increase of the RRR of the used copper evokes almost no advantage above 77 K, hence only the cold part can be improved by increasing the RRR [153].

3.3.3 Data evaluation & measurement procedure

Within the NearT_c measurements, the critical current $I_c|_{T=\text{const.}}$ of the recorded $V(I)|_{T=\text{const.}}$ curves were evaluated. As described in section 3.2.3, the electrical field criterion $E(I = I_c) = E_c$ with $E = V/l$ and the voltage-taps distance l was chosen for this work to determine the critical current I_c. Based on the resolution of the used nanovoltmeters and the noise level, the electrical field criterion E_c was set to $100\,\mathrm{\mu V\,m^{-1}}$. As an abort criterion, i.e. quench criterion, $250\,\mathrm{\mu V\,m^{-1}}$ was defined.

$V(I)$ curves were recorded with a typical current ramp rate of $1\,\mathrm{A\,s^{-1}}$, while the sample temperature T_s was stabilised at certain levels in the range of T_c to $T_c - 1\,\mathrm{K}$ with steps of 0.1 K. In average five $V(I)$ curves were recorded at every temperature level. A typical V-I recording and the subsequent I_c evaluation is shown in figure 3.20(a) and 3.20(b). No significant current-transfer voltage could be observed and consequently only the offset voltage was corrected. In contrast to the cable measurements, recording clearly above the threshold E_c could be performed. Hence, the critical current could be evaluated by interpolation of the recording with a sampling rate of 200 ms. The actual sample temperature at the I_c determination point, was also received by interpolating the temperature recording, annotated in the I_c analysis (cf. figure 3.20(b)). The n value was evaluated according the standard of I_c measurement for Nb_3Sn wires [157] by fitting a slope in the double-log depiction around the criterion, as shown in figure 3.19.

Due to initial stabilisation problems, the current-sharing temperature $T_{cs}|_{I=\text{const.}}$ was analysed redundantly by recording $V(T)|_{I=\text{const.}}$ curves with a typical temperature ramp rate of $0.2\,\mathrm{K\,min^{-1}}$. Therefore, the sample current I was set to certain value in the range from 1 A to 100 A with steps greater than

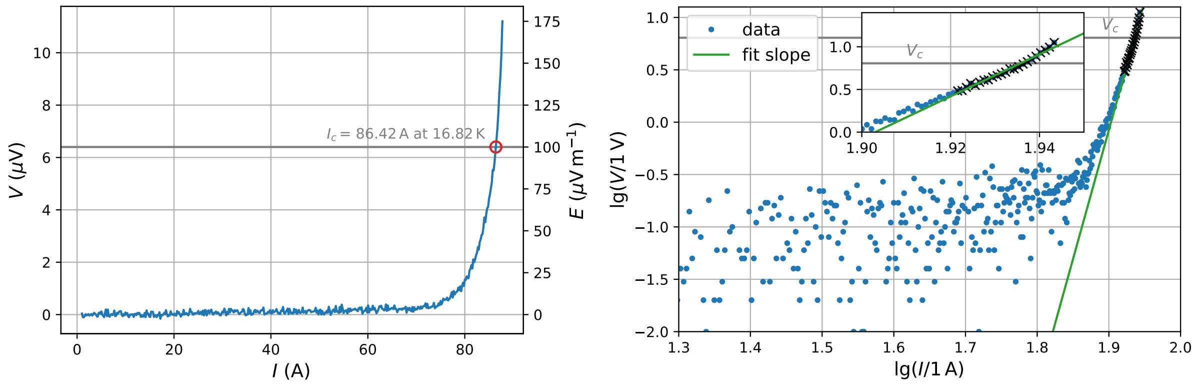

(a) (b)

Figure 3.19: Illustration of the I_c and n value evaluation, according the standard [157]. **(a)** Offset-corrected $V(I)$ relation to determine the critical current I_c (red marker) at the critical field criterion $E_c = 100\,\mu\mathrm{V\,m}^{-1}$. **(b)** Evaluation of the n value, by fitting the linear slope in double-log depiction around the voltage criterion $V_c = E_c l$ with the voltage-tap separation l. Data points used for the fitting are marked with crosses. The evaluation of the n value is enlarged in the small plot.

5 A. At least three $V(T)$ curves were measured at every current level, to check repeatability of the measurement procedure. A typical V-T measurement and the subsequent T_{cs} evaluation is shown in 3.20(c) and 3.20(d). Analogue to the I_c evaluation, the current-sharing temperature as well as the actual current were interpolated at the determination point $E(T = T_{cs}) = E_c$, annotated in the analysis (cf. figure 3.20(d).)

The developed resistance measurement allowed the evaluation of the resistive transition, i.e. the critical temperature T_c, and the RRR. A resistance recording, including the sample temperature, in the transition region is shown in figure 3.20(e). In order to trace possible delays of heat transfer, the resistive transition was measured with an increasing and a decreasing temperature ramp, designated as R_{up} and R_{down}, respectively. The subsequent analysis is plotted in figure 3.20(f), which reveals no hysteresis effect. At least three $R(T)$ measurements with a typical temperature ramp of $0.1\,\mathrm{K\,min}^{-1}$ were performed to test the reliability of the measurement. For the data interpretation, the "mid-point" criterion was used. Hence, the resistive plateau and the transition were fit linearly. The temperature at the intersection of the two fits, labelled with $T_{c,tan}$, and the temperature at the zero point of the transition fit, labelled with $T_{c,zero}$, are further used to characterise the resistive transition. The "mid-point" critical temperature $T_{c,midpoint}$ and transition width ΔT_c are defined as

$$T_{c,midpoint} = \frac{T_{c,tan} + T_{c,zero}}{2} \quad \text{and} \quad \Delta T_c = T_{c,tan} - T_{c,zero}, \tag{3.28}$$

and were used for the analysis in section 4.2.2. Additionally, the RRR was evaluated to get information about the copper matrix after transverse stress applied at RT. It was performed in the course of the cool down of the system. The residual resistance ratio RRR [156] was defined as

$$RRR := \frac{\rho(T_s = 293\,\mathrm{K})}{\rho(T_s = 19\,\mathrm{K})}. \tag{3.29}$$

In the end, it has to be mentioned that the transition width ΔT_c as well as the n value depends strongly on the definition, particularly the n value on the used threshold E_c, and has to be taken into account while comparing the reported values by other authors.

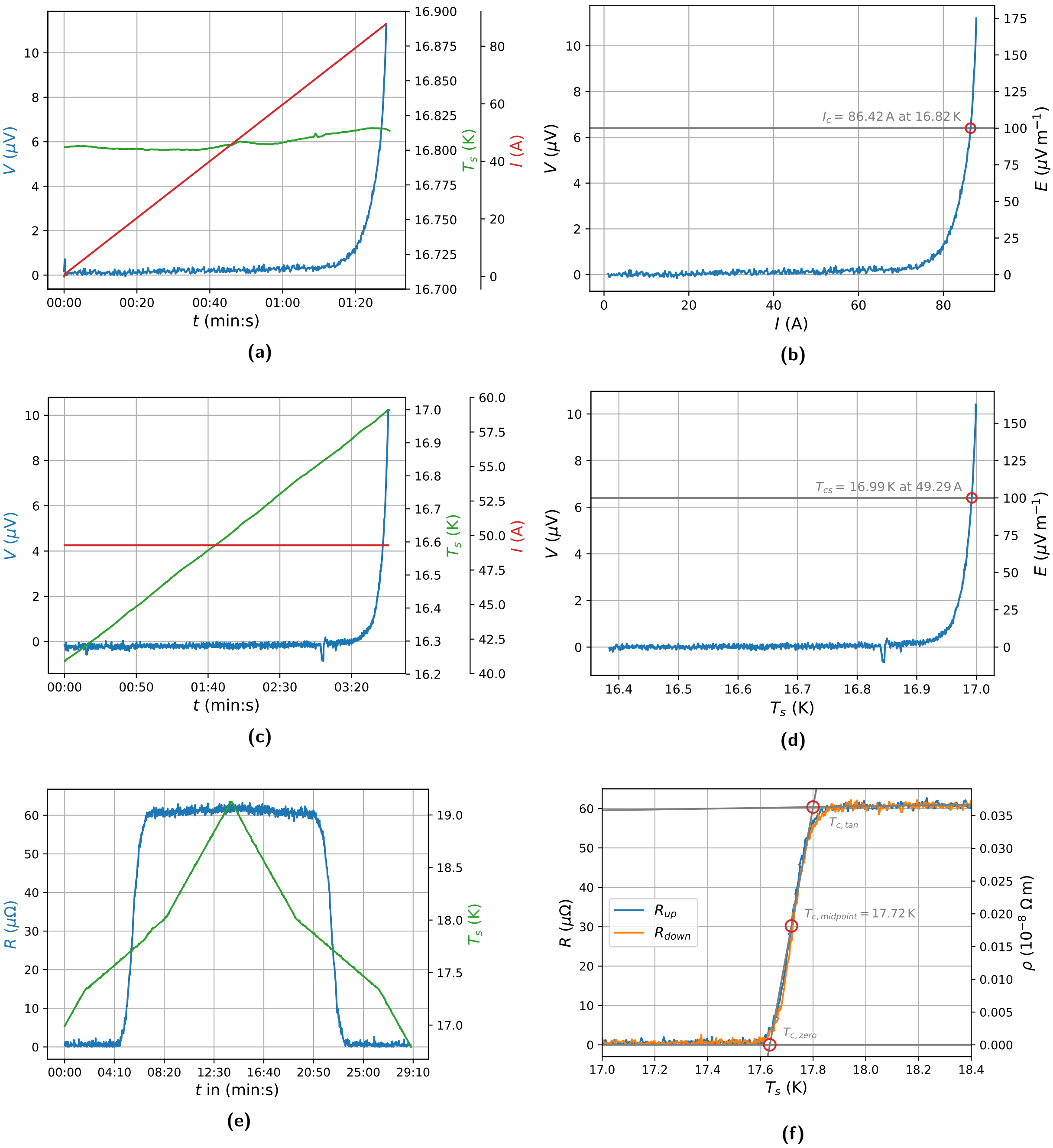

Figure 3.20: Typical measurement recordings and analysis performed with the NearT_c setup. **(a)** V-I recording at $T_s = 16.8\,\mathrm{K}$ with $dI/dt = 1\,\mathrm{A\,s^{-1}}$. **(b)** I_c analysis of (a) with an electrical field criterion $E_c = 100\,\mathrm{\mu V\,m^{-1}}$. **(c)** V-T recording at $I = 50\,\mathrm{A}$ with $dT/dt = 0.2\,\mathrm{K\,min^{-1}}$. **(d)** T_{cs} analysis of (b) with an electrical field criterion $E_c = 100\,\mathrm{\mu V\,m^{-1}}$. **(e)** Thermovoltage-compensated resistance measurement around $T = T_c$ with $dT/dt = \pm 0.1\,\mathrm{K\,min^{-1}}$. **(f)** Resistive transition on the base of (e).

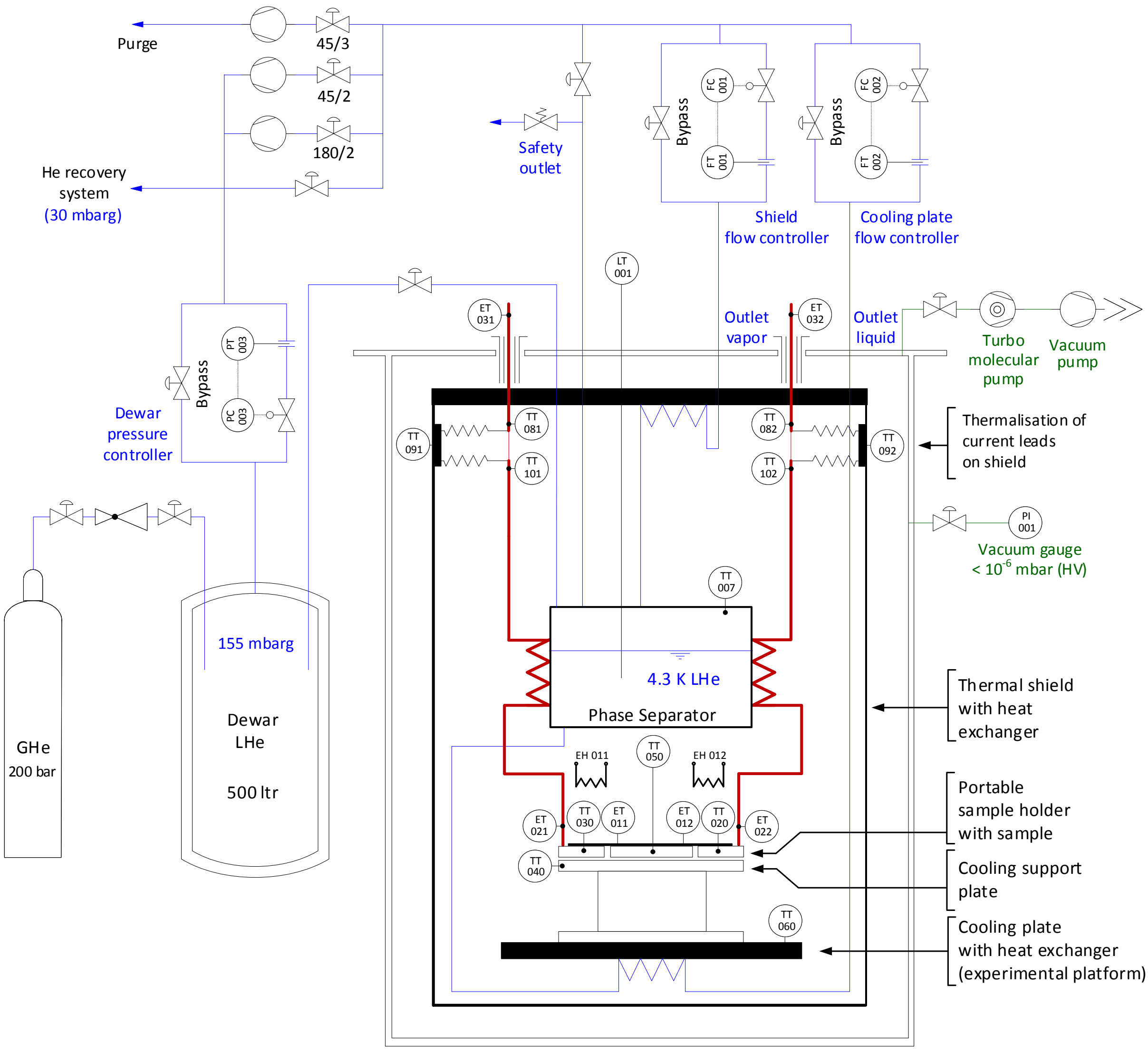

Figure 3.21: PID of the setup in the cryostat, showing the thermalisation of the current leads at the thermal shield and at the LHe phase separator, before reaching the variable temperature platform housing the sample.

3.4 Measurements of wires with the SQUID magnetometer

Additional magnetisation measurements were performed to confirm the results of the transport current measurements of the wire. It extended the measurement range of the wire investigation to lower temperatures and various applied fields. Moreover, this campaign was also aiming at clarifying the suitability of magnetometric methods for crack detection. Magnetisation measurements are a common and efficient tool to investigate the properties of superconductors.

The magnetisation of a superconductor, especially the irreversible magnetisation of a hard superconductor, contains indirectly information about additional quantities, e.g. intrinsic properties and the critical current. By the help of sufficiently accurate models, the desired variables can be derived quantitatively. In general, magnetometry has substantial advantages over transport current measurement:

- The heating of the specimen is negligible and sample contacts are not necessary. Hence, no current-transfer length has to be respected.
- Measurements can be performed in temperature and field ranges, which usually are not accessible by transport current measurements due to extremely high critical currents (several kA).
- Magnetisation measurements are less time consuming, which implies a lower consumption of liquid helium.

Nevertheless, magnetometry has also drawbacks:

- Weak control of underlying assumptions, e.g. granularity of sample.
- Used models are only valid under certain requirements, e.g. assumption of a point-like sample requires a much smaller sample length than the pick-up coil assembly.
- Careful data analysis is mandatory to avoid misinterpretation.

Within this work, the magnetisation measurements were performed on transverse loaded and non-loaded samples with a length of approximately 4 mm. The used SQUID magnetometer *Quantum Design MPMS XL* and the sample holder at TU Wien (Atominstitut) can be seen in figure 3.22. The system facilitates magnetisation measurements in a temperature range from 1.9 K to 400 K with a stability of ±0.5 %. Moreover, it provides an applied field of up to 7 T with 0.01 % non-uniformity in the measurement region. The system has a liquid helium consumption of roughly $5\,\mathrm{L\,d^{-1}}$, when operating at low temperatures. The samples were always perpendicular installed to the applied field, to simulate similar condition as observed in a magnet.

The SQUID magnetometer employs a second order gradiometer pick-up assembly, which houses the sample during the measurement. It is further linked to the shielded RF SQUID device via a flux transformer. Such gradiometers house a single coil with two turns clockwise and two coils of one turn counter-clockwise spaced symmetrically outside (20 mm coil diameter, 30 mm between top and bottom coil), as drawn in figure 3.23(b). They are optimised to reject outer disturbance fields and detect the dipole moment of the sample within the gradiometer. The SQUID device functions as an unsurpassed-sensitive magnetic flux-to-voltage converter and measures the net flux of the sample, which is modelled as point-like. The magnet dipole moment m of the sample is evaluated by analysing the voltage obtained from the SQUID device. The MPMS XL exhibits the following three basic measurement modes:

1. *DC measurement with standard sample holder:*
   This method represents the most basic measurement. It moves the sample through the 30 mm long gradiometer in small steps, while the SQUID response voltage and the corresponding sample position is recorded. The desired magnetic moment m of the sample can then be obtained from the recorded voltage over position curve (raw data), by fitting the data points to the theoretical curve

$$V(z) = -\frac{ma^2}{2}\left[\frac{1}{((z+d)^2+a^2)^{3/2}} - \frac{2}{(z^2+a^2)^{3/2}} + \frac{1}{((z-d)^2+a^2)^{3/2}}\right], \tag{3.30}$$

   with the actual coil radius $a = 10.1$ mm and length between the upper and lower coil $2d = 30.4$ mm, which is shown in figure 3.23(a). The Quantum Design MPMS XL software calculates the magnetic moment m from the fit function amplitude. Hence each value m is related to a raw curve $V(z)$. The final used value $m(B_{\mathrm{app}}, T)$ is by default an average over three measurements under the same condition given with the standard deviation. As shown by past investigations of T. Baumgartner in [14, p.70], the additional RSO is less vulnerable to undesired disturbance fields and hence delivers more reliable results. Thus, this mode was avoided for the final measurements presented in this work.

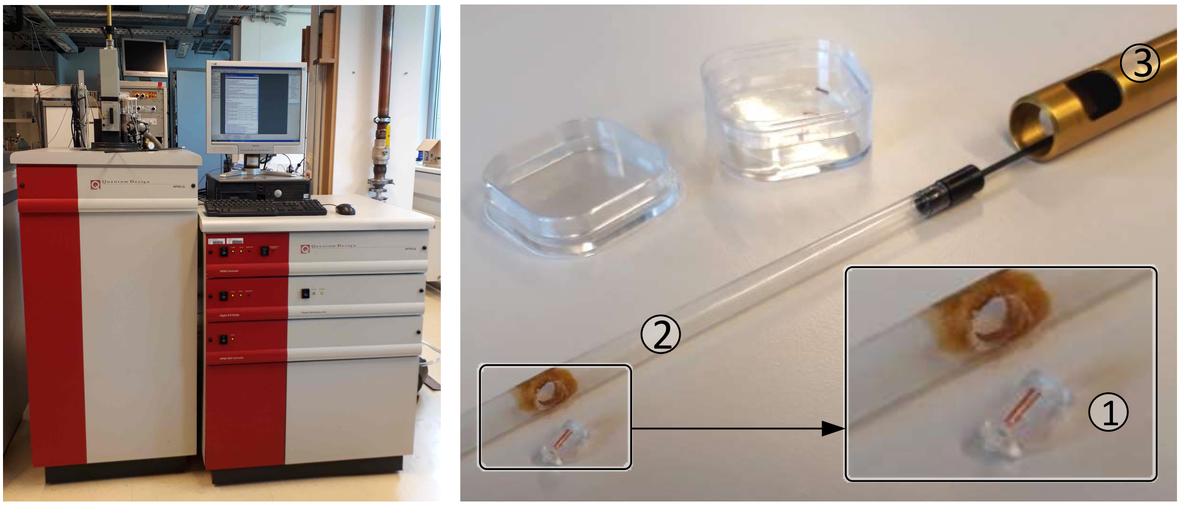

(a) **(b)**

Figure 3.22: Pictures of the used equipment for the magnetisation measurements. **(a)** SQUID magnetometer Quantum Design MPMS XL with the installed RSO. **(b)** RSO rod and sample holder made from a 180 mm long transparent straw and a 6 mm long silica glass tube housing the typical 4 mm long sample for magnetisation measurement to place the sample perpendicular to the applied field. 1. Sample in glass tube, 2. Sample holder, 3. RSO rod.

2. *DC measurement with the RSO (Reciprocating Sample Option):*
   This method was used to evaluate the critical current density $J_c(B,T)$ of wire specimens, based on the measurement of magnetisation loops. It is explained in section 3.4.1.

3. *AC susceptibility measurement:*
   This method was used to evaluate the critical temperature T_c and to extrapolate the upper critical field B_{c2} of loaded and non-loaded wires. It is further described in section 3.4.2.

3.4.1 DC measurement with the RSO

The RSO is an extended mode for DC measurements and increases the sensitivity of the system, as mentioned above. Therefore, the RSO appliance is attached to the top of the MPMS XL cryostat and the RSO rod made of brass has to be used, which is pictured in figure 3.22. After assembling the sample holder, the sample is placed between the centre pick-up coil and the upper pick-up coil, where the SQUID response function has its maximal slope (cf. figure 3.23(a)). During the measurement, the sample rapidly oscillates up and down around the centre position, which converts the system into a Vibrating Sample Magnetometer (VSM) with a SQUID sensor. The SQUID magnetometer is collecting data within the selected amount of cycles. As long as the periodical displacement of the sample stays within the linear range of the SQUID response function $V(z)$, the received voltage to sample position relation will remain linear. In the end, the MPMS XL software computes the magnetic moment by linearly fitting the data point collected during the cycles. The final used value $m(B_{\mathrm{app}},T)$ is an average over three measurements under the same condition. Amplitude and frequency of the oscillation can be set in a range of 0.5 mm to 50 mm and 0.5 Hz to 4 kHz, respectively. The chosen parameters for the presented work are listed in table 3.5.

The sample holder was made of an approximately 180 mm long straw with a diameter of around 7 mm, as recommended by Quantum Design, and glued to the sample rod with vacuum grease for the RSO measurements. The sample was placed transversely in the middle of the sample holder by using a small silica glass tube, which ensures a reproducible installation of the sample, perpendicular to the applied field during the measurement. The sample was additionally fixed with vacuum grease.

In order to obtain the critical current density, the magnetisation loops $m(B_{\mathrm{app}})$ at a certain constant temperature T of the sample was measured automatically. Therefore, the sample was magnetised before with an applied field of −3 T. Subsequently, the applied field B_{app} was ramped from zero the maximum and back to zero. Hence, two-quadrant magnetisation loops were recorded. The irreversible magnetic moment is given approximately by

$$m_{\mathrm{irr}}(B) = \frac{m_{\mathrm{dec}}(B = B_{\mathrm{app}} + B_{\mathrm{self}}) - m_{\mathrm{inc}}(B = B_{\mathrm{app}} - B_{\mathrm{self}})}{2}, \tag{3.31}$$

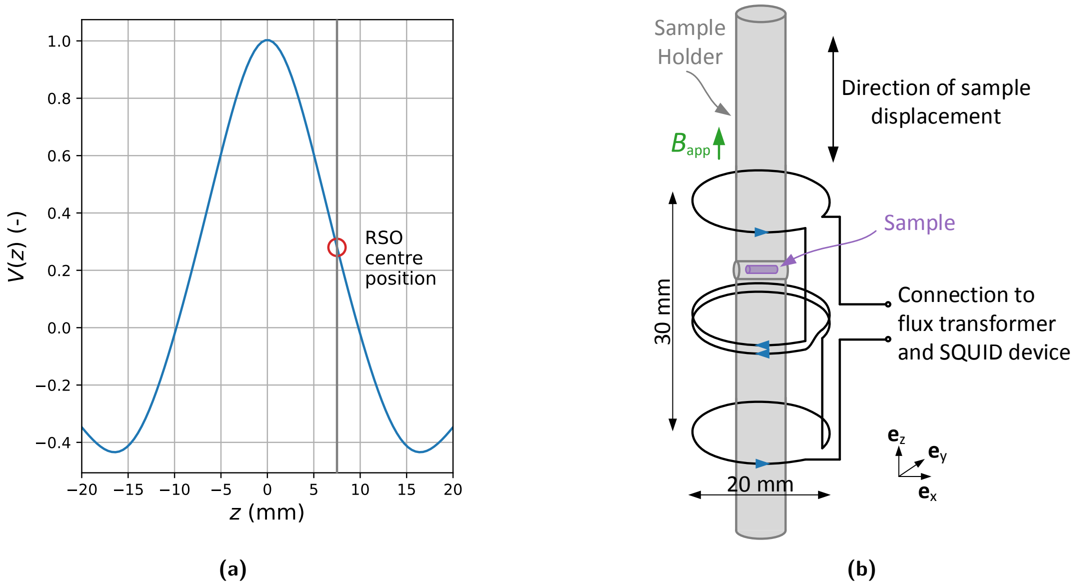

Figure 3.23: **(a)** SQUID sensor response as a function of the sample position in the gradiometer with the middle coil as the centre $z = 0\,\mathrm{mm}$. **(b)** Second order gradiometer of the SQUID magnetometer used to measure the dipole moment of the samples.

with $m_{\mathrm{dec}}(B)$ and $m_{\mathrm{inc}}(B)$ being the magnetic moments measured in the decreasing and increasing applied field, respectively. The quantity B_{self} is the magnetic self-field of the sample, which depends on the irreversible currents in the sample having different signs on the decreasing and increasing measurement loop. Consequently and indicated in the equation 3.31, the self-field contributes either positively or negatively to the magnetic field B in case of the decreasing or increasing loop. Hence, the calculation of the irreversible magnetisation $m_{\mathrm{irr}}(B)$ implies inherently a first-order self-field correction and only higher order components are not considered. Previous investigations of RRP wires concluded that the self-field B_{self} stays below 0.15 T at even high critical currents above $5 \cdot 10^{10}\,\mathrm{A\,m^{-2}}$ and thus contributes only a minor contribution to the entire magnetic field B for $B > B_{\mathrm{self}}$ [14, p.90]. For these reasons, it was decided that the first-order self-field correction is sufficient for the present evaluation, i.e. $m_{\mathrm{irr}}(B)$ defined by equation 3.31 was assumed for the following analysis.

The relation between irreversible magnetisation $m_{\mathrm{irr}}(B)$, which is indirectly measured with the magnetometer, and the critical current density $J_{\mathrm{c}}(B, T)$ depends only on geometric factors, which will be demonstrated as follows.

In general, the magnetic moment $\mathbf{m}$ of a current distribution $J(\mathbf{r})$ within a closed volume $\mathcal{V}$ is defined as

$$\mathbf{m} = \frac{1}{2}\int_{\mathcal{V}} \mathbf{r} \times \mathbf{J}(\mathbf{r})\mathrm{d}\mathcal{V}. \tag{3.32}$$

The circumstances within the superconductor during the above-explained magnetisation measurement can be described with the Bean's critical state model[1] [18]. This assumes the superconductor as a fully penetrated hard superconductor and $J(\mathbf{r}) = J_{\mathrm{c}}$ throughout the entire superconducting volume, which leads to

$$\mathbf{J}(\mathbf{r}) = J_{\mathrm{c}}\,\mathbf{e}_{\mathrm{J}}(\mathbf{r}), \tag{3.33}$$

with $\mathbf{e}_{\mathrm{J}}(\mathbf{r})$ as the local direction of the current. Using equation 3.33 in equation 3.32 delivers

$$\mathbf{m}_{\mathrm{irr}} = J_{\mathrm{c}}\,\frac{1}{2}\int_{\mathcal{V}} \mathbf{r} \times \mathbf{e}_{\mathrm{J}}(\mathbf{r})\,\mathrm{d}\mathcal{V}, \tag{3.34}$$

and implies that the irreversible magnetic moment of the superconductor is proportional to its critical current density and the proportional factor is only depending on the geometric matter, as was assumed before.

In order to derive a relation between the magnetic dipole moment and the critical current, the subelements were modelled to derive an analytical solution. A detailed model would be helical tubes oriented transversely to the applied field, which are coupled magnetically. Considering that the analytical

[1]The model assumes an ideally hard superconductor and is used to assess the critical current of technical superconductors from their irreversible magnetisation. It implies the Schubnikov phase with a macroscopic homogeneous magnetic field distribution. The field generates a current density within the material, which is assumed as constant and equal to the critical current density.

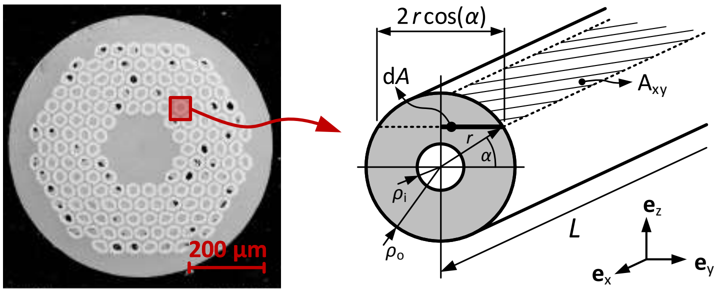

Figure 3.24: Modelling of the superconducting sub-elements as straight, parallel and hollow cylinders without magnetic coupling to receive an analytical relation between the magnetic dipole moment (z direction) and the corresponding planar current loop (XY-plane). Considering that the length and the diameter of the samples are small in respect to the sub-element twist pitch, the simplifications are reasonable.

description of helical tubes are quite complex and the sample's dimensions are much smaller than the sub-element twist pitch, some helpful simplification without major deviation of the reality can be made. Hence, the sub-elements are idealised as straight, parallel and hollow cylinders without any coupling. The used model, including the coordinate system, is drawn in figure 3.24.

The following part derives the relation between the magnetic dipole moment and the critical current of a single idealised sub-element and is, in the end, extrapolated to the moment of the entire wire by multiplying it with the number of sub-elements.

Considering the applied field is parallel to the z-axis, the current loops, which are producing the magnetic moment, are flowing parallel to the XY-plane with the amount J_c according to the Bean model. It can be calculated by splitting the sub-element into infinitesimal flat slices parallel to the XY-plane, carrying a circular-flowing infinitesimal current $\mathrm{d}I = \mathrm{d}I_c$. Hence, the moment $\mathrm{d}\mathbf{m}$ of the infinitesimal slice is defined as

$$\mathrm{d}\mathbf{m} = \underbrace{J_c \mathrm{d}A}_{\mathrm{d}I_c} \; \underbrace{A_{xy}\mathbf{e}_z}_{\mathbf{A}_{xy}}, \tag{3.35}$$

with the infinitesimal cross-section $\mathrm{d}A$, through which the current density J_c flows. The vector area $\mathbf{A}_{xy} = 2\,r\cos(\alpha)\,L$ with the sample length L, which is illustrated in figure 3.24. In the next step, the entire magnetic dipole moment of an idealised sub-element can be calculated by accumulating $\mathrm{d}\mathbf{m}$ of all slices, hence integrating the whole cross-section (YZ-plane) of the sub-element. Therefore the infinitesimal cross-section $\mathrm{d}A$ is transferred in polar coordinate by using the Jacobian determinant

$$\mathrm{d}A = \mathrm{d}x\,\mathrm{d}y = \left|\det\frac{\partial(x,y)}{\partial(r,\alpha)}\right| \mathrm{d}r\,\mathrm{d}\alpha = r\,\mathrm{d}r\,\mathrm{d}\alpha, \tag{3.36}$$

and leads to

$$\mathrm{d}\mathbf{m} = J_c\,2\,L\,r^2\mathrm{d}r\,\mathrm{d}\alpha\cos(\alpha)\,\mathbf{e}_z. \tag{3.37}$$

The integration over the half annulus with ρ_i and ρ_o as the inner and outer radii delivers the irreversible magnetic moment of a single sub-element

$$\begin{aligned} \mathbf{m}_{irr} &= \int_{\rho_i}^{\rho_o}\int_{-\frac{\pi}{2}}^{\frac{\pi}{2}} d\mathbf{m} = 2\int_{\rho_i}^{\rho_o}\int_{0}^{\frac{\pi}{2}} d\mathbf{m} \\ &= 4J_cL\int_{\rho_i}^{\rho_o}\int_{0}^{\frac{\pi}{2}} r^2\cos(\alpha)\mathrm{d}r\mathrm{d}\alpha\mathbf{e}_z = 4J_cL\left.\frac{\rho^3}{3}\right|_{\rho_i}^{\rho_o}\sin(\alpha)|_0^{\frac{\pi}{2}}\,\mathbf{e}_z \\ &= \frac{4}{3}J_cL({\rho_o}^3 - {\rho_i}^3)\,e_z. \end{aligned} \tag{3.38}$$

Finally, the result got multiplied with N, the number of sub-elements, to achieve the irreversible magnetic moment of the entire wire

$$\mathbf{m}_{irr} = \frac{4}{3}J_cNL({\rho_o}^3 - {\rho_i}^3)\mathbf{e}_z. \tag{3.39}$$

For the present measurement condition, the irreversible magnetic moment can be obtained by evaluating the magnetic moment parallel to the applied field, hence m' (z direction), and leads to

$$m_{irr} = \frac{4}{3}J_cNL({\rho_o}^3 - {\rho_i}^3). \tag{3.40}$$

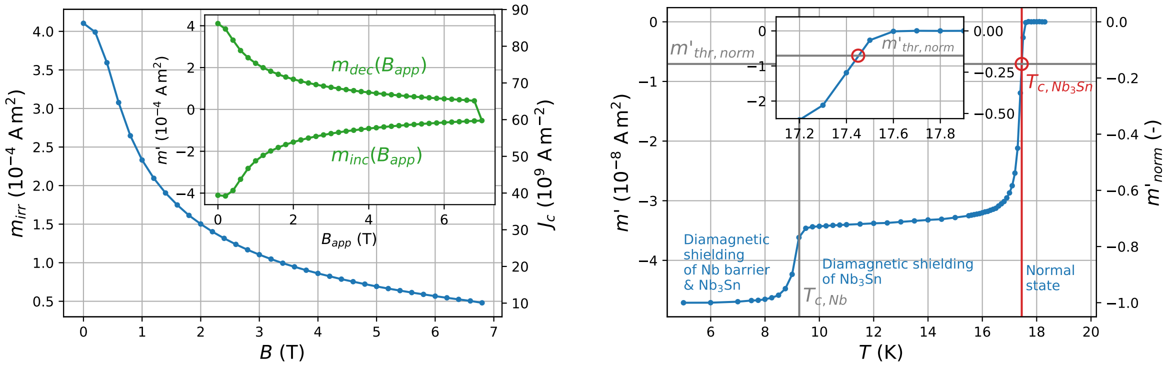

(a) (b)

Figure 3.25: Typical measurement data obtained by using the SQUID magnetometer. **(a)** Two quadrants of the magnetisation loop of the non-loaded sample after a pre-magnetisation of −3 T (small plot) measured with the RSO and related calculation of the irreversible magnetisation. **(b)** AC susceptibility measurement (in-phase-component) of a non-loaded sample for T_c evaluation of Nb_3Sn according a defined threshold m'_{thr}. The transition of the Nb at $T = 9.3$ K as well as the transition of the reacted Nb_3Sn at 17.45 K are marked with vertical lines. The evaluation of T_{c,Nb_3Sn} is magnified in the small plot.

The final hollow cylinder relation, used for the RSO measurement in this work was

$$J_c = \frac{4}{3}\frac{1}{NL({\rho_o}^3 - {\rho_i}^3)} = m_{irr}\gamma(N, L, \rho_o, \rho_i), \tag{3.41}$$

with the scalar geometry factor $\gamma(N, L, \rho_o, \rho_i)$ in m^{-4} depending only on easily determinable variables. The length L was obtained individually for every specimen with a micrometre gauge and the number of sub-elements N as well as the outer and inner radius of the superconducting A-15 phase, ρ_o and ρ_i, respectively, were identified by a SEM and is annotated in figure 2.2. The practical use of the equation 3.41 is demonstrated by the secondary axis of figure 3.25(a). The postulation of the model and the derivation were firstly done by T. Baumgartner et al. [15]. Similar investigations were performed for powder-in-tube Nb_3Sn by Lindenhovius et al. [98].

Table 3.5: Settings used for the RSO measurements to evaluate the critical current density J_c.

Parameter	Setting
Amplitude	2 mm
Frequency	4 Hz
Numbers of cycles	20
Measurements per data point	3

Table 3.6: Settings used for AC susceptibility measurements to determine the critical temperature T_c.

Parameter	Setting
Amplitude	30 µT
Frequency	33 Hz
Block per measurements	3
Measurements per data point	3

3.4.2 AC susceptibility measurement

An AC susceptometer is established in the form of the AC measurement option, which is frequently used to detect and characterise thermodynamic phase changes, e.g. the transition of Nb_3Sn wires at T_c. A small copper coil around the sample chamber is installed to generate an alternating magnetic field within a frequency range from 0.01 Hz to 1 kHz and an amplitude $B_{app,AC}$ of up to 0.4 mT. The alternating field can be optionally superimposed by the applied DC field $B_{app,DC}$. It should be mentioned here that the magnetic field on the surface of the sample can be up to $(1/1-\eta)$-higher than the macroscopic applied field[2], which is important by e.g. evaluating the lower critical field B_{c1}. Therefore, the effective magnetic field $B_{eff} = (1/1-\eta)B_{app}$ is often established, which represents the maximal value of the magnetic field on the surface of the sample.

The AC field causes a time-dependent moment in the sample. The field of the time-dependent moment induces a current in the pickup coils, which allows measurements without sample motion. AC

[2]The demagnetising factor $0 < \eta < 1$, which depends only on the sample's geometry, considers the enhanced magnetic field at the surface caused by the magnetisation of the sample (shielding currents). Long cylinders transverse to the applied field, i.e. the idealised sub-element, have a demagnetising factor of $\eta = 1/2$ [165, p.25].

fields with low frequency are commonly used to evaluate more precisely the slope $\chi = {}^{dM}/_{dH}$ of a sample's DC magnetisation curve $M(H)$, called susceptibility. In combination with a DC bias field, different parts of the magnetisation curve are accessible.

For the purpose of the present work, higher frequencies were used and the entire settings are summarised in table 3.6. Due to the hysteretic behaviour of a hard superconductor in the Schubnikov phase the magnetic moment may lag behind the applied AC field $B_{app,AC} \cos(\omega t)$. Therefore, the so-called AC susceptibility χ is defined as a complex quantity with magnitude and phase, which can be split into a real part χ' (in-phase) and imaginary part χ'' (out-of-phase). The latter indicates dissipative processes in the sample. The MPMS XL is measuring the first harmonics of the in-phase component m' and out-of-phase m'' of the magnetic moment and with the relation $M = {}^{m}/_{V} = \chi {}^{B}/_{\mu_0}$ follows

$$m(t) = \underbrace{\chi' V \frac{B_{eff,AC}}{\mu_0}}_{m'} \cos(\omega t) + \underbrace{\chi'' V \frac{B_{eff,AC}}{\mu_0}}_{m''} \sin(\omega t). \quad (3.42)$$

The volume AC susceptibility $\chi = \chi' - i\chi''$ can be than calculated by

$$\chi' = \frac{\mu_0}{V B_{eff,AC}} m' \qquad \text{and} \qquad \chi'' = \frac{\mu_0}{V B_{eff,AC}} m'', \quad (3.43)$$

with the superconducting volume V of the sample. At this point, it should be noted that the assumption of the ideal diamagnetism and accordingly the calculation of B_{eff} using the demagnetisation factor η is only valid if the sample is in the Meißner phase. In the Schubnikov phase, the magnetic field penetrates into the material, as explained in section 1.2. Consequently, the magnetic self-field of the sample based on its geometry has to be calculated, e.g. numerically and by the use of the Bean model. The sample's self-field and the applied field can then be superimposed to get the effective field B_{eff}.

The measurement procedure can be broken down into blocks, and each of them is corresponding to a two-point measurement. A certain number of blocks are summarised to one measurement. Each final data point is a result of three repetitive measurements. The average value, including standard deviation, is stored in the output file. According to the MPMS XL manual, the RSO rod can also be used for the AC option. Consequently, it was used to avoid possible inaccuracies by using the standard sample holder, as mentioned at the beginning of the section. The sample was also placed perpendicular to the applied field. In fact, the RSO and AC measurements were performed automatically and subsequently without disassembling the sample from the magnetometer. Besides, the temperature resolution of the measurements was increased around the transition point up to 0.02 K and reduced during the remaining duration of the temperature scan to save measurement time.

Evaluation of the critical temperature T_c

Despite the AC susceptibility offers a lot of additional information, it was only used to determine T_c. Due to that reason, only the corresponding magnetic dipole moments m' and m'' were analysed, which are proportional to χ' and χ'', respectively. As long as the conditions $T < T_c$ and $B_{app,AC} < (1-\eta)B_{c1}(T)$ are valid, the sample stays in the Meißner state, hence it is ideally diametric with a susceptibility of $\chi' \approx -1$ and $\chi'' \approx 0$. Above the critical temperature, a superconductor has typically a small susceptibility $|\chi'| \approx 0$. The transition between these two states can be used to determinate the critical temperature T_c.

Therefore, the sample temperature was ramped up typically from 5 K to 19 K during an applied AC field with an amplitude of 30 µT. A typical response of a 4 mm long sample can be seen in figure 3.25(b) as well as in figure 3.26(a), and the appearing effects are described as follows.

- At low temperature, the Nb_3Sn and the niobium barrier of the sub-elements are superconducting. Meißner screening currents generate a magnetic moment. Above the transition of Nb, which can be clearly identified at $T_{c,Nb} = 9.3$ K, only the Nb_3Sn parts are superconducting. The critical temperature of niobium was not essential for the scope of the thesis and hence not further investigated. At around $T \approx 17.5$ K, the A-15 phase is transferring into the normal state resulting in $m' \approx 0$, which was the studied part.

- The behaviour of Nb_3Sn in the superconducting state above $T_{c,Nb}$ and until the actual transition of the A-15 phase reveals information about the homogeneity and micro-structure morphology of the reacted Nb_3Sn. A continuous creeping rise of the in-phase component m' until the transition T_{c,Nb_3Sn}, in contrast to a sharp jump at T_{c,Nb_3Sn}, is an indication that already some parts of the Nb_3Sn area turned into the Schubnikov or normal phase.

- Moreover, the AC method delivers also the out-of-phase component m''. It is shown with the complete information of a typical scan of a non-loaded sample in figure 3.26(b). It is almost zero, except slightly below the transition of the niobium and the Nb_3Sn. As mentioned, the out-of-phase component indicates the dissipation process in the sample. Thus, the peak of m'' represents the maximum of energy loss due to flux flow and absorption, and indicates the beginning of the Schubnikov phase just below the sample transforms into the normal state.

In order to determine the critical temperature utilizing AC measurements, all measured scans m' were normalised and evaluated at a normalised threshold ${m'}_{\mathrm{thr,norm}} = 0.15$, as indicated in figure 3.25(b).

Evaluation of the upper critical field B_{c2}

Motivated by the measured difference of T_c of wires loaded with particular transverse stress at RT, the upper critical field B_{c2} was estimated by the help of AC susceptibility measurements. In order to measure the temperature dependency of $B_{c2}(T)$, the critical temperature T_c at different DC bias fields $B_{\mathrm{app,DC}}$ was measured. Unfortunately, the accuracy of the above-described threshold criterion turned out to be not sufficient for scans with applied DC fields. Consequently, the peak criterion was used for the estimation of B_{c2}. Therefore, the transition of selected samples was measured repeatedly with higher resolution. Subsequently, the peak of m'' was used to determine T_c during a particular applied bias field, as indicated in figure 3.26(b). Due to the limitation of the applied DC field of 7 T, $B_{c2}(T)$ was evaluated at high temperatures only ($T \geq 3/4\, T_c$).

Nb_3Sn sub-elements within superconducting composite wires can be identified as so-called dirty superconductors, due to their impurities and disorder. Without going into detail, dirty superconductors are characterised by an electronic mean free path much smaller than the BCS coherence length, i.e. $l \ll \xi_{\mathrm{BCS}}$. Under consideration of the dirty limit and without the Pauli paramagnetic limit[3], the WHH expression for the zero-temperature value of the upper critical field $B_{c2}(0)$ can be simplified to

$$B_{c2}(0) = 0.693\, {T_c}^* \left(-\frac{\mathrm{d}B_{c2}}{\mathrm{d}T}\right)_{T={T_c}^*} \tag{3.44}$$

with the effective critical temperature ${T_c}^*$. Equation 3.44 is commonly used to estimate $B_{c2}(0)$ based on $T_c(B)$ measurements. The effective critical temperature ${T_c}^*$ was used instead of the measured critical temperature T_c at zero applied DC field to reduce the influence of inhomogeneities. The critical temperatures measured at applied DC fields in the range of 2 T to 7 T were used to fit the linear behaviour of $B_{c2}(T)$ at high temperatures

$$\left(-\frac{\mathrm{d}B_{c2}}{\mathrm{d}T}\right)_{T={T_c}^*}. \tag{3.45}$$

The received linear fit was further used to determine ${T_c}^*$, which is known as the extrapolated intercept with the temperature axis.

A typical evaluation of the slope and ${T_c}^*$ can be seen in figure 3.26(b). The critical temperatures, measured at certain applied fields, are plotted in the B-T diagram (coloured dots). The linear fit of the slope is plotted as a dashed black line. Points, used for the fit approximation, are additionally marked with black crosses. The difference of the extrapolated effective ${T_c}^*$ (black triangle) and T_c (blue dot) is apparent. The small plot shows the peak of the out-of-phase components m'' at a certain DC bias field in the corresponding colour. At an applied field greater than $(1-\eta)B_{c1}(T)$, the samples are explicitly in the Schubnikov phase during the temperature scan, which arises in a lower and more widespread peak of m'' at the transition to the normal state.

[3]This means $\alpha = 0$. The paramagnetic limitation parameter α, also called Maki parameter [102, 103], is used within the WHH theory to derive the temperature dependence of B_{c2} including the Pauli spin paramagnetism and spin-orbit scattering based on the GLAG theory [76, 77, 177].

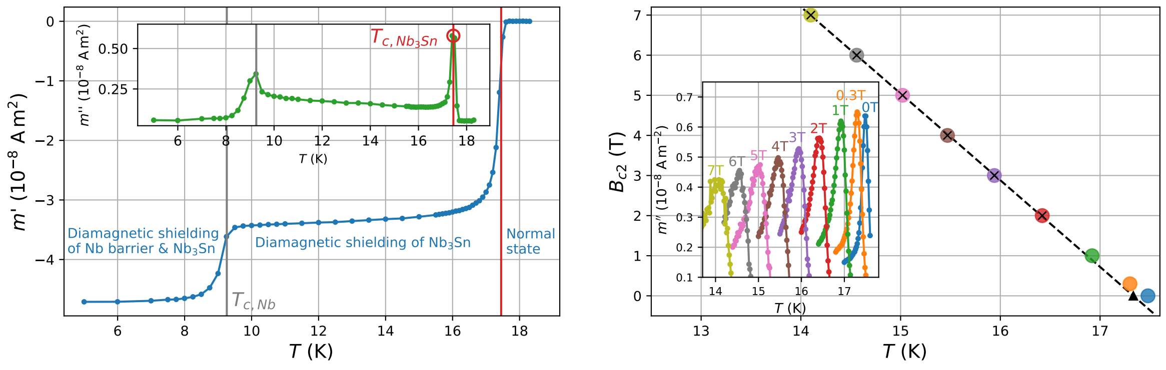

(a) **(b)**

Figure 3.26: Typical estimation of the upper critical field $B_{c2}(0)$ by using AC measurements and the WHH expression for dirty superconductors. **(a)** AC susceptibility scan with T_c evaluation according the m'' peak criterion. The peak of m'' indicates the dissipation within the sample slightly below the transition. **(b)** Evaluation of the sloop dB_{c2}/dT at high temperatures for the WHH expression. The measured T_c at a certain DC bias field (cf. (a)) are plotted in the B-T diagram (coloured dots) as well as the linear fit (dashed line). The used points for the fitting of the slope are marked with a black cross. The effective critical temperature ${T_c}^*$ is marked with a black triangle. The corresponding out-of-phase component m'' at a certain DC bias field used for the T_c is shown in the small plot with the same colour.

3.5 Microscopy of metallographically prepared cables & wires

For the presented work, a field emission gun scanning electron microscope (FEG-SEM), especially a *FEI Quanta 250 FEG* for the cable investigation and a *ZEISS FEG Sigma* for the wire investigation, was chosen to perform the microscopy.

Both, back-scattered electron (BSE) imaging and secondary electron (SE) imaging were used. The BSE imaging delivers an image proportional to the atomic number of the observed material. Due to its high contrast, it was primarily used to get an overview of the specimen and the different material components, e.g. niobium diffusion barrier. The SE imaging, implemented with an Everhart-Thornley detector (ETD) in the present case, delivers mainly information about the surface of the specimen. Hence, it was used to analyse the shape of the cracks or to expose initial polishing problems. Additional, an energy dispersive X-ray analysis (EDX) was used to identify the components of a sub-element.

In general, an accelerator voltage of 10 kV with a working distance from 8 mm to 12 mm was used with magnifications from 100 to 2000 to characterise cracks with widths of down to approximately 0.2 µm. For the inspection of the crack surfaces, an accelerator voltage of 40 kV and a magnification of up to 4000 were partially used.

Due to the average size of cracks, the magnification range of optical microscopes (OM) was sufficient for prior or intermediated inspection. In this case, the digital OM *Keyence VHX-1000E* with the universal lens *VH-Z100UR* was used.

Chapter 4

Results & Discussion

All results achieved in the frame of the presented work are summarised and interpreted in this chapter. The results of the critical current measurements and the complementary microscopic investigations on the cable experiment are provided in section 4.1 and held information of the degradation close to the actual situation in a magnet. Section 4.2 presents the results of the wire investigations, i.e. the transport and magnetisation measurements as well as the microscopy. It will offer and discuss the measured data about the cause and effect of the transverse stress exposed at RT on Nb_3Sn as well as the feasibility of the NearT_c concept. Finally, the conclusion in section 4.3 summaries the essential achievements and an outlook in section 4.4 contributes suggestions for further investigations.

4.1 Results of cable investigations

This section presents the results of the cable investigations, which are based on the stress application at RT and the subsequent I_c measurement of three specimens. In order to provide microscopic information for the cause analysis, the final 200 MPa loaded measured area and a non-loaded area of specimen 1 were metallographic prepared for a SEM autopsy. Besides, a load study with remaining parts of specimen 1 was performed to analyse the behaviour of the sub-elements after certain stress at RT.

4.1.1 Stress exertion

Table 4.1, table 4.2 and table 4.3 summarise the recordings during the pressing procedure at RT prior to the critical current measurement with the FRESCA test station. This procedure was iteratively performed with increasing load and a minimum step size of 10 MPa until the specimen showed a critical current degradation of around 10 %. The tables compare the targeted (nominal) stress $\sigma_{\text{nom}} = F_{\text{nom}}/A_{\text{nom}}$ with the stress $\sigma_{\text{LC},\Sigma} = F_{\text{LC},\Sigma}/A_{\text{nom}}$ determined with the direct force measurements using the load cells and the nominal pressing area A_{nom}. The maximal measured force within the around 2 min long stress exertion was used for this evaluation. Since the error of the actual stress from the nominal stress was smaller than 2.1 %, the nominal values were used to present the results in section 4.1.2. Additional, the load balance reports the force allocation among the support points of the four load cells. It holds information about the deviation from the desired evenly distributed force $F_{\text{nom},\Sigma}/4$ for each support point, which was adjusted in advance for the high-pressure region within the hydraulic press refurbishment.

In the experiments with specimen 1 and specimen 2, all pressure steps were performed with the same pressing die described in section 3.1.1. The difference of the specimen's width originates from the different impregnation mould used for the preparation of the specimen 2. The experiment with the wider specimen 3 including titanium bars in a sandwich structure (cf. figure 2.4(b)) exceeded the capacity of the hydraulic system of maximal 180 kN unexpectedly. Accordingly, a shorter die with an equal radius of 3 mm on the edges was made allowing an exertion above 210 MPa with a smaller nominal pressing area.

Additional to the force measurement, pressure-sensitive films were used for the stress measurement, as described in section 3.1. Figure 4.1, figure 4.2 and figure 4.3 show the HHS type films after the stress exertion of the last three steps on the particular specimen. Some stress peaks could be observed, which are caused by the surface roughness of the impregnated specimen and can be traced back to the impregnation process. The almost point-symmetric stress distributions are resulting from the optimisation of the load balance and the stress distribution.

Despite the valuable contribution of the Prescale films during optimisation, it was decided to make only a local analysis with these films at the final experiments. Derived global values were deceptive, due to the measurement range of the films and a comparison with the force $F_{LC,\Sigma}$ was debatable. Stress values outside the measurement range are not included in the statistics, which resulted in a sharp constraining cut of the almost Gauß-shaped stress distribution in the histogram in figure 3.2(c). Consequently, the spatial average value of the two-dimensional stress map of stress exertions with a target stress σ_{nom} near the measurement range boundary was inherently falsified and the integrated entire force F_p likewise. As explained in the reference [46], the reliability of F_p increases with the effective used area and the distance of the nominal stress to the measurement range boundaries. Furthermore, the Prescale film exposed to a stress above 250 MPa got deformed so that only a limited local assessment could be made.

Table 4.1: Results of specimen 1 (HT15OC0190, 11 T dipole project) with a nominal pressing area of $A_{nom} = (44 \times 15.6)\,\text{mm}^2$.

Nominal		Force measurement					
σ_{nom} (MPa)	F_{nom} (kN)	$F_{LC,\Sigma}$ (kN)	$\sigma_{LC,\Sigma}$ (MPa)	Load balance (-)	(-)	(-)	(-)
50	34.32	33.60	48.95	1.29	1.13	0.82	0.76
100	68.64	69.37	101.06	1.17	1.09	0.87	0.86
125	85.80	85.59	124.69	1.16	1.07	0.91	0.86
150	102.96	104.12	151.69	1.14	1.07	0.93	0.86
175	120.12	118.74	172.99	1.11	1.06	0.93	0.89
200	137.28	138.16	201.28	1.11	1.05	0.93	0.92

Table 4.2: Results of specimen 2 (HT15OC0210, 11 T dipole project) with a nominal pressing area of $A_{nom} = (44 \times 15.8)\,\text{mm}^2$.

Nominal		Force measurement					
σ_{nom} (MPa)	F_{nom} (kN)	$F_{LC,\Sigma}$ (kN)	$\sigma_{LC,\Sigma}$ (MPa)	Load balance (-)	(-)	(-)	(-)
50	34.76	34.88	50.17	1.03	0.93	0.97	1.07
100	69.52	69.63	100.16	1.00	0.99	0.99	1.02
125	86.90	86.99	125.13	0.99	1.00	1.00	1.01
150	104.28	104.21	149.90	0.99	1.02	0.99	1.00
170	118.18	118.45	170.38	0.98	1.00	1.01	1.01
180	125.14	125.48	180.49	0.99	1.02	0.99	0.99

Table 4.3: Results of specimen 3 (HT16OC0217, MQXF project) with a nominal pressing area of $A_{nom,1} = (44 \times 19.3)\,\text{mm}^2$ until 210 MPa and $A_{nom,2} = (35 \times 19.3)\,\text{mm}^2$ from 225 MPa, respectively.

Nominal		Force measurement					
σ_{nom} (MPa)	F_{nom} (kN)	$F_{LC,\Sigma}$ (kN)	$\sigma_{LC,\Sigma}$ (MPa)	Load balance (-)	(-)	(-)	(-)
125	106.15	106.78	125.74	0.98	0.98	1.03	1.01
150	127.38	127.42	150.05	0.98	0.98	1.03	1.01
170	144.36	144.41	170.05	0.98	0.98	1.03	1.01
185	157.10	157.38	185.33	0.98	0.98	1.03	1.00
200	169.84	169.91	200.08	0.96	0.97	1.04	1.03
210	178.33	178.59	210.30	0.98	0.99	1.02	1.01
225	151.99	152.44	225.67	0.98	0.99	1.02	1.01
240	162.12	162.59	240.70	0.98	1.00	1.01	1.01
255	172.25	172.40	255.22	0.97	1.00	1.01	1.02

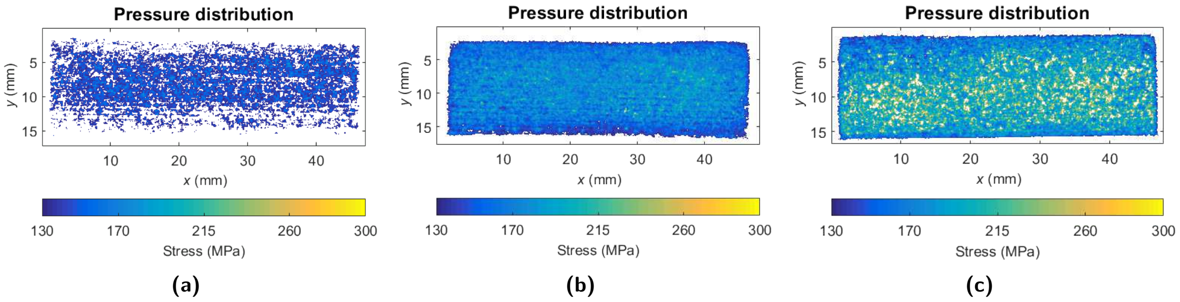

Figure 4.1: Evaluation of pressure-sensitive films (type HHS) of specimen 1 after the application of a nominal stress of **(a)** 150 MPa **(b)** 175 MPa **(c)** 200 MPa.

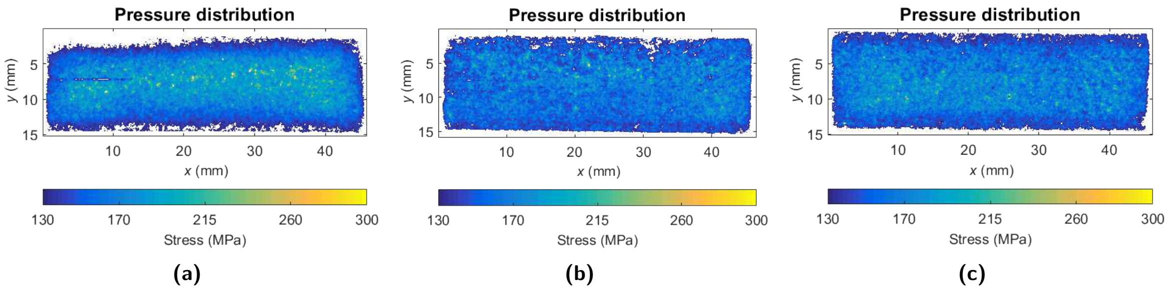

Figure 4.2: Evaluation of pressure-sensitive films (type HHS) of specimen 2 after the application of a nominal stress of **(a)** 150 MPa **(b)** 170 MPa **(c)** 180 MPa.

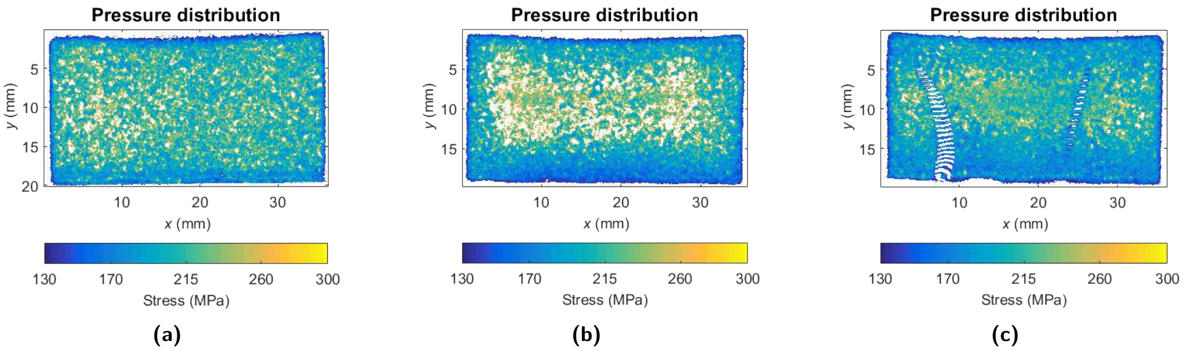

Figure 4.3: Evaluation of pressure-sensitive films (type HHS) of specimen 3 after the application of a nominal stress of **(a)** 225 MPa **(b)** 240 MPa **(c)** 255 MPa. Films exposed to stress greater than 250 MPa got deformed, which can be observed in (c) and led to a restricted assessment of the stress distribution.

4.1.2 Transport current measurements

After every pressure step at room temperature reported in the above section, the critical current of the specimens was measured with the FRESCA cable test station. In order to perform a relative analysis, all virgin specimens were measured at the beginning shortly after an extensive training phase. Since every specimen was made of a single cable type, the analysis is focusing on the upper cable and the lower cable was evaluated for confirmation only.

The critical current of the specimens was evaluated at $T = 4.3\,\mathrm{K}$ with current ramps of $100\,\mathrm{A\,s^{-1}}$. Specimen 1 and specimen 2 were measured at applied fields from 7 T to 9 T, in steps of 0.5 T and additionally at the maximum $B_{\mathrm{app,max}} = 9.6\,\mathrm{T}$. Specimen 3 had a higher critical current due to the different cable and strand properties, listed in table 2.2 and 2.4. In combination with the FRESCA measurement window, constrained by a maximal applied field of 9.6 T and a maximal operation current of 32 kA, specimen 3 could only be characterised at 9.0 T and 9.6 T. The non-loaded specimens were also tested at $T = 1.9\,\mathrm{K}$. Due to constraints, further load steps were not be measured at this temperature, which did not allow interpreting the results.

Figure 4.4(a), figure 4.5(a) and figure 4.6(a) show the completed critical current results I_c (markers) of the particular specimen as a function of the peak field $B_{\mathrm{peak}}(I)$. The latter is derived in section 3.2.2 for the present specimen geometries. Additional, the scaling law curves (lines) derived by the Kramer relation $I_c = C\,b^{-1/2}(1-b)^{1/2}$ with $b = {}^{B}/_{B_{c2}^*}$ and C and $B_{c2}{}^*$ as fitting parameters were plotted for the virgin state and the highest pressure step [86]. The critical current of the corresponding non-cabled virgin wires was plotted additionally as a reference. These results, provided by CERN (TE-MSC-SCD), were measured conformable to the standard IEC61788-2 [157] and presented according to section 3.2.2.

The recorded V-I curves including corresponding fit functions at the highest applied field of all pressure steps are plotted in figure 4.4(b), figure 4.5(b) and figure 4.6(b) for the respective specimen, representing the closest measurement case to the situation in a magnet. As pointed out in section 3.2.3, the V-I curves were corrected for the analysis, i.e. the undesired induction offset voltage and the ohmic part in the virgin measurement data were substituted. Due to the few measurement points within the resistive transition, a reduction of the criterion E_c to $3\,\mathrm{\mu V\,m^{-1}}$ was obligatory to prevent extrapolation uncertainties, i.e. to ensure that measurement points are available around the I_c determination point. Every specimen was measured at a distinct condition at least three times. The recording with the most points at the transition was taken for the presented analysis to prevent uncertainties of the used fit approximation.

Due to the substantial degradation of specimen 1, it was decided that data points above 5 kA were included in the evaluation. Specimen 2 and 3 were analysed with data points above 10 kA, as defined in section 3.2.3. The dependency of the effective upper critical field $B_{c2}{}^*(4.3\,\mathrm{K})$ on the transverse stress was not clearly determinable by using the Kramer plot. This can be reasoned by the limitation of the applied field to 9.6 T, which is significantly smaller than $B_{c2}(4.3\,\mathrm{K})$ of Nb_3Sn composite superconductors.

Table 4.4, table 4.5 and table 4.6 are summarising the results of the particular specimen. In order to present the degradation, the values are normalised to the virgin measurement and listed in an additional column. Figure 4.7 visualises an overview of the achieved results.

Table 4.4: Results of specimen 1 at $T = 4.3\,\mathrm{K}$ and $\max(B_{\mathrm{app}}) = 9.6\,\mathrm{T}$.

Stress σ_{nom} (MPa)	Upper cable I_c (kA)	(-)
0	22.10	–
50	22.25	1.01
100	22.23	1.01
125	22.18	1.00
150	22.19	1.00
175	21.54	0.97
200	7.77	0.35

Table 4.5: Results of specimen 2 at $T = 4.3\,\mathrm{K}$ and $\max(B_{\mathrm{app}}) = 9.6\,\mathrm{T}$.

Stress σ_{nom} (MPa)	Upper I_c (kA)	(-)
0	20.50	–
50	20.80	1.01
100	20.79	1.01
125	20.84	1.02
150	20.95	1.02
170	20.40	1.00
180	18.84	0.92

Table 4.6: Results of specimen 3 at $T = 4.3\,\mathrm{K}$ and $\max(B_{\mathrm{app}}) = 9.6\,\mathrm{T}$.

Stress σ_{nom} (MPa)	Upper cable I_c (kA)	(-)
0	30.45	–
125	30.40	1.00
150	30.30	1.00
170	30.21	0.99
185	30.29	0.99
200	30.26	0.99
210	30.29	0.99
225	30.07	0.99
240	29.74	0.98
255	28.40	0.93

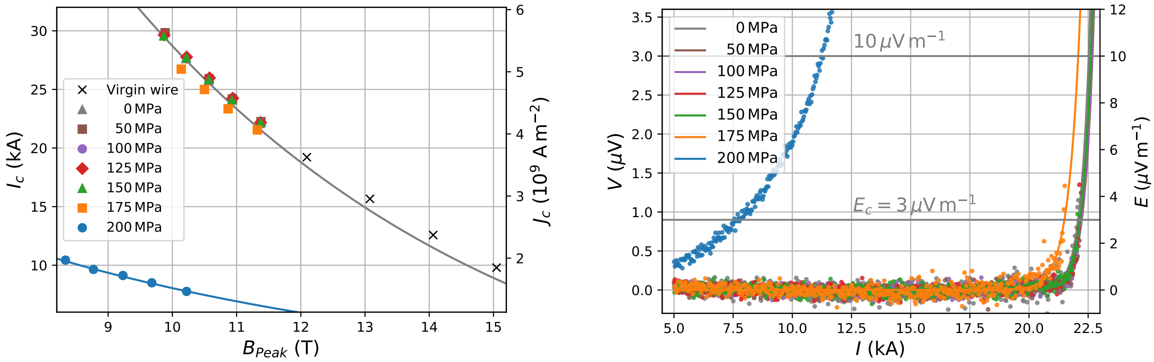

(a) **(b)**

Figure 4.4: Results of specimen 1. **(a)** Critical current of the upper cable as a function of the peak field at $T = 4.3$ K after each pressure level with Kramer law fit for the virgin and the highest pressure step in the corresponding colour. The black crosses without Kramer law fit refer to the I_c measurements of the non-cabled wire of the same type. **(b)** Comparison of corrected V–I characteristics of the upper cable at $T = 4.3$ K and max$(B_{app}) = 9.6$ T after each pressure level.

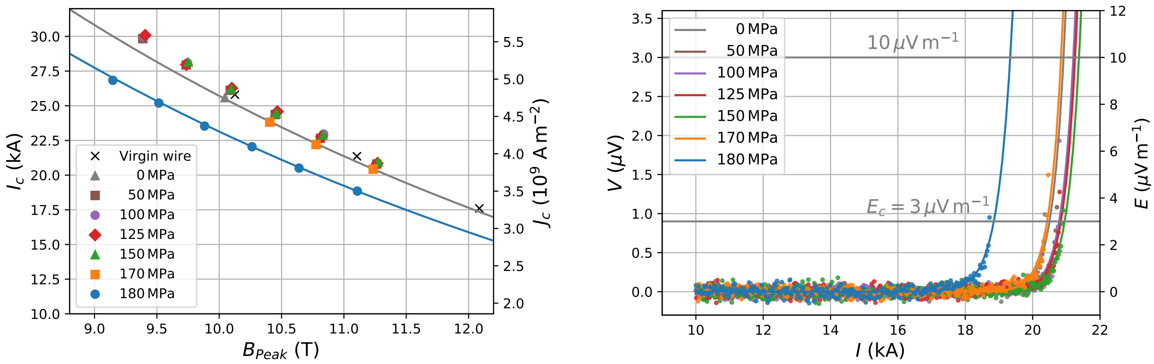

(a) **(b)**

Figure 4.5: Results of specimen 2. **(a)** Critical current of the upper cable as a function of the peak field at $T = 4.3$ K after each pressure level with Kramer law fit for the virgin and the highest pressure step in the corresponding colour. The black crosses without Kramer law fit refer to the I_c measurements of the non-cabled wire of the same type. **(b)** Comparison of corrected V–I characteristics of the upper cable at $T = 4.3$ K and max$(B_{app}) = 9.6$ T after each pressure level.

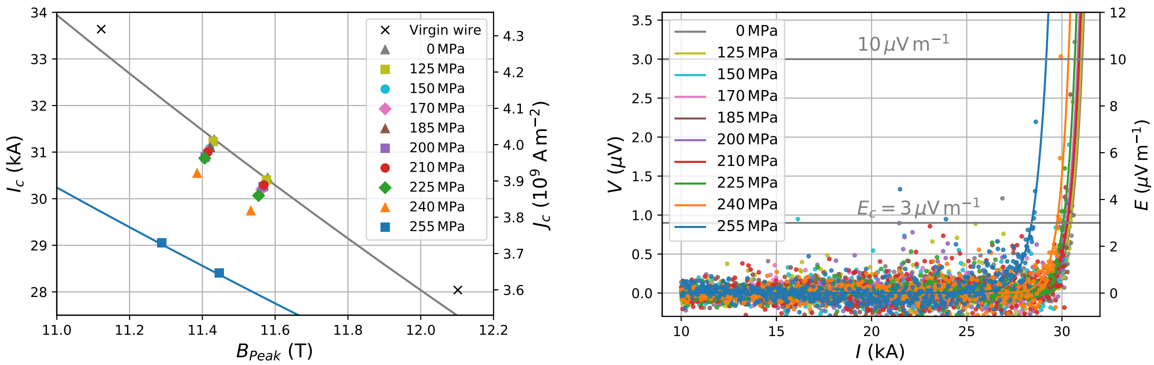

(a) **(b)**

Figure 4.6: Results of specimen 3. **(a)** Critical current of the upper cable as a function of the peak field at $T = 4.3$ K after each pressure level with Kramer law fit for the virgin and the highest pressure step in the corresponding colour. The black crosses without Kramer law fit refer to the I_c measurements of the non-cabled wire of the same type. **(b)** Comparison of corrected V–I characteristics of the upper cable at $T = 4.3$ K and max$(B_{app}) = 9.6$ T after each pressure level. Due to the greater dimension of the cable type higher test currents were necessary to reach I_c.

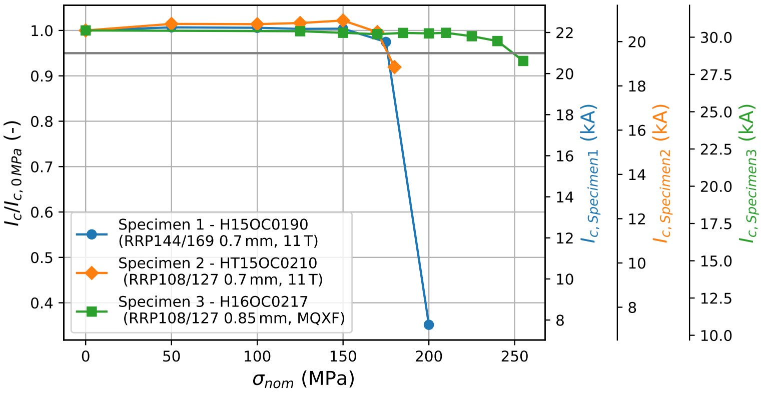

Figure 4.7: Comparison of the critical currents normalised to the non-loaded performance of respective specimens (upper cable) at $T = 4.3$ K and $\max(B_{\text{app}}) = 9.6$ T including a 5 % degradation threshold. The better performance of specimen 3 can be justified with the change of stress arrangement by using titanium bars in sandwich configuration.

4.1.3 Microscopic investigations

After the I_c measurements of specimen 1 were completed up to a nominal stress of 200 MPa, the sample was cut and metallographically prepared. The originally measured loaded region, as well as a non-loaded region, was subjected to a microscopic investigation. As described in figure 2.5(a), the transverse (XZ-plane) and longitudinal (XY-plane) cross-sections were metallographically prepared for autopsy to observe the mechanical consequence of the transverse stress.

The centre part of the transverse cross-section of the non-loaded region can be seen in figure 4.8, including labelling of the components. It revealed several known facts, e.g. the pre-reacted deformation of the strands due to cabling and the partial hemming bends of the core, which are further investigated by e.g. J. Fleiter *et al.* [61]. The primary purpose of this observation was to confirm a doubtless metallographic process without generating misleading cracks. In the transverse and longitudinal cuts of the non-loaded sample, the absence of cracks could be approved within the observed area.

The transverse cross-section of the loaded part revealed many cracks. The highest crack density could be observed in the centre part, which can be seen in figure 4.9. Cracks with a typical width down to 0.5 µm were taken into account in the presented inspection. A characteristic spatial X-shape crack pattern within the strands could be observed, as shown in the magnified micrograph figure 4.9(b). Depending on the former deformation due to cabling, the pattern was slightly asymmetrical. However, this pattern helps to estimate in which depth of the longitudinal cross-section the sample has to be prepared for a further crack investigation. Figure 4.9(d) shows a cracked sub-element in detail. The cracks tend to be parallel to the applied transverse stress and extend from the inner residual α-bronze to the niobium diffusion barrier. Voids tend to act as stress concentrators that induce larger cracks.

The longitudinal cross-sections were further prepared to identify the shape and propagation of the cracks detected in the transverse cross-section described above. Therefore, the upper row of strands (upper cable) was examined. About one-third of the row was removed planarly by metallographic preparation. Figure 4.10 presents the non-loaded part, including labelling of the components. An overview of the loaded sample is provided in figure 4.11, which displays a part of the cross-section of a damaged strand. The examined cracks preferred to propagate in longitudinal direction, i.e. longitudinal cracks, and drifting finally to the outer border of the sub-elements.

The remaining parts of the approximately 1.7 m long specimen 1 without any voltage-taps and heaters were further used to estimate the crack initiation threshold experimentally. For this purpose, it was necessary to inspect the transverse cross-section of different loaded samples. Consequently, the pieces were loaded according to the same procedure, as described in section 3.1.1. Subsequently, a transverse cross-section of the pressing area was prepared with the same procedure as the samples described above. Then, the region with the highest expected crack density, the centre upper part according to the above SEM analysis, was observed of every piece with an optical microscope (OM). No cracks in the mentioned region could be observed in samples loaded with less than 175 MPa.

Figure 4.12 shows a comparison of a strand from the same position in the centre part of the upper cable (upper row of strands) after the stress levels of 150 MPa, 175 MPa and 200 MPa. Sub-elements of the 150 MPa load case (figure 4.12(a) and (d)) are undamaged. The 175 MPa load case (figure 4.12(c) and 4.12(f)) can be considered as the threshold of crack initiation followed by the 200 MPa load case (figure 4.12(b) and (e)) with clearly ruptured sub-elements. Hence, the observed crack initiation after a specific stress correlates with the results of the particular I_c measurements presented in section 4.1.2.

The FEM analysis based on a model obtained by X-ray tomography gave an overview of the spatial stress distribution in the specimen [180]. An 1.6 times higher stress on the actual cables compared to the externally applied stress on the compound specimen could be estimated. Unfortunately, the resolution of the X-ray tomography only facilitates a FEM modelling on strand level. Consequently, the wires were simulated as a homogeneous material with an elastic modulus of 108 GPa.

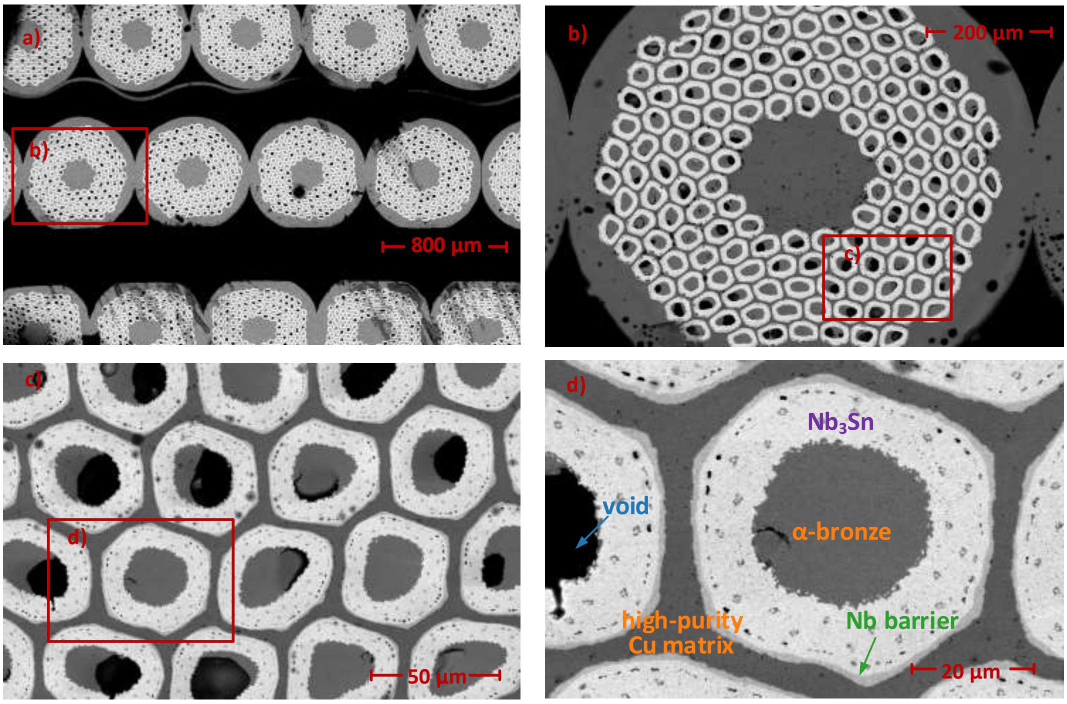

Figure 4.8: SEM micrographs of transverse cross-section of a non-loaded region of specimen 1 (centre part).

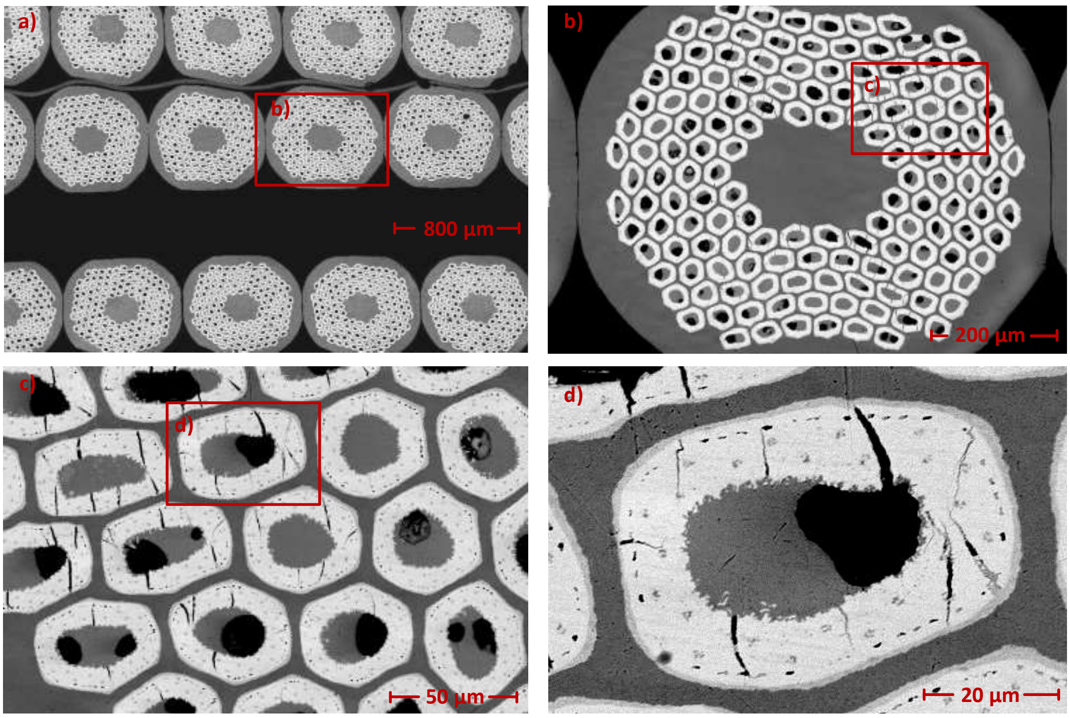

Figure 4.9: SEM micrographs of transverse cross-section of the 200 MPa loaded region of specimen 1 (centre part).

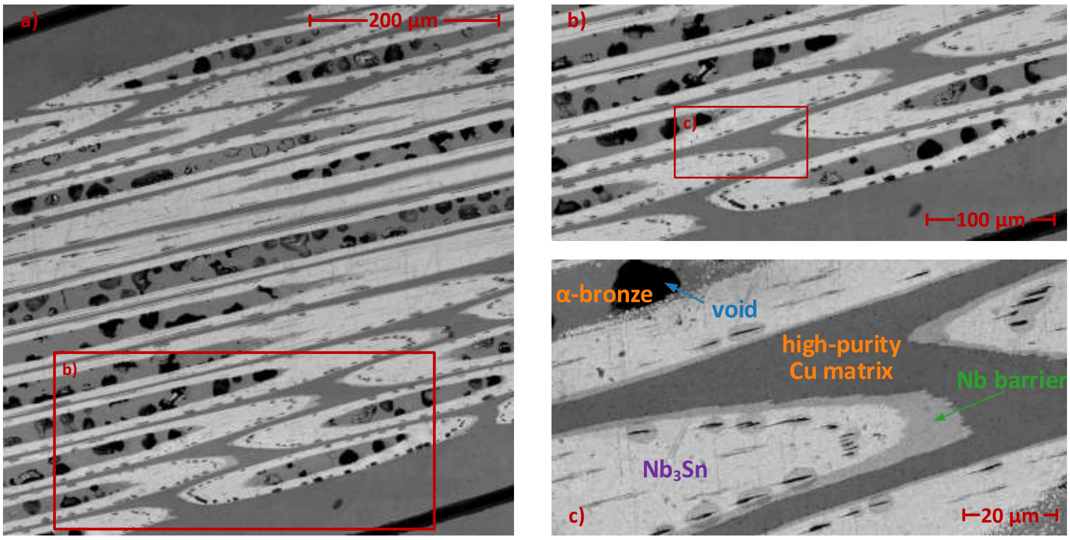

Figure 4.10: SEM micrographs of longitudinal cross-section of a non-loaded region of specimen 1 (centre of upper strand layer of upper cable).

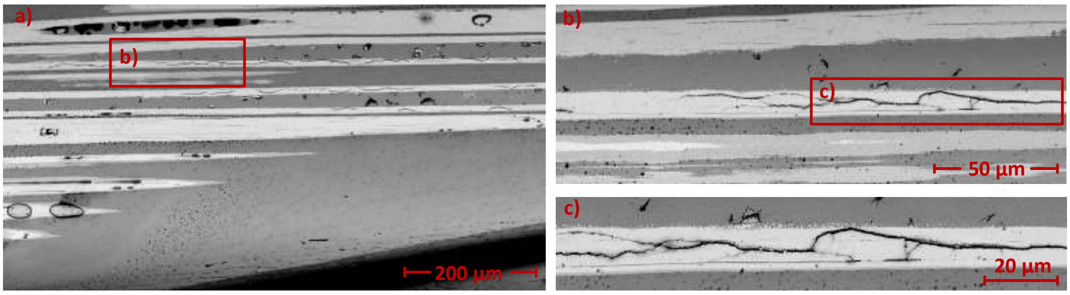

Figure 4.11: SEM micrographs of longitudinal cross-section of the 200 MPa loaded area of specimen 1 (centre of upper strand layer of upper cable).

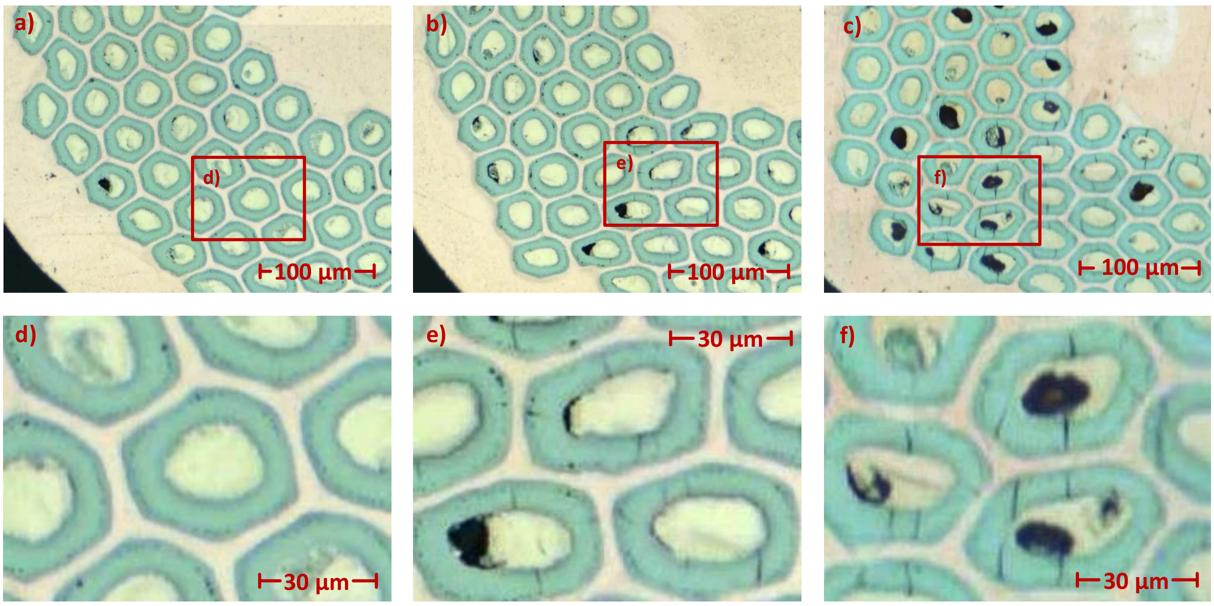

Figure 4.12: OM micrographs of transverse metallographic cross-section of the same located strand within remaining pieces of specimen 1 after exertion of **(a,d)** 150 MPa, **(b,e)** 175 MPa and **(c,f)** 200 MPa (centre of upper strand layer of upper cable). The first crack initiation could be detected at the 175 MPa loaded sample, which correlates with the I_c results.

4.1.4 Discussion

Critical current measurement and stress distribution

Specimen 1 and 2 showed a similar behaviour due to their equal mechanical arrangement. An irreversible degradation less than 5 % after a nominal load of 175 MPa directly applied on the bare impregnated cables at RT could be specified. This confirms the conventional limitation of 150 MPa for collaring a magnet coil with an additional margin. Nevertheless, local deviations from the coil dimensions due to the accepted production tolerances shall not be exposed to local stress above 175 MPa during the force-restraining procedure to ensure less than 5 % degradation. Considering that the currently produced 11 T dipole coils have a nominal length of 5.5 m, it is a technical challenge to monitor and control this requirement during collaring the coil and welding the shrinking cylinder.

Specimen 1 was additionally exposed to 200 MPa, which shows a tremendous degradation resulting in a very low n value in combination with a severe I_c degradation. This could be traced down independently of the applied field to current sharing, arising from confirmed fracture of the sub-elements. For specimen 2, the pressure steps were defined in smaller steps around the expected degradation. The particular results and hence the drop of performance in the range of 175 MPa confirmed the results of specimen 1, considering that they are having similar dimensions. No significant difference could be measured, due to the different sub-element size and additional C-shaped Mika insulation of the particular specimen.

In order to yield an outcome close to the situation in a coil during magnet assembly, impregnated Rutherford cables were chosen for the experiment. This allows creating a similar load case, as observed in full size loaded coil assemblies. Nevertheless, the homogeneous stress on the specimen's surface, which is also the aim for the collaring of the magnets, gives only an indirect statement about the intrinsic stress threshold on the superconducting sub-elements. The latter is finally accountable for the observed cracks and the crucial performance loss. The mechanical properties, e.g. Young's modulus, Poisson's ratio and yield strength, of

- the relatively soft epoxy resin and additional insulation layers,
- the annealed copper stabiliser,

as well as the dimensional properties of the composite compound, such as

- the cable configuration,

influence mainly the relationship between the applied external stress on the surface and the local stress on the sub-elements. The mentioned FEM analysis of F. Wolf *et al.* [180] correlates the stress distribution with the crack pattern, but unfortunately could not be used to evaluate the decisive stress on the sub-elements. Additional the determination of the material parameters are investigated within the FCC 16 T dipole programme [141, 142, 181] and HL-LHC project [40, 131].

Strain caused degradation due to the residual stress due to the resulting from the plastic deformations of the soft copper matrix beneath the crack initiation level of 175 MPa could not be clarified unequivocally based on the presented results [55]. A similar experiment performed by B. Bordini *et al.* [26] applying transverse stress on cables during operation at 4.3 K revealed a significant field dependency, which is an evidence for strain effects. A small degradation at 90 MPa and a 24 % degradation of the quench current at 11.6 T and 155 MPa was measured in this experiment. Unfortunately, it does not provide information about the irreversible degradation at low temperature.

It also has to be taken into account, for comparing the results with other publications, that the mechanical properties of Nb_3Sn composite compounds at RT and low temperature differ. Hence, the performance loss of Nb_3Sn cables caused by stress at RT differs from that caused by stress at low temperatures [118].

Specimen 3 was additionally tested with another mechanical structure, which makes it difficult to compare with specimen 1 and 2. By adding the titanium bars in a sandwich arrangement, the spatial stress situation within the specimen is changed, thus also on the cables. The solid titanium bars homogenise the stress distribution, which made the Polyimide foils dispensable and the Prescale films gave only a little estimation about the situation on the epoxy resin or the cable. The applied force on the specimen in the XZ-plane is distributed over a broader range than the actual pressing die profile, and a lower average stress on the cables within a larger area at equal force can be assumed. The latter may be the reason for the lower sensitivity of stress with a degradation less than 5 % after a nominal stress of 240 MPa at RT.

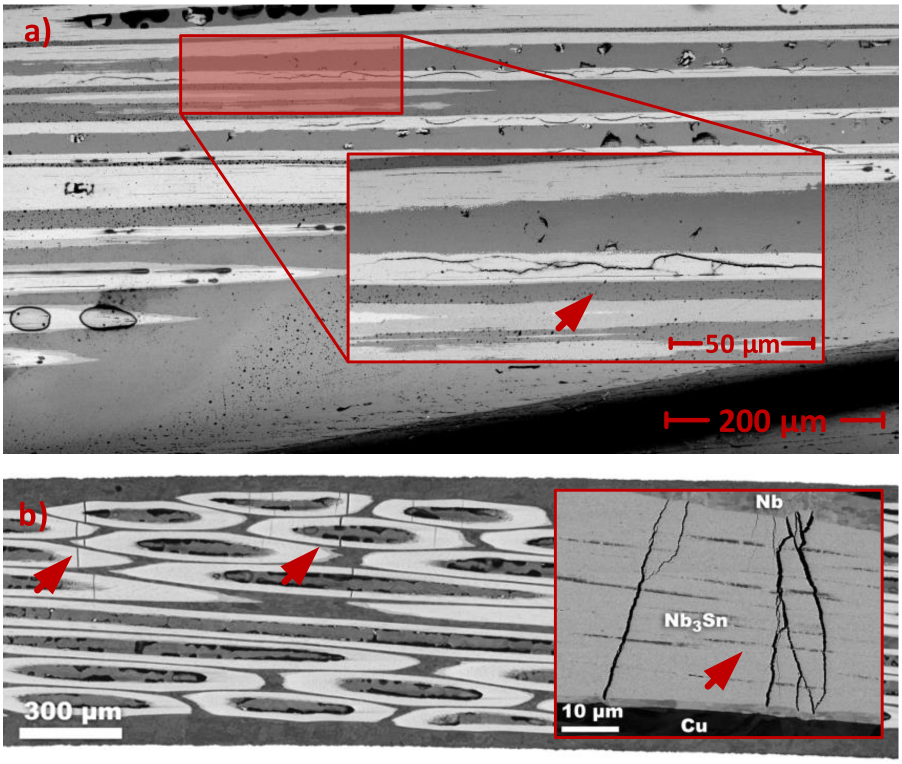

Figure 4.13: Comparison of SEM micrographs. **(a)** Longitudinal cracks caused by transverse stress in impregnated Rutherford cable double stack of RRP wires. **(b)** Transverse cracks caused by bending stress of a single RRP wire (Information taken from reference [101, p.83-84] with marks by the present author).

Nevertheless, the high requirements of cable tests with currents above 10 kA restricted the investigation, so that finally only the critical current at an electrical field criterion of $E_c = 3\,\mu\mathrm{V\,m^{-1}}$ could be used unequivocally. This was also the trigger to investigate the degradation process on single wires, which is described in section 4.2.

Microscopic investigation

The microscopic investigations of specimen 1 revealed cracks in the superconducting sub-elements. Furthermore, their spatial distribution within the specimen could be inspected. They can be assumed to be the main reason for I_c degradation, particularly due to the following stress study (cf. figure 4.12). The transverse cross-section showed information about the crack distribution. This also gave an estimation of the stress distribution within the cable and the wire. In general, the systematic crack distribution in the observed region was overlaid by statistical variation due to fabrication uncertainties, e.g.

- the hemming fold of the core,
- the gap between the upper and lower row of strands due to impregnation,
- the pre-reacted deformation on the cable edges due to cabling and
- Kirkendall voids,

which makes a local stress analysis within the composite compound challenging. Voids are encouraging cracks, due to the stress concentration at the cavities' surface. One is aware of this optimisation potential regarding mechanical improvements by the RHT, which was further investigated by e.g. C. Scheuerlein *et al.* [138], C. Barth *et al.* [12] and Y. Zhai *et al.* [185].

The longitudinal cross-section revealed the typical shape of the cracks, which are mostly in longitudinal direction and drifting to the border of the sub-elements. They differ from cracks generated by bending or tensile stress, which cause transverse cracks in sub-elements published, for instance, by M. C. Jewell *et al.* [81, 101] and C. Sanabria *et al.* [134]. The longitudinal shape of the inspected cracks formed in the most cases only a shrinkage of the effective superconducting cross-section and not an entire interruption of the superconducting material in transport current direction. Figure 4.13 clarifies this matter by comparing the presented results with the past investigation mentioned above.

Table 4.7: Results of the load application of all wires used in this investigation by the mean of the projected area $A_{proj} = (44 \times 0.7)\,\mathrm{mm}^2$.

Nominal			Transport	Magnetisation	Microscopy
σ_{nom} (MPa)	$F_{nom}{}'$ (kN m^{-1})	F_{nom} (kN)	$\sigma_{LC,\Sigma}$ (MPa)	$\sigma_{LC,\Sigma}$ (MPa)	$\sigma_{LC,\Sigma}$ (MPa)
25	17.50	0.77	29.19	26.55	27.11
50	35.00	1.54	50.90	50.22	50.97
75	52.50	2.31	74.94	75.54	76.43
100	70.00	3.08	100.07	99.96	101.06
112.5	78.75	3.47	113.57	112.53	–
125	87.50	3.85	125.49	125.32	125.74
150	105.00	4.62	150.97	150.55	150.80
200	140.00	6.16	–	199.70	200.09

Summing up the evidences, i.e. the presence of cracks and the absence of a measurable field-dependency, rise the assumption that the degradation process is purely a mechanical effect. Consequently, this affects the thermal stability of the cable negatively. The applied stress at RT influences the superconducting performance of the cable indirectly, due to mechanical fractures of the sub-elements. The verified cracks evoke an allocation of the transport current from the superconductor to the copper stabiliser, which causes dissipation and hence instability. This behaviour, so-called current sharing, can further quantitatively be modelled by an electrical network of a normal- and superconducting path to reach a prediction of the stability loss, e.g. as introduced by Z. J. J. Stekley *et al.* [154].

4.2 Results of wire investigations

This section presents the results of the wire investigations, which were launched after the completion of the measurements of cable specimen 1. It consists of three supplementary parts:

- the transport current measurements with the self-designed NearT_c setup,
- the magnetisation measurements with a SQUID magnetometer and
- the microscopic investigations.

They were performed to identify the cause and effect of a specific amount of applied transverse stress at RT on the superconducting Nb_3Sn, as a simplified case of the cable experiment. Furthermore, the feasibility of the used NearT_c concept is assessed on the base of the presented data.

4.2.1 Stress exertion

The stresses on the specimens used for these investigations are listed in table 4.7. In order to create a better comparison with the cable results in section 4.1, the nominal pressure $\sigma_{nom} = F_{nom}/A_{proj}$ is defined as the force divided by the central longitudinal cross-section $A_{proj} = (44 \times 0.7)\,\mathrm{mm}^2$ with the pressing die length $l = 44\,\mathrm{mm}$ and the nominal wire diameter of 0.7 mm. Additional, the length-related force $F_{nom}{}' = F_{nom}/l$ is listed together with the absolute nominal force F_{nom}. The right part of the table lists the evaluated stress $\sigma_{LC,\Sigma}$ of every specimen used in the corresponding sub-studies. The high error of the 25 MPa load case is reasoned by the fact that values below 1 kN are close to the lower limit of the hydraulic system. Expect from this, only minor errors of the actual stress from the nominal stress smaller than 1.9 % could be observed. This reasons that the nominal values were used to present the superconducting results in the next sections.

The transport current measurements were stopped after a nominal load of 150 MPa applied at RT. The microscopic study was performed before the transport and magnetisation measurements. The additional load case of 112.5 MPa was inserted afterwards. The results showed that load case was not essential for the microscopic characterisation. Thus, it was decided to disregard this case in the microscopic investigation. Due to the restriction, explained in section 3.3, the stresses for the transport current measurement were always performed on the same specimen. The magnetisation and microscopic observations were performed for every stress level on a particular specimen of the same RHT, which enabled also the metallographic preparation in a single embedment.

Although the external force on the wire was measured, it gives only indirect information on the stress within the wire. In terms of contact mechanics, the presented situation can be idealised two-dimensionally as the touch of a confirming half space, the pressing die, with a non-conforming cycle, the multi-filamentary wire, at a single point. This leads to a stress concentration at the contact point and can be identified as a Hertzian contact problem [78, 175].

Accordingly, the non-linear stress distribution, especially the local maxima, within the wire is significantly higher than the measured external force. Furthermore, the inhomogeneity of the idealised cycle due to the sub-elements, consisting of other materials like Nb_3Sn and α-bronze, have to be considered. The FEM simulation of P. Ebermann *et al.* [47] provides further information concerning this matter.

4.2.2 Transport current measurements with the NearT_c setup

Feasibility study of measurement concept and experimental setup

The chosen principle, characterising the critical current of Nb_3Sn wires in self-field close to the critical temperature, could be validated successfully by conductive cooling of the wire mounted on the base of a liquid helium heat exchanger.

The crucial experimental temperature stability was appropriate to measure $I_c(T)$ reliably at the chosen temperature steps of 100 mK and $T_{cs}(I)$ with the chosen current levels. The data obtained to characterise the wire after a certain stress level is shown in figure 4.14. As shown in figure 4.14(a), typically five determination of the critical current $I_c(T)$ at a defined set temperature T were performed. This was done to increase the reliability of the measurement, which was influenced especially at the beginning of the work by temperature instabilities. It was also the trigger to establish current-sharing temperature measurements, illustrated in figure 4.14(b). The temperature-depending disturbances on the measured voltage $V(t)$ are inherently compensated by the analysis, i.e. plot of $V(t)$ over T obtained by the recording of $T(t)$. This led to higher repeatability in contrast to the $V(I)$ curves of figure 4.14(a), so that typically only three repetitions were performed for a particular $T_{cs}(I)$.

Subsequently, the results of both measurement types are plotted over the measured temperature in figure 4.15. A fit approximation $I_c(T) \propto [1 - (T/T_c)^{1.5}]^{\eta}$ with $\eta = 2.5$, derived from the USL [55], is added to the plot and shows a good agreement.

The control accuracy of the sample temperature T_s could be established within a band of ±10 mK to ±20 mK at roughly 13 K with the mass flow controller and the heat exchanger on the experimental platform. It was finally improved to a band of ±2.5 mK to ±5 mK close to T_c by using the feed-back control with heaters on both current connector plates.

Within the feasibility check, the profile of the sample temperature was recorded, and their AC parts are shown in figure 4.16 to assess the error. The blue and orange signals were recorded before and after enabling the temperature control, respectively. The periodicity of the signals is evident, which could be traced down to flow-driven thermal instabilities in the helium tubes of the system. In general, they can occur in tubes of cryogenic systems having a temperature gradient and containing helium, e.g. from the dewar vessel filled with liquid helium (4.3 K) to the recovery line (approximately 300 K) in the present case. The density ratio of liquid and vapour helium at the boiling point is 7.4 and the density ratio of liquid helium and gaseous helium at 0 °C and atmospheric pressure is 698.6 [54]. The tubes of the setup comprised an unavoidable two-phase helium flow, due to the heat load generated by the required temperature of the sample platform range of 15 K to 20 K.

Considering the mentioned different density of helium in the two present thermodynamic phases, the pressure and consequently the temperature in the tubes were changing periodically with a noticeable magnitude.

These oscillations were reduced preventively by the pressure regulator of the dewar vessel with a nominal pressure of 155 mbar (gauge), as indicated in figure 3.21. The frequency of the fundamental oscillation was similar at every measurement, i.e. 20 mHz to 40 mHz. The fundamental oscillation and the corresponding harmonics are determined primarily by the setup-depending properties, e.g. length and diameter of the transfer line and helium tubes inside the cryostat.

On the basis of an around 5 min long capture of the recorded temperature signals with a sampling time of 240 ms, a Power Spectral Density (PSD) estimate was performed. This was done by using the Welch's method [176] and applying a Hann window function to reduce the spectral leakage of the discrete Fourier transformation. Figure 4.16 shows the sample temperature including their spectral distribution with and without temperature controller. It is clear that the active temperature control on the connector plates reduced primarily low-frequency oscillations, which is discussed further in section 4.2.5.

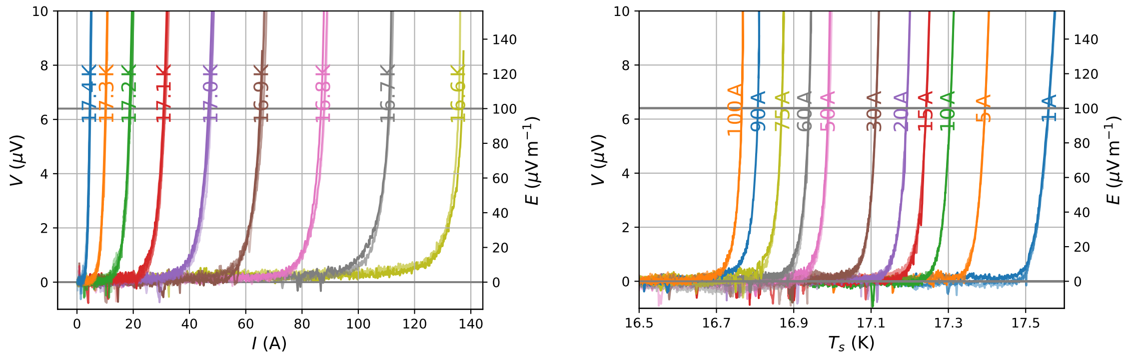

(a) **(b)**

Figure 4.14: Measurements performed with the NearT_c setup to characterise the specimen after a specific applied stress at RT. **(a)** $V(I)$ curves at certain nominal set temperature levels and **(b)** $V(T)$ curves during a certain nominal current of the wire specimen. Every condition was measured at least three times and the results are plotted in the same colour overlapped in different brightness. A clear and repeatable difference can be seen between the chosen nominal set temperature and current levels for the $V(I)$ and $V(T)$ recordings, respectively (cf. labels in the plot).

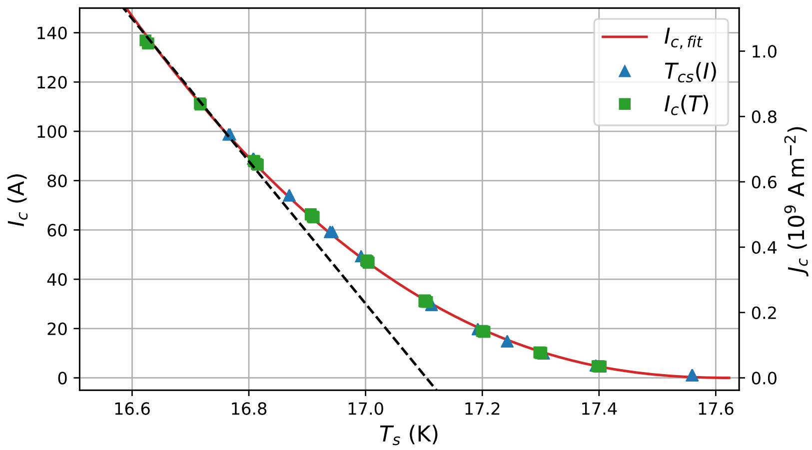

Figure 4.15: Evaluated $I_c(T)$ and $T_{cs}(I)$ of recordings shown in figure 4.14 as a function of the measured temperature with the fit approximation function $I_c(T) \propto [1-(T/T_c)^{1.5}]^{\eta}$ with $\eta = 2.5$. The black dashed line represents the slope $-\mathrm{d}I_c/\mathrm{d}T$ based on the fit approximation in the upper operation range of 90 A to 150 A.

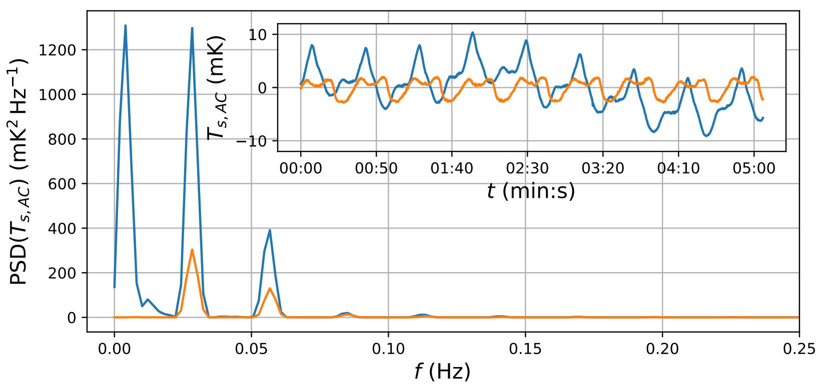

Figure 4.16: Observation of the sample temperature stability. The small plot shows the AC component of $T_s(t)$ without (blue) and with (orange) temperature controller with a sampling time T_a = 240 ms. The recording without temperature controller had a DC component of 12.614 K and a peak-to-peak value of 20 mK. The recording with the temperature controller had a DC component of 16.500 K, the nominal set temperature, and a peak-to-peak value of 5 mK. The larger plot shows the power spectral density of the corresponding time signals in the small plot. The active temperature regulation intends a low-frequency rejection primarily.

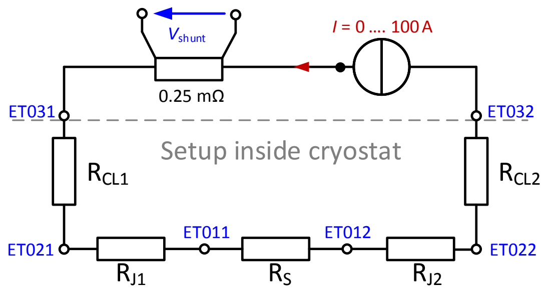

Table 4.8: Schematics of the electrical measurement circuit for the estimation of the Joule heating. The used voltage-taps can be checked in the PID (cf. figure 3.21).

Table 4.9: Results of the system identification test with $T_s = 15.5\,\text{K}$

$R_{J,x}$	$6\,\mu\Omega$
$R_{CL,x}$	$767\,\mu\Omega$
$P_J(I = 100\,\text{A})$	$120\,\text{mW}$
$P_\Sigma(I = 100\,\text{A})$	$15.5\,\text{W}$

The average liquid helium consumption was in the order of $7\,\text{L}\,\text{h}^{-1}$. A system test with $T_s = 15.5\,\text{K}$ and a current up to $I = 100\,\text{A}$ was used to estimate the electrical parameter of the measurement circuit. Due to the additional voltage-taps on the top and bottom end of every current lead (cf. figure 3.21), following voltages

- $V_1 = \text{ET011} - \text{ET012}$,
- $V_2 = \text{ET021} - \text{ET022}$ and
- $V_3 = \text{ET031} - \text{ET032}$

could be defined, illustrated in figure 4.8. Assuming a symmetrical structure, the resistance of the low-temperature junctions to the specimen $R_{Jx} = {}^{V_2 - V_1}/_{2I}$, and the resistance of current leads $R_{CLx} = {}^{V_3 - V_2}/_{2I}$, with x for the left and right part, were acquired. The resistance R_{Jx} represent the soldering joint of the sample and the contact resistance from the current lead to the sample holder implemented by clamping with indium foils. The evaluated Joule dissipation $P_J = (V_2 - V_1)I$ on the sample holder and the entire setup $P_\Sigma = (V_3 - V_1)I$ were also evaluated and summarised in table 4.9. The additional heating of a few Watt compared to the current lead estimation is reasoned on several modifications, which were performed before the first commissioning. First, the installation was finally performed with copper having a lower RRR. Second, bending of the copper rods was necessary during construction, which also affects the RRR negatively. It represents the entire Joule heating measured from the outside of the cryostat, which also includes additional contact resistances. The thermal analysis of the setup was not further focus of the investigation.

The sample temperature T_s was defined as the arithmetic mean of the connector plates temperatures T_{left} and T_{right}, which were feed-back controlled independently by using the mounted heaters and temperature sensors (cf. figure 3.15). The temperature along the sample was not monitored and a linear temperature profile between the two electrical connections of the sample was assumed. This rose the suspicion of undetectable accumulation of heat energy in this adiabatic system and consequently, corruption of the measurements results.

A hidden heat-up of the sample would influence the temperature-depending critical current, which holds indirect information on the sample temperature. The measurements at the same condition in figure 4.14 were performed repeatedly several times in sequence and no iterative decreasing tendency of I_c could be observed with the chosen settings. This proved indirectly that no hidden heat accumulation occurs. Even repetitive recording of $V(T)$ curves for T_{cs}, which implied a necessary temperature rise of up to 1.5 K, did not show iterative heating of the sample, i.e. decreasing tendency of T_{cs}.

Measurement results

After the feasibility check of the measurement principle, the specimen characterisation after every stress application at RT was performed, according to the elaborated procedure explained in the above section.

The summary of the high-current results can be seen in the $I_c(T)$ diagram in figure 4.17. The rectangles and the triangles represent the results of I_c and T_{cs} measurements, respectively, whereby the evaluated actual temperature at the respective transition was used. A fit approximation $I_c(T) \propto [1 - ({}^{T}/_{T_c})^{1.5}]^\eta$ with $\eta = 2.5$ was computed for every pressure step and added to the plot as a solid line. The slope $-{}^{dI_c}/_{dT}$ between 90 A and 150 A was typically in the range of 0.29 to 0.05 A mK^{-1}, as listed in table 4.10. Figure 4.18 presents the critical current and the current-sharing temperature as a function of the nominal applied stress at RT, as extracted from figure 4.17.

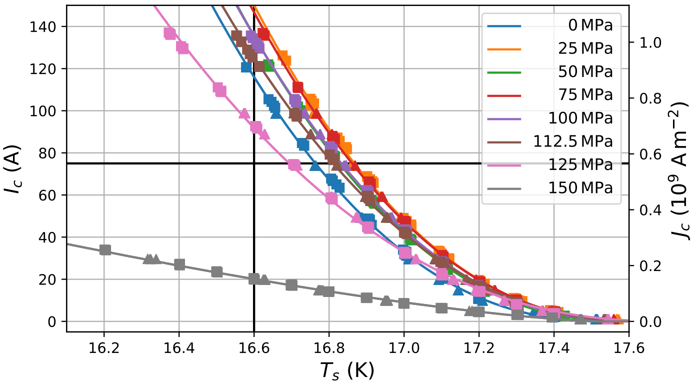

Figure 4.17: Results of high-current transport measurements in the $I(T)$ diagram. Critical current I_c (rectangles) and current-sharing temperature T_{cs} (triangles) summarised with corresponding fit approximations (solid line in corresponding colour). Values along the black lines are extracted in figure 4.18.

Table 4.10: Results of high-current transport measurement. Slope $-dI_c/dT$ on the base of the respective fit approximation between 90 A and 150 A in figure 4.17.

σ_{nom} (MPa)	$-dI_c/dT$ (A mK^{-1})
0	0.28
25	0.29
50	0.29
75	0.29
100	0.28
112.5	0.26
125	0.22
150	0.05

The wire performance improved slightly until 75 MPa, followed by degradation starting from 100 MPa. The obtained degradation threshold at 100 MPa correlates with the crack initiation at 100 MPa elaborated in section 4.2.4. Due to high I_c degradation, the measurements were stopped after 150 MPa.

In order to offer a comparison of the recorded data after a particular stress at RT, figure 4.19 shows an excerpt of the recordings. Three measured curves after every pressure step were plotted in the same colour and different brightness. The $V(I)$ curves for the I_c evaluation are partly influenced by temporal imperfect temperature stabilisation, which can also be seen in the more sensitive n values plotted in figure 4.20. The points and the error-bars represent the arithmetic mean values and the standard deviation of typically three to five measurements, respectively. However, the decreasing tendency of the n value by rising applied stress is recognisable. Additionally, the n value over the measured temperature range is plotted, which shows a decrease with increasing temperature.

Figure 4.21 and table 4.11 summarise the results of the low-resistance measurements. The critical temperature improves after the application of 25 MPa transverse pressure until the wire got heavily damaged after 150 MPa. The RRR decreased after 100 MPa, due to the plastic deformation of the copper matrix.

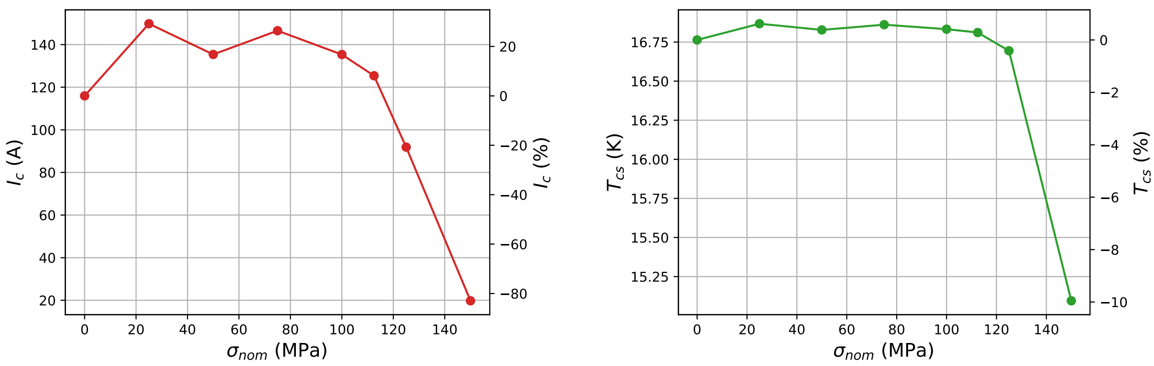

(a) **(b)**

Figure 4.18: Results of the transport current measurements. **(a)** Critical current I_c as a function of the applied stress σ_{nom} at RT during $T = 16.6$ K. **(b)** Current-sharing temperature T_{cs} as a function of the nominal applied stress σ_{nom} at RT during $I = 75$ A.

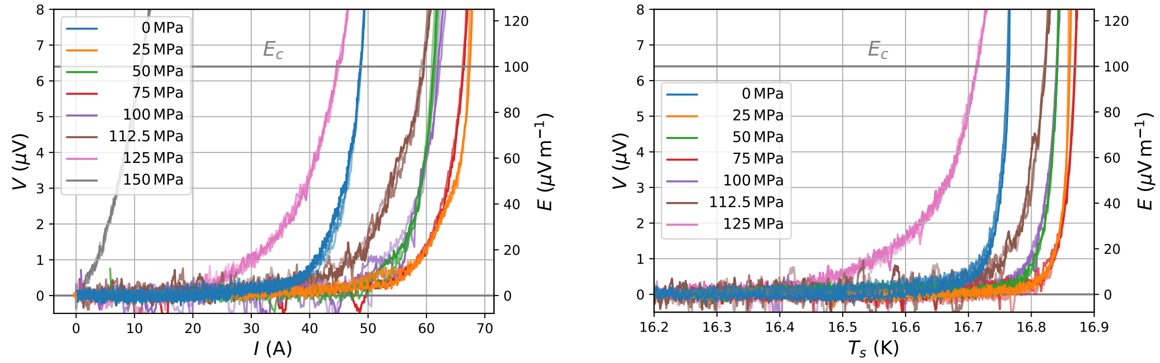

(a) **(b)**

Figure 4.19: Excerpt of the transport current measurements. **(a)** Typical $V(I)$ curves at $T = 16.9$ K. **(b)** Typical $V(T)$ curves at $I = 75$ A. A repetition of three measurements at the same condition is plotted in the same colour overlapped in different brightness.

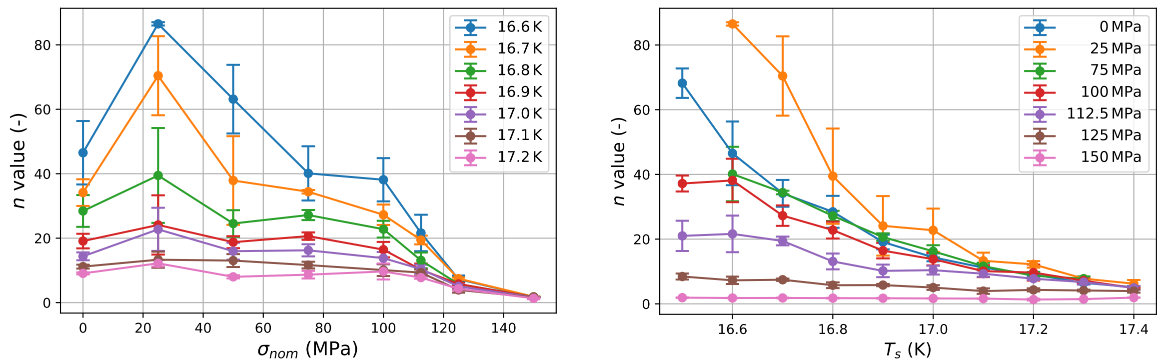

(a) **(b)**

Figure 4.20: Results of the n value analysis of the $V(I)$ curves. **(a)** n value as a function of the nominal applied stress σ_{nom} at RT. **(b)** n value as a function of the sample temperature.

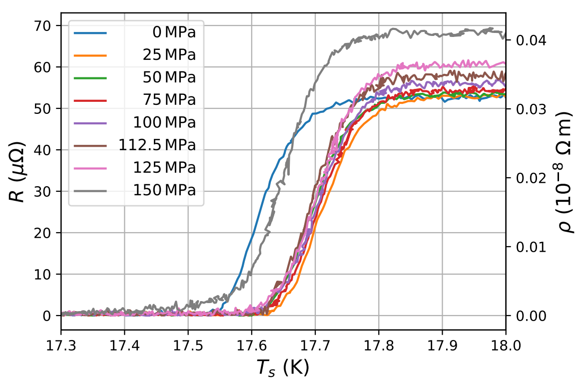

Figure 4.21: Results of low-resistance measurements for critical temperature T_{c} and Residual Resistance Ratio RRR evaluation.

Table 4.11: Results of low-resistance measurements: T_{c} and $RRR := \rho(293\,\text{K})/\rho(19\,\text{K})$.

σ_{nom} (MPa)	$T_{\text{c,midpoint}}$ (K)	ΔT_{c} (K)	RRR (-)
0	17.62	0.17	97.9
25	17.72	0.18	97.4
50	17.70	0.17	97.4
75	17.71	0.16	97.5
100	17.71	0.17	92.5
112.5	17.70	0.16	92.5
125	17.71	0.18	87.0
150	17.65	0.23	76.2

4.2.3 Magnetisation measurements

The magnetisation measurements were performed with samples exposed to transverse stress at RT up to 200 MPa, and the stress after each step on the respective sample is listed in table 4.7.

Figure 4.22 summarises the results of the measurements at 4.2 K. It represents the behaviour at a common temperature range used for superconducting magnets, the atmospheric boiling point of helium, far below T_c, i.e. $T/T_{c,Nb_3Sn} \approx 0.2$. Figure 4.22(a) gives an overview of $J_c(B, 4.2\,K)$ calculated from the irreversible magnetisation $m_{irr}(B, 4.2\,K)$, by using the relation derived in section 3.4.1. The corresponding magnetisation loops are shown in the small plot and their abnormal fluctuations at low fields can be traced back to flux jumps. They show an unstable behaviour occurring during operation due to local disturbances resulting in an avalanche of depinned vortices.

This well-known phenomenon was not a further objective of the work and hence not taken into consideration. Figure 4.22(b) extracts the obtained critical current density out of the stable measurement region at $B = 6\,T$, as a function of the stress applied on the respective sample. A degradation threshold at 100 MPa can be clearly recognised and correlates with the crack initiation threshold observed by the metallographic investigation.

Figure 4.23 shows the results of the same samples and measurement procedure but at a sample temperature of $T = 16\,K$, i.e. $T/T_{c,Nb_3Sn} \approx 0.9$. The measured magnetic moment above 2 T approaches the noise level of the magnetometer, which is in the range of $5 \cdot 10^{-9}\,A\,m^2$. When speaking about disturbances, flux jumps in the SQUID sensor can not be excluded, which are resulting in a shift of the measured flux by the magnetic flux quantum Φ_0. Figure 4.23(b) is an extraction of the stable measurement range at $B = 0.5\,T$. Except for the 25 MPa case, these results show an improvement at low-stress levels and degradation at stresses above 100 MPa, which confirms the behaviour obtained by the transport current measurements.

In summary, the results reflect qualitatively the tendency obtained by the transport current measurements. Besides, it can be recognised, that the effect is exaggerated at the lower temperature, i.e. in the presented case at $T = 16\,K$.

Additional, the critical current density at self-field in the range of 5 K to 18 K was assessed, shown in figure 4.24. It represents a close situation to the performed transport current measurements near T_c in self-field. Except for the 25 MPa case, the results confirm qualitatively the performance improvement of samples, loaded with a stress below the crack threshold, and the degradation of samples, applied with stress above the observed crack initiation.

The analysis of T_c based on the AC susceptibility measurements, illustrated in figure 4.25, also shows an improvement in the low-stress range, where no cracks could be found. According to the unified scaling law $J_c(B, T)$ by J. W. Ekin [55], the critical current density is changing due to variations of T_c, which generates a shift of the function along the T-axis.

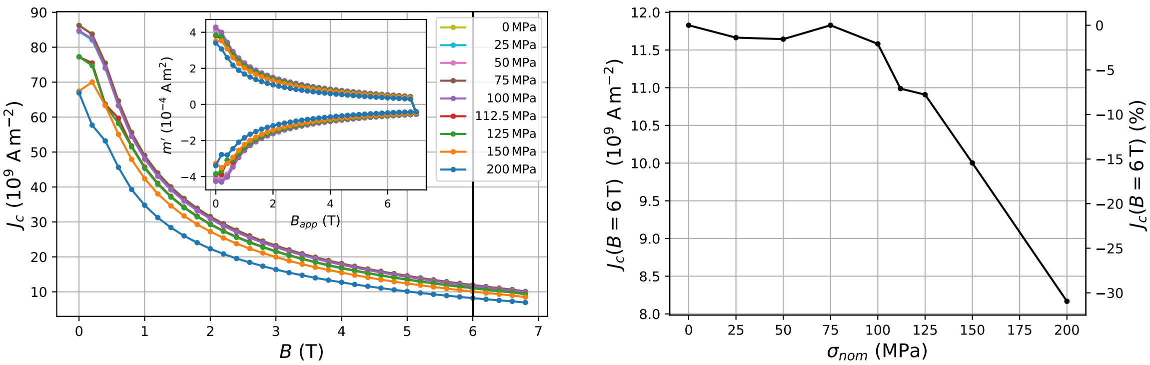

(a) (b)

Figure 4.22: Results of the magnetisation measurements at $T = 4.2\,K$. **(a)** $J_c(B, 4.2\,K)$ of loaded and non-loaded samples by evaluating the irreversible magnetisation m_{irr} out of the magnetisation loops m', shown in the small plot. **(b)** Critical current density $J_c(6\,T, 4.2\,K)$ as a function of the applied stress σ_{nom} at RT extracted from (a).

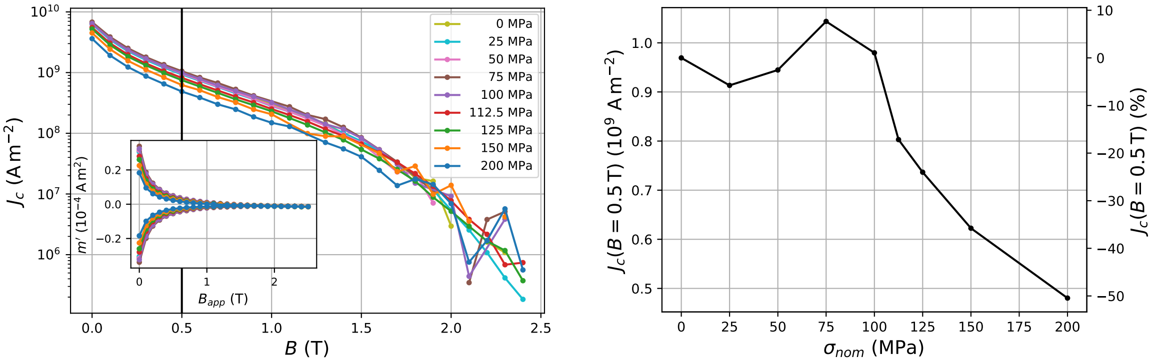

(a) **(b)**

Figure 4.23: Results of the magnetisation measurements at $T = 16\,\text{K}$. **(a)** $J_c(B, 16\,\text{K})$ of loaded and non-loaded samples by evaluating the irreversible magnetisation m_{irr} out of the magnetisation loops m', shown in the small plot. **(b)** Critical current density $J_c(0.5\,\text{T}, 16\,\text{K})$ as a function of the applied stress σ_{nom} at RT extracted from (a).

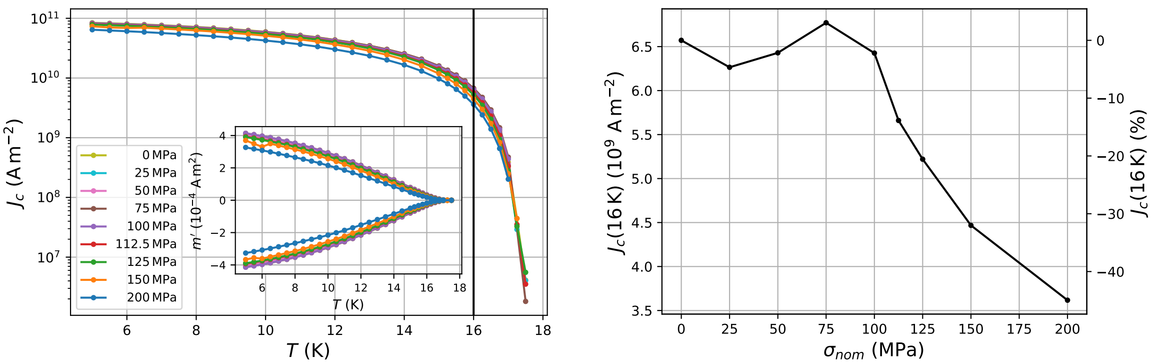

(a) **(b)**

Figure 4.24: Results of the magnetisation measurements at self-field. **(a)** $J_c(B_{\text{self}}, T)$ of loaded and non-loaded samples by evaluating the irreversible magnetisation m_{irr} out of the magnetisation loops m', shown in small plot. **(b)** Critical current density $J_c(B_{\text{self}}, 16\,\text{K})$ as a function of the applied stress σ_{nom} at RT extracted from (a).

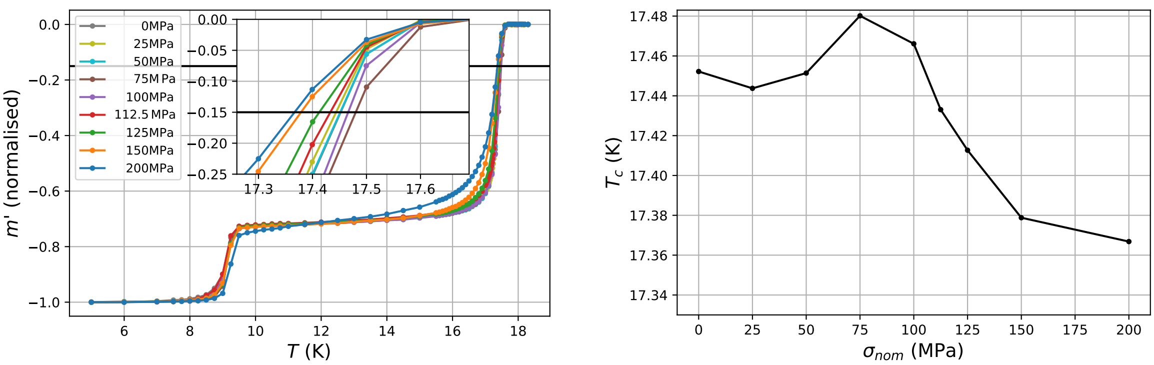

(a) **(b)**

Figure 4.25: Results of the AC susceptibility measurements. **(a)** Normalised AC magnetic moment m' of loaded and non-loaded samples with a magnified view of the area used for the criterion in the small plot. **(b)** Critical temperature T_c as a function of the applied stress σ_{nom} at RT extracted from (a) by using the threshold criterion at ${m'}_{\text{thr,norm}} = 0.15$.

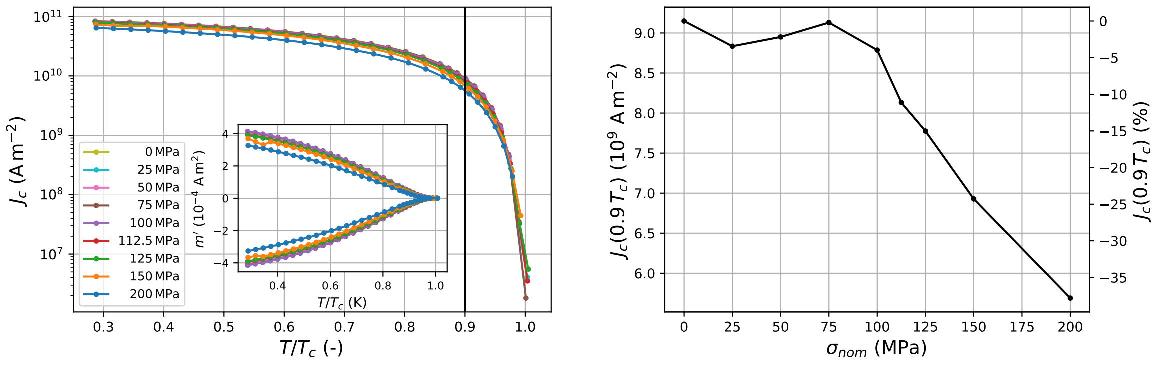

(a) **(b)**

Figure 4.26: Normalised results of the magnetisation measurements at self-field. **(a)** $J_c(B_{self}, t)$ of loaded and non-loaded samples over the reduced temperature $t = T/T_c$. The critical current, shown in figure 4.24, is plotted as a function of t by using the T_c results, shown in figure 4.25. **(b)** Critical current density $J_c(B_{self}, t = 0.9)$ as a function of the applied stress σ_{nom} at RT extracted from (a).

Due to the local value of dI_c/dT, the impact is stronger near T_c in contrast to the common operation range of 4.2 K and 1.9 K. Consequently, the results of the self-field measurements were normalised to the reduced temperature $t = T/T_c$ and are shown in figure 4.26. In order to derive t of every sample, the results of T_c shown figure 4.25 were used. It is recognisable that the effect on the corrected $J_c(B_{self}, t)$ occurs weaker, as obtained at $T = 4.2$ K.

Subsequently after the analysis of T_c, the temperature dependence of the upper critical field $B_{c2}(T)$ of a reference wire as well as samples after applying transverse pressure of 75 MPa, 100 MPa and 200 MPa were investigated. Figure 4.27 and table 4.12 summarise the results by applying the WHH expression, as explained in section 3.4.2. They also improved at 75 MPa and 100 MPa followed by a decrease, leading to a reduction of approximately 8.5 % at 200 MPa. Figure 4.27 shows beside the measured data (crosses) the respective fit approximation (line), which extrapolates $B_{c2}(T)$ outside the measurement range, i.e. 7 T. For the fit function, the common expression

$$B_{c2}(T) = B_{c2}(0)\left[1 - \left(\frac{T}{{T_c}^*}\right)^{\nu}\right] \tag{4.1}$$

with ν as a fitting parameter was used. $B_{c2}(0)$ was calculated from the WHH expression and the effective critical current ${T_c}^*$, obtained by extrapolation the slope $(dB_{c2}/dT)_{T={T_c}^*}$ to the T-axis. Equation 4.1 is commonly used in the literature and the usually reported value ν is in the order of 1.5 [55]. For the present data, the parameter ν was in the range of 1.50 to 1.52.

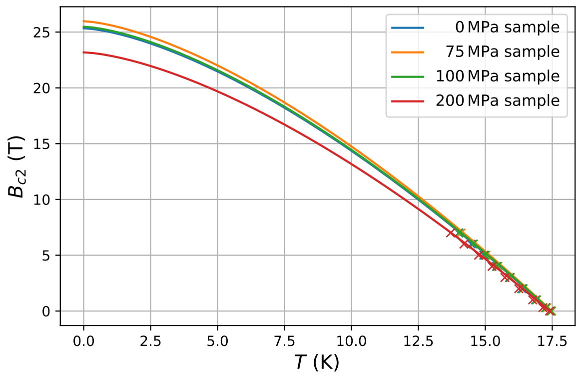

Figure 4.27: Upper critical field $B_{c2}(T)$ as a function of the temperature T (solid line) based on the in-field T_c analysis (crosses) of 0, 75, 100 and 200 MPa loaded samples. The crosses refer to the peak in the imaginary part of the AC susceptibility.

Table 4.12: Results of the upper critical field evaluated by using the WHH expression.

σ_{nom} (MPa)	$\left(\frac{dB_{c2}}{dT}\right)_{T={T_c}^*}$ (K T^{-1})	${T_c}^*$ (K)	$B_{c2}(0)$ (T)	(-)
0	-2.11	17.31	25.34	–
75	-2.16	17.33	25.97	1.03
100	-2.12	17.34	25.48	1.01
200	-1.93	17.30	23.18	0.92

Table 4.13: Plastic deformation and crack formation obtained from SEM analysis. Cracks with a typical width down to 0.5 µm are considered in the presented inspection.

σ_{nom} (MPa)	transverse CS 1 h_{wire} (μm)	w_{wire} (μm)	$n_{damaged}$ (-)	transverse CS 2 h_{wire} (μm)	w_{wire} (μm)	$n_{damaged}$ (-)	Comment
0	710	710	0	–	–	–	Reacted
25	708	708	0	–	–	–	
50	706	713	0	703	716	0	
75	696	711	0	696	720	0	
100	694	720	4	693	721	0	
125	674	733	41	697	730	49	
150	653	736	65	656	740	59	
175	610	760	82	613	766	80	
200	589	794	88	585	700	86	
0	702	702	–	–	–	–	Non-reacted
200	654	716	–	–	–	–	

4.2.4 Microscopic investigations

Besides the transport current and magnetisation measurements, a metallographic investigation campaign was launched. It delivers additional microscopic information to determine the cause of the corresponding macroscopic behaviour. Therefore wires were exposed to transverse stress at RT according to table 4.7.

The achieved microscopic information supports the results observed at impregnated Rutherford cables loaded with transverse stress at RT reported in section 4.1. The characteristic spatial X-shape crack distribution in the transverse cross-sections could be observed as well. The crack shape, observed in the longitudinal cross-section, was also in longitudinal direction.

Figure 4.28 gives an overview of the crack distribution and an indication of the stress formation, which is similar to the observed crack propagation in a Rutherford cable depicted figure 4.9(b). The first plastic deformation of the copper matrix was observed after 50 MPa, and the first cracks in the Nb_3Sn sub-elements could be detected after a load of 100 MPa. A quantitative evaluation of the two investigated transverse cross-sections at each stress level is given in table 4.13. It comprises the remaining height w_{wire} and width w_{wire} of the wire as well as the number of damaged sub-elements labelled with $n_{damaged}$.

Considering that the sub-elements are twisted for electrodynamic reasons, every sub-element is passing the cracked region within the pitch length of nominal 14 mm (cf. table 2.1). This further implies that the stress distribution in a specific cross-section on the hexagonal sub-element grid changes slightly depending on its orientation. Furthermore, it can be observed that voids promote cracks and cause a variation of the spatial distribution of the crack evolution.

For a comparison, data of a non-loaded non-reacted wire with a non-annealed copper matrix, used during the Rutherford cabling, and a loaded non-reacted wire were added to table 4.13. The deformation of the 200 MPa loaded non-reacted wire is comparable to the 150 MPa loaded reacted wire. This is an indicator that the annealed copper matrix after the RHT provides less mechanical stability for the fragile Nb_3Sn sub-elements.

The longitudinal cross-sections in figure 4.29 provide information about the shape of the cracks. Due to the intended tilt angular of the metallographic preparation, areas with almost no cracks, i.e. horizontal middle, and areas with a high crack density can be observed (cf. figure 2.5(b)). The cracks tend to be in longitudinal direction, but are drifting to the surface of the sub-elements. This leads to a reduction of the superconducting cross-section and consequently reduction of I_c. At higher loads, the sub-elements suffer strong splintering in parallel to the transport current direction.

Figure 4.30 summarises the SEM investigations of the chemically extracted sub-elements. No cracks could be found on the non-loaded sub-elements, which confirms the absence of misleading cracks caused by the metallographic mechanical preparation of the micrographs discussed above. On the loaded samples, cracks and broken sub-elements can be observed. The cracked sub-elements confirm the crack shape observed in the longitudinal cross-section. A closer look on the crack surface identified them as an inter-granular brittle fracture along the grain boundaries.

The FEM analysis within the working group could confirm the results of the microscopic investigation [47]. The obtained crack pattern of the transverse cross-section shown in figure 4.28 correlates with the simulated stress distribution. Cracks in the sub-elements after a load of 100 MPa could be confirmed by using a yield strength of 400 MPa for the sub-elements. The increasing stresses led more and more to an ovalisation of the wire by using the given pressing arrangement. Hence, the FEM simulation showed a local remaining tension strain on the sub-elements based on the plastic deformation of the copper matrix.

It should be noted that the plastic deformation caused also dislocations of the sub-elements in height. Due to that, an additional axial tension strain on the sub-elements of the NearT_c sample between the voltage-tap could not unequivocally be excluded.

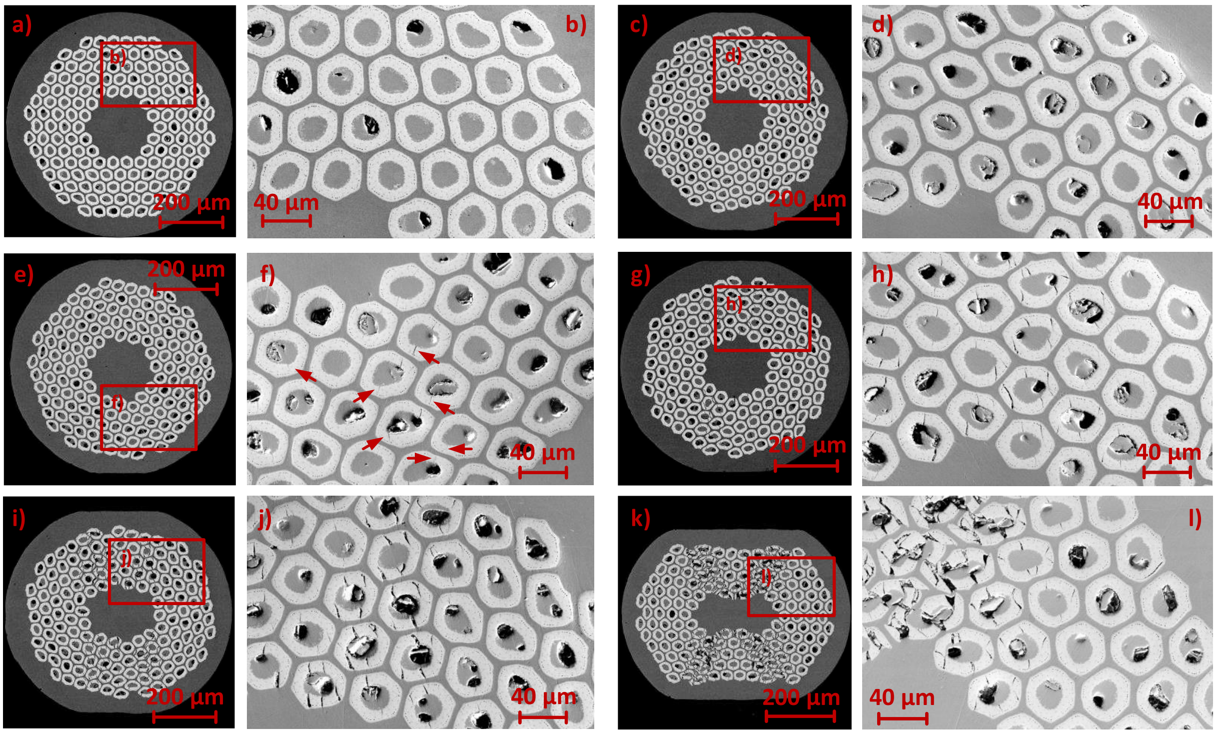

Figure 4.28: SEM micrographs of a transverse cross-sections of a reference wire **(a,b)** and wires after applying a transverse pressure of **(c,d)** 75 MPa, **(e,f)** 100 MPa, **(g,h)** 125 MPa, **(i,j)** 150 MPa and **(k,l)** 200 MPa. The first cracks, which could be observed after a nominal load of 100 MPa, are marked by arrows.

4.2.5 Discussion

Change of superconducting properties caused by transverse stress at RT

The results of the transport current and magnetisation measurements in combination with the microscopic investigation allow splitting the interpretation of the results in two regimes:

- **Low-pressure regime at RT** ($\sigma_{\mathrm{nom}} \leq 75$ MPa):
  Although no cracks could be found in this regime, a change of the extrinsic and intrinsic superconducting parameters could be measured. Even an improving tendency was observed. This finding motivates the assumption that the strain situation on the SC sub-elements within the wire got changed. Based on the SEM micrographs and the FEM analysis mentioned above [47], the wire got already plastically deformed below the crack initiation, causing a residual strain on the Nb_3Sn sub-elements. Thus, this affects the strain situation within the wire beside the thermal-induced pre-compression ε_{m} at low temperature. Hence, a change of the strain-depending superconducting properties can be expected, which has been well elaborated and summarised, e.g. by J. W. Ekin [55] and P. Bruzzone [29]. N. Mitchell [112] models the thermal contraction of Nb_3Sn composite wires from the A-15 formation at around 650 °C to operation temperature at 4 K, whereby ε_{m} of internal tin type wires can be assumed in the range of −0.2 % to −0.25 %. As pointed out in

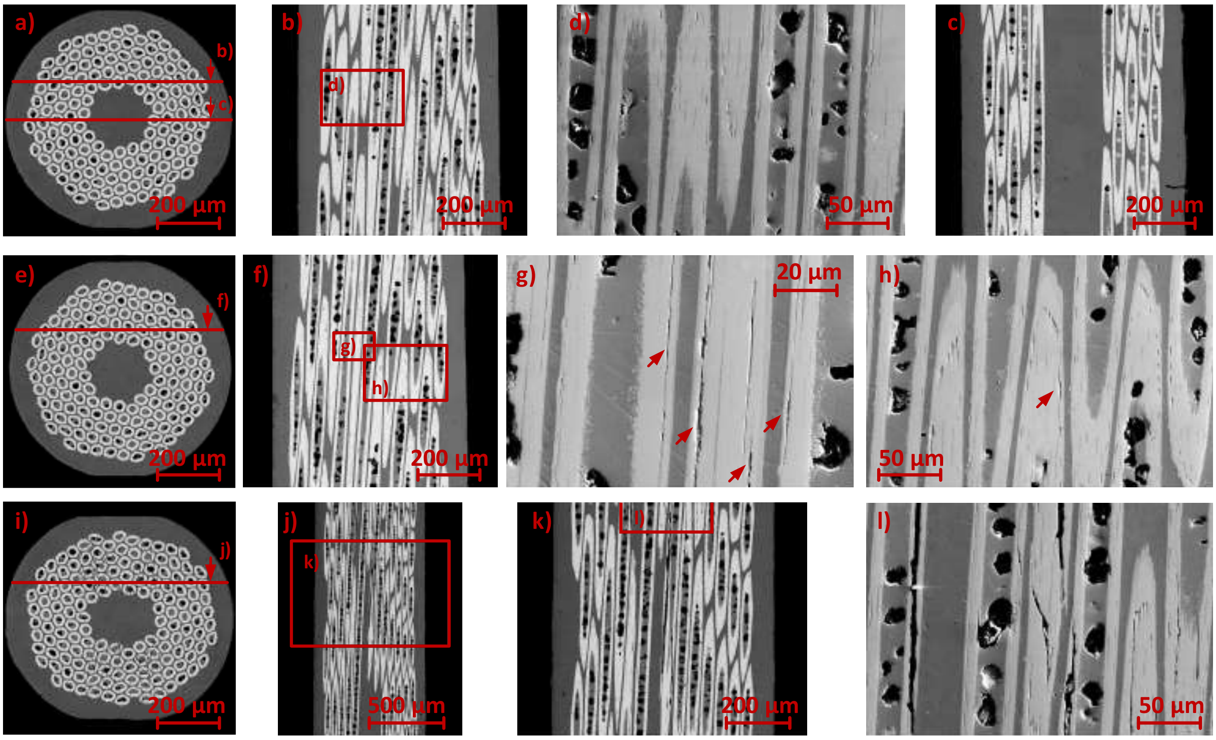

Figure 4.29: SEM micrographs of longitudinal cross-sections of wires after applying a transverse pressure of **(a-d)** 75 MPa, **(e-h)** 100 MPa and **(i-l)** 150 MPa. The first cracks, which could be observed after a nominal load of 100 MPa, are marked by arrows.

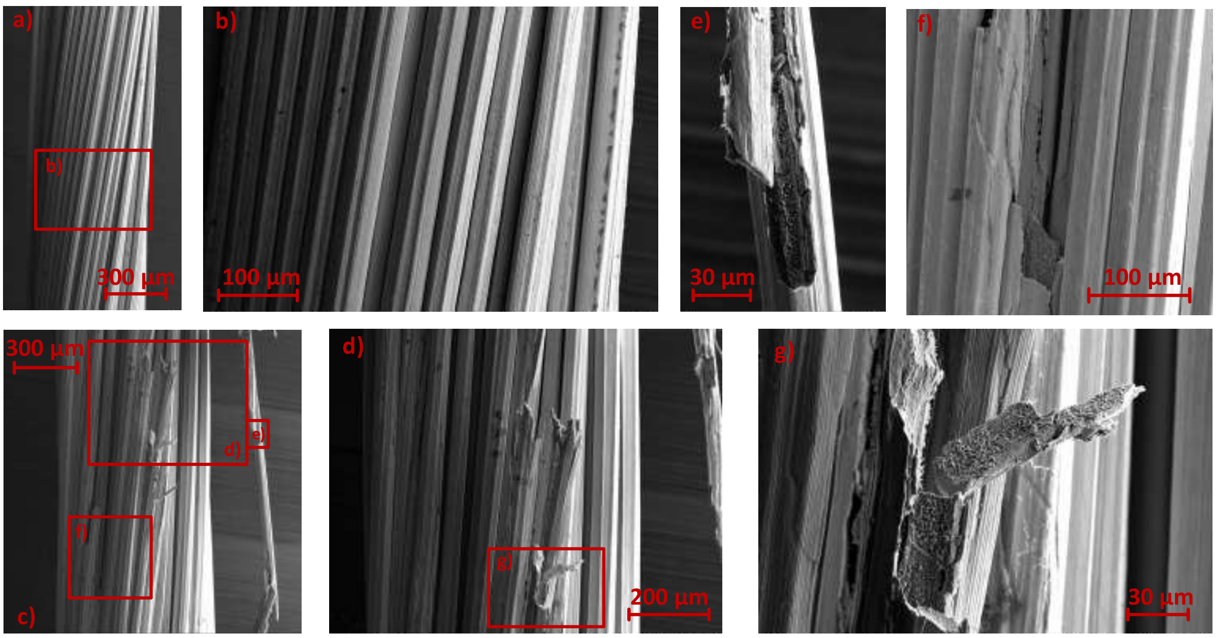

Figure 4.30: SEM micrographs of an etched **(a,b)** reference wire and an etched wire after applying a transverse pressure of **(c-g)** 200 MPa revealed clearly the splintering of the brittle Nb_3Sn sub-elements due to the transverse load as well as the surface of the fracture.

section 1.2.3, the strain dependency of the upper critical field $B_{c2}(\varepsilon)$ and the critical temperature $T_c(\varepsilon)$ can be described by a power law fit approximation within moderate strain (reversible strain effect).

The USL $F_p = I_c(B,T,\varepsilon)\,B = C\,g(\varepsilon)\,h(t)\,f(b)$ considers strain dependency within the moderate strain limit by the establishment of the strain scaling factor $g(\varepsilon)$ (cf. equation 1.15). The FEM analysis showed a generation of local tension strain due to the deformation of the copper stabiliser at RT, designated as $\varepsilon_{res,RT}$. The slightly I_c improvement measured within this regime can be interpreted as visualised in figure 4.31. The intrinsic strain $\varepsilon_0 = \varepsilon - \varepsilon_m$ is shifted oppositely by the above-mentioned pre-strain $\varepsilon_{res,RT}$ caused at RT, modelled as $\varepsilon_0 = \varepsilon - \varepsilon_m + \varepsilon_{res,RT}$. Hence, it counteracts or locally relieves the pre-compression ε_m. The measurements are performed always in the released situation ($\varepsilon = 0$) so that an improvement of $I_c(\varepsilon_{res,RT})$ could be measured initially. The best performance was measured after a load of 75 MPa. Hence, it can be assumed that the average residual tension strain $\varepsilon_{res,RT}$ after 75 MPa amounts in the range of the compression pre-strain ε_m and compensates it suitably. This behaviour stops with the irreversible strain limit $\varepsilon_{irr,RT}$ at RT, which generated fractures in the sub-elements and is further explained in the next paragraph.

Hence, this improving effect has the same origin as the effect observed in experiments with applied tension stress during the I_c measurements of wire, e.g. G. Mondonico *et al.* [114] and B. Seeber *et al.* [146]. In these experiments, the compensating force is applied at low temperature instead of the plastic deformation at RT in the present case. Also, a permanent deformation of the copper matrix affecting the critical current during the experiment is discussed by C. Calzolaio *et al.* [31], interpreting it already as an irreversible strain effect. However, it has to be considered that the mechanical properties at RT differ from those at low temperature, i.e. $\varepsilon_{irr,RT} \neq \varepsilon_{irr}$. The residual strain of a coil assembly resulting from applied stress at RT was also investigated recently by C. Scheuerlein *et al.* [141]. At RT, the strain maps of 11 T dipole coil sections was acquired by using fast high energy synchrotron X-ray and neutron diffraction, and such experiments can be recommended for further investigation of the present topic as well.

Although the cable specimen 2 shows an improvement in the low-stress range partly, the above-described phenomenon could not be observed unequivocal in the cable experiment. One of the reason could be that the strands within the cable are spatially strongly constrained by the embedment with epoxy resin. Hence, strong deformation is prevented, which was responsible for the residual tension pre-strain and consequently improvement of I_c within the wire investigation.

- **High-pressure regime at RT** ($\sigma_{nom} > 75$ MPa):

  On the base of the microscopic examination, the crack initiation starts at the load of 100 MPa, which correlates with the first continuous decrease of I_c.

  Although the decrease of B_{c2} and T_c measured by magnetometry indicates the presence of strain, the crack formation causes the primary loss of I_c. Consequently, the wire's performance degrades in this regime due to the same mechanism as observed in strands of Rutherford cables within the cable experiment (irreversible strain effect). The above-mentioned FEM analysis showed that the maximal residual strain $\varepsilon_{irr,RT}$ within a wire's cross section after a load of 100 MPa amounts to 0.44 % [47]. This is in a good agreement with the irreversible strain limit ε_{irr} in the range of 0.42 % to 0.45 % of internal tin type wires reported by C. Senatore [148].

  The results of the microscopic investigation confirm all conclusions of the former microscopy of the cable specimen 1, discussed detailed in section 4.1.4. Cracks tend to be in longitudinal direction, i.e. parallel to transport current, and drifting to the border of the sub-element. This observed longitudinal cracks are less critical concerning the I_c performance as cracks resulting from bending or axial stress, which are in transverse direction as investigated by M. J. Jewell *et al.* [81]. Similar research employing metallographic autopsy was performed by C. Sanabria *et al.* [134].

  The crack formation above a transverse load of 100 MPa found in this work can be identified as a purely mechanical process. The cracks harm the thermal stability of the wire and the I_c performance. Hence, the transport current has to evade the superconductor locally due to a crack and consequently flows in the copper stabiliser, generating dissipation and resulting in an earlier quench. This mechanism, so-called current sharing, reasons also the measured decrease of the n value, observed particularly in this regime [154]. This phenomenon contrasts the detected intrinsic strain-dependency in the low-stress regime.

At this point, it should be mentioned that investigations on reacted wires after pre-bending stress at RT were made by H. Oguro *et al.* [119]. The measurements with an applied field up to 18 T at 4.2 K of pre-bended Nb-rod-processed CuNb/Nb_3Sn wire showed also a clear enhancement of I_c followed

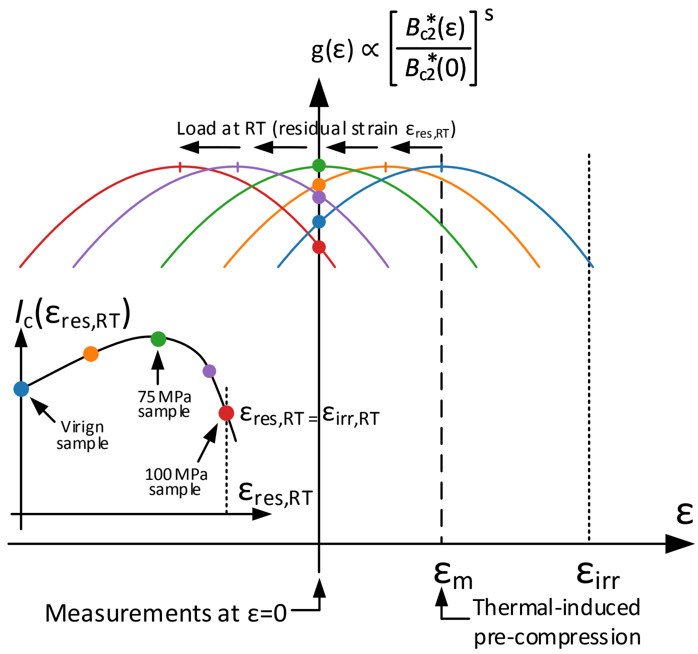

Figure 4.31: Interpretation of the results by the use of the strain scaling law $g(\varepsilon)$ of the USL $F_\mathrm{p} = I_\mathrm{c}(B,T,\varepsilon)\,B = C\,g(\varepsilon)\,h(t)\,f(b)$ for moderate strain [54, 55]. According to the SEM examination and the FEM analysis, the stress applied at room temperature causes plastic deformation of the copper stabiliser without cracks in sub-elements. Hence, a residual strain $\varepsilon_\mathrm{res,RT}$ within the wire is the consequence. Iterative increasing load within the experiment can be interpreted as a horizontal shift of $g(\varepsilon)$. This leads to an improvement of $I_\mathrm{c}(\varepsilon_\mathrm{res,RT})$ for moderate strain until the crack initiation caused at room temperature ($\varepsilon_\mathrm{irr,RT}$).

by degradation at higher bending strain. They confirm the previous investigation of the "pre-bending" treatment of CuNb/(Nb,Ti)$_3$Sn wires regarding the "react and wind" coil manufacturing technique of S. Awaji *et al.* [8].

Concept and implementation of NearT_c

The NearT_c concept was implemented successfully by conductive cooling of the 160 mm long specimen in a vacuum atmosphere with a sample temperature variation of ±5 mK. Moreover, it has been shown that the irreversible degradation of transverse stress applied at RT can be measured in the chosen temperature range from 16 K to 17.5 K.

From a more general perspective, a measurement of the $I_\mathrm{c}(T)$ behaviour up to a current of 150 A, i.e. $1.1 \cdot 10^9$ A m^{-2}, was performed. Compared to measurements of $I_\mathrm{c}(B)$ in liquid helium, an equal accuracy of the results is coupled to a higher technical effort, due to the required temperature control in mK-range.

Within the author's literature research, some experiments targeting the same temperature range could be found. B. ten Haken *et al.* [160] implemented a variable-temperature measurement with currents up to around 120 A. This was performed in a gaseous helium environment by using electrical heaters on the sample holder. Measurement results of Nb$_3$Sn wires at an applied field up to 13 T with sample temperatures in the range of 5 K to 8 K and a maximal error of ±40 mK were published.

Additional L. F. Goodrich *et al.* [70] described an implementation of $I_\mathrm{c}(T)$ up to 200 A of Nb-Ti and Nb$_3$Sn wires. Therefore a continuous-flow cryostat based on gaseous helium with high flow rates of up to 0.3 L s^{-1} was employed to implement high-current variable-temperature measurements above 4.2 K. A linear fit of the temperature at zero field measurements was reported with a standard deviation of 10 mK. Subsequently, L. F. Goodrich *et al.* [69] published the construction and operation of a continuous-flow cryostat for measurements with test currents up to 400 A at a variable sample temperature in the range of 4 K to 120 K.

Following arguments should be taken into account, when using the **NearT_c concept**:

- The NearT_c measurement principle only allows determining parameters, which affect the $I_\mathrm{c}(T)$ diagram. Information about the upper critical field B_c2, field-dependency of the observed effects as well as the impact on the pinning force $F_\mathrm{p} = I_\mathrm{c}(B)/B$ is lacking. Hence, such measurements are often used to determine the temperature margin of the superconductors for magnet applications.

- Effects, which are directly influencing the critical current, e.g. thermal stability, are surely traceable by evaluating $I_c(T)$. Due to the fact, that similar current densities are used as by common measurements of $I_c(B, 4.2\,K)$ in liquid helium, the observed effect will occur in a similar magnitude. This is also the reason, why especially influences caused by cracks are well determined by the NearT_c method. The setup was designed with 150 A, however the use of HTS current leads could extend the range to 300 A demonstrated by e.g. Y. S. Choi *et al.* [36].

- The magnetisation measurements confirmed the results qualitatively but also made aware of a dependency of the critical current close to T_c on the variation of T_c. The comparison of figure 4.24 and 4.26 points out this fact particularly. The behaviour can be explained with the high slope dI_c/dT, as mentioned in section 4.2.3. In the present case, it exaggerated the effective impact on the critical current. Hence, for a non-relative comparison of NearT_c measurements, it is recommended to present the results $I_c(t)$ as a function of reduced temperature $t = T/T_c$ with an indication of the additionally measured T_c.

- Finally, the inhomogeneity of Nb_3Sn sub-elements within composite superconductors has to be considered. As explained the section 3.4, the out-of-phase magnetic moment m'' as a function of the temperature gives information about the homogeneity of the superconducting material. It is strongly influenced by the diffusion process while the A-15 phase is formed. An inhomogeneous superconducting material leads unavoidably to a spatial distribution of T_c. During critical current measurements close to T_c some parts of the sub-elements are already in the resistive state, which implies inherently a reduced effective SC cross-section.

  Deepening research regarding the spatial T_c distribution of SC wires was performed, for instance, by B. Seeber *et al.* [147]. The distribution of T_c was acquired by measuring the specific heat and using the method proposed by C. Senatore *et al.* [149]. Baumgartner *et al.* [16] studied the evaluation of the T_c distribution by using susceptibility measurements with confirmation by scanning Hall probe microscopy (SHPM) and EDX. These methods, which require only small samples, can be revived supplementally to assess the effect of the inhomogeneity on the results received by the NearT_c measurements.

Nevertheless, within the construction, commissioning and operation of the **NearT_c setup** several drawbacks arose and their elaborated solutions should not be unstated:

- In general, helium is not a convenient cooling medium for high-current measurements with operation temperature in the range of 15 K to 20 K, which comprises large amount of Joule heating. A temperature of 4.2 K is per se not necessary for Nb_3Sn samples, based on the measurement principle explained in section 1.2.4. The coexistence of helium in the liquid and gaseous state in the tubes led to flow-driven thermal instabilities, which affected significantly the crucial temperature stability. Beside the actual temperature control concept, this problem was counteracted by the control of the dewar pressure and the deployment of the more robust current-sharing temperature T_{cs}. Additional, the number of repetitions of I_c measurement at the same condition was increased, to increase the reliability of the measurement.

  However, it shall be stated that helium is frequently used to establish a variable temperature in the range of 5 K to 300 K for application with vanish or low currents below 1 A. For instance, continuous-flow helium cryostats are often used to implement low-temperature scanning microscopes or T_c evaluations. In this case, the sample chamber, having a diameter of a few centimetres, is cooled from the bottom by a continuous helium gas flow. This is achieved by the constant supply of liquid helium through a needing valve by generating a vacuum in the chamber. Subsequently, the liquid is vaporised by a heater before entering the sample chamber. The temperature of the gas flow, and consequently of the sample chamber, can be regulated by both the flow rate and the power of the gas heater.

- The technological effort to reach high-current measurement results with the same quality is much higher compared to results from common measurements in liquid helium. First, the specific heat capacity $c_p \propto dQ/dT$ of liquid helium is much higher than of copper, i.e. $5.3\,J\,g^{-1}\,K^{-1}$ compared to $10^{-4}\,J\,g^{-1}\,K^{-1}$ at 4.2 K, respectively [54]. This means that the occurrence of heat energy in a helium bath leads only to a minor temperature rise compared to the thermal contact to a copper plate. Moreover, the latent heat of vaporisation of saturated two-phase helium provides an additional temperature stability, as discussed in section 1.2.4. These properties make a temperature stabilisation inherently easier in common measurements using liquid helium. However, helium can be used to stabilise other cryogenic systems. R. Li *et al.* [97] utilised the high specific heat of pressured helium in a cooper pot to reach an improved temperature stability at the 4 K stage of a cryogenic refrigerator system.

Second, the temperature control of a distributed spatially system is more difficult compared to the current control of a background magnet. Moreover, it is closer to the common application, considering that most of the superconducting accelerator magnets are cooled with liquid or superfluid helium at a temperature of 4.2 K or 1.9 K, respectively. This is also probably the reason, why such measurements are more established for characterisation of superconducting wires in the field of magnet development. However, the NearT_c concept with the presented setup is a lucrative alternative to reach higher and less-expensive throughput, compared to established test stations, without the need of a background magnet and the continuous supply of liquid helium.

- An alternative closed-loop cooling method would be a system based on a cryogenic refrigerator, for which this feasibility study is targeting. The Joule heating measurement of the setup showed a value of 15.5 W and 120 mW for the entire system and the sample platform, respectively. The remaining radiation, conduction and convection heat influx can be estimated to be smaller by several orders of magnitude than the Joule heating and heat impact due to the current leads. These test results can be further used for a heat load estimation of a two-stage cryogenic refrigerator system. The original intended Gifford-McMahon (GM) cryocooler *Sumitomo CH210*[1] [89] has a first stage cooling capacity of 110 W at 77 K, second stage cooling capacity 6 W at 20 K and a minimum temperature of 10 K [152]. Hence, the estimated heat load of table 4.9 is a fraction of the nominal cooling capacity and the results of the presented work do not rule out the use of a refrigerator system. The clear advantage of a refrigerator system for this application is the fast cooling time allowing a high measurement throughput, which amounts to less than 1 h for RT to 20 K for the referred model. Moreover, it eliminates the costs due to the otherwise required continuous supply of liquid helium.
- The sample temperature analysed in the frequency domain (cf. figure 4.16) showed clearly, that an active feed-back control rejects mainly low-frequency disturbances. By the use of the adequate PID control design on the base of parameter identification of the system, the cut-off frequency could be further increased. Nevertheless, high-frequency disturbances, caused for instance by the mechanical cooling process of a mentioned refrigerator system at roughly 2 Hz, are hardly accessible by thermal actuators. This could be carried out by interrupting the thermal link from the cooling plate to the sample by the use of materials with high specific heat capacity, e.g. lead (Pb). For instance, G. Dubuis *et al.* [45] demonstrated a passive suppression of the refrigerator-depending temperature variation to the mK-range without primary loss of cooling power.

Magnetisation measurement

The magnetisation measurements confirmed the transport current measurements qualitatively and held information about intrinsic properties. The slight improvement of B_{c2} and T_c in the low-pressure regime reinforced the assumption of rearranging the strain condition due to former force exertion at RT. Nevertheless, the model used for the magnetisation results assumes the sub-elements as idealised straight hollow cylinders. This is ensured until roughly 112.5 MPa before the cylindrical shape of the sub-elements is no longer preserved due to the starting splintering. Hence, magnetometry can only be used to detect cracks or stress causing cracks in sub-elements, not their quantitative influence on the practical J_c performance.

4.3 Conclusion

The effect and cause of transverse stress at room temperature on the superconducting properties of Nb_3Sn composite superconductors were measured and analysed. This was performed to study their significance within manufacturing of Nb_3Sn accelerator magnets.

In the frame of the **cable investigation**, three impregnated Rutherford cable double stacks made of RRP wires were exposed to transverse stress at room temperature. Subsequently, the critical current I_c was measured, which delivers expedient information for the magnet manufacturing technology:

- In general, high stress on reacted cables at room temperature causes fractures in the superconducting sub-elements and harm the thermal stability of the strands, which results in current sharing

[1] Specification under the assumption of a three-phase 50 Hz power supply.

after increased stress levels. This can be concluded by the observed irreversible I_c degradation in combination with a sharp decrease of the n value independent of the applied field.

- The first two specimens, loose impregnated double stacks, retained their integrity until 150 MPa and suffered an irreversible degradation of less than 5 % after a load of 175 MPa evaluated at 4.3 K with an applied field of 9.6 T. The first specimen showed a substantial degradation after 200 MPa. The subsequent metallographic autopsy confirmed fractures in the sub-elements as the cause of degradation. Moreover, the cracks could be identified in longitudinal direction, which drifted to the surface of the sub-elements. Thus, the effective superconducting cross-section was reduced. The third cable, having titanium shims for mechanical protection, showed an irreversible degradation of 5 % after a load of 240 MPa measured at 4.3 K with an applied field of 9.6 T.

In the frame of the **wire investigation**, single Nb_3Sn RRP wires were exposed to transverse stress at room temperature. Subsequently, they were subjected to transport current and magnetisation measurements, which provide detailed information of the degradation process. In addition, a metallographic campaign was performed:

- The stress exertion below 100 MPa generated a plastic deformation of the copper stabiliser affecting the pre-strain on the superconducting sub-elements without cracks. This counteraction of the thermal pre-compression can be concluded by the improved tendency of a few percent of the transport critical current and the strain-depending intrinsic properties B_{c2} and T_c, determined by magnetometric methods. The microscopic examination confirmed the plastic deformation without crack initiation and the FEM analysis assessed a persistence tension strain on the sub-elements after stress exertion at room temperature.

- In the high-stress regime, the wire suffers current sharing due to cracks analogue to the observations in the cable specimens. This can be concluded from the detected crack initiation starting after the stress exertion of 100 MPa determined by microscopy. This correlates also with the measured drop of I_c and T_{cs} in combination with a decrease of the n value. Regarding the characteristic crack distribution and the crack shape, the SEM results are in compliance with the cable experiment.

The implemented NearT_c concept and the applied established concepts aim to provide additional assessment possibilities beside existing high-demanding and costly measurement infrastructure:

- **NearT_c concept and setup**
  The measurement of $I_c(T)$ of a Nb_3Sn wire in self-field with test currents up to 150 A was successfully implemented in the chosen temperature range of 16 K to 17.5 K. This was achieved by using a self-designed cryostat setup with a helium phase separator and a temperature controller implementing a sample temperature precision down to ±5 mK.

  The measurement equipment, the experimental geometric arrangement and the slope $\mathrm{d}I_c/\mathrm{d}T$ were sufficient to characterise the Nb_3Sn RRP wire. The measurement concept applied with the self-designed setup was shown to be suitable to measure the effect of the transverse stress at room temperature. Additional, a low-resistance measurement method was developed to evaluate the critical current T_c and the residual resistance ratio RRR.

- **Magnetometry**
  Magnetisation measurements were shown to be suitable to monitor an irreversible degradation after the exertion of transverse stress at room temperature and confirmed the transport current result of the chosen measurement range close to T_c.

- **Microscopy and FEM analysis**
  Metallographic procedures were developed and optimised to autopsy unequivocally cracks in Nb_3Sn sub-elements, proved by their absence in non-loaded samples. The transverse cross-sections were used to obtain the crack initiation and their distribution. The longitudinal cross-sections revealed the shape of the cracks. The microscopic investigation with a SEM was tested to be a valuable indication tool to detect cracks without a low-temperature equipment. The FEM analysis based on the X-ray tomography of samples was shown as a key tool to understand and assess the local stress and strain situation on the superconducting sub-elements caused by the externally applied force.

Summarising, this work offers fundamental knowledge and adequate tools for further research within this topic and, in general, for the development of Nb_3Sn conductors for high energy physics experiments.

4.4 Outlook

Section 1.5 outlines already the purpose of the thesis and the accomplished experiments. Nevertheless, some aspects stayed unfinished or were not continued. The present author wants to mention some recommendations for further research and development regarding this topic:

- **Irreversible degradation of superconducting properties caused by transverse stress applied at room temperature:**

  The degradation process was measured on a single wire type, representatively for all other Nb_3Sn wire types. The measurement of several equal specimens is recommended to be the next step, for confirming the phenomena observed within this work. Subsequently, measurements of other wire types would be useful, for receiving a statement of the different robustness of the particular wire types. Consequently, this would deliver finally applicable information for design decisions of accelerator magnets.

  Besides the minor change of superconducting properties below the fracture initiation, the leading cause of the irreversible degradation tends to be the crack formation, confirmed by the cable and wire experiment. Hence, the local stress on the sub-elements is the essential cause. As tried to emphasise, the transfer of the externally applied force within the components is non-linear, material-depending and a crucial factor, which should be investigated further. A calculation of the local stress on sub-elements based on the externally applied force would standardise all experiment-depending pressure profiles to the lowest common denominator. To implement such standardisation, FEM analysis on the base of reliable material parameter identification and statistically-based models would be essential.

  By performing a FEM simulation within the wire investigation, it was attempted to link the I_c degradation to the pre-stress on the sub-elements [47] (cf. section 4.2). This universal information could be further used to estimate the I_c degradation based on a FEM stress analysis of any specific cable or coil cross-section, which tracks the local stress values on the sub-elements. It could be used to receive a preliminary assessment of crack formations and I_c degradation caused by transverse stress at room temperature of various configurations, e.g. different impregnation materials and strand diameters without costly cable or coil tests.

  One of the aspects, which was not further continued, is the quantitative evaluation of cracks and crack density by using digital image processing, as performed in several other works. Automatic detection and quantification of cracks in sub-elements on SEM micrographs were elaborated by e.g. C. Sanabria [133] and M. C. Jewell [101]. An extrapolation of this processing to SEM micrographs of loaded cables could be used for confirmation of mentioned FEM analysis [180] (cf. section 4.1).

  It could be shown that the cracks are mainly causing current sharing, which influence the thermal stability of the wire and cable. Considering the tedious I_c measurements of cables and the only qualitative determination of the n value, it can be taken into account to describe this effect by common stability parameters. Hence, a statement of the stability loss could be reached by adopting the minimum quench energy (MQE), recently investigated by e.g. G. Willering [178] and W. M. de Rapper [41], or electrical network models, as introduced by e.g. Z. J. J. Stekly *et al.* [154].

- **Manufacturing of Nb_3Sn accelerator magnets:**

  The production of Nb_3Sn accelerator magnets of the HL-LHC project is still raising some questions and uncertainties, which are only revealed in the latest step, the training and test procedure at low temperatures. Apparently, the production of Nb_3Sn accelerator magnets requires tighter manufacturing tolerances, compared to Nb-Ti magnets, to reach a mass-production with the necessary low drop-out rate, which fulfils the requirements for the FCC aims.

  Besides many successful research activities trying to imitate the manufacturing condition within their experiments, also the processes of fabrication should be investigated in detail. An increase of the monitoring instrumentation and automation infrastructure would improve the early detection of degradation and the reproducibility of the process. Moreover, the achieved conclusions of experiments, e.g. of the present work, could be applied better to the actual situation in the manufacturing.

- **NearT_c concept and setup:**

  The NearT_c measurement concept was demonstrated to seek alternative experimental methods with higher throughput and lower economic effort. After the concept was put successfully into action, the next step is thus the optimisation. Upgrading the system to a cryocooler-based version needs further investigation of the expected heat load of the two stages by static and dynamic heat inputs.

An obvious optimisation potential is the replacement of the cold parts of the current leads by commercial HTS coated conductors made with e.g. YBCO or BiSCCO. It would reduce the Joule heating strongly and helps to reach a higher sample current, e.g. 300 A. In low-temperature systems with applied fields, HTS current leads have to be elaborately mounted to prevent possible quenches by Lorentz force induced movements. Considering that the measurement concept does not imply a background magnet, mounting of the leads is not necessary. Hence, a relative high improvement of the setup can be achieved by relative low effort.

Bibliography

[1] A. Abada et al. FCC Physics Opportunities – Future Circular Collider Conceptual Design Report Volume 1. *European Physical Journal C*, **79**:474, 2019.

[2] A. Abada et al. FCC-ee: The Lepton Collider – Future Circular Collider Conceptual Design Report Volume 2. *European Physical Journal Special Topics*, **228**(2):261, 2019.

[3] A. Abada et al. FCC-hh: The Hadron Collider – Future Circular Collider Conceptual Design Report Volume 3. *European Physical Journal Special Topics*, **228**(4):755, 2019.

[4] A. A. Abrikosov. On the Magnetic Properties of Superconductors of the Second Group. *Zhurnal Éksperimental'noĭ i Teoreticheskoĭ Fiziki*, **32**(6):1442, 1957. [Soviet physics, JETP **5**(6):1174 (1957)].

[5] J. Ahlback et al. Electromagnetic and mechanical design of a 56 mm aperture model dipole for the LHC. *IEEE Transactions on Magnetics*, **30**(4):1746, 1994.

[6] G. Apollinari, I. Béjar Alonso, O. Brüning, P. Fessia, M. Lamont, L. Rossi, and L. Tavian. High-Luminosity Large Hadron Collider (HL-LHC): Technical Design Report. Report no. CERN-2017-007-M, CERN, 1211 Geneva 23, Switzerland, 2017.

[7] B. Auchmann, S. Russenschuck, and N. Schwerg. Discrete Differential Geometry Applied to the Coil-End Design of Superconducting Magnets. *IEEE Transactions on Applied Superconductivity*, **17**(2):1165, 2007.

[8] S. Awaji, K. Watanabe, and K. Katagiri. Improvement of mechanical and superconducting properties in CuNb/(Nb,Ti)3Sn wires by applying bending strain at room temperature. *Superconductor Science and Technology*, **16**(6):733, 2003.

[9] S. Balachandran, C. Tarantini, P. J. Lee, F. Kametani, Y. Su, B. Walker, W. L. Starch, and D. C. Larbalestier. Beneficial influence of Hf and Zr additions to Nb4at%Ta on the vortex pinning of Nb_3Sn with and without an O source. *Superconductor Science and Technology*, **32**(4):044006, 2019.

[10] J. Bardeen and M. J. Stephen. Theory of the Motion of Vortices in Superconductors. *Physical Review*, **140**:A1197.

[11] J. Bardeen, L. N. Cooper, and J. R. Schrieffer. Theory of Superconductivity. *Physical Review*, **108**:1175, 1957.

[12] C. Barth, B. Seeber, A. Rack, C. Calzolaio, Y. Zhai, D. Matera, and C. Senatore. Quantitative correlation between the void morphology of niobium-tin wires and their irreversible critical current degradation upon mechanical loading. *Scientific Reports*, **8**(6589), 2018.

[13] E. Barzi, T. Wokas, and A. V. Zlobin. Sensitivity of Nb_3Sn Rutherford-type cables to transverse pressure. *IEEE Transactions on Applied Superconductivity*, **15**(2):1541, 2005.

[14] T. Baumgartner. *Effects of Fast Neutron Irradiation on Critical Current and Intrinsic Properties of State-of-the-Art Nb_3Sn wires*. PhD thesis, Vienna University of Technology, Vienna, Austria, 2013.

[15] T. Baumgartner, M. Eisterer, H. W. Weber, R. Flükiger, B. Bordini, L. Bottura, and C. Scheuerlein. Evaluation of the Critical Current Density of Multifilamentary Nb_3Sn Wires From Magnetization Measurements. *IEEE Transactions on Applied Superconductivity*, **22**(3):6000604, 2012.

[16] T. Baumgartner, J. Hecher, J. Bernardi, S. Pfeiffer, C. Senatore, and M. Eisterer. Assessing composition gradients in multifilamentary superconductors by means of magnetometry methods. *Superconductor Science and Technology*, **30**(1):014011, 2016.

[17] C. Bayer, C. Barth, P. V. Gade, K. Weiss, and R. Heller. FBI Measurement Facility for High Temperature Superconducting Cable Designs. *IEEE Transactions on Applied Superconductivity*, **24**(3):1, 2014.

[18] C. P. Bean. Magnetization of High-Field Superconductors. *Reviews of Modern Physics*, **36**:31, 1964.

[19] J. G. Bednorz and K. A. Z. Müller. Possible high T_c superconductivity in the Ba-La-Cu-O system. *Zeitschrift für Physik B Condensed Matter*, **64**:189, 1986.

[20] F. Bertinelli et al. Production and Quality Assurance of Main Busbar Interconnection Splices During the LHC 2008–2009 Shutdown. *IEEE Transactions on Applied Superconductivity*, **21**(3):1786, 2011.

[21] R. A. Beth. Complex representation and computation of two-dimensional magnetic fields. *Journal of Applied Physics*, **37**(7):2568, 1966.

[22] J. Billan et al. A Superconducting High-Luminosity Insertion in the Intersecting Storage Rings (ISR). *IEEE Transactions on Nuclear Science*, **26**(3):3179, 1979.

[23] J. P. Blewett. Radial Focusing in the Linear Accelerator. *Physical Review*, **88**:1197, 1952.

[24] B. Bordini. Self-Field Correction in Critical Current Measurements of Superconducting Wires Tested on ITER VAMAS Barrels. Internal note (EDMS no. 105765), CERN, 1211 Geneva 23, Switzerland, 2010.

[25] B. Bordini, F. Regis, O. Crettiez, P. Fessia, M. Guinchard, J. C. Perez, and I. Sexton. Conceptual Design of a New Sample Holder for the FRESCA Cable Test Station. *IEEE Transactions on Applied Superconductivity*, **20**(3):1511, 2010.

[26] B. Bordini, P. Alknes, A. Ballarino, L. Bottura, and L. Oberli. Critical Current Measurements of High-J_c Nb_3Sn Rutherford Cables Under Transverse Compression. *IEEE Transactions on Applied Superconductivity*, **24**(3):1, 2014.

[27] H. Boschman, A.P. Verweij, W. A. J. Wessel, H. H. J. ten Kate, and L. J. M. van de Klundert. Effect of transverse loads up to 300 MPa on the critical currents of Nb_3Sn cables. *IEEE Transactions on Magnetics*, **27**(2):1831, 1991.

[28] O. S. Brüning, P. Collier, P. Lebrun, S. Myers, R. Ostojic, J. Poole, and P. Proudlock. LHC Design Report. URL `http://cds.cern.ch/record/782076`. [Online; Accessed September 2019]. Report no. CERN-2004-003-V-1, CERN, 1211 Geneva 23, Switzerland, 2004.

[29] P. Bruzzone. Review of Design Aspects for High Current Nb_3Sn Conductors. *IEEE Transactions on Applied Superconductivity*, **21**(3):2036, 2011.

[30] J. Cabanes, M. Garlasche, B. Bordini, and A. Dallocchio. Simulation of the cabling process for Rutherford cables: An advanced finite element model. *Cryogenics*, **80**:33, 2016.

[31] C. Calzolaio, G. Mondonico, A. Ballarino, B. Bordini, L. Bottura, L. Oberli, and C. Senatore. Electromechanical properties of PIT Nb_3Sn wires under transverse stress: experimental results and FEM analysis. *Superconductor Science and Technology*, **28**(5):055014, 2015.

[32] M. Cantoni, C. Scheuerlein, P.-Y. Pfirter, F. de Borman, J. Rossen, G. Arnau, L. Oberli, and P. Lee. Sn concentration gradients in powder-in-tube superconductors. *Journal of Physics: Conference Series*, **234**(2):022005, 2010.

[33] S. Caspi et al. Canted–Cosine–Theta Magnet (CCT)—A Concept for High Field Accelerator Magnets. *IEEE Transactions on Applied Superconductivity*, **24**(3):1, 2014.

[34] CERN Document Server. URL `https://cds.cern.ch`. [Online; Accessed September 2019]. CERN, 1211 Geneva 23, Switzerland.

[35] N. Cheggour, T. C. Stauffer, W. Starch, P. J. Lee, J. D. Splett, L. F. Goodrich, and A. K. Ghosh. Precipitous change of the irreversible strain limit with heat-treatment temperature in Nb_3Sn wires made by the restacked-rod process. *Scientific Reports*, **8**:13048, 2018.

[36] Y. S. Choi, T. A. Painter, D. L. Kim, H. S. Yang, and B. S. Lee. Semi-retractable current lead cooled by a cryocooler for high field magnet. *IEEE Transactions on Applied Superconductivity*, **19**(3):2210, 2009.

[37] N. C. Christofilos. Focusing System for Ions and Electrons. United States Patent 2736799, 1950.

[38] E. D. Courant, M. S. Livingston, and H. S. Snyder. The Strong-Focusing Synchroton – A New High Energy Accelerator. *Physical Review*, **88**:1190, 1952.

[39] E. D. Courant, M. S. Livingston, H. S. Snyder, and J. P. Blewett. Origin of the "Strong-Focusing" Principle. *Physical Review*, **91**:202, 1953.

[40] M. Daly, C. H. Löffler, D. Smekens, A. T. Fontenla, O. S. de Frutos, M. Guinchard, and F. Savary. Multiscale approach to the mechanical behavior of epoxy impregnated Nb_3Sn coils for the 11 T dipole. *IEEE Transactions on Applied Superconductivity*, **28**(3):1, 2018.

[41] W. M. de Rapper. *Thermal stability of Nb_3Sn Rutherford cables for accelerator magnets*. PhD thesis, University of Twente, Enschede, The Netherlands, 2014.

[42] B. S. Deaver and W. M. Fairbank. Experimental Evidence for Quantized Flux in Superconducting Cylinders. *Physical Review Letters*, **7**:43, 1961.

[43] P. G. deGennes. *Superconductivity of Metals and Alloys*. CRC Press, Bocan Raton, USA, 1966. ISBN 978-0738201016.

[44] R. Doll and M. Näbauer. Experimental Proof of Magnetic Flux Quantization in a Superconducting Ring. *Physical Review Letters*, **7**:51, 1961.

[45] G. Dubuis, X.He, and I. Božović. Sub-millikelvin stabilization of a closed cycle cryocooler. *Review of Scientific Instruments*, **85**(10):103902, 2014.

[46] P. Ebermann and F. Wolf. Evaluation script for analysing pressure measurement films with office scanners. Internal note (EDMS no. 188555), CERN, 1211 Geneva 23, Switzerland, 2017.

[47] P. Ebermann, T. Baumgartner, M. Daly, A. Gallifa Terricabras, T. Koettig, F. Lackner, C. Scheuerlein, and M. Eisterer. Influence of transverse stress exerted at room temperature on the superconducting properties of Nb_3Sn wires. *Superconductor Science and Technology*, **32**(9):095010, 2019.

[48] P. Ebermann et al. Irreversible degradation of Nb_3Sn Rutherford cables due to transverse compressive stress at room temperature. *Superconductor Science and Technology*, **31**(6):065009, 2018.

[49] C. Eck et al. LHC computing Grid: Technical Design Report. URL `https://cds.cern.ch/record/840543`. [Online; Accessed September 2019]. Report no. CERN-LHCC-2005-024, CERN, 1211 Geneva 23, Switzerland, 2005.

[50] M Eisterer. Towards optimized Nb_3Sn. *Superconductor Science and Technology*, **32**(4):040501, 2019.

[51] J. W. Ekin. Current transfer in multifilamentary superconductors. I. Theory. *Journal of Applied Physics*, **49**(6):3406, 1978.

[52] J. W. Ekin. Strain scaling law for flux pinning in practical superconductors. Part 1: Basic relationship and application to Nb_3Sn conductors. *Cryogenics*, **20**(11):611, 1980.

[53] J. W. Ekin. Four-dimensional J-B-T-ε critical surface for superconductors. *Journal of Applied Physics*, **54**(1):303, 1983.

[54] J. W. Ekin. *Experimental Techniques for Low-Temperature Measurements*. Oxford University Press, Oxford, UK, 2006. ISBN 978-0198570547.

[55] J. W. Ekin. Unified scaling law for flux pinning in practical superconductors: I. Separability postulate, raw scaling data and parameterization at moderate strains. *Superconductor Science and Technology*, **23**(8):083001, 2010.

[56] J. W. Ekin, A. F. Clark, and J. C. Ho. Current transfer in multifilamentary superconductors. II. Experimental results. *Journal of Applied Physics*, **49**(6):3410, 1978.

[57] J. W. Ekin, N. Cheggour, L. Goodrich, J. Splett, B. Bordini, and D. Richter. Unified Scaling Law for flux pinning in practical superconductors: II. Parameter testing, scaling constants, and the Extrapolative Scaling Expression. *Superconductor Science and Technology*, **29**(12):123002, 2016.

[58] J. W. Ekin, N. Cheggour, L. Goodrich, and J. Splett. Unified Scaling Law for flux pinning in practical superconductors: III. Minimum datasets, core parameters, and application of the Extrapolative Scaling Expression. *Superconductor Science and Technology*, **30**(3):033005, 2017.

[59] G. M. Eliashberg. Interactions between Electrons and Lattice Vibrations in a Superconductor. *Zhurnal Éksperimental'noĭ i Teoreticheskoĭ Fiziki*, **38**(3):966, 1960. [Soviet physics, JETP **11**(3):696 (1960)].

[60] J. Fleiter, B. Bordini, A. Ballarino, L. Oberli, S. Izquierdo, and L. Bottura. Quench Propagation in Nb_3Sn Rutherford Cables for the Hi-Lumi Quadrupole Magnets. *IEEE Transactions on Applied Superconductivity*, **25**(3):1, 2015.

[61] J. Fleiter, A. Ballarino, A. Bonasia, B. Bordini, and D. Richter. Optimization of Nb_3Sn Rutherford Cables Geometry for the High-Luminosity LHC. *IEEE Transactions on Applied Superconductivity*, **27**(4):1, 2017.

[62] J. Fleiter, S. Peggiani, A. Bonasia, and A. Ballarino. Characterization of Nb_3Sn Rutherford cable degradation due to strands cross-over. *IEEE Transactions on Applied Superconductivity*, **28**(4):1, 2018.

[63] R. Flükiger, D. Uglietti, C. Senatore, and F. Buta. Microstructure, composition and critical current density of superconducting Nb_3Sn wires. *Cryogenics*, **48**(7):293, 2008.

[64] Fujifilm, Heesenstraße 31, 40549 Düsseldorf, Germany. Pressure measurement film – Prescale. URL `https://www.fujifilm.com/products/prescale`. [Online; Accessed September 2019].

[65] A. Gallifa Terricabras. Microscopy inspection of Nb_3Sn RRP strands and Nb_3Sn Rutherford cables after transverse compressive tests at room temperature. Internal note (EDMS no. 1994865), CERN, 1211 Geneva 23, Switzerland, 2018.

[66] A. Godeke. *Performance boundaries in Nb_3Sn*. PhD thesis, University of Twente, Enschede, The Netherlands, 2005.

[67] A. Godeke, M. Dhalle, A. Morelli, L. Stobbelaar, H. van Weeren, H. J. N. van Eck, W. Abbas, A. Nijhuis, A. den Ouden, and B. ten Haken. A device to investigate the axial strain dependence of the critical current density in superconductors. *Review of Scientific Instruments*, **75**(12):5112, 2004.

[68] W. Goldacker, S. I. Schlachter, R. Nast, H. Reiner, S. Zimmer, H. Kiesel, and A. Nyilas. Bending strain investigations on BSCCO(2223) tapes at 77 K applying a new bending technique. *AIP Conference Proceedings*, **614**(1):469, 2002.

[69] L. F. Goodrich and T. C. Stauffer. Hysteresis in Transport Critical-Current Measurements of Oxide Superconductors. *Journal of Research of the National Institute of Standards and Technology*, **106**:657, 2001.

[70] L. F. Goodrich, L. T. Medina, and T. C. Stauffer. High Critical-Current Measurements in Liquid and Gaseous Helium. *Advances in Cryogenic Engineering Materials, vol. 44. Springer, Boston, MA*, pages 873-880, 1998.

[71] L. P. Gor'kov. Microscopic Derivation of the Ginzburg-Landau Equations in the Theory of Superconductivity. *Zhurnal Éksperimental'noĭ i Teoreticheskoĭ Fiziki*, **36**(6):1918, 1959. [Soviet physics, JETP **9**(6):1364 (1959)].

[72] L. P. Gor'kov. Theory of Superconducting Alloys in a Strong Magnetic Field near the Critical Temperature. *Zhurnal Éksperimental'noĭ i Teoreticheskoĭ Fiziki*, **37**(5):1407, 1960. [Soviet physics, JETP **10**(5):998 (1960)].

[73] S. A. Gourlay et al. Magnet R&D for the US LHC Accelerator Research Program (LARP). *IEEE Transactions on Applied Superconductivity*, **16**(2):324, 2006.

[74] V. Guritanu, W. Goldacker, F. Bouquet, Y. Wang, R. Lortz, G. Goll, and A. Junod. Specific heat of Nb_3Sn: The case for a second energy gap. *Physical Review B*, **70**:184526, 2004.

[75] H. Kamerlingh Onnes. Further experiments with liquid helium. C. On the change of electric resistance of pure metals at very low temperatures etc. IV. The resistance of pure mercury at helium temperatures. *Leiden Communications*, **120b**, 1911.

[76] E. Helfand and N. R. Werthamer. Temperature and Purity Dependence of the Superconducting Critical Field, H_{c2}. *Physical Review Letters*, **13**:686, 1964.

[77] E. Helfand and N. R. Werthamer. Temperature and Purity Dependence of the Superconducting Critical Field, H_{c2}. II. *Physical Review*, **147**:288, 1966.

[78] H. Hertz. Über die Berührung Fester Elastischer Körper. *Journal für die Reine und Angewandte Mathematik*, 92:156, 1881.

[79] J. K. Hulm and R. D. Blaugher. Superconducting Solid Solution Alloys of the Transition Elements. *Physical Review*, **123**:1569, 1961.

[80] B. Jakob, G. Pasztor, M. Bona, and A. Asner. Reduced sensitivity of Nb_3Sn epoxy-impregnated cable to transverse stress. *Cryogenics*, **31**(5):390, 1991.

[81] M. C. Jewell, P. J. Lee, and D. C. Larbalestier. The influence of Nb_3Sn strand geometry on filament breakage under bend strain as revealed by metallography. *Superconductor Science and Technology*, **16**(9):1005, 2003.

[82] Y. Kamihara, H. Hiramatsu, M. Hirano, R. Kawamura, H. Yanagi, T. Kamiya, and H. Hosono. Iron-based layered superconductor: LaOFeP. *Journal of the American Chemical Society*, **128**:10012, 2006.

[83] A .R. Kantrowitz and Z. J. J. Stekly. A New Principle for the Construction of Stabilized Superconducting Coils. *Applied Physics Letters*, **6**:56, 1965.

[84] M. Karppinen et al. Design of 11 T Twin-Aperture Nb_3Sn Dipole Demonstrator Magnet for LHC Upgrades. *IEEE Transactions on Applied Superconductivity*, **22**(3):4901504, 2012.

[85] U. M. Kelly et al. Nb_3Sn Wire Shape and Cross-Sectional Area Inhomogeneity in Rutherford Cables. *IEEE Transactions on Applied Superconductivity*, **28**(4):1, 2018.

[86] E. J. Kramer. Scaling laws for flux pinning in hard superconductors. *Journal of Applied Physics*, **44**(3):1360, 1973.

[87] F. Lackner. Private conversation. CERN, 1211 Geneva 23, Switzerland, 2018.

[88] F. Lackner. Status of the wound conductor task. Presented on the FCC week 2018, Amsterdam, The Netherlands, 2018. URL `https://indico.cern.ch/event/656491/timetable/?view=nicecompact`. [Online; Accessed September 2019].

[89] F. Lackner and C. Scheuerlein. Justification for the purchase of two Sumitomo CH-210 cryocoolers. Internal purchase request (EDH-DAI no. 6414099), CERN, 1211 Geneva 23, Switzerland, 2016.

[90] F. Lackner et al. Fabrication of the 7.3-m-Long Coils for the Prototype of MQXFB, the Nb_3Sn Low-β Quadrupole Magnet for the HiLumi LHC. *IEEE Transactions on Applied Superconductivity*, **28**(3):1, 2018.

[91] L. D. Landau and V. L. Ginzburg. On the theory of superconductivity. *Zhurnal Éksperimental'noĭ i Teoreticheskoĭ Fiziki*, **20**:1064, 1950.

[92] D. Leroy, G. Spigo, A. P. Verweij, H. Boschman, R. Dubbeldam, and J. G. Pelayo. Design and manufacture of a large-bore 10 T superconducting dipole for the CERN cable test facility. *IEEE Transactions on Applied Superconductivity*, **10**(1):178, 2000.

[93] LHC Experiments Committee. ALICE: Technical Proposal. URL `https://cds.cern.ch/record/293391`. [Online; Accessed September 2019]. Report no. CERN-LHCC-95-71, CERN, 1211 Geneva 23, Switzerland, 1995.

[94] LHC Experiments Committee. ATLAS: Technical Proposal for a general-purpose pp Experiment at the Large Hadron Collider at CERN. URL `https://cds.cern.ch/record/290968`. [Online; Accessed September 2019]. Report no. CERN-LHCC-94-43, CERN, 1211 Geneva 23, Switzerland, 1994.

[95] LHC Experiments Committee. CMS: Technical Proposal. URL `https://cds.cern.ch/record/290969`. [Online; Accessed September 2019]. Report no. CERN-LHCC-94-38, CERN, 1211 Geneva 23, Switzerland, 1994.

[96] LHC Experiments Committee. LHCb: Technical Proposal. URL `https://cds.cern.ch/record/622031`. [Online; Accessed September 2019]. Report no. CERN-LHCC-98-004, CERN, 1211 Geneva 23, Switzerland, 1998.

[97] R. Li, A. Onishi, T. Satoh, and Y. Kanazawa. Temperature Stabilization on Cold Stage of 4 K G-M Cryocooler. *Cryocoolers 9. Springer, Boston, MA*, pages 765-771, 1997.

[98] J. H. Londenhovius, E. M. Hornveld, A. den Ouden, W. A. J. Wessel, and H. H. J. ten Kate. Progress in the development of Nb_3Sn conductors based on the "Powder in tube" method with finer filaments. *IEEE Transactions on Applied Superconductivity*, **9**(2):1451, 1999.

[99] F. London and H. London. The Electromagnetic Equations of the Supraconductor. *Proceedings of the Royal Society of London Series A*, **149**:71, 1935.

[100] C. Lorin, D. Durante, and M. Segreti. EuroCirCol 16 T Block-Coils Dipole Option for the Future Circular Collider. *IEEE Transactions on Applied Superconductivity*, **27**(4):1, 2017.

[101] M. C. Jewell. *The effect of strand architecture on the fracture propensity on niobium-tin composite wires*. PhD thesis, University of Wisconsin – Madison, Madison, Wisconsin, USA, 2019.

[102] K. Maki. The magnetic properties of superconducting alloys I. *Physics Physique Fizika*, **1**:21, 1964.

[103] K. Maki. The magnetic properties of superconducting alloys. II. *Physics Physique Fizika*, **1**:127, 1964.

[104] M. Mangano, P. Azzi, M. D'Onofrio, and M. Mccullough. Physics at its limits. *CERN Courier*, 57 (4):34, 2017. URL `https://cds.cern.ch/record/2259560`. [Online; Accessed September 2019].

[105] V. Marinozzi, G. Bellomo, B. Caiffi, P. Fabbricatore, S. Farinon, A. M. Ricci, M. Sorbi, and M. Statera. Conceptual design of a 16 T cos θ bending dipole for the future circular collider. *IEEE Transactions on Applied Superconductivity*, **28**(3):1, 2018.

[106] W. D. Markiewicz. Elastic stiffness model for the critical temperature T_c of Nb_3Sn including strain dependence. *Cryogenics*, **44**:767, 2004.

[107] B. T. Matthias, T. H. Geballe, S. Geller, and E. Corenzwit. Superconductivity of Nb_3Sn. *Physical Review*, **95**:1435, 1954.

[108] W. L. McMillan. Transition temperature of strong-coupled superconductors. *Physical Review*, **167**:331, 1968.

[109] W. Meißner and R. Ochsenfeld. Ein neuer Effekt bei Eintritt der Supraleitfähigkeit. *Naturwissenschaften*, **21**:787, 1933.

[110] M. G. T. Mentink. *An experimental and computational study of strain sensitivity in superconducting Nb_3Sn*. PhD thesis, University of Twente, Enschede, The Netherlands, 2014.

[111] A. Milanese and M. Bohdanowicz. Twin aperture bending magnets and quadrupoles for FCC-ee. *IEEE Transactions on Applied Superconductivity*, **28**(3):1, 2018.

[112] N. Mitchell. Finite element simulations of elasto-plastic processes in Nb_3Sn strands. *Cryogenics*, **45**(7):501, 2005.

[113] H. Müller and Th. Schneider. Heat treatment of Nb_3Sn conductors. *Cryogenics*, **48**(7):323, 2008.

[114] G. Mondonico, B. Seeber, A. Ferreira, B. Bordini, L. Oberli, L. Bottura, A. Ballarino, R. Flükiger, and C. Senatore. Effect of quasi-hydrostatical radial pressure on I_c of Nb_3Sn wires. *Superconductor Science and Technology*, **25**(11):115002, 2012.

[115] D. F. Moore, R. B. Zubeck, J. M. Rowell, and M. R. Beasley. Energy gaps of the $A-15$ superconductors Nb_3Sn, V_3Si, and Nb_3Ge measured by tunneling. *Physical Review B*, **20**:2721, 1979.

[116] L. Muzzi et al. Direct observation of Nb_3Sn lattice deformation by high-energy x-ray diffraction in internal-tin wires subject to mechanical loads at 4.2 K. *Superconductor Science and Technology*, **25**(5):054006, 2012.

[117] J. Nagamatsu, N. Nakagawa, T. Muranaka, Y. Zenitani, and J. Akimitsu. Superconductivity at 39 K in magnesium diboride. *Nature*, **410**:63, 2001.

[118] H. Oguro, S. Awaji, K. Watanabe, M. Sugimoto, and H. Tsubouchi. Mechanical and superconducting properties of Nb_3Sn wires with Nb-rod-processed CuNb reinforcement. *Superconductor Science and Technology*, **26**(9):094002, 2013.

[119] H. Oguro, S. Awaji, K. Watanabe, M. Sugimoto, and H. Tsubouchi. Prebending Effect for Mechanical and Superconducting Properties of Nb-Rod-Processed Cu–Nb Internal-Reinforced Nb_3Sn Wires. *IEEE Transactions on Applied Superconductivity*, **24**(3):1, 2014.

[120] T. P. Orlando, E. J. McNiff, S. Foner, and M. R. Beasley. Critical fields, Pauli paramagnetic limiting, and material parameters of Nb_3Sn and V_3Si. *Physical Review B*, **19**:4545, 1979.

[121] A. B. Pippard and W. L. Bragg. An experimental and theoretical study of the relation between magnetic field and current in a superconductor. *Proceedings of the Royal Society of London Series A*, **216**(1127):547, 1953.

[122] D. Pulikowski, F. Lackner, C. Scheuerlein, D. Meinel, F. Savary, D. Tommasini, and M. Pajor. Testing mechanical behavior of Nb_3Sn Rutherford cable during coil winding. *IEEE Transactions on Applied Superconductivity*, **27**(4):1, 2017.

[123] D. Pulikowski, F. Lackner, C. Scheuerlein, F. Savary, D. Tommasini, and M. Pajor. Windability tests of Nb_3Sn Rutherford cables for HL-LHC and FCC. *IEEE Transactions on Applied Superconductivity*, **28**(3):1, 2018.

[124] PyVISA – Python VISA bindings for GPIB, RS232, TCP/IP and USB instruments. URL `https://pypi.org/project/PyVISA`. [Online; Accessed September 2019].

[125] R. McFee. Optimum Input Leads for Cryogenic Apparatus. *Review of Scientific Instruments*, **30**(2):98, 1959.

[126] I. I. Rabi. A Method of Producing Uniform Magnetic Fields. *Review of Scientific Instruments*, **5**(2):78, 1934.

[127] J. N. Rjabinin and L. W. Schubnikow. Magnetic Properties and Critical Currents of Supra-conducting Alloys. *Nature*, **135**:581, 1935.

[128] L. Rossi and L. Bottura. Superconducting magnets for particle accelerators. *Reviews of Accelerator Science and Technology*, **5**:51, 2012.

[129] ROXIE (Routine for the Optimization of magnet X-sections, Inverse field calculation and coil End design) programme package. URL `https://cern.ch/roxie`. [Online; Accessed September 2019]. CERN, 1211 Geneva 23, Switzerland.

[130] J. Royet and R. Scanlan. Manufacture of keystoned flat superconducting cables for use in SSC dipoles. *IEEE Transactions on Magnetics*, **23**(2):480, 1987.

[131] J. L. Rudeiros Fernandez, J. C. Perez, S. Ferradas Troitino, M. Guinchard, P. Grosclaude, M. Crouvizier, S. Langeslag, S. Izquierdo Bermudez, and F. Savary. Characterisation of the Mechanical Properties of Impregnated Nb_3Sn Coils. *IEEE Transactions on Applied Superconductivity*, **29**(5):1, 2019.

[132] S. Russenschuck. *Field Computation for Accelerator Magnet*. Wiley-VCH Verlag, Weinheim, Germany, 2010. ISBN 978-3527407699.

[133] C. Sanabria. *A new understanding of the heat treatment of Nb_3Sn superconducting wires*. PhD thesis, Florida State University, Tallahassee, Florida, USA, 2017.

[134] C. Sanabria, P. J. Lee, W. Starch, I. Pong, A. Vostner, M. C. Jewell, A. Devred, and D. C. Larbalestier. Evidence that filament fracture occurs in an ITER toroidal field conductor after cyclic Lorentz force loading in SULTAN. *Superconductor Science and Technology*, **25**(7):075007, 2012.

[135] F. Savary. WP11 in a nutshell – 11 T Dipoles. Internal note (EDMS no. 1559231), CERN, 1211 Geneva 23, Switzerland, 2015.

[136] F. Savary et al. Progress on the Development of the Nb_3Sn 11 T Dipole for the High Luminosity Upgrade of LHC. *IEEE Transactions on Applied Superconductivity*, **27**(4):1, 2017.

[137] C. Scheuerlein, M. Di Michiel, and A. Haibel. On the formation of voids in internal tin Nb_3Sn superconductors. *Applied Physics Letters*, **90**(13):132510, 2007.

[138] C. Scheuerlein, M. Di Michiel, and F. Buta. Synchrotron Radiation Techniques for the Characterization of Nb_3Sn Superconductors. *IEEE Transactions on Applied Superconductivity*, **19**(3):2653, 2009.

[139] C. Scheuerlein, G. Willering, A. Verweij, A. Bonasia, L. Oberli, M. Taborelli, and R. Richter. Aluminum strand coating for increasing the interstrand contact resistance in Rutherford type superconducting cables. *IEEE Transactions on Applied Superconductivity*, **19**(3):2463, 2009.

[140] C. Scheuerlein, M. Di Michiel, G. Arnau, R. Flükiger, F. Buta, I. Pong, L. Oberli, and L. Bottura. Coarse Nb_3Sn Grain Formation and Phase Evolution During the Reaction of a High Sn Content Internal Tin Strand. *IEEE Transactions on Applied Superconductivity*, **21**(3):2554, 2011.

[141] C. Scheuerlein, M. Di Michiel, M. Hofmann, M. Lorentzon, F. Lackner, R. Flükiger, F. Savary, and L. Bottura. Residual strain in the Nb_3Sn 11 T dipole magnet coils for HL-LHC. *Superconductor Science and Technology*, **30**(12):125002, 2017.

[142] C. Scheuerlein, F. Wolf, M. Lorentzon, and M. Hofmann. Direct measurement of Nb_3Sn filament loading strain and stress in accelerator magnet coil segments. *Superconductor Science and Technology*, **32**(4):045011, 2019.

[143] D. Schoerling et al. The 16 T Dipole Development Program for FCC and HE-LHC. *IEEE Transactions on Applied Superconductivity*, **29**(5):1, 2019.

[144] SciPy: Open source scientific tools for Python. URL `https://www.scipy.org`. [Online; Accessed September 2019].

[145] B. Seeber, A. Ferreira, V. Abacherli, T. Boutboul, L. Oberli, and R. Flükiger. Transport Properties up to 1000 A of Nb_3Sn Wires Under Transverse Compressive Stress. *IEEE Transactions on Applied Superconductivity*, **17**(2):2643, 2007.

[146] B. Seeber, A. Ferreira, F. Buta, C. Senatore, T. Boutboul, L. Oberli, and R. Flükiger. Transport Properties of a PIT-Nb_3Sn Strand Under Transverse Compressive and Axial Tensile Stress. *IEEE Transactions on Applied Superconductivity*, **18**(2):976, 2008.

[147] B. Seeber, C. Senatore, F. Buta, R. Flükiger, T. Boutboul, C. Scheuerlein, L. Oberli, and L. Rossi. Electromechanical behaviour of PIT Nb_3Sn wires for NED. *Proceedings - Workshop on Accelerator Magnet Superconductors, Design and Optimization, WAMSDO 2008*, page 37, 2009.

[148] C. Senatore. Electromechanical Properties of Technical Superconductors. Presented on the ESAS/EASITrain Summer School on Applied Superconductivity, Vienna, Austria, 2018. URL `https://indico.cern.ch/event/663949/timetable`. [Online; Accessed September 2019].

[149] C. Senatore, D. Uglietti, V. Abacherli, A. Junod, and R. Flükiger. Specific Heat, A Method to Determine the T_c Distribution in Industrial Nb_3Sn Wires Prepared by Various Techniques. *IEEE Transactions on Applied Superconductivity*, **17**(2):2611, 2007.

[150] R. S. Shankhachur, P. Potluri, S. Canfer, and G. Ellwood. Braiding ultrathin layer for insulation of superconducting Rutherford cables. *Journal of Industrial Textiles*, **46**(5):827, 2016.

[151] A. Shepelev and D. Larbalestier. The discovery of type II superconductors. *CERN Courier*, 51(9): 17, 2011. URL `https://cds.cern.ch/record/1734730`. [Online; Accessed September 2019].

[152] SHI Cryogenics Group, Daimlerweg 5a, 64293 Darmstadt, Germany. CH-210 10K Cryocooler Series. URL `http://www.shicryogenics.com/products/10k-cryocoolers/ch-210-10k-cryocooler-series`. [Online; Accessed September 2019].

[153] N. J. Simon, E. S. Drexler, and R. P. Reed. Properties of Copper and Copper Alloys at Cryogenic Temperature. *NIST Monograph*, **117**:7, 1991. URL `https://trc.nist.gov/cryogenics/materials/OFHCCopper/OFHC_Copper_rev1.htm`. [Online; Accessed September 2019].

[154] Z. J. J. Stekly and J. L. Zar. Stable superconducting coils. *IEEE Transactions on Nuclear Science*, **12**(3):367, 1965.

[155] M. D. Sumption, E. W. Collings, R. M. Scanlan, A. Nijhuis, and H. H. J. ten Kate. Core-suppressed AC loss and strand-moderated contact resistance in a Nb-Sn Rutherford cable. *Cryogenics*, **39**(1):1, 1999.

[156] Superconductivity Part 11: Residual resistance ratio measurement – Residual resistance ratio measurement of Nb_3Sn Composite Superconductors. *CEI/IEC 61788-11:2003*, 2003.

[157] Superconductivity Part 2: Critical Current Measurements – DC Critical Current of Nb_3Sn Composite Superconductors. *CEI/IEC 61788-2:2006*, 2006.

[158] C. Tarantini, C. Segal, Z. H. Sung, P. J. Lee, L. Oberli, A. Ballarino, L. Bottura, and D. C. Larbalestier. Composition and connectivity variability of the A15 phase in PIT Nb_3Sn wires. *Superconductor Science and Technology*, **28**(9):095001, 2015.

[159] B. ten Haken, A. Godeke, and H. H. J. ten Kate. The Influence of Compressive and Tensile Axial Strain on the Critical Properties of Nb_3Sn Conductors. *IEEE Transactions on Applied Superconductivity*, 5(2):1909, 1995.

[160] B. ten Haken, A. Godeke, and H. H. J. ten Kate. The strain dependence of the critical properties of Nb_3Sn conductors. *Journal of Applied Physics*, **85**(6):3247, 1999.

[161] H. H. J. ten Kate, H. W. Weijers, and J. M. van Oort. Critical current degradation in Nb_3Sn cables under transverse pressure. *IEEE Transactions on Applied Superconductivity*, **3**(1):1334, 1993.

[162] The MathWorks Inc., Natick, USA. MATLAB R2017a. URL `https://www.mathworks.com`. [Online; Accessed September 2019].

[163] L. Thilly, C. Scheuerlein, U. Stuhr, B. Bordini, and B. Seeber. Residual Strain in a Nb_3Sn Strand Mounted on a Barrel for Critical Current Measurements. *IEEE Transactions on Applied Superconductivity*, **19**(3):2645, 2009.

[164] L. Thilly, M. Di Michiel, C. Scheuerlein, and B. Bordini. Nb_3Sn nucleation and growth in multifilament superconducting strands monitored by high resolution synchrotron diffraction during in situ reaction. *Applied Physics Letters*, **99**(12):122508, 2011.

[165] M. Tinkham. *Introduction to Superconductivity*. Dover Publications, Mineola, USA, 2004. ISBN 978-0486435039.

[166] D. Tommasini et al. The 16 T Dipole Development Program for FCC. *IEEE Transactions on Applied Superconductivity*, **27**(4):1, 2017.

[167] D. Tommasini et al. Status of the 16 T Dipole Development Program for a Future Hadron Collider. *IEEE Transactions on Applied Superconductivity*, **28**(3):1, 2018.

[168] D. Uglietti, B. Seeber, V. Abächerli, A. Pollini, D. Eckert, and R. Flükiger. A device for critical current versus strain measurements up to 1000 A and 17 T on 80 cm long HTS and LTS technical superconductors. *Superconductor Science and Technology*, **16**(9):1000, 2003.

[169] D. F. Valentinis, C. Berthod, B. Bordini, and L. Rossi. A theory of the strain-dependent critical field in Nb_3Sn, based on anharmonic phonon generation. *Superconductor Science and Technology*, **27**(2):025008, 2013.

[170] W. van de Camp. Critical Current versus Transverse Stress and Thermal Stability of a RRP Nb_3Sn Rutherford Cable. Master's thesis, University of Twente, Enschede, The Netherlands, 2012.

[171] D. van Delft and P. Kes. The discovery of superconductivity. *Physics Today*, **63**(9):38, 2010.

[172] J. van Nugteren et al. Powering of an HTS dipole insert-magnet operated standalone in helium gas between 5 and 85 K. *Superconductor Science and Technology*, **31**(6):065002, 2018.

[173] A. P. Verweij, J. Genest, A. Knezovic, D. F. Leroy, J. Marzolf, and L. R. Oberli. 1.9 K test facility for the reception of the superconducting cables for the LHC. *IEEE Transactions on Applied Superconductivity*, **9**(2):153, 1999.

[174] C. R. Walters, I. M. Davidson, and G. E. Tuck. Long sample high sensitivity critical current measurements under strain. *Cryogenics*, **26**(7):406, 1986.

[175] C. Warren, C. Young, and R. G. Budynas. *Roark's Formulas for Stress and Strain*. McGraw-Hill Education, New York, USA, 2001. ISBN 978-0070725423.

[176] P. Welch. The use of fast Fourier transform for the estimation of power spectra: A method based on time averaging over short, modified periodograms. *IEEE Transactions on Audio and Electroacoustics*, **15**(2):70, 1967.

[177] N. R. Werthamer, E. Helfand, and P. C. Hohenberg. Temperature and Purity Dependence of the Superconducting Critical Field, H_{c2}. III. Electron Spin and Spin-Orbit Effects. *Physical Review*, **147**:295, 1966.

[178] G. Willering. *Stability of Superconducting Rutherfordcables for accelerator magnets*. PhD thesis, University of Twente, Enschede, The Netherlands, 2009.

[179] M. N. Wilson. *Superconducting Magnets*. Clarendon Press Oxford, Oxford, UK, 1983. ISBN 978-0198548102.

[180] F. Wolf, P. Ebermann, F. Lackner, D. Mosbach, C. Scheuerlein, K. Schladitz, and D. Schoerling. Characterization of the stress distribution on Nb_3Sn Rutherford cables under transverse compression. *IEEE Transactions on Applied Superconductivity*, **28**(3):1, 2018.

[181] F. Wolf, F. Lackner, M. Hofmann, C. Scheuerlein, D. Schoerling, and D. Tommasini. Effect of epoxy volume fraction on the stiffness of Nb_3Sn Rutherford cable stacks. *IEEE Transactions on Applied Superconductivity*, **29**(5):1, 2019.

[182] C. Wyss. LEP Design Report. URL `https://cds.cern.ch/record/314187`. [Online; Accessed September 2019]. Report no. CERN-AC-96-01-LEP-2, CERN, 1211 Geneva 23, Switzerland, 1996.

[183] X. Xu, M. Sumption, X. Peng, and E. W. Collings. Refinement of Nb_3Sn grain size by the generation of ZrO2 precipitates in Nb_3Sn wires. *Applied Physics Letters*, **104**(8):082602, 2014.

[184] X. Xu, M. D. Sumption, and X. Peng. Internally Oxidized Nb_3Sn Strands with Fine Grain Size and High Critical Current Density. *Advanced Materials*, **27**(8):1346, 2015.

[185] Y. Zhai, L. D'Hauthuille, C. Barth, and C. Senatore. Finite-Element Analysis of Transverse Compressive and Thermal Loads on Nb_3Sn Wires With Voids. *IEEE Transactions on Applied Superconductivity*, **26**(4):1, 2016.

[186] C. Zhou, M. Dhallé, H. H. J. ten Kate, and A. Nijhuis. The Effect of Strain on the Transport Properties of Superconducting Strand and Cable in a Conduit Conductor. *IEEE Transactions on Applied Superconductivity*, **29**(1):1, 2019.

Curriculum Vitae

Personal information

Name	**Patrick Ebermann**
Birth	3rd of July 1987, Tulln (Austria)
Citizenship	Austria
Address	Hofuren 49, 4574 Nennigkofen, Switzerland

Academic and educational background

Since 2015	**Doctoral programme in engineering sciences: Technical physics,** Vienna University of Technology in collaboration with CERN. PhD thesis: *Relevance of the irreversible degradation of superconducting Nb_3Sn wires and cables caused by transverse stress at room temperature within the FCC study at CERN.*
2012–2015	**Master programme in automation,** Vienna University of Technology. Master thesis: *Buildup and control of a demonstrator with sensorless controlled active magnetic bearings and a synchronous reluctance machine.*
2008-2012	**Bachelor programme in electrical engineering and information technology,** Vienna University of Technology.
2002-2007	**College of electronics specialising in technical computer science,** Höhere Technische Bundeslehranstalt Hollabrunn.
1994-2002	Primary and lower secondary school Groß Weikersdorf.

Languages

German	Mother tongue
English	C1
French	A1

Publications

2019	**P. Ebermann**, T. Baumgartner, J. Behnsen, M. Daly, A. Gallifa Terricabras, T. Koettig, F. Lackner, C. Scheuerlein and M. Eisterer. Influence of transverse stress exerted at room temperature on the superconducting properties of Nb_3Sn wires. *Superconductor Science and Technology*, **32**(9):095010, 2019.
2018	**P. Ebermann**, J. Bernardi, J. Fleiter, F. Lackner, F. Meuter, M. Pieler, C. Scheuerlein, D. Schoerling, F. Wolf, A. Ballarino, L. Bottura, D. Tommasini, F. Savary, and M. Eisterer. Irreversible degradation of Nb_3Sn Rutherford cables due to transverse compressive stress at room temperature. *Superconductor Science and Technology*, **31**(6):065009, 2018. F. Wolf, **P. Ebermann**, F. Lackner, D. Mosbach, C. Scheuerlein, K. Schladitz, and D. Schoerling. Characterization of the stress distribution on Nb_3Sn Rutherford cables under transverse compression. *IEEE Transactions on Applied Superconductivity* **28**(3):1, 2018. U. M. Kelly, S. Richter, C. Redenbach, K. Schladitz, C. Scheuerlein, F. Wolf, **P. Ebermann**, F. Lackner, D. Schoerling, and D. Meinel. Nb_3Sn Wire Shape and Cross-Sectional Area Inhomogeneity in Rutherford Cables. *IEEE Transactions on Applied Superconductivity* **28**(4):1, 2018.
2015	M. Hofer, **P. Ebermann**, M. Schrödl. Fully position sensorless control of a magnetically levitated Reluctance Synchronous Machine by three phase active magnetic bearings. *2015 IEEE Symposium on Sensorless Control for Electrical Drives (SLED)* pages 1-5, 2015.